University of Bath

PHD

The stability of free convective boundary layer flows

Paul, Manosh C.

Award date:
2002

Awarding institution:
University of Bath

Link to publication

Alternative formats
If you require this document in an alternative format, please contact:
openaccess@bath.ac.uk

Copyright of this thesis rests with the author. Access is subject to the above licence, if given. If no licence is specified above, original content in this thesis is licensed under the terms of the Creative Commons Attribution-NonCommercial 4.0 International (CC BY-NC-ND 4.0) Licence (https://creativecommons.org/licenses/by-nc-nd/4.0/). Any third-party copyright material present remains the property of its respective owner(s) and is licensed under its existing terms.

Take down policy
If you consider content within Bath's Research Portal to be in breach of UK law, please contact: openaccess@bath.ac.uk with the details. Your claim will be investigated and, where appropriate, the item will be removed from public view as soon as possible.

Download date: 05. May. 2023

THE STABILITY OF FREE CONVECTIVE BOUNDARY LAYER FLOWS

Submitted by Manosh C. Paul
for the degree of
Doctor of Philosophy
of the University of Bath
2002

COPYRIGHT

Attention is drawn to the fact that copyright of this thesis rests with its author. This copy of the thesis has been supplied on condition that anyone who consults it is understood to recognise that its copyright rests with its author and no information derived from it may be published without the prior written consent of the author.

This thesis may be made available for consultation within the University library and may be photocopied or lent to other libraries for the purposes of consultation.

UMI Number: U601895

All rights reserved

INFORMATION TO ALL USERS
The quality of this reproduction is dependent upon the quality of the copy submitted.

In the unlikely event that the author did not send a complete manuscript
and there are missing pages, these will be noted. Also, if material had to be removed,
a note will indicate the deletion.

UMI U601895
Published by ProQuest LLC 2013. Copyright in the Dissertation held by the Author.
Microform Edition © ProQuest LLC.
All rights reserved. This work is protected against
unauthorized copying under Title 17, United States Code.

ProQuest LLC
789 East Eisenhower Parkway
P.O. Box 1346
Ann Arbor, MI 48106-1346

UNIVERSITY OF BATH
LIBRARY
65 - 4 MAR 2003
PhD.

To my parents

Late Debendra Nath Paul
Purnima Rani Paul

Contents

Acknowledgements

First of all, I would like to thank and express deepest gratidude to my supervisors Dr D. A. S. Rees and Dr M. Wilson for their guidance, support and encouragement throughout the work. In particular, Dr D. A. S. Rees, as principal supervisor constantly guided and suggested me to achieve the goal. His observations, comments and constructive suggestions helped me to establish the overall direction of research and move forward to the deep investigation. I am greatly indebted to him for all the help that I received and the experiences that I have gained.

I acknowledge gratefully the receipt of an Overseas Research Studentship (ORS) and a University of Bath Studentship which has supported my studies.

Thanks to all my colleagues, friends, and family who encouraged and assisted me during the studies.

Special thanks to my wife, Jharna, for her patience, love, support, and encouragement during the course of my research.

Manosh C. Paul
September 2002

Abstract

This thesis describes a study of the stability of free convective boundary layer flow over a heated flat plate with respect to wave and vortex disturbances. Four problems are considered using a variety of numerical and analytical methods. We begin with a general introduction in Chapter 1 and a review of the previous works which are relevant to this thesis is presented in Chapter 2.

In Chapter 3 we examine the stability of free convective boundary layer flow over a vertical heated flat plate with respect to two-dimensional wave disturbances. In particular we determine the effect of the overall external geometry on the stability criterion. The fluid domain is taken to be bounded by two semi-infinite flat plates forming a wedge of angle α. The vertical plate is held at a uniform hot temperature while the other is either insulated or is held at the ambient temperature of the fluid. The basic flow used in the analysis is a two-term boundary-layer approximation using the method of matched asymptotic expansions. A modified version of the Keller-box method is used to solve the linearised wave-disturbance equations numerically, whilst the basic flow is solved by using standard a shooting method with Newton-Raphson iteration together with a 4^{th} order Runge-Kutta scheme. The neutral curves have been delineated for different values of wedge angle, α, where the working fluids are water and air. We find that the critical distance from the leading edge beyond which disturbances grow is strongly dependent on α, and this suggests that the external geometry of the fluid domain exerts a considerable influence on stability criteria. We consider two fluids, air ($Pr = 0.7$) and water ($Pr = 6.7$).

In Chapter 4 we examine the vortex mode of instability of free convective boundary layer flow over an inclined upward facing heated flat surface. We assume that the disturbances have the form of longitudinal vortices but are stationary in the streamwise direction. Again the fluid domain is taken to be bounded by two semi-infinite flat plates forming a wedge of angle α. However the uniform hot plate is inclined with angle δ from the vertical, while the other is either insulated or is held at the ambient temperature of the fluid. The basic flow used in the analysis is a two-term boundary layer approximation using matched asymptotic expansion techniques. We find that the neutral distance from the leading edge is strongly dependent on both δ and α. We also consider here two fluids, air ($Pr = 0.7$) and water ($Pr = 6.7$).

In Chapter 5 numerical techniques (DNS) are used to study the receptivity of the boundary layer flow over a heated vertical flat plate to small-amplitude thermal disturbances placed fairly close to the leading edge. The fully elliptic nonlinear time dependent Navier-Stokes and energy equations are solved to determine the steady state boundary-layer flow, while a linearised version of the same code is used to determine the stability characteristics. We investigate (i) the ultimate fate of localised thermal disturbances and (ii) the effect of localised surface temperature oscillations as a means of understanding the stability characteristics of the boundary layer. We show that there is a favoured frequency of excitation for the time-periodic disturbance which maximises the local response. We consider only air ($Pr = 0.7$) as working fluid. Detailed results are compared with those obtained using parallel flow theory.

In Chapter 6 we extend the DNS techniques of Chapter 5 to study the nonlinear receptivity of the free convective boundary layer flow by introducing only time periodic thermal disturbances near the leading edge. When the amplitude of the disturbances is sufficiently small we recover the results of the linear theory of Chapter 5. However, nonlinear effects are found to manifest themselves in a variety of ways. When the excitation frequency is sufficiently below the most dangerous frequency cell-splitting occurs and there is a superharmonic transition to waves with double, triple or quadruple the number of cells, depending on the precise frequency. At higher frequencies the opposite process occurs. Cell merging takes place which we call a subharmonic transition.

Finally, in Chapter 7 we write a general discussion with a recommendation of future works.

Nomenclature

The notation used in this thesis is given here in the following order: Roman characters, Greek symbols, Subscripts, Superscripts, and Abbreviations.

Roman Characters

a, b	scaling factors
A	disturbance amplitude
A_0	a constant
d	natural lengthscale, $\left(\frac{\nu^2}{g\beta\Delta T}\right)^{1/3}$
F, G, H, S, Q	disturbances
$\mathcal{F}$	differentiation of F with respect to k $(= \frac{\partial F}{\partial k})$
F_0, H_0	zero/leading order boundary layer solutions
F_1, H_1	first order boundary layer solutions
g	gravitational acceleration
$\mathcal{G}$	differentiation of G with respect to k $(= \frac{\partial G}{\partial k})$
$\mathcal{H}$	differentiation of H with respect to k $(= \frac{\partial H}{\partial k})$
J	Jacobian operator
k	spatial wavenumber $(= 2\pi/l)$ (or vortex wavenumber)
K	maximum local asymptotic heat transfer
l	spatial wavelength
M	maximum absolute value of heat transfer

P	dynamical fluid pressure
Pr	Prandtl number ($= \frac{\nu}{\kappa}$)
$\bar{r}$	dimensional radial distance from origin, $(\bar{x}^2 + \bar{y}^2)^{1/2}$
r	nondimensional radial distance from origin, $(x^2 + y^2)^{1/2}$
$\mathcal{S}$	differentiation of S with respect to k ($= \frac{\partial S}{\partial k}$)
t	nondimensional time
$\bar{t}$	time
T	temperature of fluid
$\bar{u}, \bar{v}$	dimensional fluid velocities in the $\bar{x}$, $\bar{y}$ directions
u, v, w	fluid velocities in the x, y, and z directions
$\hat{u}, \hat{v}, \hat{w}$	perturbation fluid velocity components
U	natural velocity scale, $(g\beta\nu\Delta T)^{1/3}$
$\bar{x}, \bar{y}$	Cartesian coordinates
x, y, z	nondimensional Cartesian coordinates

Greek Symbols

α	wedge angle
β	coefficient of thermal expansion
δ	inclination of heated surface from the vertical
δt	timestep
$\delta\xi$	steplength in ξ direction

$\delta\eta$	steplength in η direction
γ	scaled wedge angle ($= \frac{12\alpha}{\pi}$)
ΔT	temperature difference between hot and cold ($= T_w - T_\infty$)
ϵ	small value ($\ll 1$)
ζ	representative variable
ξ, η	similarity variables
θ	scaled temperature
κ	thermal diffusivity
λ	temporal growth rate ($= \lambda_R + i\lambda_I$)
λ_I	imaginary part of λ (but -$\lambda_I = \lambda$, a frequency in Chapters 5, 6)
ν	fluid viscosity
ρ	density of fluid
ϕ	angular coordinate
ψ	streamfunction
Ψ	streamfunction in outer region
ω	vorticity
$\bar{\psi}, \bar{\omega}, \bar{\theta}$	steady flow variables
$\hat{\psi}, \hat{\omega}, \hat{\theta}$	perturbation variables

Subscripts

B	basic flow

$basic$	basic boundary layer approximation
$b1$	start of buffer region
$b2$	end of buffer region
c	critical value
D	disturbance
I	imaginary part
max	maximum value
$mean$	mean value
min	minimum value
n	normal derivative
new	present iteration value
old	previous iteration value
opt	optimum value
R	real part
w	wall or heated surface
∞	ambient conditions

Superscripts

$*$	scaled distance value
$'$	derivatives with respect to η

Abbreviations

BF	Buffer Function
DNS	Direct Numerical Simulation
HT	Heat Transfer
PDE	Partial Differential Equation
PFA	Parallel Flow Approximation
RC	Receptivity Coefficient
TS	Tollmien-Schlichting

List of Figures

Chapter 1

Introduction

The general problem of stability of free convection boundary layer flows is a combination of the problems of hydrodynamic instability and thermal instability. It is well known that boundary layer flows are unstable under certain conditions in the sense that a small disturbance imposed on the basic flow can grow indefinitely in time; this is often a hydrodynamic instability. It is also well known that a static fluid in a gravitational field in which a constant temperature gradient is maintained is unstable under certain conditions. This thermal instability arises when the gravity vector has a component parallel to the temperature gradient and when lighter fluid lies under heavier fluid.

When a flow is analysed for its stability various possibilities exist. A stability analysis may consider either small or large amplitude disturbances. If all small amplitude disturbances decay with time ($t \rightarrow \infty$) then the flow is said to be

linearly stable since the equations solved are the full equations which have been linearised about the basic flow. In this case the perturbation of each quantity can be resolved into independent components or modes varying with time t, and contains an exponential factor $e^{\lambda t}$ for some complex constant. If the real part of λ is found to be positive for any mode, the system is deemed unstable because a general initial small perturbation of the system would grow exponentially in time. Otherwise the system is stable. If all large amplitude disturbances decay then the flow is globally stable and is unique; such an analysis is termed an *energy stability* analysis as it considers the variation with time of an energy functional. In many cases, such as the Bénard problem, the two methods give identical results. But there are flows, such as Hagen-Poiseuille flow, which may be destabilised by large disturbances, but not by small disturbances.

When a flow in an unbounded domain is unstable it is also possible to characterise the instability according to whether it is convective (or, less confusingly in the free convection context, advective) or absolute. Advective instabilities grow in time but will eventually decay at any chosen position within the boundary layer – in such cases the speed of advection is greater than upstream diffusion. The main subject of this thesis, wave instabilities in vertical free convective boundary layer flow, is an example of an advective instability. On the other hand, upstream diffusion is a stronger influence than speed of advection for absolute instabilities. A growing region of instability will develop both upstream and downstream of its point of introduction.

In this thesis we consider the instability of thermal boundary layer flows from uniform temperature heated surfaces. Most of this work is concerned with a vertical surface, but one chapter is devoted to inclined surfaces. It is now well-known that the primary instability for a vertical case occurs in the form of two-dimensional waves travelling in the streamwise direction (see Nachtsheim (1963)). This instability is advective in nature. But when the plate is inclined upward facing, there is a different mode of instability which mainfests itself in the form of longitudinal vortices. These vortices appear at some distance from the leading edge and grow in the downstream direction. These have been observed experimentally by Sparrow & Husar (1969) and Lloyd & Sparrow (1970) and the instability is absolute. Further experiments suggest that there is a transition from waves to vortices when the plate is lowered to a point somewhere between 14^0 and 17^0 from the vertical, when considering water as the working fluid.

It is not the intention of this thesis to examine the transition in modal identities as the surface inclination varies. Our intension is to attempt a more accurate analysis and a deeper understanding of the primary instability mechanisms of vertical and inclined thermal boundary layer flow. To this end we use a more accurate representation of the basic boundary layer: (i) using a two-term matched asymptotic expansion in a traditional parallel-flow approximation analysis and (ii) a numerical solution of the full equations in linearised and nonlinear elliptic simulations.

The thesis broadly takes the following format. Chapter 2 contains a review of the

previous work related to the wave and vortex type of instabilities of free convective boundary layer flows. In Chapter 3, we analyse how a higher order analysis of the basic flow affects the linear instability of vertical free convection flow. The fluid domain is bounded by two separate flat plates forming a wedge angle α (see Figure 3.1). The hot plate is positioned vertically with a uniform surface temperature while the other is insulated or is held at the ambient temperature of the fluid. The second plate is at an arbitrary angle. The full disturbance equations are reduced to ordinary differential form in the usual way and are solved numerically to determine how the shape of the overall fluid domain affects the stability criteria. We use a standard shooting method which employs Newton-Raphson techniques and a 4th order Runge-Kutta method, but a modified version of the Keller-box method is used to solve the disturbance equations. Although the leading order basic flow is independent of wedge angle α, further terms are a function of α and these have a strong effect on the stability criterion.

In Chapter 4 the influence of higher order effects on the vortex instability of thermal boundary layer flow from inclined surfaces is analysed. As in the previous chapter, the fluid domain is bounded by two semi-infinite flat plates (see Figure 4.1). In this case there is a second angle, the inclination angle δ, which corresponds to the position of the upward facing hot plate from the vertical. We use the same matched asymptotic expansion method which is described in Chapter 3 to study the basic flow. We find that the leading order basic term is independent of both α and δ when written approximately, but further terms are functions of α and δ. The effect on the stability of varying both parameters α

and δ is investigated.

In Chapter 5 we perform a numerical investigation (Direct Numerical Simulation) of the linear instability of thermal boundary layer flow over a vertical surface. The instability is generated by introducing various thermal disturbances near the leading edge. This process is well known as a 'receptivity' mechanism by which the external disturbance is converted into instability waves. When the initial amplitude of the disturbance is small, these modes are referred to as the Tollmien-Schlichting (TS) type in Blasius boundary layer flow. The numerical scheme is a second order accurate finite difference method in both time and space. We find that the instability is advective and the response of the boundary layer consists of a starting transient followed by the large-time asymptotic state.

The corresponding non-linear wave instabilities are studied in Chapter 6. The same numerical techniques used in Chapter 5 have also been implemented here. We find that there are various types of asymptotic periodic response which we term as harmonic, superharmonic and subharmonic. An asymptotic response is said to be superharmonic if its fundamental frequency is a multiple n ($n = 2, 3, 4, ...$) of the original frequency. On the other hand the response is subharmonic if its fundamental frequency is a fraction $\frac{1}{n}$ ($n = 2, 3, 4, ...$) of the original frequency. The type of response which arises can depend fairly sensitively on the governing parameters such as the forcing frequency and amplitude. We present various types of superharmonic transitions to waves with double, triple, and quadruple the number of cells. We also present subharmonic transitions consid-

ering higher excitation frequencies. In these cases the opposite process occurs and cell merging takes place. The superharmonic and subharmonic transitions are common phenomena in the field of nonlinear instabilities and frequently occur in various branches of engineering and the physical sciences. We also find that, for higher excitation frequencies, when the nonlinearity is saturated, the mean flow differs from the main basic flow and there is distortion of mean flow between the linear and nonlinear regime. The mean flow distortion contributes to the nonlinear saturation and that itself is generated by the instability development.

Conclusions and recommendations for future work are presented in Chapter 7.

Chapter 2

Review of previous work

In this Chapter we review the published literature and describe the general background for the flows considered here more specifically. The current knowledge of thermal boundary layer instabilities is discussed, a brief outline of the role of receptivity is given and the methods used in studying boundary layer instabilities are summarised.

2.1 The parallel flow approximation

It is well known that the process of laminar/turbulent transition inside boundary layers is caused by a sequence of instabilities. The presence of non-linear terms in the Navier-Stokes equations are all that is required to generate instabilities. The earliest stability analyses were of plane Poiseuille flow between two parallel plates,

which consists of a flow with parallel streamlines. A straightforward linearised stability analysis reduces the governing Partial Differential Equations (PDEs) to ordinary differential form because the flow is a parallel flow. This resulting equation is known as the Orr-Sommerfeld equation and it presupposes that the amplitude of the waves is small. This equation was first derived by Orr (1907) and Sommerfeld (1908).

Later, Tollmien (1929) analysed the stability criterion for Blasius boundary layer flow using the same methodology. Such boundary layers have streamlines which are only approximately parallel and therefore an Orr-Sommerfeld-like equation is obtained only by neglecting terms which are from non-parallel sources such as the slow growth of the boundary layer – it is this procedure which is known as the parallel flow approximation. By proceding in this way Tollmien computed the critical local Reynolds number (or, equivalently, x_c, the location beyond which waves are amplified) and found the neutral stability curve (identifying the range of unstable wave frequencies). Schlichting (1933) extended Tollmien's analysis by including growth rates. The two-dimensional waves modelled in such analyses are today known as Tollmien-Schlichting (TS) waves.

The parallel flow approximation has been used very extensively on a wide range of nonparallel flows in the hope that the ensuing results are accurate.

Haaland & Sparrow (1973b,c) allowed for the nonparallelism which is inherent in free convective flows by incorporating x-dependent terms in their disturbance

equations, which are the equivalent to the Orr-Somerfeld equations. In Haaland & Sparrow (1973b), they concluded that such nonparallel effects serve to increase slightly the neutral distance relative to that obtained by Nachtsheim (1963) who used parallel flow theory.

Smith (1979) determined a 4-term representation of the neutral curve (upper and left hand branch) for Blasius flow using both parallel and fully nonparallel theories in the limit of large x and found fairly good agreement with a numerical approach. More recently Healey (1995) has been able to recover a large part of the neutral curve for Blasius flow using a large -x analysis and this yields a good approximation to the curve obtained using the Parallel Flow Approximation (PFA). Thus, for waves, it appears that PFA can yield accurate stability criteria.

For vortices however Hall (1982, 1983) showed easily that the PFA does not even yield the correct type of exponential decay of the disturbances into the external field. Recent work on the linear vortex development in free convection boundary layers in porous media has shown that the PFA yields neutral distances which are substantially larger than those obtained using a constant nonparallel theory (see Rees 2001). Thus, for vortices, the PFA can yield results which are quantitatively and qualitatively misleading. In other contexts, the PFA has been found to give inaccurate and sometimes unphysical results for the nonlinear interactions of the waves and vortices (see Hall & Smith (1988)).

2.2 Overview of thermal boundary layer instability

There is a very large literature associated with the analysis of thermal boundary layer instabilities. A comprehensive review of the wider topic of thermal boundary layer flows in general may be found in Gebhart (1979) where over thirty papers on thermal boundary layer instabilities are quoted. However, many of these are concerned with either thermal plumes or convection induced by constant heat flux surfaces. There are only few papers dealing with constant temperature surfaces, to our knowledge. The present knowledge of how thermal boundary layers induced by a constant temperature surface affect the transition to turbulence has progressed only slightly beyond what is known by means of linear theory based on the parallel flow approximation. Here, we attempt to give a brief review of this literature.

2.2.1 Wave instabilities

The basic flow for the vertical free convection boundary layer flow arises from the presence of buoyancy forces, but the primary instability is hydrodynamic in origin since it cannot be thermoconvective. Thus this boundary layer shares some stability characteristics with the Blasius boundary layer and it is subject to a primary mode of instability in the form of two-dimensional waves travelling in the

streamwise direction (see Nachtsheim (1963), Hieber & Gebhart (1971), Haaland & Sparrow (1973a), Godaux & Gebhart (1974), and Szewczyk (1962)). In terms of predicting the streamwise station beyond which wave disturbances grow, there appears to be a fairly good correlation between experimental work and (linear) theoretical studies based on the parallel flow approximation, as demonstrated by Smith (1979), for Blasius flow. There is a strong correspondence between the vertical thermal boundary layer and Blasius boundary layer, where waves comprise the primary instability.

The most recent theoretical and experimental works associated with the stability of the free convection thermal boundary layers have been undertaken by Armfield, Brooker, Daniels, Patterson and Schöpf. One set of studies is concerned with the flow which is generated by a suddenly heated vertical wall (see Daniels & Patterson (1997), Brooker *et al* (2000), Daniels & Patterson (2001), Patterson *et al* (2002)); and the other is the sudden heating of the sidewalls in a rectangular cavity (see Schöpf & Patterson (1996), Brooker *et al* (1997)). In Brooker *et al* (2000), two different situations are considered. Firstly, random perturbations, by which an artificial external heat soruce is distributed throughout the boundary layer. Secondly, this perturbation heat source is a continuous sinusoidal function in space.

The early experiment by Szewczyk (1962), who used water, showed that the developing waves are themselves destabilised by the appearance of a twin longitudinal vortex structure. One of the vortices lies close to the heated surface, and

the other lies further out, beyond the point where the basic streamwise velocity achieves its maximum value. He notes a very distinct backward-facing hook-like structure which exists in the developing flow upstream of the transition to fully developed turbulence. His experiment was for a constant temperature surface and to date there are no theoretical studies of this particular aspect, and the paper is the only one to date which hints at secondary instability mechanisms for vertical boundary layer stability.

2.2.2 Vortex instabilities

Sparrow & Husar (1969) performed experiments on an inclined heated surface in water and observed that the flow was unstable to three-dimensional longitudinal vortices. The wavelength of these vortices was found to be strongly dependent on the overall temperature difference between the surface and the ambient surrounding but practically independent of the angle of inclination. Lloyd & Sparrow (1970) continued these experiments by investigating the stability of natural convection flow induced by upward facing surfaces inclined away from the vertical. With water as the working fluid, it was found that waves provided the dominant primary mode of instability whenever the inclination is less than 14^0 from the vertical. When the inclination is greater than 17^0, however, the instability is characterised by longitudinal vortices. In the intermediate range of inclinations waves and vortices seem to coexist; there appears to be a gradual change from one mode of instability to another with no evidence of hysteresis.

On the theoretical side, which again comprises only linear stability analyses to date (with one exception detailed below), Iyer & Kelly (1974), on using the parallel flow approximation, found that both modes become linearly unstable at the same downstream location at an inclination from the vertical of only 4^0. They argue that this result is consistent with the experimental work when account is taken of modal amplification rates. Both modes individually are sufficiently strong to be first observed at the same streamwise location when the inclination is 17^0. This paper deals with water as the working fluid, for which the Prandtl number was taken to be 6.7.

Recently, experiments were conducted by Zuercher *et al* (1998) to study longitudinal vortices on the upper surface of an inclined heated plate. This is the first time that the spatial growth rate of vortices (to determine how the circulation in the vortices grows with distance from the leading edge) have been found using velocity measurements. They also found a general qualitative agreement with the results of Iyer & Kelly (1974) and concluded that the theoretical prediction of growth rate is generally higher than experimental measurement.

Many other linear stability analyses for the generally inclined problem have appeared in the literature with varying degrees of complexity. In this regard we would like to mention the paper by Kahawita & Meroney (1974) and the slightly more recent very comprehensive analysis by Chen & Tzuoo (1982). However, all these papers have the common feature that some variant of parallel flow approximation has been assumed, despite appearances to the contrary in at least one

title (see Haaland & Sparrow (1973a)).

From the above it is clear that the global picture of the form taken by the primary instability at onset is known, at least for a $Pr = 6.7$ fluid. However, little can be stated about the interaction between waves and vortices at inclinations near to the vertical. Linear theory is unable to help in this regard, and therefore nonlinear effects must be taken into account in order to describe these modal interactions and to clarify the role played by the form of the disturbance initiating the primary instabilities.

The situation regarding the form of the secondary instability is not nearly so well-known. A paper by Chen *et al* (1991) on the inclined boundary layer describes the weakly nonlinear development of a longitudinal vortex disturbance. This work, which also relies on the parallel flow approximation, examines spanwise pairing of vortices as a possible means of initiating the transition to turbulence. This analysis would seem to apply when the heated surface is at moderate angles from the horizontal, and is motivated by the appearance of the secondary modes shown in photographs of experiments by Lloyd & Sparrow (1970). On the other hand, when the heated surface is much closer to the horizontal, Lloyd & Sparrow's experiments suggest that longitudinal vortices are destabilised by a pair of oblique vortices. The resulting disturbance planform has the vortices displaying wavy boundaries.

The delineation of the various secondary instability mechanisms would seem to

be a much more complicated task than that of the primary instabilities. Indeed there is no guarantee that the above brief survey covers all possible mechanisms, especially as some papers from which we have drawn information were concerned only with the primary mechanisms.

The rather depressing picture we have drawn shows that much more work could and should be devoted to understanding and delineating both primary and secondary mechanisms for various Prandtl numbers.

2.3 Receptivity works

Receptivity is a classic mechanism by which external disturbances in the free stream such as vorticity, velocity, or sound, enter into the boundary layer (as small fluctuations of the basic state) and excite unstable modes. The process by which external disturbances are converted into Tollmien-Schlichting (TS) type instability waves, is called the receptivity of the boundary layer. When disturbances are periodic in time and of sufficiently small amplitude, then the resulting Tollmien-Schlichting (TS) waves will also be time-periodic.

The 'receptivity co-efficient' is defined as the ratio of the maximum TS wave amplitude at an x-location and the amplitude of the imposed free-stream disturbance, which is denoted as $RC_x = \frac{|AMP_{TS}|}{|AMP_{FSD}|}$ (see Wanderley & Corke (2001) and Haddad & Corke (1998)), but different investigators have defined this co-efficient

in different ways, even giving different names such as 'receptivity efficiency' (see Collis & Lele (1999)).

The term 'receptivity' was first introduced by Morkovin (1969) and this is the first stage of the transition process. In our receptivity problems (see Chapters 5 and 6), we consider a thermal receptivity process by which external temperature disturbances are imposed near the leading edge. The TS waves generated then grow or decay in accordance with an approximate linear stability theory. The present receptivity results suggest that the waves experience considerable decay before reaching their neutral stability point, which is physically expected.

In Chapters 5 and 6 we have applied the thermal equivalent of the "vibrating ribbon experiment" to vertical free convection. Once the flow has settled and transients have excited the computational domain, it is possible to determine how the amplitude of the disturbance (as given, say, by the maximum heat transfer over one period) varies with both x and the disturbance frequency. The resulting neutral curve may then be compared with parallel flow theory.

Early analytical studies of receptivity were based on the Orr-Sommerfeld equation to describe the induction of free-stream disturbances into the boundary layer (see Rogler & Reshotko (1975) and Tam (1981)). Again, the understanding of the receptivity process has largely come from asymptotic analysis. In this regard, we can mention the receptivity studies of Goldstein (1983, 1985). His works have been focused on localised disturbances from either the leading edge

(Goldstein 1983) or changes in the wall geometry (Goldstein 1985), including local roughness. His analysis explains how long-wavelength free-stream disturbances can generate much shorter wavelength Tollmien-Schlichting waves. Goldstein (1983) also recognised three general classes of the receptivity regions: (1) the leading edge region where the boundary layer is thinner and grows rapidly; the motion is governed by the unsteady boundary-layer equation, (2) regions further downstream where the boundary layer is forced to make a rapid adjustment; the motion is governed by the Orr-Sommerfeld equation, and (3) overlap regions where the Tollmien-Schlichting wave solutions of region 1 and region 2 match, in the sense of the matched-asymptotic-expansion.

Recently, experimental work relating to boundary layer receptivity has appeared in the literature (Chiu *et al* (1995), Westin *et al* (1998), Dietz (1998, 1999), King & Breuer (2001)). Dietz (1999) investigated experimentally the local boundary layer receptivity to a periodic convected disturbance. In his experiment, a vibrating ribbon is positioned upstream of a flat plate leading edge. The wake from this ribbon provides an effective convective disturbance for forcing boundary layer wave instabilities. The surface roughness of the plate also acted as a local source of receptivity.

Haddad & Corke (1998) performed a numerical simulation (finite difference scheme, second-order accurate throughout the grid) to study receptivity of the flow over a parabolic leading edge in a uniform flow with small amplitude acoustic disturbances. They chose a parabolic body in order to exclude jumps in curvature

which are known sites of receptivity and which occur where elliptic leading edges are matched to finite thickness flat plates (see Wanderley & Corke (2001)). Haddad & Corke showed that the leading edge receptivity increases with decreasing nose radius, and it will be maximum for an infinitely sharp flate plate.

In the sense of leading edge curvature, we can mention recent numerical and theoretical receptivity work by Collis & Lele (1999). Their model was a parabolic type of cylinder with a swept wing leading edge. They found receptivity results by numerical calculations with surface roughness placed at various locations on the wall. Comparing with the theoretical solutions, they concluded that non-parallel effects significantly attenuate the initial amplitude of stationary crossflow instability waves downstream when the roughness is near to the leading edge. They also found that the convex surface curvature enhances receptivity.

There are also some receptivity works in the literature where a suction or blowing slot near to the leading edge of the surface is used to generate Tollmien-Schlichting waves inside the boundary layer (see Crouch (1997), Fasel (2002), Bake *et al* (2002) for example). Fasel (2002) used DNS techniques to investigate laminar-turbulent transition in a flat plate boundary layer. In his analysis, a normal velocity $v(x,t)$ component which is proportion to $v_s(x)cos(\lambda t)$ is used in the narrow suction or blowing slot to generate a two-dimensional TS wave. Outside of this suction zone $v_s(x)$ is a 5th order polynomial function which goes to zero smoothly at both ends. He found that the disturbance amplitudes have a critical level and a fundamental resonance-type secondary instability causes the

breakdown of the TS-wavepackets into turbulent spots. A similar wall-normal velocity boundary condition in the suction slot was used by Bake *et al* (2002) for DNS. They also compared the DNS results with experimental results.

2.4 Numerical methods

The term, "Direct Numerical Simulation" (DNS) refers to the highly accurate numerical solution of the full Navier-Stokes equations. In DNS, finite difference, finite element, and spectral methods are all employed, sometimes simultaneously. Therefore the details of the methods employed by DNS practitioners vary somewhat. For example, Huser & Biringen (1993) used a 5th order finite difference method on a staggered grid in their very detailed study of the instability of Poiseuille flow in a square duct. In the related problem of expansions in channel flow Sandham & Kleiser (1992) used finite differences in the cross-stream direction and Fourier expansions (Spectral method) in the steamwise and spanwise directions. Rist & Fasel (1995) used 4th order finite differences in the downstream and surface-normal directions (spatially) and a spectral method in the spanwise direction to analyse the 3D development of controlled transition in a flat-plate boundary layer. Our finite difference techniques are 2nd order accurate in both space and time.

The work of a group based in the Institut für Aerodynamik und Gasdynamik, Universität Stuttgart, Germany, is of more relevance to the DNS work described

here. Recent works by Fasel & Konzelmann (1990), Fasel *et al* (1990), Kloker *et al* (1993), Rist & Fasel (1995), Wassermann & Kloker (2002), and Bake *et al* (2002) address the time-dependent evolution of the Blasius boundary layer and the development of the late stages of the transition to turbulence. These authors have developed a vorticity-velocity formulation of the Navier-Stokes equations which are solved using 4th order differencing in all three co-ordinate directions and time.

In long-term numerical integrations of the full Navier-Stokes equations, the usual finite difference discretisation of the nonlinear advection terms can introduce nonlinear computational instability and which do not conserve the total integral of the kinetic energy and momentum in the absence of diffusion (n.b. this type of computational instability may also occur in a linear equation with nonconstant coefficients). For 2D flows the streamfunction-vorticity formulation may be used, for which Arakawa (1966) derived the special form of the finite difference Jacobian which prevents nonlinear computational instability and thereby permits reliable long-term numerical integrations. We use Arakawa's techniques to discretise the Jacobian terms in our DNS (see in section 5.3.3).

Direct Numerical Simulation requires a large amount of computer resources such as CPU and memory. Therefore, more recently, a different method, PSE (Parabolised Stability Equations) has become a popular approach to allow inclusion of nonparallel and nonlinear effect in the stability analysis. PSE is mainly developed by Herbert and Bertolotti (see in Bertolotti *et al* (1992)). In PSE, TS-waves, the waveform eigenfunctions, the wavelength, and the growth rate all

vary slowly in the downstream direction; hence the equivalent boundary layer approximations can be made.

2.5 Outflow boundary conditions

The treatment of the outflow boundary requires special attention when undertaking numerical simulations of spatially evolving processes in boundary layers using the complete Navier-Stokes equations. We need to specify and implement boundary conditions into the numerical model so that the disturbances can pass through this boundary without causing any unphysical upstream effects or reflections. Kloker *et al* (1993) discussed six different types of outflow conditions and they concluded that very good results are obtained when the disturbances to the basic flow are spatially suppressed in the outflow so-called "buffer region". In this region, the disturbance components are multiplied by a weighting function (which is called the "buffer function") after each time step. The buffer function takes value 1 at the beginning of the buffer region and decreases gradually to 0 at the end. This approach has been extensively used by many investigators, for example: Kral & Fasel (1994), Haddad & Corke (1998), Collis & Lele (1999), Wanderley & Corke (2001), and Fasel (2002).

The buffer function which is used in Collis & Lele (1999) is a *sponge function*, and it was derived originally by Israeli & Orszag (1981). For this purpose, they

have used a cubic function f_s (*sponge function*) as

$$f_s(x) \propto \begin{cases} \left(\frac{x-x_s}{x_e-x_s}\right)^3 & x \in (x_s, x_e] \\ 0 & \text{otherwise} \end{cases} .$$

In this expression, x_s denotes the start of the sponge function and x_e the end. For their calculations, they used the domain ratio as $\frac{x_s}{x_e} = 0.8$, where x_e is the end of the computational domain. In this regard, the domain ratio is approximately 0.83 in our computational domain although the function we use here is different. Finally, they updated the solution by multiplying the disturbance to the basic flow by f_s.

Haddad & Corke (1998) and Wanderley & Corke (2001) used a streamwise weighting function defined as

$$s(i) = \frac{1 + \tanh(arg)}{2},$$

where

$$arg = 4\left\{1 - \frac{2(i - i_{buf})}{(i_{max} - i_{buf})}\right\}.$$

where i is the numerical index in the streamwise direction, i_{buf} is the index i at the beginning of the buffer zone, and i_{max} is the maximum value of i. The elliptic terms in the equations are multiplied by the weighting function. At the begining of the buffer zone, $s = 1$ and at the end $s = 0$. The length of the buffer region which they used is four times that of the TS wavelength.

In our numerical computations, we have used Kloker's idea, which is discussed

in section 5.3.6 and no reflections were observed; this is very similar to Collis & Lele's *sponge function* and Haddad & Corke's *buffer function.*

Chapter 3

The influence of higher order effects on the linear wave instability of vertical free convective boundary layer flow

3.1 Summary

We determine how higher order terms in the boundary layer expansion for the basic steady flow affect the well-known stability criteria for the classical vertical free convective boundary layer flow from a uniform temperature surface which was first considered by Nachtsheim (1963). The fluid is bounded by two semi-

infinite flat plates, one of which is the vertical heated surface while the other is either insulated or at the ambient temperature of the medium (see Figure 3.1). The surfaces form a wedge of angle α. Thus the basic flow is obtained using the method of matched asymptotic expansions, and although the leading order boundary layer flow is independent of α, further terms are functions of α. We then determine how the shape of the overall fluid domain which exists outside the boundary layer affects the stability criterion.

3.2 Governing equations

We consider the two-dimensional free convective boundary layer flow from a vertical semi-infinite heated plate. The system is as described above and is shown in Figure 3.1. Apart from the fluid Prandtl number, which we take as $Pr = 0.7$ and 6.7 in this work, the only other parameter is the wedge angle, α. A Cartesian frame of reference is chosen, where the x-axis is aligned vertically with the heated surface, and the y- axis is perpendicular to this.

The equations which describe the free convection from a vertical plate are the incompressible continuity, Navier-Stokes, and energy equations. For unsteady two dimensional flow this system, subject to the Boussinesq approximation, is written in the dimensional form

$$\frac{\partial \bar{u}}{\partial \bar{x}} + \frac{\partial \bar{v}}{\partial \bar{y}} = 0, \tag{3.1}$$

$$\frac{\partial \bar{u}}{\partial \bar{t}} + \bar{u}\frac{\partial \bar{u}}{\partial \bar{x}} + \bar{v}\frac{\partial \bar{u}}{\partial \bar{y}} = -\frac{1}{\rho}\frac{\partial P}{\partial \bar{x}} + \nu\left(\frac{\partial^2 \bar{u}}{\partial \bar{x}^2} + \frac{\partial^2 \bar{u}}{\partial \bar{y}^2}\right) + g\beta\,(T - T_\infty)\,, \tag{3.2}$$

$$\frac{\partial \bar{v}}{\partial \bar{t}} + \bar{u}\frac{\partial \bar{v}}{\partial \bar{x}} + \bar{v}\frac{\partial \bar{v}}{\partial \bar{y}} = -\frac{1}{\rho}\frac{\partial P}{\partial \bar{y}} + \nu\left(\frac{\partial^2 \bar{v}}{\partial \bar{x}^2} + \frac{\partial^2 \bar{v}}{\partial \bar{y}^2}\right), \tag{3.3}$$

$$\frac{\partial T}{\partial \bar{t}} + \bar{u}\frac{\partial T}{\partial \bar{x}} + \bar{v}\frac{\partial T}{\partial \bar{y}} = \kappa\left(\frac{\partial^2 T}{\partial \bar{x}^2} + \frac{\partial^2 T}{\partial \bar{y}^2}\right). \tag{3.4}$$

Here $\bar{u}$ and $\bar{v}$ are the velocity components in the $\bar{x}$ and $\bar{y}$-directions, respectively, $\bar{t}$ is time, P is the dynamic pressure, T is the temperature, g is the gravitational acceleration in the negative $\bar{x}$-direction, ρ is the density of the fluid, ν is the kinematic viscosity, κ is the diffusivity and β is the coefficient of thermal expansion.

The boundary conditions for equations (3.1)-(3.4) for the case of an isothermal plate are:

$$\bar{u} = \bar{v} = 0, \quad T = T_w \quad \text{at} \quad \bar{y} = 0, \quad \bar{x} \geq 0 \tag{3.5}$$

$$\bar{u} = \bar{v} = 0, \quad \text{and either} \quad T_n = 0 \quad \text{or} \quad T = T_\infty \quad \text{on the second surface,} \tag{3.6}$$

and

$$T \to T_\infty \quad \text{as} \quad \bar{r} = (\bar{x}^2 + \bar{y}^2)^{1/2} \to \infty, \tag{3.7}$$

where T_w is the temperature of the plate, T_∞ is the ambient temperature of the fluid with $T_w > T_\infty$, and n as a subscript denotes the normal derivative. Equations (3.1)-(3.7) may be nondimensionalised using the following transformations:

$$(\bar{x}, \bar{y}) = d(x, y), \tag{3.8}$$

$$(\bar{u}, \bar{v}) = U(u, v), \tag{3.9}$$

$$\bar{t} = \left(\frac{d}{U}\right) t, \tag{3.10}$$

$$\bar{p} = \rho U^2 p, \tag{3.11}$$

$$T - T_\infty = (T_w - T_\infty)\,\theta, \tag{3.12}$$

where the natural length and velocity scales, d and U, are given by,

$$d = \left(\frac{\nu^2}{g\beta\Delta T}\right)^{1/3}, \tag{3.13}$$

and

$$U = (g\beta\nu\Delta T)^{1/3}. \tag{3.14}$$

A further simplification is afforded by the introduction of a streamfunction, ψ, according to $\bar{u} = \psi_{\bar{y}}$ and $\bar{v} = -\psi_{\bar{x}}$, and the vorticity, ω. Equations (3.1)-(3.4) now become

$$\nabla^2\psi = \omega, \tag{3.15}$$

$$\nabla^2\omega = \frac{\partial\omega}{\partial t} + \frac{\partial\psi}{\partial y}\frac{\partial\omega}{\partial x} - \frac{\partial\psi}{\partial x}\frac{\partial\omega}{\partial y} - \frac{\partial\theta}{\partial y}, \tag{3.16}$$

$$\frac{1}{Pr}\nabla^2\theta = \frac{\partial\theta}{\partial t} + \frac{\partial\psi}{\partial y}\frac{\partial\theta}{\partial x} - \frac{\partial\psi}{\partial x}\frac{\partial\theta}{\partial y}, \tag{3.17}$$

where $Pr = \nu/\kappa$ is the Prandtl number. The lengthscale defined in equation (3.13) is equivalent to setting the usual Grashof number to unity; such a procedure has also been used in studies of vortex disturbances in thermal boundary layer

flows in porous media undertaken by Rees (2001) and Rees (2002) where the Darcy-Rayleigh number is set to unity.

The corresponding boundary conditions may be written as follows

$$\psi_y = \psi = 0, \quad \theta = 1 \quad \text{at} \quad y = 0, \quad x \geq 0 \quad [\text{i.e. } \phi = 0] \tag{3.18}$$

$$\psi = \psi_n = 0, \quad \text{and either} \quad \theta_n = 0 \quad \text{or} \quad \theta = 0 \quad \text{on } \phi = \alpha, \tag{3.19}$$

and

$$\theta \to 0 \quad \text{as} \quad r = (x^2 + y^2)^{1/2} \to \infty. \tag{3.20}$$

In (3.18) and (3.19) the angle ϕ denotes the angle from the vertical and therefore the boundary surfaces are located at $\phi = 0$ and $\phi = \alpha$; see Figure 3.1.

3.3 Basic flow analysis

In this section we determine the two-term solution of the undisturbed basic boundary layer flow using the method of matched asymptotic expansions. The basic flow, which we denote by the subscript B, is steady and two-dimensional and it satisfies the equations

$$\nabla^2 \psi_B = \omega_B, \tag{3.21}$$

$$\nabla^2 \omega_B = \frac{\partial \psi_B}{\partial y}\frac{\partial \omega_B}{\partial x} - \frac{\partial \psi_B}{\partial x}\frac{\partial \omega_B}{\partial y} - \frac{\partial \theta_B}{\partial y}, \tag{3.22}$$

$$\frac{1}{Pr}\nabla^2\theta_B = \frac{\partial\psi_B}{\partial y}\frac{\partial\theta_B}{\partial x} - \frac{\partial\psi_B}{\partial x}\frac{\partial\theta_B}{\partial y}, \tag{3.23}$$

where ψ_B is the basic flow streamfunction and ω_B denotes the basic vorticity, as defined by (3.21). Equations (3.21)-(3.23) are to be solved subject to the boundary layer approximation. Therefore we introduce the following expansions for the streamfunction and temperature in the boundary layer region,

$$\psi_B = x^{3/4}F_0(\eta) + F_1(\eta) + \cdots\cdots \tag{3.24}$$

$$\theta_B = H_0(\eta) + x^{-3/4}H_1(\eta) + \cdots\cdots \tag{3.25}$$

where the similarity variable η is given by

$$\eta = \frac{y}{x^{1/4}}, \tag{3.26}$$

and we apply the boundary layer approximation wherein we assume that $x \gg y$. We will refer to F_0 and H_0 as the leading (or zeroth) order terms while F_1 and H_1 are the first order terms.

The equations for the zeroth order terms, F_0 and H_0, correspond to the classical problem:

$$F_0''' + \tfrac{3}{4}F_0F_0'' - \tfrac{1}{2}F_0'F_0' + H_0 = 0, \tag{3.27}$$

$$H_0'' + \tfrac{3}{4}Pr\, F_0H_0' = 0, \tag{3.28}$$

subject to

$$F_0(0) = F_0'(0) = 0, \quad H_0(0) = 1, \tag{3.29}$$

$$F_0'(\infty) = H_0(\infty) = 0. \tag{3.30}$$

Numerical integration of equations (3.27)-(3.30) for water ($Pr = 6.7$) results in the values

$$F_0''(0) = 0.64301, \quad H_0'(0) = -0.73584, \tag{3.31}$$

while the corresponding values for air ($Pr = 0.7$) are

$$F_0''(0) = 0.95995, \quad H_0'(0) = -0.35318. \tag{3.32}$$

Given that solutions to equation (3.28) decay exponentially to zero, the region outside the boundary layer is isothermal and we may ignore the temperature field in this potential flow region. If we denote by Ψ the outer-region streamfunction, then we may expand it according to

$$\Psi_B = r^{3/4}\Psi_0(\phi) + \Psi_1(\phi) + \cdots\cdots \tag{3.33}$$

where the polar coordinates, r and ϕ, are defined as

$$x = r\cos\phi, \qquad y = r\sin\phi. \tag{3.34}$$

If $F_0(\infty)$ is denoted by A_0 then, as shown by Yang & Jerger (1964), Ψ_0 satisfies

$$\nabla^2 \Psi_0 = 0, \tag{3.35}$$

subject to

$$\Psi_0(\phi = 0) = A_0, \qquad \Psi_0(\phi = \alpha) = 0, \tag{3.36}$$

where the inhomogeneous boundary condition represents an asymptotic matching of Ψ with the first term of the boundary layer solution. The solution of equation (3.35) can be written as

$$\Psi_0 = -A_0 \frac{\sin \frac{3}{4}(\phi - \alpha)}{\sin \frac{3}{4}\alpha}. \tag{3.37}$$

We note, for later reference, that this solution is singular when $\alpha = 0$ and when $\alpha = 4\pi/3$.

On expanding equation (3.37) around $\phi = 0$ and rewriting the result in terms of the similarity variable, η, it follows that the behaviour of Ψ_0 in the matching region is given by

$$\Psi_0 \sim A_0 \left(1 - \tfrac{3}{4}\eta x^{-3/4} \cot \tfrac{3}{4}\alpha + \cdots\right). \tag{3.38}$$

The second term in (3.38) now provides the matching condition for the second streamfunction term in the boundary layer expansion, (3.24).

As shown by Yang & Jerger (1964), the equations for F_1 and H_1, the first order

boundary layer terms, are

$$F_1''' + \tfrac{3}{4}F_0F_1'' - \tfrac{1}{4}F_0'F_1' + H_1 = 0, \tag{3.39}$$

$$H_1'' + \tfrac{3}{4}Pr\,(F_0H_1)' = 0, \tag{3.40}$$

subject to

$$F_1(0) = F_1'(0) = 0, \quad H_1(0) = 0, \tag{3.41}$$

$$F_1'(\infty) = -\tfrac{3}{4}A_0 \cot \tfrac{3}{4}\alpha, \quad H_1(\infty) = 0 \tag{3.42}$$

where the inhomogeneous boundary condition represents a matching with the $O(x^{-3/4})$ term in equation (3.38). Since F_1 is proportional to $\cot \frac{3\alpha}{4}$, different solutions may exist for different values of α. For an example, at $\alpha = \pi$ the numerical integration of equations (3.39)-(3.42) results in the values for water ($Pr = 6.7$) are

$$F_1''(0) = 0.13908, \quad H_1'(0) = 0, \tag{3.43}$$

while the corresponding values for air ($Pr = 0.7$) are

$$F_1''(0) = 0.39967, \quad H_1'(0) = 0. \tag{3.44}$$

We note that

$$H_1 = 0 \tag{3.45}$$

may be derived analytically from equation (3.40), and therefore there is no correction to the temperature field at this order.

3.4 Linear stability analysis

In this section we develop the linear stability equations for the basic flow given above by substituting

$$\psi(x,y,t) = \psi_B(x,y) + \epsilon\,\psi_D(x,y,t) \tag{3.46}$$

$$\omega(x,y,t) = \omega_B(x,y) + \epsilon\,\omega_D(x,y,t) \tag{3.47}$$

$$\theta(x,y,t) = \theta_B(x,y) + \epsilon\,\theta_D(x,y,t) \tag{3.48}$$

into equations (3.15)-(3.17). It is important to note that the asymptotic theory of the last section is being used to obtain what is hoped to be a closer approximation to the exact basic flow than is provided by the leading order boundary layer solution, even though the solutions obtained above are valid strictly in the limit $x \to \infty$.

On taking $|\epsilon| \ll 1$ and linearising we obtain the following system of linearised disturbance equations in streamfunction/vorticity form:

$$\nabla^2\psi_D = \omega_D, \tag{3.49}$$

$$\nabla^2\omega_D = \frac{\partial\omega_D}{\partial t} + \frac{\partial\psi_B}{\partial y}\frac{\partial\omega_D}{\partial x} + \frac{\partial\psi_D}{\partial y}\frac{\partial\omega_B}{\partial x} - \frac{\partial\psi_B}{\partial x}\frac{\partial\omega_D}{\partial y} - \frac{\partial\psi_D}{\partial x}\frac{\partial\omega_B}{\partial y} - \frac{\partial\theta_D}{\partial y}, \tag{3.50}$$

$$\frac{1}{Pr}\nabla^2\theta_D = \frac{\partial\theta_D}{\partial t} + \frac{\partial\psi_B}{\partial y}\frac{\partial\theta_D}{\partial x} + \frac{\partial\psi_D}{\partial y}\frac{\partial\theta_B}{\partial x} - \frac{\partial\psi_B}{\partial x}\frac{\partial\theta_D}{\partial y} - \frac{\partial\psi_D}{\partial x}\frac{\partial\theta_B}{\partial y}, \tag{3.51}$$

where $\omega_B \approx \psi_{Byy}$ represents the vorticity corresponding to the basic flow. The appropriate boundary conditions used to solve the disturbance equations are

$$\psi_{Dy} = \psi_D = 0, \quad \theta_D = 0 \quad \text{at} \quad y = 0, x \geq 0 \tag{3.52}$$

$$\psi_{Dy} \to 0, \quad \omega_D \to 0 \quad \theta_D \to 0 \quad \text{as} \quad y \to \infty. \tag{3.53}$$

We now impose the parallel flow approximation where we assume that the disturbances have solutions of the form,

$$\begin{pmatrix} \psi_D \\ \omega_D \\ \theta_D \end{pmatrix} = \begin{pmatrix} F(y) \\ G(y) \\ H(y) \end{pmatrix} e^{(ikx+\lambda t)} \tag{3.54}$$

where the amplitudes $F(y)$, $G(y)$, and $H(y)$ are complex functions of y. Here k is a real positive quantity and represents the wavenumber of the disturbance, and $\lambda = \lambda_R + i\lambda_I$ is the complex temporal growth rate. Neutral stability corresponds to $\lambda_R = 0$ and the computed value of λ_I is related to the wavespeed of the disturbance which is $-\lambda_I/k$. The neutral stability condition $\lambda_R = 0$ leads to a relation between k and x in the form of a curve in the $(k,\ x)$ plane and which is referred to as the neutral curve. In practice the flow is elliptic, and therefore the substitution of (3.54) is used simply to obtain a set of ordinary differential equations.

Equation (3.54) may now be substituted into equations (3.49)-(3.51), and on

changing the variable from y to η, the disturbance equations take the forms,

$$F'' - k^2 x^{1/2} F = x^{1/2} G \tag{3.55}$$

$$G'' + \frac{\partial \psi_B}{\partial x} x^{1/4} G' - \Big[k^2 + i\lambda_I + ik\frac{\partial \psi_B}{\partial y}\Big] x^{1/2} G$$

$$= \frac{\partial \omega_B}{\partial x} x^{1/4} F' - ik\frac{\partial \omega_B}{\partial y} x^{1/2} F - x^{1/4} H' \tag{3.56}$$

$$H'' + Pr\frac{\partial \psi_B}{\partial x} x^{1/4} H' - \Big[k^2 + iPr\lambda_I + ikPr\frac{\partial \psi_B}{\partial y}\Big] x^{1/2} H$$

$$= Pr\Big[\frac{\partial \theta_B}{\partial x} x^{1/4} F' - ikx^{1/2}\frac{\partial \theta_B}{\partial y} F\Big] \tag{3.57}$$

where primes represent derivatives with respect to η. The boundary conditions to be satisfied by the disturbances are that

$$F' = F = H = 0 \quad \text{at} \quad \eta = 0 \tag{3.58}$$

$$F, G, H \to 0 \quad \text{as} \quad \eta \to \infty. \tag{3.59}$$

As this complex homogeneous system forms a 12th order eigenvalue problem for x and λ_I in terms of the wavenumber, k, an additional (complex) normalisation condition at $\eta = 0$ is required to solve the disturbance equations and it is taken to be

$$H' = 1. \tag{3.60}$$

This extra boundary condition means that we may solve equations (3.55)-(3.60) and determine the eigenvalues, x and λ_I. A suitably modified version of the

Keller-box method is used to solve this ordinary differential eigensystem and it is discussed in the next section.

To summarise the stability results, it is necessary to find out the value of the critical distance x_c. However this value is a function of wavenumber k. Therefore it is necessary to minimise x with respect to k. In order to do this, we implement equations (3.55)-(3.60) with a further new set which is obtained from (3.55)-(3.60) by differentiating with respect to k and setting $\frac{\partial x}{\partial k} = 0$. If we now define $\mathcal{F}$, $\mathcal{G}$ and $\mathcal{H}$ according to,

$$\mathcal{F} = \frac{\partial F}{\partial k}, \qquad \mathcal{G} = \frac{\partial G}{\partial k} \qquad \text{and} \qquad \mathcal{H} = \frac{\partial H}{\partial k} \tag{3.61}$$

then $\mathcal{F}$, $\mathcal{G}$ and $\mathcal{H}$ satisfy

$$\mathcal{F}'' - k^2 x^{1/2}\mathcal{F} = x^{1/2}\mathcal{G} + 2kx^{1/2}F \tag{3.62}$$

$$\begin{aligned}
&\mathcal{G}'' + \frac{\partial \psi_B}{\partial x}x^{1/4}\mathcal{G}' - \Big[k^2 + i\lambda_I + ik\frac{\partial \psi_B}{\partial y}\Big]x^{1/2}\mathcal{G} \\
&\qquad = \frac{\partial \omega_B}{\partial x}x^{1/4}\mathcal{F}' - ik\frac{\partial \omega_B}{\partial y}x^{1/2}\mathcal{F} - x^{1/4}\mathcal{H}' \\
&\qquad -i\frac{\partial \omega_B}{\partial y}x^{1/2}F + \Big[2k + i\frac{\partial \lambda_I}{\partial k} + i\frac{\partial \psi_B}{\partial y}\Big]x^{1/2}G
\end{aligned} \tag{3.63}$$

$$\begin{aligned}
&\mathcal{H}'' + Pr\frac{\partial \psi_B}{\partial x}x^{1/4}\mathcal{H}' - \Big[k^2 + iPr\lambda_I + ikPr\frac{\partial \psi_B}{\partial y}\Big]x^{1/2}\mathcal{H} \\
&\qquad = Pr\Big[\frac{\partial \theta_B}{\partial x}x^{1/4}\mathcal{F}' - ikx^{1/2}\frac{\partial \theta_B}{\partial y}\mathcal{F} - ikx^{1/2}\frac{\partial \theta_B}{\partial y}F\Big] \\
&\qquad + \Big[2k + iPr\frac{\partial \lambda_I}{\partial k} + ikPr\frac{\partial \psi_B}{\partial y}\Big]x^{1/2}H
\end{aligned} \tag{3.64}$$

and the corresponding boundary conditions are

$$\mathcal{F}' = \mathcal{F} = \mathcal{H} = 0 \quad \text{at} \quad \eta = 0 \tag{3.65}$$

$$\mathcal{F}, \mathcal{G}, \mathcal{H} \to 0 \quad \text{as} \quad \eta \to \infty. \tag{3.66}$$

The normalisation condition at $\eta = 0$ is derived from (3.60) and it is

$$\mathcal{H}'(0) = 0. \tag{3.67}$$

Now this extended system of complex equations is a 24^{th} order ordinary differential eigenvalue problem with the specified 14 complex (or 28 real) boundary conditions and the eigenvalues x, k, λ_I and $\frac{\partial \lambda_I}{\partial k}$. The same numerical techniques are employed to solve this system of equations.

3.5 Numerical method

In this section the numerical solutions of the basic flow equations (3.27)-(3.30), and (3.39)-(3.42) and the disturbance equations (3.55)-(3.60) and (4.46)-(3.67) are discussed. The equations for the basic flow were solved using a standard shooting method which employs the Newton-Raphson iteration techniques. In this method the ordinary differential equations (3.27), (3.28), (3.39), and (3.40) are written as a first order system of ordinary differential equations and a 4th order Runge-Kutta method is employed to solve them. These solutions are accurate

to at least six significant figures.

When solving the disturbance equations it was observed that the vorticity, G, and temperature function, H, both decay to zero very quickly as η increases, but that the streamfunction, F, does not. Therefore we introduced the alternative boundary condition

$$F' + kx^{1/4}F \to 0 \quad \text{as} \quad \eta \to \infty \tag{3.68}$$

which allows the streamfunction to exhibit the appropriate exponential decay rate well before the streamfunction attains small values. Thus we were able to solve the problem on a smaller computational domain than would otherwise be necessary. All these disturbance equations are in complex form, and after resolution into their real and imaginary parts we have twelve second order ordinary linear differential equations together with four eigenvalues, x, λ_I, k and $\frac{\partial \lambda_I}{\partial k}$.

Due to the stiffness of the eigensystem (especially for large values of $kx^{1/4}$) the Runge-Kutta method was abandoned in favour of a direct method. Thus a modified version of the Keller-box code was employed to solve the disturbance equations. For this type of method it is not necessary always to insist that the governing equations are reduced to first order form, and the present code solves the six second order differential equations using straightforward second order accurate central difference approximations. When the difference equations are suitably arranged the presence of the eigenvalues causes the Jacobian matrix of the Newton-Raphson iteration scheme, which is a central part of the Keller box methodology, to have extra rows and columns over and above its usual block

tridiagonal structure:

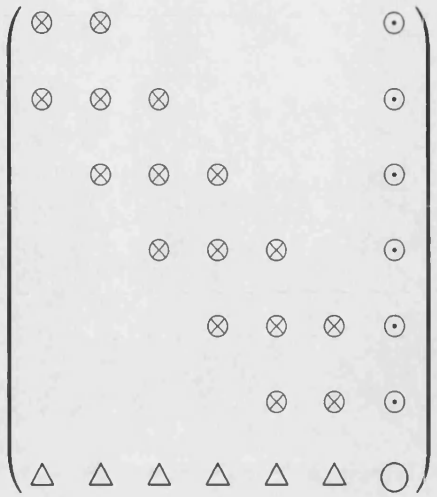

where $\otimes$ denotes a submatrix block corresponding the equations (3.55)-(3.57), $\odot$ represents blocks corresponding to derivatives of equations (3.55) to (3.57) with respect to the eigenvalues, $\triangle$ represents entries corresponding to the normalisation condition, and $\bigcirc$ is a block with zero entries. Therefore the block-Thomas algorithm had to be modified to account for this structural change; very similar schemes were used by Lewis *et al* (1995) and Shu & Wilkes (1995).

To illustrate the above method, we consider a 4^{th} order ordinary differential eigenvalue problem which is given by

$$\frac{d^4y}{dx^4} - ky = 0 \tag{3.69}$$

with the boundary conditions

$$y(0) = y''(0) = 0, \tag{3.70}$$

$$y(1) = y''(1) = 0, \tag{3.71}$$

where all the variables are representative variables and do not have any relation with the main problem.

We may define a new variable, z, which transforms (3.69) into two second order ordinary differential equations as follows,

$$y'' - z = 0, \tag{3.72}$$

$$z'' - ky = 0. \tag{3.73}$$

Hence the boundary conditions (3.70)-(3.71) reduce to

$$y(0) = z(0) = 0, \tag{3.74}$$

$$y(1) = z(1) = 0, \tag{3.75}$$

This is a homogeneous system with eigenvalue k. We require an extra boundary condition to solve them and which is taken to be

$$\int_0^1 y^2 dx = 1 \tag{3.76}$$

The second order accurate central difference method is used to discretised equations (3.72)-(3.73). Here we present this method using only three grid points as

the extension to larger numbers of grid points is straightforward. Now the difference equations may be arranged and written in the following matrix form which is the Jacobian matrix obtained from the standard Newton-Raphson iteration scheme.

$$
\left(\begin{array}{cc|cc|cc|c}
-\frac{2}{\delta x^2} & -1 & \frac{1}{\delta x^2} & & & & \\
-k & -\frac{2}{\delta x^2} & & \frac{1}{\delta x^2} & & & -y_1 \\
\hline
\frac{1}{\delta x^2} & & -\frac{2}{\delta x^2} & -1 & \frac{1}{\delta x^2} & & \\
 & \frac{1}{\delta x^2} & -k & -\frac{2}{\delta x^2} & & \frac{1}{\delta x^2} & -y_2 \\
\hline
 & & \frac{1}{\delta x^2} & & -\frac{2}{\delta x^2} & -1 & \\
 & & & \frac{1}{\delta x^2} & -k & -\frac{2}{\delta x^2} & -y_3 \\
\hline
2y_1\delta x & & 2y_2\delta x & & 2y_3\delta x & &
\end{array}\right)
\times
\left(\begin{array}{c}
\delta y_1 \\ \delta z_1 \\ \hline \delta y_2 \\ \delta z_2 \\ \hline \delta y_3 \\ \delta z_3 \\ \hline \delta k
\end{array}\right)
$$

$$
= -
\left(\begin{array}{c}
(-2y_1 + y_2)/\delta x^2 - z_1 \\
(-2z_1 + z_2)/\delta x^2 - ky_1 \\
\hline
(y_1 - 2y_2 + y_3)/\delta x^2 - z_2 \\
(z_1 - 2z_2 + z_3)/\delta x^2 - ky_2 \\
\hline
(y_2 - 2y_3)/\delta x^2 - z_3 \\
(z_2 - 2z_3)/\delta x^2 - ky_3 \\
\hline
\sum_{i=1}^{n} y_i^2 \delta x^2 - 1
\end{array}\right)
$$

The above Jacobian matrix is a block-tridiagonal structure where the individual submatrix blocks are 2×2 matrices with extra rows and columns. This matrix may be solved using a suitable modified block tridiagonal matrix algorithm.

3.6 Numerical results

In this section we discuss the stability results of free convection flow of both water ($Pr = 6.7$) and air ($Pr = 0.7$). Results using both the leading order boundary layer flow and two-term approximation are presented.

We have used $\eta_\infty = 10$ with 100 grid points, which gives the steplength $d\eta = 0.1$, for both cases.

3.6.1 Stability criteria using the one-term approximation

The stability results presented here correspond to retaining only the leading order basic boundary layer flow. It is noted that the leading order basic flow is independent of wedge angle α, and therefore the stability results do not vary with α.

Figure 3.2 shows the neutral curves plotted in the (k, x) plane for both the cases of air and water. The critical distance for air ($Pr = 0.7$) is calculated to be $x_c \simeq 106.974$ with the corresponding wavenumber $k_c \simeq 0.051$, while for water ($Pr = 6.7$) is calculated to be $x_c \simeq 43.461$ with $k_c \simeq 0.146$. When $x > x_c$, the flow is unstable with a positive growth rate (i.e. $\lambda_R > 0$); on the other hand the flow is stable when $x < x_c$ since the growth rate is negative (i.e. $\lambda_R < 0$). On the neutral curve the growth rate is zero ($\lambda_R = 0$) by definition.

Figure 3.2 shows that x_c for water is smaller than air. This suggests that destabilisation takes place nearer to the leading edge for water. However this is true only in terms of nondimensional distances and it is not necessarily true always for dimensional x.

In (3.13) the length scale d is defined. The neutral distances are now $106.974 d_{air}$ and $43.461 d_{water}$. For a given situation g and ΔT are taken to be the same. We need to compare

$$106.974 \left(\frac{\nu^2}{\beta}\right)^{1/3}_{air} \qquad \text{and} \qquad 43.461 \left(\frac{\nu^2}{\beta}\right)^{1/3}_{water}.$$

In fact, if we consider $\Delta T = 10^0 C$ and $g = 9.81 N$, at the Atmospheric pressure the values of ν, β are $1.50 \times 10^{-5} m^2 s^{-1}$, $3.40 \times 10^{-3} K^{-1}$ for air and $10.04 \times 10^{-7} m^2 s^{-1}$, $2.1 \times 10^{-4} K^{-1}$ for water respectively. Therefore the dimensional critical distance $\bar{x}_c$ is equal to $9.382 cm$ for air and $1.589 cm$ for water, smaller than for air.

Figure 3.3 shows the variation of the disturbance frequency $(-\lambda_I)$ on the neutral curve plotted in Figure 3.2. The critical frequency for air ($Pr = 0.7$, curve 'b' in this figure) is calculated to be $-\lambda_I \simeq 0.263$ with corresponding $x_c \simeq 106.974$, while for water ($Pr = 6.7$, curve 'a') it is $-\lambda_I \simeq 0.292$ with $x_c \simeq 43.461$.

3.6.2 Higher order effects on stability

For $Pr = 6.7$

We present first our stability calculations for water for which we take $Pr = 6.7$. The first order streamwise basic velocity profiles are plotted in Figures 3.4 and 3.5, where the different curves correspond to the different values of the wedge angle. In these Figures (and subsequent figures related to the wedge angle) we have used a scaled value of α defined according to

$$\gamma = \frac{12\alpha}{\pi}. \tag{3.77}$$

Before presenting the detailed results from the stability analysis it is necessary to consider first some of the implications of the dependence of F_1 on α. The magnitude of F_1 is proportional to $\cot\frac{3\alpha}{4}$. This function is zero when $\alpha = \frac{2}{3}\pi$ and therefore the two-term approximation to the boundary layer flow is identical to the one-term approximation in this case. When $\alpha = 0$ and $\alpha = \frac{4}{3}\pi$, then F_1 is infinite and therefore the asymptotic expansion breaks down in these limits. The function $\cot\frac{3\alpha}{4}$ has period $\frac{4}{3}\pi$ and therefore all the results presented below for a wedge angle α satisfying $0 < \alpha < \frac{2}{3}\pi$ also apply for the range $\frac{4}{3}\pi < \alpha < 2\pi$. Finally we note that F_1 is positive when $\frac{2}{3}\pi < \alpha < \frac{4}{3}\pi$ and therefore the streamwise velocity of the basic flow is greater than that given by the leading order boundary layer theory. For other values of α the basic flow is slower.

Detailed stability results in the form of x-k neutral curves are shown in Figures 3.6 and 3.7 where the different curves correspond to different values of the wedge angle. Here we see that there are very substantial variations in the shapes of the curves and that the minimum value of x also varies considerably as α varies. Figure 3.6 shows curves corresponding to the range $0 < \gamma < 8$ (i.e. $0 < \alpha < \frac{2}{3}\pi$), or, equivalently, $16 < \gamma < 24$ (i.e. $\frac{4}{3}\pi < \alpha < 2\pi$). Those corresponding to the intermediate range, $8 < \gamma < 16$ (i.e. $\frac{2}{3}\pi < \alpha < \frac{4}{3}\pi$) are displayed in Figure 3.7.

When the wedge angle is $\alpha = \frac{2}{3}\pi$ ($\gamma = 8$) the neutral stability curve is unimodal and displays the usual characteristic for boundary layer flows of having a maximum wavenumber for which instability may be expected. As the wedge angle decreases from this value towards zero the curve rises and the critical distance increases. The reason for this may be understood in terms of the effect of the second term in the basic vertical velocity which is negative, and increasingly so as α decreases. If, crudely speaking, we were to assume that instability takes place when the maximum streamwise velocity within the boundary layer attains a certain threshold value, then the decrease in this velocity due to the second term in the basic flow boundary layer analysis means that a greater distance from the leading edge is required before instability can take place.

On the other hand, when α increases from $\frac{2}{3}\pi$, the second term in the boundary layer flow increases the upwards velocity making the flow more susceptible to instability. This is seen quite clearly in Figure 3.7, where the neutral curve is also found to attain a more complicated bimodal form. In this case, as $\alpha \to \frac{4}{3}\pi$,

the singular case mentioned above for which the asymptotic expansion breaks down, the critical value of x gets increasingly close to zero.

The results from Figures 3.6 and 3.7 are summarised in Figure 3.8 in which is displayed the variation with γ of the local extrema of the neutral curves. We see that there is very little variation of the critical value of x over most of this range, thereby lending confidence to analyses based only on the leading order boundary layer flow. However, anomalous results occur in the region fairly close to $\alpha = 0$ and $\alpha = \frac{4}{3}\pi$ due to the incipient breakdown of the asymptotic analysis, and it is highly likely that a much more accurate representation of the basic flow will be required for such cases, and this may very well need to involve a full solution of the elliptic governing equations.

Another summary of stability results are shown in Figure 3.9, where the critical wavenumbers are plotted against the scaled wedge angle γ. There is also little variation of of critical value of k over most of the range, but large variations do occur near $\gamma = 0$ and 16.

For $Pr = 0.7$

Equivalent results for the case of air, for which $Pr = 0.7$, are shown in Figures 3.10 to 3.15. The first order basic boundary layer velocity profiles show identical behaviour to that observed for the water case: when $\alpha = \frac{2}{3}\pi$ or $\gamma = 8$, $F_1' = 0$; when $\alpha < \frac{2}{3}\pi$ then $F_1' < 0$ and when $\frac{2}{3}\pi < \alpha < \frac{4}{3}\pi$ then $F_1' > 0$.

Again the neutral curve corresponding to the leading order boundary layer flow is given by the case $\gamma = 8$ in Figure 3.12, and the curve is unimodal. As γ decreases towards zero the neutral values of x increase in general, but the detailed evolution is complicated by the fact that the neutral curve becomes bimodal. When γ is close to 8 the left hand minimum corresponds to the smaller minimum, whereas the right hand one assumes this dominance as γ decreases.

Figure 3.13 shows that the neutral values of x decrease towards zero as γ increases towards 16 (or α towards $\frac{4}{3}\pi$); in this regard the behaviour is identical to that shown in Figure 3.7. However, the curves assume increasingly bizarre shapes as γ increases.

The overall variation in the extrema of the neutral curves with α is given in Figure 3.14. In the ranges $1 < \gamma < 5$ and $17 < \gamma < 21$ (i.e. $\frac{1}{12} < \alpha/\pi < \frac{5}{12}$ and $\frac{17}{12} < \alpha/\pi < \frac{21}{12}$) there is very little variation in the critical value of x. But outside of these ranges there is a very strong variation suggesting that the thermal boundary layer flow of air is particularly sensitive to the external geometry in terms of its stability characteristics.

A large variation of critical wavenumbers against γ is seen in Figure 3.15. Although for water the variation in k_c is generally small (see in Figure 3.9), for the case of air, it is very significant.

3.7 Conclusions

Over much of the range of wedge angles the criterion for the onset of wave convection in water does not vary greatly from that found when using only the leading order basic flow. However, when the wedge angle is close to $4\pi/3$ (or to 0) the results become unreliable due to the fact that the second term in the asymptotic expansion becomes unbounded and the asymptotic expansion ceases to be uniformly valid. For wedge angles less than this value, the basic flow is increased in strength relative to the leading order flow and instability is enhanced, whereas the opposite effect is found at wedge angles greater than $\frac{2}{3}\pi$. For air the neutral distance is much more sensitive to α than for water.

It is generally recognised that there is a fundamental inconsistency in the study of the stability of boundary layer flows when using the parallel flow approximation. The basic flow is derived on the basis of an asymptotic theory as $x \to \infty$, but the stability analysis yields a finite, sometimes fairly small, value of x. It may be argued that the basic flow may still be particularly accurate, despite it being the first term of an asymptotic theory. In the present chapter it is clear that the leading order thermal boundary layer using water is quite accurate since the variation in the stability criterion with wedge angle is small over almost all the range of angles. However, the parallel flow approximation, which is used in the stability analysis is also an approximation, and it may yield spurious results, as seen in Figure 3.13.

The equivalent analysis for vortex instabilities in convective boundary layers in porous media was undertaken by Storesletten & Rees (1998) who also found a very substantial variation in the critical distance with wedge angle. In that context higher order terms in the basic flow become infinite only as $\alpha \to 0^+$. However, the conclusion there is that the variation in the value of x_c with α is too great for the theory to be deemed reliable. This is due to the fact that the basic flow is not sufficiently well-represented by the three-term asymptotic expansion used by them.

For the present flow we would recommend in general that the stability characteristics should be studied using a more accurate basic flow, but the determination of this involves the computation of a steady elliptic system of partial differential equations which is of equal difficulty to a detailed unsteady simulation of the full equations, and therefore a direct fully numerical approach should be adopted. Such work has been undertaken and appears in Chapter 5 of this thesis.

Chapter 4

The influence of higher order effects on the vortex instability of thermal boundary layer flow from inclined surfaces

4.1 Summary

In the present chapter we again consider the influence of higher order effects on the stability of free convective boundary layer flow. Now however we study a generally inclined boundary layer and assume that the disturbances have the form of longitudinal vortices. As in Chapter 3, we assume that the fluid is bounded

by two semi-infinite flat plates. One of these is the heated upward facing surface, the other is either insulated or is at the ambient temperature of the medium. The surfaces again form a wedge of angle α, and the heated surface is inclined at an angle δ to the vertical (see Figure 4.1). Although the leading order basic flow may be written in a form which is independent of both α and δ, further terms are functions of α and δ. We investigate the effect on the stability of varying α and δ. In general we find that the critical distance is very strongly dependent on both these factors.

The basic flow used in the analysis is a two-term boundary layer approximation using the method of matched asymptotic expansions. A modified version of the Keller-box method is again used to solve the linearised disturbance equations numerically, whilst the basic flow is solved by a standard shooting method employing Newton-Raphson iteration techniques. We consider two types of fluids, air ($Pr = 0.7$) and water ($Pr = 6.7$) as working fluids.

In § 4.2 we derive the governing equations for thermal boundary layer flow from an inclined surface. A basic flow analysis is presented in § 4.3 using matched asymptotic expansions. The equations satisfied by the vortex disturbances are derived in § 4.4 using a small perturbation technique. The stability results are presented briefly in § 4.5. We give our conclusions in § 4.6.

4.2 Governing equations of motion

We consider the instability of free convective boundary layer flow from an inclined semi-infinite heated plate. A sketch of the flow configuration is shown in Figure 4.1. The equations which describe free convection are taken to be the incompressible continuity, Navier-Stokes, and energy equations. The unsteady equations of motion subject to the Boussinesq approximation are written in the nondimensional form,

$$\frac{\partial u}{\partial x}+\frac{\partial v}{\partial y}+\frac{\partial w}{\partial z}=0, \tag{4.1}$$

$$\frac{\partial u}{\partial t}+u\frac{\partial u}{\partial x}+v\frac{\partial u}{\partial y}+w\frac{\partial u}{\partial z}=-\frac{\partial P}{\partial x}+\frac{\partial^2 u}{\partial x^2}+\frac{\partial^2 u}{\partial y^2}+\frac{\partial^2 u}{\partial z^2}+\theta\cos\delta, \tag{4.2}$$

$$\frac{\partial v}{\partial t}+u\frac{\partial v}{\partial x}+v\frac{\partial v}{\partial y}+w\frac{\partial v}{\partial z}=-\frac{\partial P}{\partial y}+\frac{\partial^2 v}{\partial x^2}+\frac{\partial^2 v}{\partial y^2}+\frac{\partial^2 v}{\partial z^2}+\theta\sin\delta, \tag{4.3}$$

$$\frac{\partial w}{\partial t}+u\frac{\partial w}{\partial x}+v\frac{\partial w}{\partial y}+w\frac{\partial w}{\partial z}=-\frac{\partial P}{\partial z}+\frac{\partial^2 w}{\partial x^2}+\frac{\partial^2 w}{\partial y^2}+\frac{\partial^2 w}{\partial z^2}, \tag{4.4}$$

$$\frac{\partial \theta}{\partial t}+u\frac{\partial \theta}{\partial x}+v\frac{\partial \theta}{\partial y}+w\frac{\partial \theta}{\partial z}=\frac{1}{Pr}\left(\frac{\partial^2 \theta}{\partial x^2}+\frac{\partial^2 \theta}{\partial y^2}+\frac{\partial^2 \theta}{\partial z^2}\right). \tag{4.5}$$

Here x, y and z are the streamwise, cross-stream and spanwise Cartesian coordinates, and u, v and w are the corresponding fluid velocity components, P is the dynamical pressure, θ is the fluid temperature, t is time, and Pr is the Prandtl number. In equations (4.1)-(4.5) the angle of inclination of the semi-infinite surface from the vertical is δ, where $0<\delta<\pi/2$ corresponds to an upward facing surface with the leading edge placed below the rest of the surface.

Equations (4.1)-(4.5) have been nondimensionalised in such a way that the Grashof

number has been set to unity; this procedure is identical to that described in Chapter 3.

The surface $y = 0$, $x \geq 0$, is isothermal and is maintained at the nondimensional temperature $\theta = 1$, whilst the other surface is held at the temperature $\theta = 0$ or else is insulated. The corresponding boundary conditions may be written as follows

$$u = v = w = 0, \quad \theta = 1 \quad \text{at} \quad y = 0, \quad x \geq 0, \quad \text{on} \quad \phi = 0 \tag{4.6}$$

$$u = v = w = 0, \quad \theta = 0 \quad \text{on} \quad \phi = \alpha \tag{4.7}$$

Here ϕ is measured counter clockwise from the heated surface.

4.3 Basic flow analysis

In this section we determine the two-term solution of the undisturbed basic boundary layer flow using the method of matched asymptotic expansions. Very similar asymptotic expansions were derived in Chapter 3 to analyse the basic flow. The basic flow is steady and two-dimensional and may be written in streamfunction-vorticity form. If we assume that all z and t derivatives are zero and set

$$u = \frac{\partial \psi_B}{\partial y} \quad \text{and} \quad v = -\frac{\partial \psi_B}{\partial x} \tag{4.8}$$

into equations (4.1)-(4.22), then we obtain the following set of equations for the basic flow,

$$\nabla^2 \psi_B = \omega_B \tag{4.9}$$

$$\nabla^2 \omega_B = \frac{\partial \psi_B}{\partial y}\frac{\partial \omega_B}{\partial x} - \frac{\partial \psi_B}{\partial x}\frac{\partial \omega_B}{\partial y} - \frac{\partial \theta_B}{\partial y}\cos\delta + \frac{\partial \theta_B}{\partial x}\sin\delta \tag{4.10}$$

$$\frac{1}{Pr}\nabla^2 \theta_B = \frac{\partial \psi_B}{\partial y}\frac{\partial \theta_B}{\partial x} - \frac{\partial \psi_B}{\partial x}\frac{\partial \theta_B}{\partial y} \tag{4.11}$$

subject to the boundary conditions,

$$\psi_B = \frac{\partial \psi_B}{\partial y} = 0, \quad \theta_B = 1, \quad \text{at} \quad y = 0, \quad \text{on} \quad \phi = 0 \tag{4.12}$$

$$\psi_B = \psi_{B_n} = 0, \quad \theta_B = 0, \quad \text{on} \quad \phi = \alpha. \tag{4.13}$$

Here n as a subscript denotes the normal derivative.

The basic flow analysis follows in roughly the same way as in Chapter 3, where a matched asymptotic expansion was used to determine a series solution for the flow and temperature field. In the boundary layer region ($x \gg y$) these expansions for the streamfunction and temperature are taken to be

$$\psi_B = x^{3/4}(\cos\delta)^{1/4}[F_0(\eta) + x^{-3/4}F_1(\eta) + \cdots\cdots] \tag{4.14}$$

$$\theta_B = H_0(\eta) + x^{-3/4}H_1(\eta) + \cdots\cdots \tag{4.15}$$

where the similarity variable η is given by

$$\eta = \frac{y}{x^{1/4}} (\cos\delta)^{1/4}. \tag{4.16}$$

The functions F_0, F_1, H_0, and H_1 which appear in equations (4.14)-(4.15) satisfy the following ordinary differential equations

$$F_0'''' + \tfrac{3}{4} F_0 F_0''' - \tfrac{1}{2} F_0' F_0' + H_0 = 0, \tag{4.17}$$

$$H_0'' + \tfrac{3}{4} Pr\, F_0 H_0' = 0, \tag{4.18}$$

$$F_1'''' + \tfrac{3}{4} F_0 F_1''' - \tfrac{1}{4} F_0' F_1' + H_1 = \tfrac{1}{4} \tan\delta (\cos\delta)^{-1/4} \left(\eta H_0 - \int_0^\eta H_0(\xi) d\xi \right), \tag{4.19}$$

$$H_1'' + \tfrac{3}{4} Pr\, (F_0 H_1)' = 0, \tag{4.20}$$

At $\eta = 0$ these functions satisfy the boundary conditions

$$F_0 = F_0' = F_1 = F_1' = 0, \tag{4.21}$$

$$H_0 = 1, \quad H_1 = 0. \tag{4.22}$$

whilst the boundary conditions which allow an asymptotic match with the outer region flow (i.e. as $\eta \to \infty$) are that

$$F_0' \to 0, \quad F_1' \to -\tfrac{3}{4} F_0(\infty) (\cos\delta)^{-1/4} \cot(\tfrac{3}{4}\alpha) \tag{4.23}$$

$$H_0 \to 0, \quad H_1 \to 0. \tag{4.24}$$

We have omitted the details of the outer flow for the sake of brevity.

We note that the system of equations (4.17)-(4.24) have to be solved numerically using a standard shooting method scheme which was discussed in Chapter 3. Given the form of the similarity variable in (4.16) the leading order boundary layer flow is not dependent on α and δ. But the second term is dependent on these parameters. The basic solution again has a singularity when $\alpha = 0$ and $\frac{4}{3}\pi$.

4.4 Linear stability analysis

In this section we develop the linear stability equations for the basic flow given above. It is well-known that the primary mode of instability for an upward facing inclined hot surface usually takes the form of streamwise vortices (Sparrow & Husar (1969)) and hence we will restrict attention to small amplitude disturbances of this form. We will also assume that the disturbances are locally independent of x; the same assumption was made by Kahawita & Meroney (1974), Chen & Tzuoo (1982), and Haaland & Sparrow (1973a) to examine the vortex instabilities of free convection flow along inclined surfaces. Therefore we perturb the basic solutions by setting

$$u(x, y, z, t) = u_B(x, y) + \epsilon\, \hat{u}(x, y, z, t)$$

$$v(x,y,z,t) = v_B(x,y) + \epsilon\,\hat{v}(x,y,z,t)$$

$$w(x,y,z,t) = \epsilon\,\hat{w}(x,y,z,t) \tag{4.25}$$

$$P(x,y,z,t) = P_B(x,y) + \epsilon\,\hat{P}(x,y,z,t)$$

$$\theta(x,y,z,t) = \theta_B(x,y) + \epsilon\,\hat{\theta}(x,y,z,t)$$

where a hat corresponds to the disturbance component. The amplitude parameter ϵ is assumed to be small asymptotically ($\epsilon \ll 1$) and the substitution of equations (4.25) into the full governing equations (4.1)-(4.5) gives the following set of linearised disturbance equations,

$$\frac{\partial \hat{u}}{\partial x} + \frac{\partial \hat{v}}{\partial y} + \frac{\partial \hat{w}}{\partial z} = 0, \tag{4.26}$$

$$\frac{\partial \hat{u}}{\partial t} + u_B\frac{\partial \hat{u}}{\partial x} + \hat{u}\frac{\partial u_B}{\partial x} + v_B\frac{\partial \hat{u}}{\partial y} + \hat{v}\frac{\partial u_B}{\partial y} = -\frac{\partial \hat{P}}{\partial x} + \frac{\partial^2 \hat{u}}{\partial x^2} + \frac{\partial^2 \hat{u}}{\partial y^2} + \frac{\partial^2 \hat{u}}{\partial z^2} + \hat{\theta}\cos\delta, \tag{4.27}$$

$$\frac{\partial \hat{v}}{\partial t} + u_B\frac{\partial \hat{v}}{\partial x} + \hat{u}\frac{\partial v_B}{\partial x} + v_B\frac{\partial \hat{v}}{\partial y} + \frac{\partial v_B}{\partial y}\hat{v} = -\frac{\partial \hat{P}}{\partial y} + \frac{\partial^2 \hat{v}}{\partial x^2} + \frac{\partial^2 \hat{v}}{\partial y^2} + \frac{\partial^2 \hat{v}}{\partial z^2} + \hat{\theta}\sin\delta, \tag{4.28}$$

$$\frac{\partial \hat{w}}{\partial t} + u_B\frac{\partial \hat{w}}{\partial x} + v_B\frac{\partial \hat{w}}{\partial y} = -\frac{\partial \hat{P}}{\partial z} + \frac{\partial^2 \hat{w}}{\partial x^2} + \frac{\partial^2 \hat{w}}{\partial y^2} + \frac{\partial^2 \hat{w}}{\partial z^2}, \tag{4.29}$$

$$\frac{\partial \hat{\theta}}{\partial t} + u_B\frac{\partial \hat{\theta}}{\partial x} + \hat{u}\frac{\partial \theta_B}{\partial x} + v_B\frac{\partial \hat{\theta}}{\partial y} + \hat{v}\frac{\partial \theta_B}{\partial y} = \frac{1}{Pr}\left(\frac{\partial^2 \hat{\theta}}{\partial x^2} + \frac{\partial^2 \hat{\theta}}{\partial y^2} + \frac{\partial^2 \hat{\theta}}{\partial z^2}\right). \tag{4.30}$$

and the appropriate boundary conditions required to solve the above disturbance equations are

$$\hat{u} = \hat{v} = \hat{w} = \hat{\theta} = 0, \quad \text{at} \quad y = 0, \tag{4.31}$$

$$\hat{u}, \hat{v}, \hat{w}, \hat{\theta} \to 0, \quad \text{as} \quad y \to \infty. \tag{4.32}$$

Experimental results (see Sparrow & Husar (1969) and Lloyd & Sparrow (1970)) indicate that the vortices which appear at some distance from the leading edge are steady and amplify downstream. These vortices must of necessity have a fixed spanwise wavenumber k, and therefore we will assume that the onset of convection corresponds to $\lambda = 0$ if all disturbances are taken to be proportional to $e^{\lambda t}$. We also assume that at neutrality, the disturbances are independent of x; in this regard we follow Chen & Tzuoo (1982), and Haaland & Sparrow (1973a) since our aim here is to determine how a more accurate representation of the basic flow affects the stability criterion. In view of all these considerations we assume that the various components of the vortex disturbances are functions of y and z, and are periodic in the spanwise direction z. Consequently, the disturbance quantities $\hat{u}$, $\hat{v}$, $\hat{w}$, $\hat{\theta}$, and $\hat{P}$ may be Fourier decomposed as

$$\hat{u} = F(y)\cos kz, \tag{4.33}$$

$$\hat{v} = G(y)\cos kz, \tag{4.34}$$

$$\hat{w} = H(y)\sin kz, \tag{4.35}$$

$$\hat{\theta} = S(y)\cos kz, \tag{4.36}$$

$$\hat{P} = Q(y)\cos kz. \tag{4.37}$$

where $F(y)$, $G(y)$, $H(y)$, $S(y)$, and $Q(y)$ are functions of y, and k is the spanwise wavenumber of the disturbances.

Equations (4.33)-(4.37) may now be substituted into equations (4.26)-(4.32). For computational convenience, we eliminate Q and H to obtain three equations involving only F, G, and S. We then make a change of variables from (x, y) to (x, η) where η is defined in equation (4.16). The disturbance equations now become

$$F'' - v_B X F' - \left(k^2 + \frac{\partial u_B}{\partial x}\right) X^2 F = X^2 \left(\frac{\partial u_B}{\partial y} G - S \cos\delta\right) \tag{4.38}$$

$$G^{iv} - v_B X G''' - \left(2k^2 + \frac{\partial v_B}{\partial y}\right) X^2 G'' + k^2 v_B X^3 G' + k^2 \left(k^2 + \frac{\partial v_B}{\partial y}\right) X^4 G$$

$$= -k^2 \frac{\partial v_B}{\partial x} X^4 F + k^2 X^4 S \sin\delta \tag{4.39}$$

$$S'' - Pr\, v_B X S' - k^2 X^2 S = Pr\, X^2 \left(\frac{\partial \theta_B}{\partial x} F + \frac{\partial \theta_B}{\partial y} G\right) \tag{4.40}$$

where X, a scaled streamwise coordinate, is defined as

$$X(x, \delta) = \left(\frac{x}{\cos\delta}\right)^{1/4} \tag{4.41}$$

and where primes represent derivatives with respect to η. The corresponding boundary conditions to be satisfied by the disturbance equations are that

$$F = G = G' = S = 0, \quad \text{at} \quad \eta = 0, \tag{4.42}$$

and

$$F, G, G', S \to 0, \quad \text{as} \quad \eta \to \infty. \tag{4.43}$$

The system of equations (4.38)-(4.43) is homogeneous and form an 8^{th} order real eigenvalue problem for x in terms of k and Pr. Non-trivial solutions may be obtained by defining the normalisation condition

$$S'(0) = 1. \tag{4.44}$$

Equations (4.42)-(4.44) now contain nine conditions to solve the eighth order system of equations (4.38)-(4.40) together with the eigenvalue, k.

Again to summarise the stability results, it is necessary to find out the value of the critical distance x_c. However this value is a function of wavenumber k. Therefore it is necessary to minimise x with respect to k. In order to do this, we implement equations (4.38)-(4.40) with a further new set which is obtained from (4.38)-(4.40) by differentiating with respect to k and setting $\frac{\partial x}{\partial k} = 0$. If we now define $\mathcal{F}$, $\mathcal{G}$ and $\mathcal{S}$ according to,

$$\mathcal{F} = \frac{\partial F}{\partial k}, \qquad \mathcal{G} = \frac{\partial G}{\partial k} \qquad \text{and} \qquad \mathcal{S} = \frac{\partial S}{\partial k} \tag{4.45}$$

then $\mathcal{F}$, $\mathcal{G}$ and $\mathcal{S}$ satisfy

$$\mathcal{F}'' - v_B X \mathcal{F}' - \left(k^2 + \frac{\partial u_B}{\partial x}\right) X^2 \mathcal{F} = X^2 \left(\frac{\partial u_B}{\partial y}\mathcal{G} - \mathcal{S}\cos\delta\right) + 2kX^2 F \tag{4.46}$$

$$\mathcal{G}^{iv} - v_B X \mathcal{G}''' - \left(2k^2 + \frac{\partial v_B}{\partial y}\right) X^2 \mathcal{G}'' + k^2 v_B X^3 \mathcal{G}' + k^2 \left(k^2 + \frac{\partial v_B}{\partial y}\right) X^4 \mathcal{G}$$

$$= k^2X^4\mathcal{S}\sin\delta - k^2\frac{\partial v_B}{\partial x}X^4\mathcal{F} - 2k\frac{\partial v_B}{\partial x}X^4F - 2kv_BX^2G'$$

$$+4kX^2G'' - 2k\left(2k^2 + v_B\right)X^4G + 2kX^4S\sin\delta \tag{4.47}$$

$$\mathcal{S}'' - Pr\,v_BX\mathcal{S}' - k^2X^2\mathcal{S} = Pr\,X^2\left(\frac{\partial\theta_B}{\partial x}\mathcal{F} + \frac{\partial\theta_B}{\partial y}\mathcal{G}\right) + 2kX^2S \tag{4.48}$$

and the corresponding boundary conditions are

$$\mathcal{F} = \mathcal{G} = \mathcal{G}' = \mathcal{S} = 0 \quad \text{at} \quad \eta = 0 \tag{4.49}$$

$$\mathcal{F}, \mathcal{G}, \mathcal{G}', \mathcal{S} \to 0 \quad \text{as} \quad \eta \to \infty. \tag{4.50}$$

The normalisation condition at $\eta = 0$ is derived from (4.44) and is

$$\mathcal{S}'(0) = 0. \tag{4.51}$$

Now the equations (4.38)-(4.40) and (4.46)-(4.48) are a 16^{th} order ordinary system of equations together with the eigenvalues X and k. This system of equations must be solved with 18 boundary conditions which are specified in (4.42)-(4.44) and (4.49)-(4.51).

We again use a suitable modified version of the Keller-box method to solve this ordinary differential eigensystem. The method is identical to that used for the wave instability problem discussed in Chapter 3 and differs only in the fact that we are solving an 8^{th} order rather than a 16^{th} order eigenvalue problem (or 16^{th} order rather than a 32^{nd} order system when allowing for the minimisation of x_c

over k). Once more the basic flow equations (4.17)-(4.24) were solved using a 4^{th} order Runge-Kutta method coupled to a shooting method algorithm.

We have used $\eta_\infty = 10$ with $d\eta = 0.1$ for $Pr = 0.7$ and 6.7 and found that sufficiently accurate results are obtained for the stability analysis.

4.5 Numerical results

In this section we present details of the numerical results. We have scaled the critical distance x_c and wavenumber k_c with respect to the inclination δ ($0^0 \leq \delta < 90^0$) using

$$\hat{x}_c = x_c \delta^{4/3}, \tag{4.52}$$

$$\hat{k}_c = k_c \delta^{-1/4}. \tag{4.53}$$

The reason for these scalings is that when δ is close to 0 (i.e. the surface is close to vertical), the critical distance x_c becomes infinite, but the new scaling gives a finite critical distance, $\hat{x}_c = 26.35$ (for $Pr = 0.7$), as $\delta \to 0$. A similar type of scaling was used by Storesletten & Rees (1998) and Hsu & Cheng (1979) to analyse vortex instabilities in porous media, although the power of δ used in those studies is different. Therefore we will present the results of the variation of x_c, $\hat{x}_c$ and k_c, $\hat{k}_c$ with both wedge angle α and inclination angle δ in considering both the one-term and two-term basic boundary layer flow.

Before presenting the detailed results of our stability analysis it is necessary to consider first some of the implications of the dependence of F_1' on α. One component of the solution for F_1' is proportional to $\cot\frac{3}{4}\alpha$; see the boundary condition (4.23). Although this function is zero when $\alpha = \frac{2}{3}\pi = 120^0$, the two-term boundary layer solution is not identical to the one-term solution, because there is a second component of F_1' which corresponds to the inhomogeneous term in (4.19). Therefore the two-term stability results when $\alpha = \frac{2}{3}\pi$ will not be identical to those obtained using only the one-term solution. This is unlike the case considered in the previous chapter where F_1' is proportional to $\cot\frac{3}{4}\pi$.

Again, when $\alpha = 0$ and $\alpha = \frac{4}{3}\pi = 240^0$, F_1' is infinite and the asymptotic series breaks down in these limits. Furthermore, the function $\cot\frac{3}{4}\alpha$ has period $\frac{4}{3}\pi$ and therefore all the results for the range $0 < \alpha \leq \frac{2}{3}\pi$ also apply for the range $\frac{4}{3}\pi < \alpha \leq 2\pi$. Finally we note that F_1' is positive when $\frac{2}{3}\pi \leq \alpha < \frac{4}{3}\pi$, and therefore the two-term streamwise velocity is greater than that given by the one-term only. For other values of α the basic flow is slower.

4.5.1 Neutral stability for $Pr = 0.7$

First we present here the stability characteristics for air by choosing the Prandtl number, $Pr = 0.7$. These are summarised in Figures 4.2 to 4.8.

Figure 4.2 displays the variation of the critical distance x_c against the inclination angle δ for air. A selection of wedge angles has been taken in the range $0^0 < \alpha <$

240^0; a detailed choice of α values is shown clearly in Figure 4.4. We note that the dashed curve corresponds to taking only the one-term solutions of the basic boundary layer flow; this is also true in the following Figures 4.3, 4.4, and 4.5. For all values of α the critical distance x_c increases as δ decreases. This implies that when the isothermal plate approaches the vertical, the free convective flow is more stable with respect to vortex disturbance. In this situation, the critical distance x_c becomes infinite and hence the vortex mode of instability does not take place. This is due to the decreasing effect of the buoyancy force in the normal direction of the plate and shows that the streamwise vortices are a thermo-convective instability in this context. Unfortunately it is impossible to compare this behaviour with experimental work, such as Lloyd & Sparrow (1970), since waves take over as the dominant instability mechanism as δ decreases.

Figure 4.2 also shows that there is a very substantial variation in the critical value of x_c as α varies for fixed values of δ. This suggests that the external flow has a substantial effect on the stability criterion.

The variation of the critical wavenumber, k_c, with inclination angle, δ, is plotted in Figure 4.3. As the angle of inclination increases, k_c increases. This may be understood if one were to assume that the wavelength of the vortex always remains roughly of the same order of magnitude as the boundary layer thickness. Now since x_c decreases as δ increases, the boundary layer thickness at onset also decreases and therefore k_c should be expected to increase.

From Figure 4.3 we see that for any fixed value of δ the value of k_c is almost independent of the wedge angle α. This is a surprising result given the variation of x_c with α and the above argument.

Figure 4.4 displays the variation of the scaled critical distance $\hat{x}_c$ against the inclination angle δ for the previous set of discrete values of α in the range $5^0 \leq \alpha \leq 235^0$. We note here again that for the dashed curve, which corresponds to taking only the one-term solution of the basic boundary layer flow, this result is very close to that obtained for $\alpha = 130^0$. In this case, for which the heated surface is inclined, the two-term approach to the basic flow when $\alpha = \frac{2}{3}\pi = 120^0$ is not identical to the one-term approach, unlike when the surface is vertical.

Figure 4.4 shows more clearly than Figure 4.2 the variation of the neutral distance with α, and confirms that the variation is very substantial. Therefore it is clearly understood that the external domain exerts a very large influnce on the stability characteristics of the flow. However, when the heated surface is close to the vertical, i.e. δ is small, then there appears to be little variation in the critical distance $\hat{x}_c$. The unscaled value x_c is asymptotically large as $\delta \rightarrow 0$, and therefore the second term in the boundary layer expansion is asymptotically small compared with the one term basic boundary layer solution.

Although we omit presentation of detailed (x-k) neutral curves, these again become increasingly bizarre shapes as α approaches 240^0; this is why the curves for large values of α terminate prematurely. Although the variation in $\hat{k}_c$ with

α, shown in Figure 4.5, appears to be larger than is shown in Figure 4.3, the vertical scale used in Figure 4.5 is greatly expanded. Again this confirms the near independence of $\hat{k}_c$ with respect to α.

Figures 4.2 to 4.5 used δ as the abscissa; the corresponding variation of the neutral values with α as the abscissa are depicted in Figures 4.6 to 4.8.

Figure 4.6 displays the effect on the critical distance $\hat{x}_c$ of varying the wedge angle α. Here we have chosen to use different surface inclinations $\delta = 5^0$, 10^0, 20^0, 30^0, 40^0, 50^0, 60^0, 70^0, and 80^0. The dotted ($\bullet$) results correspond to considering only the leading order basic flow. The computed value $\hat{x}_c$ shows quite marked variation with α. The number of terms in the basic flow has a very significant effect on the critical distance and this effect increases as δ increases. When δ is very small (e.g. $\delta = 5^0$), there is little difference between the results using the one-term and two-term approximations, and it is within this regime that waves are more likely to appear. However, when α is close to either 0^0 and 240^0, $\hat{x}_c$ begins to show large variations. As mentioned in Chapter 3, the first order velocity component (F_1') becomes very large in these limits. When δ increases, this variation also increases and is quite large even at $\delta = 40^0$.

Figure 4.7 appears to show clearly that x_c does not vary much with α, in contradiction to the conclusion based on Figure 4.6. However this is simply a matter of the vertical scale used in the figure where the absolute variations are more evident than relative variations. However Figure 4.8 confirms emphatically our

earlier observation that the wavenumber is almost independent of α.

4.5.2 Neutral stability for $Pr = 6.7$

Equivalent results for the case of water, for which $Pr = 6.7$, are shown in Figures 4.9 to 4.15. The general trends described above for air also occur for water.

Figure 4.9 shows the same trend that the critical distance x_c becomes infinite as $\delta \to 0$. In general, comparing with the results for air, the critical distances for water are smaller. However, this is true only in terms of the nondimensional distances and is not necessarily always true for the dimensional distances. To illustrate this, consider a particular case. The nondimensional neutral distance derived for air ($Pr = 0.7$) at $\delta = 40^0$ and $\alpha = 120^0$ is $x_c = 36.369$, and for water ($Pr = 6.7$) it is $x_c = 23.468$.

The length scale is defined in Chapter 3 (see equation 3.13). For a given situation consider g and ΔT are to be the same. We need to compare

$$36.369\left(\frac{\nu^2}{\beta}\right)^{1/3}_{air} \qquad \text{and} \qquad 23.468\left(\frac{\nu^2}{\beta}\right)^{1/3}_{water}.$$

In fact, if we consider $\Delta T = 10^0 C$ and $g = 9.81N$, at the Atmospheric pressure the values of ν, β are $1.50 \times 10^{-5} m^2 s^{-1}$, $3.40 \times 10^{-3} K^{-1}$ for air and $10.04 \times 10^{-7} m^2 s^{-1}$, $2.1 \times 10^{-4} K^{-1}$ for water respectively. Therefore the dimensional neutral distance for air is $\bar{x}_c = 3.189cm$ and for water is $\bar{x}_c = 0.858cm$, smaller

than for air. Hence this also suggests that the destabilisation takes place nearer to the leading edge for water.

Figures 4.10 and 4.12 also show the same trend that the critical wavenumber decreases towards zero as $\delta \rightarrow 0$. But the variation of critical wavenumbers with α is greater than that for air. This is opposite to the variation of critical distances with α, see Figure 4.11, where $\hat{x}_c$ has less variation with α than for air.

Figures 4.13 to 4.15 depict the variation of neutral values with α as the abscissa. When δ is small, the difference between the results using the one-term and two-term boundary layer approximations is little. Figure 4.15 also shows the wavenumber is almost independent of α – which was same observation for the case of air.

4.6 Conclusions

We have used the theory of matched asymptotic expansions to determine a two-term approximation to the basic free convective boundary layer flow which is induced by an inclined heated surface. This flow has been analysed for stability with respect to vortex disturbances using the parallel flow approximation. The aim has been to determine what influence a more accurate representation of the basic flow has on the computed stability criteria.

Although the critical distance $\hat{x}_c$ is strongly dependent on the angle of inclination

δ, we have found that it also varies substantially with changes in the wedge angle α. In this regard we may say that stability criteria derived using the leading order boundary layer flow are unreliable in general since the basic flow is clearly inadequately represented using one-term. However, the presence of the second term in the basic flow yields stability criteria which are dependent on the overall shape of the convective domain. The only exception to this situation is when the heated surface is close to the vertical, for it is only in this limit that the second boundary layer terms are small compared with the leading order terms, and therefore the leading order criterion is accurate. However, it is in this regime that wave-like instabilities become more important than vortices.

Chapter 5

Receptivity of free convection flow from a heated vertical surface. I. Linear waves

5.1 Summary

Our objective is to perform a numerical investigation of the linear instability of thermal boundary layer flow over a vertical surface by introducing thermal disturbances near the leading edge. The nonlinear elliptic time-dependent Navier-Stokes equations are solved to obtain the steady state flow, and this solution is then used to linearise the full equations. The fully elliptic linearised perturbation equations are then solved in order to determine the stability characteristics of the

boundary layer.

The imposition of a localised thermal disturbance at one point in time and near to the leading edge is found to develop in both space and time. As the leading and trailing edge of the developing disturbance both accelerate downstream and leave the computational domain, the wave instability is confirmed as being convective (advective) in nature.

The majority of this chapter is concerned with the response of the boundary layer to time-periodic variations in the surface temperature near the leading edge. This may be regarded as a thermal equivalent of the classical vibrating ribbon experiment. We find that the response of the boundary layer consists of a transient, which is advected along the boundary layer and eventually disappears from the computational domain, and a time-periodic flow. The amplitude of the time-periodic response depends very strongly on the forcing frequency, but it is found that the forcing frequency which gives the largest response varies with the location at which the amplitude is measured. This optimum frequency increases with disturbance downstream. The results of these elliptic calculations are compared with those obtained by assuming the parallel flow approximation, as described by the "two-term" solutions of Chapter 3.

5.2 Equations of motion and boundary conditions

5.2.1 Governing equations

We consider the two-dimensional free convective boundary layer flow from a vertical semi-infinite heated plate. A schematic diagram of the flow domain showing the coordinate directions, the transformed coordinates and the boundary conditions is shown in Figure 5.1. A Cartesian frame of reference is chosen, where the $\bar{x}$-axis is aligned vertically upwards with the heated surface, and the $\bar{y}$-axis is perpendicular to this. The equations which describe the free convection from a vertical plate are taken to be the incompressible continuity, Navier-Stokes, and energy equations subject to the Oberbeck-Boussinesq approximation. For unsteady two dimensional flow this system is written in the dimensional form

$$\frac{\partial \bar{u}}{\partial \bar{x}} + \frac{\partial \bar{v}}{\partial \bar{y}} = 0, \tag{5.1}$$

$$\frac{\partial \bar{u}}{\partial \bar{t}} + \bar{u}\frac{\partial \bar{u}}{\partial \bar{x}} + \bar{v}\frac{\partial \bar{u}}{\partial \bar{y}} = -\frac{1}{\rho}\frac{\partial P}{\partial \bar{x}} + \nu\left(\frac{\partial^2 \bar{u}}{\partial \bar{x}^2} + \frac{\partial^2 \bar{u}}{\partial \bar{y}^2}\right) + g\beta(T - T_\infty), \tag{5.2}$$

$$\frac{\partial \bar{v}}{\partial \bar{t}} + \bar{u}\frac{\partial \bar{v}}{\partial \bar{x}} + \bar{v}\frac{\partial \bar{v}}{\partial \bar{y}} = -\frac{1}{\rho}\frac{\partial P}{\partial \bar{y}} + \nu\left(\frac{\partial^2 \bar{v}}{\partial \bar{x}^2} + \frac{\partial^2 \bar{v}}{\partial \bar{y}^2}\right), \tag{5.3}$$

$$\frac{\partial T}{\partial \bar{t}} + \bar{u}\frac{\partial T}{\partial \bar{x}} + \bar{v}\frac{\partial T}{\partial \bar{y}} = \kappa\left(\frac{\partial^2 T}{\partial \bar{x}^2} + \frac{\partial^2 T}{\partial \bar{y}^2}\right), \tag{5.4}$$

where $\bar{u}$ and $\bar{v}$ are the velocity components in the $\bar{x}$ and $\bar{y}$-directions, respectively, P is the dynamic pressure, T is the temperature of the fluid, $\bar{t}$ is the time, g is the gravitational acceleration in the negative $\bar{x}$-direction, ρ is the density of the fluid, ν is the kinematic viscosity, κ is the diffusivity and β is the coefficient of thermal expansion.

In non-dimensionalising the variables, the following dimensionless groups of variables have been introduced,

$$(\bar{x}, \bar{y}) = d(x, y),$$

$$(\bar{u}, \bar{v}) = U(u, v),$$

$$\bar{t} = \frac{d}{U} t,$$

$$T - T_\infty = (T_w - T_\infty)\theta, \tag{5.5}$$

where natural length and velocity scales are given by,

$$d = \left(\frac{\nu^2}{g\beta\Delta T}\right)^{1/3},$$

$$U = (g\beta\Delta T\nu)^{1/3}. \tag{5.6}$$

Here T_w is the temperature of the plate and T_∞ is the ambient temperature of the fluid with $T_w > T_\infty$. On using those dimensionless variables which are defined in equations (5.5) and (5.6), the continuity, Navier-Stokes, and energy conservation equations may be rewritten in non-dimensional stream function (ψ), vorticity

(ω), and temperature (θ) form,

$$\nabla^2\psi = \omega, \tag{5.7}$$

$$\frac{\partial\omega}{\partial t} = \nabla^2\omega + \frac{\partial\psi}{\partial x}\frac{\partial\omega}{\partial y} - \frac{\partial\psi}{\partial y}\frac{\partial\omega}{\partial x} + \frac{\partial\theta}{\partial y}, \tag{5.8}$$

$$\frac{\partial\theta}{\partial t} = \frac{1}{Pr}\nabla^2\theta + \frac{\partial\psi}{\partial x}\frac{\partial\theta}{\partial y} - \frac{\partial\psi}{\partial y}\frac{\partial\theta}{\partial x}, \tag{5.9}$$

where the stream function is defined by $u = \psi_y$, $v = -\psi_x$ and the vorticity is defined by (5.7). In equation (5.9) the Prandtl number is given by $Pr = \nu/\kappa$. It is important to note that our scalings do not cause a Grashof number to appear in the governing nondimensional equations. That this is acceptable follows from the fact that there is no externally defined length scale in the idealised configuration being studied, and that the lengthscale defined in equation (5.6) is equivalent to setting the usual Grashof number to unity; such a procedure has also been used in studies of vortex disturbances in thermal boundary layer flows in porous media undertaken by Rees (2001) and Rees (2002).

5.2.2 Coordinate transformation

The usual boundary layer approximation to equations (5.7)-(5.9) is satisfied by the solutions

$$\psi = x^{3/4}f(\eta), \quad \theta = g(\eta), \quad \omega = x^{1/4}f''(\eta) \tag{5.10}$$

(see Pohlhausen (1921); Ostrach (1953)) where $\eta = y/x^{1/4}$ is the similarity variable and the functions f and g satisfy the leading order boundary layer equations,

$$f''' + \tfrac{3}{4} f f' - \tfrac{1}{2} f' f' + g = 0, \tag{5.11}$$

$$g'' + \tfrac{3}{4} Pr\, f g' = 0, \tag{5.12}$$

subject to the boundary conditions

$$f(0) = f'(0) = g(0) - 1 = 0, \tag{5.13}$$

$$f', g \to 0 \quad \text{as} \quad \eta \to \infty. \tag{5.14}$$

This form of the similarity variable motivates the use of the Schwartz-Christoffel transformation

$$\left[\tfrac{3}{4}(\xi + i\eta)\right]^4 = (x + iy)^3 \tag{5.15}$$

which we use because it guarantees an orthogonal grid optimising the iterative numerical solution of Poisson equations such as (5.7) by maintaining diagonal dominance. In polar coordinates, the transformation may be written in the form,

$$\xi = \tfrac{4}{3} r^{3/4} \cos \tfrac{3}{4}\phi, \tag{5.16}$$

$$\eta = \tfrac{4}{3} r^{3/4} \sin \tfrac{3}{4}\phi, \tag{5.17}$$

where r is the nondimensional radial distance from the origin and ϕ is the angle

from the upward vertical. In terms of ξ and η, equations (5.7) to (5.9) become

$$\frac{\partial^2\psi}{\partial\xi^2} + \frac{\partial^2\psi}{\partial\eta^2} = C\omega, \tag{5.18}$$

$$C\frac{\partial\omega}{\partial t} = \frac{\partial^2\omega}{\partial\xi^2} + \frac{\partial^2\omega}{\partial\eta^2} + \frac{\partial\psi}{\partial\xi}\frac{\partial\omega}{\partial\eta} - \frac{\partial\psi}{\partial\eta}\frac{\partial\omega}{\partial\xi} + C^{1/2}\left(\frac{\partial\theta}{\partial\xi}\sin\tfrac{1}{4}\phi + \frac{\partial\theta}{\partial\eta}\cos\tfrac{1}{4}\phi\right), \tag{5.19}$$

$$C\frac{\partial\theta}{\partial t} = \frac{1}{Pr}\left(\frac{\partial^2\theta}{\partial\xi^2} + \frac{\partial^2\theta}{\partial\eta^2}\right) + \frac{\partial\psi}{\partial\xi}\frac{\partial\theta}{\partial\eta} - \frac{\partial\psi}{\partial\eta}\frac{\partial\theta}{\partial\xi}, \tag{5.20}$$

where the function, C, is given by

$$C(\xi,\eta) = \left(\tfrac{3}{4}\right)^{2/3}\left(\xi^2+\eta^2\right)^{1/3}. \tag{5.21}$$

We note that it is not possible to write these equations explicitly in terms of ξ and η, but the ϕ-dependent terms in (5.19) may easily be computed using the definitions of ξ and η in equation (5.16).

5.2.3 Boundary conditions

The corresponding boundary conditions to be used to solve the equations (5.18)-(5.20) are

$$\psi = \psi_\eta = 0, \quad \theta = 1 \quad \text{on} \quad \eta = \eta_{min} = 0, \tag{5.22}$$

$$\psi = \psi_\xi = 0, \quad \theta_\xi = 0 \quad \text{on} \quad \xi = \xi_{min}, \tag{5.23}$$

$$\psi_\eta = 0, \quad \omega = 0, \quad \theta = 0 \quad \text{on} \quad \eta = \eta_{max}. \tag{5.24}$$

The conditions on ψ on $\eta = \eta_{min}$ and $\xi = \xi_{min}$ correspond to the no-slip condition, while the conditions on ψ and ω given in (5.24) correspond to the conditions satisfied by the self-similar boundary layer solution and therefore η_{max} must be sufficiently large to contain the developing disturbances. The thermal boundary conditions correspond to a unit temperature heated surface, a zero ambient temperature and an insulated surface at $\xi = \xi_{min}$.

In our computations we take $\xi_{min} = 20$; this means that the corresponding curved surface is nearly horizontal, as displayed in Figure 5.1. Given the form of C in equation (5.21) and its presence multiplying the left hand sides of (5.19) and (5.20), the value of ξ_{min} chosen allows us to use the DuFort-Frankel method to march the solution in time. If ξ_{min} had been chosen to be 0, which corresponds to a second plane surface at an angle of 120^0 to the heated surface, then a more difficult and computationally slower fully implicit method, such as that used by Rees & Bassom (1993), would need to be adopted. Although the present choice of ξ_{min} is a device which simplifies the computational code development, the fact that the flow is advectively unstable, rather than absolutely unstable, suggests that the effect of this slight change in the computational domain is minimal.

The boundary conditions at outflow at $\xi = \xi_{max}$ are discussed at length and are given in § 5.3.

5.2.4 Boundary layer approximation

The steady state boundary layer approximation may also be recovered from equations (5.18)-(5.20) in the following forms

$$\frac{\partial^2\psi}{\partial\eta^2} = \left(\tfrac{3}{4}\xi\right)^{2/3}\omega, \tag{5.25}$$

$$\frac{\partial^2\omega}{\partial\eta^2} + \frac{\partial\psi}{\partial\xi}\frac{\partial\omega}{\partial\eta} - \frac{\partial\psi}{\partial\eta}\frac{\partial\omega}{\partial\xi} + \left(\tfrac{3}{4}\xi\right)^{1/3}\frac{\partial\theta}{\partial\eta} = 0, \tag{5.26}$$

$$\frac{1}{Pr}\frac{\partial^2\theta}{\partial\eta^2} + \frac{\partial\psi}{\partial\xi}\frac{\partial\theta}{\partial\eta} - \frac{\partial\psi}{\partial\eta}\frac{\partial\theta}{\partial\xi} = 0, \tag{5.27}$$

where it has been assumed that $\xi \gg \eta$. The solution in this coordinate system is

$$\psi \sim \tfrac{3}{4}\xi f(\eta), \quad \omega \sim \left(\tfrac{3}{4}\xi\right)^{1/3} f''(\eta), \quad \theta \sim g(\eta), \tag{5.28}$$

where f and g satisfy equations (5.11), (5.12) and where $\frac{3}{4}\xi \sim x^{3/4}$ when $\xi \gg \eta$, as may be seen from (5.15).

5.2.5 Linearisation techniques

We consider a small disturbance in the steady flow and the flow variables are written as

$$\psi(\xi,\eta,t) = \bar{\psi}(\xi,\eta) + \epsilon\hat{\psi}(\xi,\eta,t), \tag{5.29}$$

$$\omega(\xi,\eta,t) = \bar{\omega}(\xi,\eta) + \epsilon\hat{\omega}(\xi,\eta,t), \tag{5.30}$$

$$\theta(\xi,\eta,t) = \bar{\theta}(\xi,\eta) + \epsilon\hat{\theta}(\xi,\eta,t), \tag{5.31}$$

where ϵ is asymptotically small, so that powers of ϵ may be neglected. Furthermore an overbar denotes the steady flow variables and a hat denotes the perturbation variables.

Substituting (5.29)-(5.31) into equations (5.18)-(5.20) and dropping terms that are nonlinear in ϵ leads to two sets of equations: one for the steady flow and the other for the perturbation flow. The steady flow equations are given by (5.18) to (5.20) with the addition of the overbar on all dependent variables and the omission of the time-derivative terms. The perturbation equations are given by

$$\frac{\partial^2\hat{\psi}}{\partial\xi^2} + \frac{\partial^2\hat{\psi}}{\partial\eta^2} = C\hat{\omega}, \tag{5.32}$$

$$C\frac{\partial\hat{\omega}}{\partial t} = \frac{\partial^2\hat{\omega}}{\partial\xi^2} + \frac{\partial^2\hat{\omega}}{\partial\eta^2} + \left(\frac{\partial\bar{\psi}}{\partial\xi}\frac{\partial\hat{\omega}}{\partial\eta} - \frac{\partial\bar{\psi}}{\partial\eta}\frac{\partial\hat{\omega}}{\partial\xi}\right) + \left(\frac{\partial\bar{\omega}}{\partial\eta}\frac{\partial\hat{\psi}}{\partial\xi} - \frac{\partial\bar{\omega}}{\partial\xi}\frac{\partial\hat{\psi}}{\partial\eta}\right)$$
$$+C^{1/2}\left(\frac{\partial\hat{\theta}}{\partial\xi}\sin\tfrac{1}{4}\phi + \frac{\partial\hat{\theta}}{\partial\eta}\cos\tfrac{1}{4}\phi\right), \tag{5.33}$$

$$C\frac{\partial\hat{\theta}}{\partial t} = \frac{1}{Pr}\left(\frac{\partial^2\hat{\theta}}{\partial\xi^2} + \frac{\partial^2\hat{\theta}}{\partial\eta^2}\right) + \left(\frac{\partial\bar{\psi}}{\partial\xi}\frac{\partial\hat{\theta}}{\partial\eta} - \frac{\partial\bar{\psi}}{\partial\eta}\frac{\partial\hat{\theta}}{\partial\xi}\right) + \left(\frac{\partial\bar{\theta}}{\partial\eta}\frac{\partial\hat{\psi}}{\partial\xi} - \frac{\partial\bar{\theta}}{\partial\xi}\frac{\partial\hat{\psi}}{\partial\eta}\right), \tag{5.34}$$

and the corresponding boundary conditions are

$$\hat{\psi} = \hat{\psi}_\eta = 0, \quad \hat{\theta} = 0 \quad \text{on} \quad \eta = \eta_{min} = 0, \tag{5.35}$$

$$\hat{\psi} = \hat{\psi}_\xi = 0, \quad \hat{\theta}_\xi = 0 \quad \text{on} \quad \xi = \xi_{min}, \tag{5.36}$$

$$\hat{\psi}_\eta = 0, \quad \hat{\omega} = 0, \quad \hat{\theta} = 0 \quad \text{on} \quad \eta = \eta_{max} \tag{5.37}$$

The general procedure the solving the perturbation equations is as follows. First, we compute the steady state basic flow satisfying the nonlinear equations (5.18)-(5.20). The reason for needing this is that the solution of the boundary layer equations departs quite markedly from the solution of steady elliptic equations near $\xi = \xi_{min}$. Secondly, we solve the linearised disturbance equations (5.32)-(5.34) for a variety of initial conditions/boundary conditions in order to study the stability characteristics of the boundary layer flow.

5.3 Numerical method

5.3.1 Overview

Finite difference techniques were used to solve the system of nonlinear equations (5.18)-(5.20) and the system of linear equations (5.32)-(5.34). The overall numerical scheme is second order accurate in both time and space.

The time-dependent equations are discretised using central differences and the DuFort-Frankel method is used for the time-derivative and diffusion terms.

The Jacobian terms are approximated using the Arakawa formulation (Arakawa 1966) which was designed to be particularly suitable for flows which are unstable. In this method, the physical quantities such as the kinetic energy, vorticity, and momentum itself are conserved in the absence of diffusion. Thus non-linear com-

putational instabilities cannot occur as the quadratic quantities are conserved using this finite difference approximation. This follows from the fact that if the quadratic quantities are conserved with time when summed over all grid points in a domain, the quantity itself will be bounded, at every individual grid point, throughout the entire duration of a long-term integration.

Derivative boundary conditions are approximated using a standard fictitious point approach, for although a straightforward first order approximation at a boundary does not destroy overall second order accuracy, the fictitious point method has a smaller absolute error.

The Poisson equation for the streamfunction has been solved using a multigrid correction scheme to accelerate iterative convergence. It incorporates a V-cycling algorithm involving the line Gauss-Seidel relaxation procedure. The method is based on that described in Briggs (1987). The sweeps are performed on the matrix of equations, which are in central difference approximation form, with both horizontal and vertical line sweeps per relaxation procedure. Two relaxation sweeps are undertaken on each level before moving on to either finer or coarser grids. The matrix equation is in tri-diagonal form and is solved using a tri-diagonal matrix algorithm. Some of these numerical methods are discussed separately in following subsections.

5.3.2 Central differences and the DuFort-Frankel method

The time dependent vorticity and energy equations are discretised using central difference approximations, which are second order accurate in both time and space. The DuFort-Frankel method is based on Richardson's method, which is well-known to be unconditionally unstable. The DuFort-Frankel method is obtained by replacing the central term in the finite difference molecular form of the diffusion term by the appropriate average of the values between the previous and the new time values. To illustrate this we use Fourier's two-dimensional equation in Cartesian coordinates,

$$\frac{\partial \zeta}{\partial t} = \frac{\partial^2 \zeta}{\partial x^2} + \frac{\partial^2 \zeta}{\partial y^2}, \tag{5.38}$$

where ζ is a representative variable. This may be discretized using Richardson's method as

$$\frac{\zeta_{i,j}^{n+1} - \zeta_{i,j}^{n-1}}{2\delta t} = \frac{\zeta_{i-1,j}^{n} - 2\zeta_{i,j}^{n} + \zeta_{i+1,j}^{n}}{\delta x^2} + \frac{\zeta_{i,j-1}^{n} - 2\zeta_{i,j}^{n} + \zeta_{i,j+1}^{n}}{\delta y^2}, \tag{5.39}$$

where $\zeta_{i,j}^{n}$ is the numerical approximation to $\zeta(x_i, y_j, t_n)$. The grid points for t, x and y are defined by $t_n = n\delta t$, $x_i = i\delta x$, and $y_j = j\delta y$, where the step lengths δt, δx, and δy are constant. This method has second order accuracy in both time and space, but it is unconditionally unstable. The method of DuFort-Frankel is obtained by replacing $\zeta_{i,j}^{n}$ by $(\zeta_{i,j}^{n+1} + \zeta_{i,j}^{n-1})/2$, which not only retains the second order accuracy, but also gains unconditional stability for Fourier's equation. The

DuFort-Frankel discretisation of (5.38) can be written down in moleculer form as,

$$\zeta_{i,j}^{n+1}\left(\frac{1}{2\delta t}+\frac{1}{\delta x^2}+\frac{1}{\delta y^2}\right)=\zeta_{i,j}^{n-1}\left(\frac{1}{2\delta t}-\frac{1}{\delta x^2}-\frac{1}{\delta y^2}\right)+$$

$$+\begin{pmatrix} & \frac{1}{\delta y^2} & \\ \frac{1}{\delta x^2} & 0 & \frac{1}{\delta x^2} \\ & \frac{1}{\delta y^2} & \end{pmatrix}\zeta_{i,j}^{n} \tag{5.40}$$

using standard finite difference molecule notation.

This method is unconditionally stable for the one, two and three-dimensional Fourier's equation. A great advantage of the DuFort Frankel method is that it is technically an implicit method, but that it may be encoded as an explicit scheme, thereby combining the advantages of both implicit and explicit schemes. On the other hand the Crank Nicholson method, which is frequently used for problems similar to that of (5.38), requires iteration at each timestep and iterative convergence is not guaranteed for nonlinear equations.

The DuFort-Frankel method as applied to (5.38) is unconditionally stable, but when nonlinear terms are added to the governing equations, the method loses this property. Although this is a drawback, other implicit methods, even if they were to be formally stable for nonlinear equations, may not converge.

5.3.3 Arakawa formulation for the non-linear terms

The non-linear terms in the equations are evaluated using the Arakawa (1966) formulation. This method overcomes non-linear computational instabilities associated with other central difference approximations for the Jacobian. In this method, the mean vorticity, mean kinetic energy and mean square vorticity are conserved in time (in the absence of diffusion) by combining three different approximations to the Jacobian. The method is given by

$$J(A,B) = \frac{\partial A}{\partial x}\frac{\partial B}{\partial y} - \frac{\partial B}{\partial x}\frac{\partial A}{\partial y}$$

$$\simeq \frac{1}{12\delta x \delta y}\Big[(A_{i+1,j} - A_{i-1,j})(B_{i,j+1} - B_{i,j-1})$$

$$+(A_{i,j+1} - A_{i,j-1})(B_{i+1,j} - B_{i-1,j})$$

$$+(A_{i+1,j})(B_{i+1,j+1} - B_{i+1,j-1}) - (A_{i-1,j})(B_{i-1,j+1} - B_{i-1,j-1})$$

$$-(A_{i,j+1})(B_{i+1,j+1} - B_{i-1,j+1}) + (A_{i,j-1})(B_{i+1,j-1} - B_{i-1,j-1})$$

$$+(B_{i,j+1})(A_{i+1,j+1} - A_{i-1,j+1}) - (B_{i,j-1})(A_{i+1,j-1} - A_{i-1,j-1})$$

$$-(B_{i+1,j})(A_{i+1,j+1} - A_{i+1,j-1}) + (B_{i-1,j})(A_{i-1,j+1} - A_{i-1,j-1})\Big] \qquad (5.41)$$

where the grid is again defined by $x_i = i\delta x$ and $y_j = j\delta y$. This formulation is easy to implement and less numerically diffusive than upwinding schemes for example, whilst retaining second-order accuracy. One drawback however, is that it may only be applied to a uniform grid in its present form. Its application

to non-uniform meshes has not been investigated as far as we are aware and is beyond the scope of this thesis.

5.3.4 Derivative boundary condition approximation

On $\xi = \xi_{min}$, $(i = 0)$, equation (5.18) may be approximated by

$$C\omega_{0,j} = \left(\frac{\partial^2\psi}{\partial\xi^2}\right)_{0,j} + \left(\frac{\partial^2\psi}{\partial\eta^2}\right)_{0,j}$$

$$\simeq \frac{\psi_{-1,j} + \psi_{1,j}}{\delta\xi^2}, \tag{5.42}$$

since $\psi_{0,j} = 0$ on the surface. At the $\xi = \xi_{min}$ boundary, $\psi_\xi = 0$, which implies that

$$\frac{\psi_{1,j} - \psi_{-1,j}}{2\delta\xi} = 0 \qquad \Rightarrow \qquad \psi_{-1,j} = \psi_{1,j} \tag{5.43}$$

Using equations (5.42) and (5.43) the vorticity at the $\xi = \xi_{min}$ boundary may be expressed in terms of ψ on the internal points only, and is given by

$$\omega_{0,j} \approx \frac{2}{C(\delta\xi)^2}\psi_{1,j} \tag{5.44}$$

This is often known as the ghost point or fictitious point method because of its use of $\psi_{-1,j}$ which lies outside the computational domain.

5.3.5 Multigrid scheme

The method is based on that described in Briggs (1987). In describing the multigrid method we follow the notation of Briggs which is completely unrelated to the notation of the rest of the thesis.

The Poisson equation (5.7) may be written in the form

$$Lu = f, \tag{5.45}$$

where u is the exact solution of the discretised system of partial differential equations, L represents the finite difference operator and f is the right hand forcing function. If an approximate solution, v, is given then the error is expressed as

$$e = u - v. \tag{5.46}$$

The residual, r, is a measure of the amount by which the approximation v fails to satisfy the system of equations and it is defined by,

$$r = f - Lv. \tag{5.47}$$

A very useful relation between the error and the residual, known as the residual

equation, may therefore be formed,

$$Le = r. \tag{5.48}$$

Typical relaxation schemes such as Gauss-Seidel or Successive Over-Relaxation possess what is known as the smoothing property, which makes them very effective at eliminating high-frequency, oscillatory components of the error, but they are far less effective at removing low-frequency, smooth components. On a coarse grid, the low frequency errors from the point of view of the fine grid, look more oscillatory (i.e. are higher frequency errors) and therefore the smoothing property of the relaxation scheme is more effective on the coarse grid. This forms the basis of the Multigrid method where the residual equation is used to relax on the error on successively coarser grids.

For a two level grid, with the fine grid having half the grid spacing of the coarse grid, the routine loosely follows the following strategy where superscripts denote the steplength corresponding to the grid being considered,

- Relax on $L^h u^h = f^h$ on Ω^h to obtain an approximation v^h,
- Compute the residual $r^h = f^h - L^h v^h$,
- Transfer (restrict) the residual from grid Ω^h to Ω^{2h} : $r^h \rightarrow r^{2h}$,
- Relax on the residual equation $L^{2h} e^{2h} = r^{2h}$ on Ω^{2h} to obtain an approximation to the error e^{2h},

- Transfer (prolong) the error from grid Ω^{2h} to Ω^h : $e^{2h} \rightarrow e^h$,

- Correct the approximation obtained on Ω^h with the error estimate obtained on Ω^{2h} : $v^h \rightarrow v^h + e^h$.

Here Ω^h and Ω^{2h} define the fine and coarse grids respectively and h denotes the steplength. When the maximum residual, as defined in equation (5.48) falls below a suitably small limit to get the accurate solutions of the difference equations, the procedure is deemed to have converged.

The prolongation operator is a straightforward linear interpolation routine denoted by $I_{2h}^h V^{2h} = V^h$, and defined by

$$V_{2i,2j}^h = V_{i,j}^{2h},$$

$$V_{2i+1,2j}^h = \tfrac{1}{2}(V_{i,j}^{2h} + V_{i+1,j}^{2h}),$$

$$V_{2i,2j+1}^h = \tfrac{1}{2}(V_{i,j}^{2h} + V_{i,j+1}^{2h}),$$

$$V_{2i+1,2j+1}^h = \tfrac{1}{4}(V_{i,j}^{2h} + V_{i+1,j}^{2h} + V_{i,j+1}^{2h} + V_{i+1,j+1}^{2h}). \tag{5.49}$$

The restriction operator takes the form of a full weighting routine defined by $I_h^{2h} V^h = V^{2h}$, where

$$V_{i,j}^{2h} = \tfrac{1}{16}\Big[(V_{2i+1,2j+1}^h + V_{2i-1,2j-1}^h + V_{2i+1,2j-1}^h + V_{2i-1,2j+1}^h$$

$$+2(V^h_{2i+1,2j} + V^h_{2i-1,2j} + V^h_{2i,2j+1} + V^h_{2i,2j-1}) + 4V^h_{2i,2j}\Big]. \qquad (5.50)$$

The alternative would be to utilise an injection operator, where the coarse grid value is taken direcly from the corresponding fine grid point – such a method, though more straightforward to encode, results in a less efficient algorithm.

The relaxation procedure utilised to solve for the approximation v and the error e is a straightforward Gauss-Seidel line relaxation procedure. It uses the most recent approximation in order to calculate the new approximation. Sweeps are performed on the matrix of equations, which are in central difference approximation form, with both horizontal and vertical line sweeps per relaxation procedure. Two relaxation procedures are undertaken on each level before moving on to either finer or coarser grids. The central difference operator L in equation (5.45) forms a block tri-diagonal matrix and is solved using a tri-diagonal matrix algorithm. The details of the tri-diagonal matrix algorithm are very well known and will not be repeated here.

5.3.6 Outflow boundary conditions

The conditions to be applied on the outflow boundary follow the methodology introduced by Kloker *et al* (1993). The naive imposition of boundary conditions involving either the first or second derivatives of dependent variables result in the progressive upstream propagation of spatially pointwise oscillations which

eventually degrade the evolving solution. Kloker *et al* (1993) discuss at length six different strategies for dealing with outflow conditions and conclude that, for the Blasius boundary layer at least, a very satisfactory method is to use an absorbing buffer region. Such a region is used to damp out *disturbances* to the basic flow. The method has also been used very satisfactorily in other flows; see Haddad & Corke (1998), Collis & Lele (1999), Wanderley & Corke (2001), and Fasel (2002).

For the present problem the concept of a buffer region translates into setting

$$\chi_{DIST}^{new} = BF(\xi) \times \chi_{DIST}^{old} \tag{5.51}$$

at each timestep. Here χ_{DIST} represents either the vorticity or temperature disturbances, χ^{old} is the computed value of χ obtained using the DuFort Frankel method subject to the boundary condition $\partial\chi/\partial\xi = 0$ at $\xi = \xi_{max}$, and χ^{new} is the value of χ which is used to compute χ at subsequent timesteps. The buffer function, $BF(\xi)$, takes the value, 1, in most of the computational domain, but is a 5^{th} order polynomial in ξ which decreases from 1 at the start of the buffer region to 0 at outflow. At both the beginning ($\xi = \xi_{b1}$) and the end ($\xi = \xi_{b2}$) of the buffer region the function has zero first and second derivatives. In more detail, the buffer function used was

$$BF(\xi) = 1 \qquad\qquad \xi < \xi_{b1}$$

$$BF(\xi) = 1 - 10\sigma^3 + 15\sigma^4 - 6\sigma^5 \qquad \xi_{b1} < \xi < \xi_{b2} \qquad (5.52)$$

$$BF(\xi) = 0 \qquad \xi > \xi_{b2}$$

where

$$\sigma = \frac{\xi - \xi_{b1}}{\xi_{b2} - \xi_{b1}}.$$

For nonlinear problems, such as those involving the computation of the basic steady flow and the unsteady flows which are considered in the next chapter, the outflow formula, (5.51), may be written in the following form which is suitable for solving for the true variables, rather than for disturbances,

$$\chi^{new} = BF(\xi) \times \chi^{old} + [1 - BF(\xi)] \times \chi^{basic} \qquad (5.53)$$

where χ^{basic} represents the basic boundary layer solutions of the corresponding variable (vorticity or temperature) which is obtained from the steady solutions of equations (5.18)-(5.20).

5.3.7 Grid generation and computational domain

The Poisson equation for the streamfunction was solved using the multigrid V-cycling scheme which is described in § 5.3.5. In our computations we took $\xi_{max} = 620$, $\xi_{min} = 20$, $\eta_{max} = 12$ and $\eta_{min} = 0$, with a regular grid of 480 points in the ξ direction and 48 points in the η direction. This size of grid was chosen

as a compromise between accuracy of solution and realistic computational times. Hence $\delta\xi = 5\delta\eta$, and so a line relaxation method (as opposed to a pointwise method) is required. We were able to take 5 multigrid levels and each V-cycle was comprised of 2 sweeps in both coordinate directions on the finest grid. The buffer region extended from the 400^{th} to the 480^{th} point in the ξ direction.

5.3.8 Overall algorithm

At each timestep the vorticity and temperature fields are updated for the new time level, followed by the solution of the Poisson equation for the streamfunction and finally the boundary vorticity is computed using the method given in equation (5.44).

5.3.9 Steady state solutions

Here we discuss how to find the steady state solutions from the unsteady elliptic equations (5.18)-(5.20) using the numerical methods discussed above.

Starting with the boundary layer solution as given in equation (5.28) on all grid points as the initial condition, the flow evolves rapidly near the leading edge which induces a large thermal wave to form and then to propagate downstream. This wave becomes highly nonlinear very rapidly and very thin internal shear layers develop which are resolved very poorly by the grid we use. Consequently

the method becomes unstable at later times and eventually yields temperatures which are outside of the range 0 to 1. Therefore we adopted an ad hoc strategy of removing highly nonlinear disturbances by interpolating both the θ and ω profiles from either side of the nonlinear wave. As the wave had by this time already propagated downstream of the leading edge region in which the wave had been generated, the resulting modified flow, when integrated forward in time, does not produce a wave of such a large amplitude. This procedure was continued as often as was necessary to "clean" the boundary layer of unsteady components in order to get the steady-state solution of the full equations. The procedure works only because the flow is convectively (or, less confusingly, in the context of free convection, advectively) unstable as opposed to being absolutely unstable. In an advectively unstable flow a local disturbance diffuses both upstream and downstream but here wave packets travel downstream faster than can be counteracted by upstream diffusion thereby leaving behind a steady undisturbed boundary layer. In an absolutely unstable flow the wave packet manages to diffuse upstream against the mean flow – a local disturbance placed at sufficiently large radius in the Von Karman boundary layer on a rotating disk is an example of this (see Lingwood 1997).

Figure 5.2 shows the steady state solutions which are obtained from the nonlinear elliptic equations (5.18)-(5.20) using above numerical techniques. Frame (A) in this figure represents the contours of the streamfunction ($\bar{\psi}$), while frames (B) and (C) represent the contours of the vortices ($\bar{\omega}$) and isotherms ($\bar{\theta}$) respectively. In each frame 10 levels of contour are plotted between their maximum

and minimum values. The maximum value of the streamfunction is calculated to be $\bar{\psi}(x_{max}, y_{max}) \simeq 748$ and it is minimum at the origin (x_{min}, y_{min}). The steady state temperature which is bounded between 1 and 0, while the maximum and minimum values of the vorticis are 7.45 and -1.45 respectively.

5.4 Results and discussion

In this section we focus on presenting the numerical simulation results. We discuss the effect of three different types of localised disturbance placed near the leading edge: (i) the evolution of a disturbance placed within the boundary layer at one point in time and space; (ii) the evolution of a distributed disturbance which is continuous in space, and finally (iii) time periodic local variations in the boundary temperature in order to determine the detailed effect of different disturbance frequencies.

Case (i) and (ii) are effectively initial value problems, while in (iii) we are more concerned with the long-term response to periodic forcing. In our computations we have restricted attention to air ($Pr = 0.7$) as the working fluid.

Given that the leading edge of the heated surface is at $\xi = 20$, which corresponds to $x_{min} \simeq 36.9928$, we may define an x-coordinate relative to this value according to

$$x^* = x - x_{min} \tag{5.54}$$

which gives the leading edge at $x^* = 0$.

5.4.1 Evolution of a point disturbance

A disturbance was introduced by setting $\hat{\theta} = 1$ at the point $(\xi, \eta) = (45, 1.5)$, i.e. at $(x, \eta) \simeq (110, 1.5)$ or $(x^*, \eta) \simeq (73, 1.5)$, which is fairly close to the leading edge. 7000 timesteps of length $\delta t = 0.1$ were used. Although such a point disturbance introduces a checkerboard pattern in the temperature profile at subsequent timesteps, the effect does not last long since the timestep is quite small, given that the time derivative terms in (5.19) and (5.20) are multiplied by $C(\xi, \eta)$; see (5.21).

As time advances the disturbance diffuses outwards from its point of introduction and travels along the boundary layer due to the overall upwards movement of the fluid. The perturbation temperature field in the x-y plane has been recorded at different times from $t = 25$ to $t = 400$ and these are displayed in Figure 5.3 — it is very important to note that the depicted aspect ratios of the cells are very different from what would be observed in an experiment, since in this Figure $x_{max} \simeq 3600$ and $y_{max} \simeq 60$ and therefore the cells will be greatly elongated in reality.

From these contours, both the diffusion and advection of the evolving disturbance are seen clearly with well-defined advancing leading and trailing edges. The cells at $t = 250$ show a distinctive "boomerang" shape. Such a shape arises because

the maximum velocity of the basic flow occurs away from the surface. The 7th frame ($t = 300$) corresponds to that point in time just before the advancing front encounters the buffer region. In subsequent figures the buffer region absorbs the disturbance with minimal upstream influence.

The variation in the perturbation surface rate of heat transfer $\frac{\partial \hat{\theta}}{\partial \eta}\Big|_{\eta=0}$ is displayed as a contour plot in Figure 5.4. The contours shown correspond to various plus and minus powers of 10. The lower boundary of the contours in Figure 5.4 shows how quickly the advancing front of the disturbance propagates downstream and, given the decreasing slope, is seen to accelerate. This is consistent with the fact that the basic boundary layer flow also accelerates, since the streamwise velocity is proportional to $x^{1/2}$. The upper boundary of the contours corresponds to the trailing edge of the wave packet, which also accelerates, and therefore the instability is confirmed as advective in nature. On the right hand side the buffer region corresponds to $x > 3000$ and is seen to dampen the disturbances. Although this region appears to have a significant effect on the flow, and indeed this is the intention, it has an almost negligible influence on the region upstream of it. This was tested by using a larger buffer region, and comparison of the profiles outside this larger region showed virtually no difference between the two simulations.

The disturbance depicted in Figure 5.4 grows rapidly as it travels downstream as evidenced by the fact that the contours at $x \simeq 2800$ and $t \simeq 400$ correspond to a perturbation which is more than 10^6 times stronger than at the depicted

trailing edge of the disturbance. It is also interesting to note that there seems to be a distinctive timescale associated with the evolving disturbance; the interval between successive zeros in the perturbation heat transfer may be guaged by the vertical distance between isotherms in Figure 5.4.

Figure 5.5 displays the instantaneous surface rate of heat transfer at time $t = 250$ which is defined by

$$H(x) = \left[\left(\frac{\partial\hat{\theta}}{\partial\eta}\right)_{\eta=0}\right]_{t=250}. \tag{5.55}$$

This figure corresponds to the isotherms given in the 6th frame of Figure 5.3. If the boundaries between the cells are defined to be where the surface rate of heat transfer of the perturbation is zero, as marked by circles in Figure 5.5, then we may define as a spatial "period" the distance which two neighbouring cells occupy, although we note that the train of cells is not periodic in space. The spatial frequency, k, is then 2π divided by the period. Figure 5.5 clearly shows the spatial extent of the wavepacket, but also shows how the wavelength increases with distance from the leading edge. Again, this is consistent with the fact that the basic flow accelerates in the streamwise direction.

We have also investigated the effect of changing the location of the initiating disturbance, but the overall qualitative nature of the response of the boundary layer is the same. Therefore we have not presented further results of this type. However, this section provides the context into which may be set the response of the boundary layer to time-periodic disturbances.

5.4.2 The effect of a distributed disturbance

A thermal disturbance was introduced at $t = 0$ in the region near the leading edge and which is given by

$$\hat{\theta}(\xi, \eta) = \eta e^{-\eta} e^{-a(\xi - \xi_0)^2} \tag{5.56}$$

where $a = 0.1$ is the scaling factor and $\xi_0 = 20$ $(= \xi_{min})$. We again used 7000 timesteps of length $\delta t = 0.1$ in all the computations. This disturbance is continuous in space and no checkboard patterns were observed in the early stages of the simulation.

In Figure 5.6, the perturbation temperature field in the x-y plane has been recorded at different times from $t = 25$ to $t = 400$. It is again noted that the depicted aspect ratios of the cells are different from what would be observed. These are very similar to the point disturbance case shown in Figure 5.3. The main difference between Figures 5.3 and 5.6 lies in the fact that the disturbance extends back to the leading edge, at least for early times.

Figure 5.7 represents the variation of the surface rate of heat transfer as a contour plot. These contours also correspond to various plus and minus powers of 10. Again this figure is very similar to Figure 5.4 although there are again some differences near the leading edge due to the different nature of the disturbance.

Figure 5.8 displays the surface rate of heat transfer $(H(x)$, defined in equation

5.55) at time $t = 250$. This figure also shows clearly the spatial extent of the wavepacket and how the wavelength increases with distance from the leading edge. The amplitude of H is much less than that observed in Figure 5.5 because the evolving disturbance decays near the leading edge before it enters an unstable region, at least as defined by parallel flow theory.

We have also investigated the effect of changing the location and spatial extent of the initial disturbance, but again we observed that the overall qualitative nature of the response of the boundary layer is qualitatively the same.

5.4.3 Some examples of the response to time-periodic disturbances

A time periodic thermal disturbance was introduced at the heated surface in the region near the leading edge ($\xi_0 = \xi_{min} = 20$) which is given by

$$\hat{\theta} = e^{-a(\xi-\xi_0)^2} \sin(\lambda t) \qquad \text{at} \qquad \eta = 0, \tag{5.57}$$

where λ is the temporal frequency and $a = 0.1$ is chosen to be the scaling factor. We need not investigate the effect of different amplitudes of disturbance as the present chapter is concerned solely with linearised disturbances. We used 10000 timesteps of length $\delta t = 0.1$ in all the computations. In all cases considered this length of time is more than sufficient for transient effects to decay, and for a time-

periodic response to be established. Although we are unaware of experimental work which has used time-periodic disturbances to determine the receptivity of thermal boundary layers, such disturbances were investigated by Dietz (1999) where a vibrating ribbon was positioned upstream of a flat plate to study the receptivity of an isothermal boundary-layer flow. Also there are some recent works by Brooker *et al* (1997) on the sidewall-heated cavity, where a sinusoidal time dependent external heat source was added near the leading edge to initiate disturbances for the case of direct stability analysis. A similar idea has also been used by Brooker *et al* (2000).

As in the last section, we have found that variations in the location, ξ_0, where the disturbance is centred leads to no significant downstream change in the boundary-layer response. In a similar fashion, only slight quantitative differences are found when different values of the scaling factor a are used, and therefore we concentrate exclusively on variations in the frequency, λ.

In Figures 5.9–5.15, we have plotted the time variation of the perturbation surface rate of heat transfer as contours for different values of λ. The rate of surface heat transfer is defined as

$$HT(x,t) = \left.\frac{\partial\hat{\theta}(x,\eta,t)}{\partial\eta}\right|_{\eta=0} \tag{5.58}$$

The contours in these figures are scaled with respect to the maximum and minimum values of $HT(x,t)$ in each frame, and successive contour levels are again the maximum value of $|HT(x,t)|$ multiplied by plus and minus successive powers of 10. The intention is to obtain a qualitative feel for the boundary layer response.

From Figure 5.9, it may be seen that there are two very different timescales present: (i) a relatively long one (length 20π) which is associated with the forcing frequency λ, and which is most evident at later times, and (ii) a relatively short one which is effectively a starting transient. Near the point $(x,t) \simeq (300,100)$ the transient first becomes evident and the contour bands associated with the starting transient are very similar indeed to those of the initial disturbance case, plotted in Figures 5.4 and 5.6. Clearly this is associated with the sudded imposition of the thermal forcing.

Once the transient has died away, the flow after $t \simeq 650$ is essentially time-periodic. The contour spacing at $x = 1000$ does not vary greatly and therefore we may conclude from this evidence that the disturbance is essentially neutral for this value of λ. However, there is clearly fairly strong decay in the region $x < 100$ ($x^* < 63$), which is the region where one expects all disturbances to decay since it lies below the neutral stability curve first computed by Nachtsheim (1963).

Figure 5.10 shows the response when $\lambda = 0.2$. The transient response to the disturbance dies out slightly more quickly than for the $\lambda = 0.1$ case. From the figure we see that there is approximately a tenfold increase in the disturbance amplitude near $x = 1000$ when t is large, as compared with the $\lambda = 0.1$ case shown in Figure 5.9.

Figure 5.11 shows the response when $\lambda = 0.3$. The transient response to the disturbance dies out slightly more quickly than for the $\lambda = 0.2$ case, but the eventual

periodic response now grows markedly. From the figure we see a greater than 100-fold increase in the disturbance amplitude between $x = 500$ and $x = 2000$ in the periodic regime. There remains a disparity between the computed frequency of the transient response and the imposed frequency as shown by the different spacing of the contours in the t-direction. However, the respective frequencies are fairly close, and this is what causes a beat-like variation in the envelope of the transient contours; an example is seen close to $(x, t) \simeq (2500, 400)$.

Figure 5.12 shows the response when $\lambda = 0.4$. This frequency is roughly the same as that of the transient, and therefore the eventual time-periodic response grows very substantially as it propagates downstream. The magnification in amplitude between $x = 600$ and $x = 2400$ is approximately 10^5 suggesting that we have what is essentially a resonance between the forcing and the boundary-layer response. This aspect will be dealt with more in quantitative detail below.

We now present a case corresponding to the frequency $\lambda = 0.5$, and the response returns to the situation where there are two different timescales observed (see Figure 5.13). The transient frequency is now smaller than that of the forcing frequency, which is opposite to the cases for which $\lambda < 0.4$. This figure shows clearly the decay of the periodic response near $x = 500$ and its subsequent growth a little further downstream.

Two different time scales remain for frequency $\lambda = 0.6$ (see Figure 5.14). The region over which the periodic response decays has now increased quite markedly

in size, and does so increasingly as λ increases, although the overall growth which occurs within the computational domain is still substantial.

The final case we present corresponds to the frequency $\lambda = 0.7$, and is displayed in Figure 5.15. This figure is quite similar to Figures 5.4 and 5.7 apart from near $x^* = 0$ where the periodic forcing decays. The forcing frequency, $\lambda = 0.7$, is quite high here which appears to cause decay in the time-periodic response.

In Figures 5.16 to 5.22, we have displayed the perturbation isotherms at different points in time to see how the disturbance varies with time and frequency. The contour levels are set at $\pm 10^{-n} \max_{\xi,\eta,t} |\hat{\theta}|$ for $n = 1, 2, \cdots$. These figures correspond to Figures 5.9 to 5.15, respectively.

Figure 5.16 represents perturbation isotherms for frequency $\lambda = 0.1$. Initially at time $t = 25$ the disturbance grows, and transient starts to grow at $t = 100$. The transient response leaves the computational domain when $150 < t < 625$. It is clearly observed from these frames that there are two spatial scales present, which correspond to the time scales seen in the heat transfer plots shown in Figure 5.9. After $t = 625$ there is a periodic response observed although the sampling time interval chosen (25) makes the cells to appear to travel backward and is an aliasing effect.

For the frequency $\lambda = 0.2$ (Figure 5.17) the transient dies out a little earlier than we observed for the case $\lambda = 0.1$ (Figure 5.16). At $t = 575$, the transient response finally leaves the computational domain and after that the flow is time

periodic. At $t = 800$ for example, we see that the wavelength increases with x, which confirms the effect of the acceleration of the basic flow.

There are a relatively large number of cells appearing in Figure 5.18, which corresponds to $\lambda = 0.3$, and the wavelength for the periodic flow and transient are very much closer. In these contour plots it is quite difficult to distinguish between the transient cells and the periodic cells. The wavelength still increases spatially in the streamwise direction.

The downstream growth over many orders of magnitude may be seen in Figure 5.19 for which the frequency is $\lambda = 0.4$. The initial response involves cells of relatively large wavelength but periodic flow with cells of smaller wavelength is established quite rapidly.

Figures 5.20 and 5.21 show the response to the frequencies $\lambda = 0.5$ and $\lambda = 0.6$. For these values we see the first clear sign of decay near the leading edge before growth occurs further downstream. As λ increases from these values the region of spatial decay becomes larger until at $\lambda = 0.7$ (see in Figure 5.22) there is no evidence of growth, at least as shown in the perturbation isotherms.

It is also instructive to show the variation with time of the isotherms over a half of one period after the decay of the transient flow, in order to see more clearly how the form of the disturbance varies with both t and λ. Such variations are displayed in Figures 5.23 to 5.29 where the contour levels are set at $\pm 10^{-n} \max_{\xi,\eta,t} |\hat{\theta}|$ for $n = 1, 2, \cdots$. In these figures the contours appear to fill the whole of the

computational domain from $y = 0$ to the outer edge of the boundary layer. However, the contours at the outer edge correspond to values of $|\hat{\theta}|$ which are at most 10^{-3} multiplied by the local maximum absolute value.

Figure 5.23 shows the perturbation isotherms for $\lambda = 0.1$, where the temporal period is 20π. The spatial growth over distance of the wavelength of each cell is clearly seen in this figure, as is the fact, previously noted, that there is very little variation in the amplitude of the disturbance as it tracks downstream. The maximum length of a cell in the x-direction corresponds to the penultimate cell in the middle frame; its length is approximately 980, which yields a cell aspect ratio in excess of 16, an unusually large value. When λ takes smaller values the length of the cells can be expected to increase further, and the size of the computational domain ceases to be sufficient to represent the disturbances well.

For $\lambda = 0.2$ the corresponding contours are plotted in Figure 5.24. We see that there are now considerably more cells within the computational domain. More cells appear in Figure 5.25 for $\lambda = 0.3$ and the cells decay away from the heated surface more rapidly than in the previous two figures.

The corresponding isotherms for $\lambda = 0.4$ are shown in Figure 5.26. Immediately we see that there are considerably more cells within the computational domain. Moreover the decay of the cells away from the heated surface is much greater than for $\lambda = 0.1$, as evidenced by the number of contours between the local extrema and the outer boundary. Over the whole domain the disturbance appears to grow

as x increases (although there is a short region of decay near the leading edge; see Figure 5.32) and is only damped by the buffer region. Again we see the dramatic growth in the disturbance as it tracks downstream. The distinctive boomerang shape of the cells noted earlier also occurs here.

When $\lambda = 0.5$ the wavelength of the cells has decreased yet further; see Figure 5.27. From the leading edge up to approximately $x = 500$ the disturbance clearly decays, but then commences growing at larger values of x. For larger values of λ the region over which decay occurs becomes larger – see Figures 5.28 and 5.29 which correspond to $\lambda = 0.6$ and 0.7, respectively. When growth occurs it still occurs dramatically over many order of magnitude. Later we will discuss how the length of the region of decay is related to the neutral stability curve obtained using the parallel flow approximation by Nachtsheim (1963).

5.4.4 Overview of the response to time-periodic disturbances

Figure 5.30 summarises Figures 5.23–5.29 in terms of the variation with x of the spatial wavelength of the periodic response. This variation is shown for many different values of λ. The horizontal coordinate of each circle represents the position, x, of either a maximum or a minimum rate of surface heat transfer, while the vertical coordinate gives the distance between the nearest positions of zero surface heat transfer, i.e. half a "wavelength", $l/2$. For all values of λ

the curves rise with increasing x suggesting that an increasing wavelength with distance is indeed a global feature of this boundary layer flow, which accelerates. We also note that the spatial wavelength decreases monotonically with increasing values of the temporal frequency λ. In this regard slightly anomalous behaviour occurs when λ is at and above 0.55. This may be traced to the fact that there is an adjustment in the shape of the disturbance near to the point where the heat transfer is smallest; see Figures 5.27 to 5.29.

Figure 5.31 shows the maximum absolute surface rate of heat transfer over the whole of the heated surface ($37 \leq x \leq 3600$). This quantity is defined by

$$M = \max_{(\xi,t)} \left| \left(\frac{\partial \hat{\theta}}{\partial \eta} \right)_{\eta=0} \right| \tag{5.59}$$

and is a function of the forcing frequency λ. The curve (a) corresponds to the *maximum transient response* of the boundary layer, including the transient stage, and M is maximised over time $0 \leq t \leq 800$. The curve (b) represents only the maximum over one period of the final periodic response, although, for simplicity of programming the maximisation took place over the range $800 \leq t \leq 1000$ – this response we call the *maximum asymptotic response.*

In many cases there is a substantial difference between the maximum transient response and the maximum asymptotic response. This is especially so near $\lambda = 0.3$ and $\lambda = 0.6$. Indeed, for $\lambda < 0.3$ and $\lambda > 0.6$ the maximum asymptotic response is very small compared with the values near to $\lambda = 0.4$. When $\lambda \simeq$

0.411 both maxima take the same value ($M \simeq 7981$), which is the strongest response obtainable by this boundary layer within the computational domain used, and therefore this value of λ constitutes the most dangerous disturbance frequency overall. There is also a small range of values of λ near to 0.411 where the maximum transient and asymptotic responses are identical. We note here that we have studied 90 cases choosing discrete values of λ between $\lambda = 0.05$ and $\lambda = 1.0$.

However, we need to be careful about making absolute statements regarding which excitation frequency is the most dangerous since the computational domain is necessarily finite. That this is so may be gleaned from Figure 5.32 which shows how the maximum local asymptotic response of the boundary layer varies with x for various values of λ. Specifically we plot the variation of K against x

$$K(x,\lambda) = \log_{10}\left|\max_{800<t<1000}\left(\frac{\partial\hat{\theta}}{\partial\eta}\right)_{\eta=0}\right|. \tag{5.60}$$

In other words $K(x,\lambda)$ corresponds to the maximum absolute rate of heat transfer over one period at any chosen value of x after transients have died out.

In all cases K decreases rapidly as x increases from $x \simeq 37$ ($x^* = 0$), since the leading edge of the heated surface is in a stable region, and therefore it is to be expected that disturbances should decay there. For the larger values of λ this decay lasts for a considerable distance and the decay is over many orders of magnitude. When $\lambda \geq 0.45$ the K-curves display a sudden dip just before they

begin to increase; this is related to the change in the shape of the cell referred to above, and seems to be a fairly ubiquitous phenomenon for the larger values of λ. However, when λ takes relatively small values such as 0.05, the disturbance is seen to decay slowly. Our previous comment regarding the near neutrality of the $\lambda = 0.1$ case is borne out by the fact that K hardly varies with x once $x > 1000$.

At intermediate values of λ, such as 0.3, 0.35 and 0.4, we see that the maximum asymptotic response depends on where in the boundary layer one needs the information. For example, at $x \simeq 500$, the most dangerous frequency of excitation, in the sense of yielding the largest response, corresponds to $\lambda = 0.3$. Similarly $\lambda = 0.35$ is the most dangerous frequency when considering the response of the boundary layer at $x \simeq 1300$, whereas $\lambda = 0.4$ corresponds to $x \simeq 2500$. Given the behaviour of the $\lambda = 0.45$ curve we have no reason not to expect that it will, in its turn, take over as the most dangerous excitation frequency at a larger value of x, one which is outside of the present computational domain.

By running the numerical code for $0.2 \leq \lambda \leq 0.42$ in steps of 0.01 we have found the maximum local asymptotic response at each value of x over all the different values of λ, and this is defined as

$$K_{max} = \max_{\lambda} K(x, \lambda). \tag{5.61}$$

Here we see in Figure 5.33 that initially the response is decaying and becomes neutral at $x \simeq 160$ ($x^* \simeq 123$). When $x < 160$, decaying responses are obtained

as x lies under the neutral curve (i.e. in the stable region) that we have obtained from the PFA results. But when $x > 160$, we confirmed that the region is unstable and the response grows.

The values of λ (λ_{opt}) which maximise K in (5.61) are shown in Figure 5.34. This figure shows that the frequency which maximises the boundary layer response depends on the position x. This optimum value of λ increases with x and we suspect that it will continue to do so for larger computational domains.

5.4.5 Comparison with parallel-flow linear theory

Finally, it is necessary to compare the present results, which are based upon numerical simulations of the fully elliptic equations, with those obtained using the standard linear stability theory based upon the parallel flow approximation (PFA). Such a comparison is shown in Figure 5.35 for five different values of the excitation frequency ($\lambda = 0.25, 0.35, 0.45, 0.55$, and 0.65). This figure shows (i) the neutral curve for the onset of convection using the PFA, (ii) curves which correspond to the above values of λ obtained by again assuming the PFA, and (iii) the variation of the x^* values at which the local perturbation heat transfer is zero with the local wavenumber ($k = 2\pi/l$, where l is depicted in Figure 5.30).

When $\lambda = 0.55$ the agreement between the present simulations and the PFA results is very good when $x^* > 750$ and for $\lambda = 0.65$ it is when $x^* > 1250$. At smaller values of x the poor comparison is assumed to be caused by the

change in the shape of the cells, a phenomenon which is unlikely to occur in the PFA computations which are strictly local. As λ decreases the comparison is decreasingly good suggesting that the elliptic effects become sufficiently strong, so that the PFA is no longer a suitable assumption to make. Indeed, this clearly must be the case for relatively small values of x^* (i.e. those close to the base of the neutral curve) since the spatial wavelength of the resulting cells is the same order of magnitude as the neutral distance, as shown by the vertical spacing of the symbols.

5.5 Conclusions

In this chapter we have sought to understand how the classical vertical thermal boundary layer from a uniform temperature heated surface responds to three different types of disturbance (two were different types of initial disturbance, and the third was a time-periodic thermal forcing). To this end we have solved the unsteady, fully elliptic equations of motion, rather than using approximate methods. This has meant that the flow is able to evolve freely in space and time without having its wavelength prescribed, or being computed using parabolic methods.

Our chief conclusion is that it is not possible to determine a most dangerous disturbance frequency as a global criterion. Rather, each location in the boundary layer has associated with it its own most dangerous frequency, at least in terms

of the heat transfer response to otherwise identical disturbances. We have seen that this frequency increases with increasing distance.

We have also confirmed numerically that the present boundary layer is advectively, rather than absolutely, unstable, and that the acceleration of the flow as it travels upwards results in a progressive stretching of the individual disturbance cells.

Chapter 6

Receptivity of free convection flow from a heated vertical surface. II. Nonlinear waves

6.1 Summary

In Chapter 5 we performed a detailed numerical investigation of the linear instability of the thermal boundary layer flow over a vertical surface by introducing thermal disturbances near the leading edge. The main aim in the present chapter is to extend the numerical investigation of Chapter 5 into the nonlinear regime. Attention is confined to introducing only unsteady thermal disturbances.

Although the introducing thermal disturbance amplitude is kept at 1 in Chapter 5, we find that for the nonlinear waves the magnitude of this disturbance amplitude is very important and the development of flows depends strongly on it. With the presence of nonlinear terms we find that various types of transient responses exist which are dependent on both the forcing frequency and amplitude.

6.2 Equations of motion and boundary conditions

6.2.1 Governing equations

The equations which describe the free convection from a vertical plate are taken to be the incompressible continuity, Navier-Stokes, and energy equations. For unsteady two dimensional flow this system, subject to the Boussinesq approximation, is written in the form

$$\frac{\partial^2\psi}{\partial\xi^2}+\frac{\partial^2\psi}{\partial\eta^2}=C\omega, \tag{6.1}$$

$$C\frac{\partial\omega}{\partial t}=\frac{\partial^2\omega}{\partial\xi^2}+\frac{\partial^2\omega}{\partial\eta^2}+\frac{\partial\psi}{\partial\xi}\frac{\partial\omega}{\partial\eta}-\frac{\partial\psi}{\partial\eta}\frac{\partial\omega}{\partial\xi}+C^{1/2}\left(\frac{\partial\theta}{\partial\xi}\sin\tfrac{1}{4}\phi+\frac{\partial\theta}{\partial\eta}\cos\tfrac{1}{4}\phi\right), \tag{6.2}$$

$$C\frac{\partial\theta}{\partial t}=\frac{1}{Pr}\left(\frac{\partial^2\theta}{\partial\xi^2}+\frac{\partial^2\theta}{\partial\eta^2}\right)+\frac{\partial\psi}{\partial\xi}\frac{\partial\theta}{\partial\eta}-\frac{\partial\psi}{\partial\eta}\frac{\partial\theta}{\partial\xi}, \tag{6.3}$$

where the function, C, is given by

$$C(\xi,\eta) = \left(\tfrac{3}{4}\right)^{2/3}\left(\xi^2+\eta^2\right)^{1/3}, \tag{6.4}$$

and where the coordinates ξ and η are as defined in equations (5.16) and (5.17). The boundary conditions used are given in § 5.2.3.

6.2.2 Nonlinearisation techniques

In Chapter 5 we studied the linearised disturbance equations. For nonlinear flows it proves convenient to solve the full disturbance equations. As in Chapter 5 we consider a disturbance in the steady flow by setting

$$\psi(\xi,\eta,t) = \bar{\psi}(\xi,\eta) + \hat{\psi}(\xi,\eta,t), \tag{6.5}$$

$$\omega(\xi,\eta,t) = \bar{\omega}(\xi,\eta) + \hat{\omega}(\xi,\eta,t), \tag{6.6}$$

$$\theta(\xi,\eta,t) = \bar{\theta}(\xi,\eta) + \hat{\theta}(\xi,\eta,t), \tag{6.7}$$

where an overbar denotes the steady basic flow variables and a hat denotes the perturbation about the steady flow.

The substitution of (6.5)-(6.7) into equations (6.1)-(6.3) leads to two sets of equations: one for the steady flow and another for the perturbation flow. The pertur-

bation equations are given by

$$\frac{\partial^2\hat{\psi}}{\partial\xi^2}+\frac{\partial^2\hat{\psi}}{\partial\eta^2}=C\hat{\omega}, \tag{6.8}$$

$$C\frac{\partial\hat{\omega}}{\partial t}=\frac{\partial^2\hat{\omega}}{\partial\xi^2}+\frac{\partial^2\hat{\omega}}{\partial\eta^2}+\left(\frac{\partial\bar{\psi}}{\partial\xi}\frac{\partial\hat{\omega}}{\partial\eta}-\frac{\partial\bar{\psi}}{\partial\eta}\frac{\partial\hat{\omega}}{\partial\xi}\right)+\left(\frac{\partial\bar{\omega}}{\partial\eta}\frac{\partial\hat{\psi}}{\partial\xi}-\frac{\partial\bar{\omega}}{\partial\xi}\frac{\partial\hat{\psi}}{\partial\eta}\right)$$
$$+\left(\frac{\partial\hat{\psi}}{\partial\xi}\frac{\partial\hat{\omega}}{\partial\eta}-\frac{\partial\hat{\psi}}{\partial\eta}\frac{\partial\hat{\omega}}{\partial\xi}\right)+C^{1/2}\left(\frac{\partial\hat{\theta}}{\partial\xi}\sin\tfrac{1}{4}\phi+\frac{\partial\hat{\theta}}{\partial\eta}\cos\tfrac{1}{4}\phi\right), \tag{6.9}$$

$$C\frac{\partial\hat{\theta}}{\partial t}=\frac{1}{Pr}\left(\frac{\partial^2\hat{\theta}}{\partial\xi^2}+\frac{\partial^2\hat{\theta}}{\partial\eta^2}\right)+\left(\frac{\partial\bar{\psi}}{\partial\xi}\frac{\partial\hat{\theta}}{\partial\eta}-\frac{\partial\bar{\psi}}{\partial\eta}\frac{\partial\hat{\theta}}{\partial\xi}\right)+\left(\frac{\partial\bar{\theta}}{\partial\eta}\frac{\partial\hat{\psi}}{\partial\xi}-\frac{\partial\bar{\theta}}{\partial\xi}\frac{\partial\hat{\psi}}{\partial\eta}\right)$$
$$+\left(\frac{\partial\hat{\psi}}{\partial\xi}\frac{\partial\hat{\theta}}{\partial\eta}-\frac{\partial\hat{\psi}}{\partial\eta}\frac{\partial\hat{\theta}}{\partial\xi}\right) \tag{6.10}$$

and the boundary conditions are

$$\hat{\psi}=\hat{\psi}_\eta=0,\quad \hat{\theta}=0\quad\text{on}\quad \eta=\eta_{min}=0, \tag{6.11}$$

$$\hat{\psi}=\hat{\psi}_\xi=0,\quad \hat{\theta}_\xi=0\quad\text{on}\quad \xi=\xi_{min}, \tag{6.12}$$

$$\hat{\psi}_\eta=0,\quad \hat{\omega}=0,\quad \hat{\theta}=0\quad\text{on}\quad \eta=\eta_{max}. \tag{6.13}$$

The general procedure for solving the nonlinear perturbation equations is as follows. First, we compute the steady state basic flow satisfying the nonlinear equations (6.1)-(6.3); the process by which this was obtained is given in § 5.3.9. Secondly, we solve the nonlinear disturbance equations (6.8)-(6.10) for a variety of boundary conditions (i.e. different frequencies and amplitudes) in order to determine the nonlinear stability characteristics of the boundary layer flow. The

numerical method used, together with the imposition of boundary and outflow conditions, are as given in Chapter 5 (§ 5.3).

Finally we introduce the growth of instabilities in the same way as in Chapter 5, namely, by introducing a time-periodic thermal disturbance on the heated surface near the leading edge:

$$\hat{\theta}(x,0) = Ae^{-a(\xi-\xi_0)^2}\sin(\lambda t) \tag{6.14}$$

where λ is the temporal frequency, $a = 0.1$ is the scaling factor, $\xi_0 = 20$ denotes the leading edge of the heated surface, and A is the amplitude of the disturbance. As we are considering nonlinear waves, the magnitude of A is now important. In fact when A is sufficiently large (e.g. $A = 10^{-5}$ when $\lambda = 0.4$) the starting transient is sufficiently powerful that narrow regions with rapid change are formed (i.e. regions of high shear and rate of heat transfer). The very poor resolution associated with these regions causes the numerical method to become unstable. Therefore we adopted an ad hoc procedure whereby A is regarded as a function of t which rises slowly from 10^{-8} (a level where no instability forms for all values of λ) to the required amplitude. Thus the effects of the stability transient are reduced substantially and the flow is able to settle to a time-periodic state. We used the following expression for $A(t)$:

$$\log_{10}[A(t)] = -8 + d(1 - e^{-bt})^2 \tag{6.15}$$

where it may be seen that $A(0) = 10^{-8}$ but $A(t) \to 10^{-8+d}$ as $t \to \infty$. The value $b = 0.01$ was found to yield suitable results when 15000 time steps of length 0.1 were taken.

6.3 Some results for $\lambda = 0.4$

Our investigations of how nonlinearities affect the results presented in Chapter 5 began by repeating the same cases for a variety of amplitudes, A. For all forcing frequencies, if the amplitude is sufficiently small, then the periodic response of the boundary layer is essentially the same as for linearised theory. Although waves can grow in strength through many values of magnitude as they travel downstream, it was found that an amplitude, $A = 10^{-8}$, is too small for nonlinearities to become significant within our computational domain.

In this section we consider the forcing frequency $\lambda = 0.4$ since this is approximately the most dangerous frequency for the linear regime. We have found that the maximum value of A for which we were able to find solutions is $A = 2 \times 10^{-5}$. At larger values the strength of the nonlinearity is such that the above-mentioned large gradients in ψ, θ, and ω generated cause numerical instability due to poor spatial resolution. Therefore we will concentrate on this maximum value of A.

Various views of the flow generated at this value of A are given in Figures 6.1 to 6.4. Figure 6.1 shows how the time variation of the surface rate of heat transfer

changes with location along the boundary layer. As the magnitude of the heat transfer varies substantially with ξ each curve in Figure 6.1 has been normalised to display the same amount of variation, and the mean value is located at the appropriate value of ξ. This convention also applies to other figures of the same type.

Once more the accelerating nature of the basic boundary layer may be seen by tracking the motion of, say, the local maximum perturbation heat transfer. For small values of ξ the variation in the heat transfer is sinusoidal. However a wave steepening occurs at relatively large values of ξ.

At a large value of ξ (such as $\xi = 520$ or $x = 2850$) the perturbation surface temperature gradient is seen to rise very slowly and then to decrease sharply until the next slow rise. As the temperature gradient of the basic flow is negative (for which convention has that the rate of heat transfer is positive) this means that the overall rate of heat transfer suffers a sharp rise, after which it drops slowly. The sharp rise is associated with the region near the heated surface just upstream of where the isotherms displayed in Figures 6.2 and 6.3 are widely spaced (e.g. see the black triangle in Figure 6.3).

In Figures 6.2 and 6.3 we see how the evolving wave disturbances have become sufficiently strong that a severe distortion of the overall thermal field is obtained. When A is chosen to take larger values then the amount of distortion seen in Figure 6.2 arises further upstream – this has been tested by choosing amplitudes

which are higher than $A = 2 \times 10^{-5}$, but we were unable to obtain periodic flows due to numerical instabilities.

Figure 6.3 has been plotted to look closely at the variation of the temperature gradients in a small region of x from 2500 to 3080. The black triangle indicates where the surface rate of heat transfer is a minimum over a period. At this position, the spacing of the isotherms grows slowly from $t = 1484.3$. This means that the magnitude of the temperature gradient decreases, at $t = 1492.1$ it is at its minimum. When t increases above 1492.1 the isotherms get closer rapidly and the heat transfer rises. This accords with the curves at $\xi = 520$ in Figure 6.1.

Figure 6.4 shows contours of the perturbation surface rate of heat transfer as a function of both x and t. Of particular interest here is how the symmetry between positive and negative rates is broken as the flow becomes nonlinear. At the large values of x the "nose" corresponding to $\frac{\partial \hat{\theta}}{\partial \eta}\Big|_{\eta=0} = -8 \times 10^{-2}$ occurs at a smaller value of x than does that corresponding to $\frac{\partial \hat{\theta}}{\partial \eta}\Big|_{\eta=0} = 8 \times 10^{-2}$. This lack of symmetry is caused by an essential difference in the thermal response to a strong flow towards the surface and one away from it. In the former case cold fluid is pushed rapidly towards the surface and this causes a large but negative change in the temperature gradient relative to that of the basic flow. In the latter case, the hot fluid is pulled away from the surface, but the overall temperature gradient cannot become positive since that would imply the existence of a region of fluid which is hotter than the surface – such an occurrence is impossible unless there is internal heat generation or viscous dissipative effects present. Therefore

the perturbation surface temperature gradient is bounded above by zero but is effectively unbounded below.

We obtain quantitatively similar results to those shown in Figure 6.1 to 6.4 when λ takes values fairly close to 0.4, although it is possible to use larger values of A in these cases. However, when λ differs substantially from 0.4, other nonlinear effects arise and these form the subject of the next few sections.

6.4 Superharmonic transitions ($\lambda < 0.4$)

In the previous section we presented a typical case of nonlinear wave generation where the forcing frequency is 0.4. In this section we will cover those cases for which the forcing frequency is less than 0.4. We find that, when λ is sufficiently small, the presence of nonlinearities serves to modify substantially the manner in which waves travel downstream, and the patterns obtained are entirely different from those given by linearised theory. That this should happen is easily understood if, when considering the evolution with ξ of a $\lambda = 0.2$ disturbance, it is realised that nonlinear interactions of the corresponding wavetrain with itself generates waves with double the local wavenumber. Such waves are then of roughly the same wavelength as those generated by a $\lambda = 0.4$ disturbance, and will therefore grow preferentially. This could be termed a $1 : 2$ superharmonic transition since the local wavenumber doubles at a position in the boundary layer which is dependent on the amplitude of the initiating disturbance.

We also present other superharmonic transitions, $1:3$ and $1:4$, which occur at successively smaller values of λ.

6.4.1 $1:2$ Superharmonic transition

The nonlinear evolution of the flow for values of λ close to 0.2 is considered. The manner in which the flow develops is depicted in a variety of ways in order to gain some understanding of the role played by the amplitude and frequency of the thermal disturbance. This development is shown in Figures 6.5 to 6.10.

Figure 6.5 shows the development of the waveform where the disturbance amplitude is $A = 2 \times 10^{-3}$ (i.e. $d = 5.30$ in equation (6.15)) and $\lambda = 0.18$. The waves are plotted at the different values of ξ as a pertubation rate of heat transfer against time t. Again we have normalised these perturbation values before plotting. It is clearly shown from this figure that there are two different oscillation wavelengths present. The first region is $\xi \in (70, 320)$, where the instability waves oscillate with the forcing frequency $\lambda = 0.18$. These waves are generated directly by the thermal forcing. At the end of the first region there is a fairly rapid transition to a regime which oscillates with double the original frequency; this is the second region for which $\xi > 320$. The temporal frequency within the second region is 0.36 which is close to that of the most dangerous frequency found in Chapter 5.

In Figure 6.6 we show the limit cycles of the phase trajectories of the surface rate

of heat transfer at various different positions along the surface. In this figure, as with others of its type presented later, the horizontal coordinate is the local value of $\frac{\partial \hat{\theta}}{\partial \eta}\Big|_{\eta=0}$ while the vertical coordinate is its time rate of change which was calculated using a one-sided finite difference approximation in time. Although formally of 1st order accuracy we are not interested in the quantitative data, but rather the shape of the phase trajectories and how they change.

Frame (a) in Figure 6.6 is close to being an ellipse which indicates that the waves are roughly sinusoidal. As time progresses, as shown by successive frames, the flow becomes progressively contaminated by the growing superharmonic wave. At a point just downstream of $\xi = 288$ and upstream of $\xi = 300$ (frames (c) and (d), respectively) we see a loop developing in the phase trajectory, and it is this position which may be considered to mark the transition point. At $\xi = 500$ (frame (i)) the second loop is almost identical to the first loop and this represents the full establishment of the superharmonic flow.

We emphasise that the transition from frame (a) to (i) is not a period doubling, since the curves are drawn over only one forcing period. This represents a period halving, and is one which occurs spatially, rather than temporally or as a governing parameter changes.

In Figure 6.7, we have plotted a corresponding set of perturbation isotherms over 8 equally spaced time intervals of a complete period in time since $1473.8 - 1438.9 = 34.9 \approx 2\pi/0.18$. Successive contours in this figure again correspond to a ratio of

10 between the values of maximum and minimum amplitude of the perturbation isotherms. It is noted that the values of maximum and minimum perturbation isotherms shown are $+10^{-2}$ and -10^{-2} respectively. The black triangles shown in Figure 6.7 represent one wavelength corresponding to the thermal forcing frequency. As t increases the leading cell of the two elongates compared with the second and eventually splits into three by the generation of a small cell – this is a fairly typical scenario.

Zero level contours of surface rate of perturbation heat transfer over the last few periods in time have been plotted in Figure 6.8. Here the temporal frequency value remains at $\lambda = 0.18$, but we display contours for a selection of forcing amplitudes. In this figure cells are delineated by the contours, and the number of cells which exist at a chosen value of x may be determined by placing a vertical line at that value of x and counting the intervals in between the intersections of the contours with the line. Figure 6.9 (which is a close-up view of frame (iv)) shows an example where we draw three vertical lines near the transition region. At the left vertical line position 6 cells (3 pairs) exist but which undergo a complex transformation to 12 (6 pairs) at the right vertical position. The middle line shows the manner in which the new cells appear.

The cells shown in Figure 6.7 correspond to the contours in frame (iv) of Figure 6.8. The position marked by 'a' in Figure 6.8 correspond to the appearance new cells.

In Figure 6.8 we see that there is a variation in the way in which the superharmonic transition takes place as the forcing amplitude varies. At large values of A (e.g. $A = 2 \times 10^{-3}$, frame (iv)) a region with a negative surface temperature gradient perturbation spawns an internal region with a positive perturbation, while where A is as small as $A = 2 \times 10^{-4}$ (frame (i)) it is a positive region which splits. At intermediate values of A there is a smooth transition between these states. In frame (iv) we first see a small positive region develop which has a small negative region just downstream of it. This negative region very soon disappears as the positive region grows large, after which it reappears when the positive region has become quite elongated.

It is clear from Figure 6.8 that the position at which the appearance of new cells occurs depends on the forcing amplitude, A. Figure 6.8 suggests cell-splitting occurs nearer to the leading edge as A increases. This has been investigated using many more values of A than are represented in Figure 6.8 and for the three values, $\lambda = 0.18, 0.2$, and 0.22, the results are shown in Figure 6.10. The curves shown in Figure 6.10 correspond to the first incipient creation of a new cell, or, in mathematical terms, where the heat transfer contours in Figure 6.8 have a turning point. We denote by x_c this position.

Figure 6.10 shows clearly the general trend for x_c to increase as the forcing amplitude decreases, although the evolution of x_c with A is not straightforward. On taking the $\lambda = 0.18$ curve, it is seen that there are three values at $\log_{10} A = -3.4$ (i.e. $A \approx 3.8 \times 10^{-4}$) which corresponds with the three turning points displayed

in frame (iv) of Figure 6.8. Thus as A decreases for $\lambda = 0.18$ the value of x_c increases to approximately 1960 after which it jumps to near 2130. Similar jumps occur at the other values of λ. We also see the general trend for x_c to increase as λ increases (at least over the range of values presented).

6.4.2 1 : 3 Superharmonic transition

In this section we present the nonlinear evolution of the flow considering those values of the forcing frequency which are close to $\lambda = \frac{1}{3} \times 0.4$. In this case the nonlinear interactions of the wavetrain should generate new waves with three times the local wavenumber. This development is displayed in Figures 6.11 to 6.15 in a similar fashion to those for the 1 : 2 superharmonic case.

Figure 6.11 shows the development of the waveform where the disturbance amplitude is $A = 4 \times 10^{-2}$ (i.e. $d = 6.60$ in equation (6.15)) and $\lambda = 0.13$. Again the wave amplitude is a normalised perturbation surface rate of heat transfer for each value of ξ. It is clearly shown from this figure that there are now three different oscillation wavelengths present in three different regions which are approximately, $\xi \in (70, 190)$, $\xi \in (190, 320)$ and $\xi \in (320, 520)$.

The first region is in $\xi \in (70, 190)$, is where the waves oscillate with the forcing frequency $\lambda = 0.13$ - these waves are again generated directly by the thermal forcing. At the end of the first region there is a transition to a regime which oscillates with double the original frequency. The temporal frequency within this

second region, i.e. at $\xi \in (190, 320)$ is 0.26 – this phenomenon is quite similar to that seen in Figure 6.5 of the $1:2$ superharmonic transition. At the end of the second region there is another transition and the waves now oscillate with three times the original frequency. Within this third region the temporal frequency is 0.39, which is very close to the optimum frequency found in Chapter 5.

In Figure 6.12 we show the limit cycles of the phase trajectories of the surface rate of heat transfer at various different positions along the surface. Frame (a) in the figure is again close to being an ellipse which indicates that the waves are roughly sinusiodal. As time progresses, as shown in the successive frames, the flow becomes progressively contaminated by the growing superharmonic waves. Between frames (b) and (c) the first transition occurs. Two well-established loops appear at $\xi = 313$ (frame (e)), but these are of very different amplitudes. This may be seen clearly just below $\xi = 320$ in Figure 6.11 where the wavetrain has alternating amplitudes. The second transition occurs just upstream of $\xi = 338$ (frame (f)). At $\xi = 450$ (frame (i)) the three loops are almost identical and elliptical.

In Figure 6.13 we have plotted again a corresponding set of perturbation isotherms in 8 equally spaced time intervals of a complete period in time (n.b. $1487.0 - 1439.6 = 48.3 \approx 2\pi/0.13$). The successive contours in this figure correspond to negative integer powers of 10 multiplied by the values of the maximum ($+10^{-1}$) and the minimum (-10^{-1}) amplitude of the perturbation isotherms. The black triangles shown in this figure represent one wavelength corresponding to the ther-

mal forcing frequency. As t increases the trailing cell of the two elongates first compared with the second and splits into three with the generation of a new small cell. For $t > 1463.7$ the leading cell now elongates, splits, generates a new cell and finally becomes three.

Zero level contours of the surface rate of perturbation heat transfer over the last few periods in time have been plotted in Figure 6.14. We again display contours for a selection of forcing amplitudes for the temporal frequency at $\lambda = 0.13$. Again it is clearly shown that the manner of the superharmonic transition is dependent on the forcing amplitude. For small values of A (e.g. $A = 1.4 \times 10^{-2}$ and frame (i)) a positive surface perturbation temperature gradient spawns two internal regions with negative perturbation – while for the $1 : 2$ superharmonic case it was one. On the other hand in frames (ii)-(v) both positive and negative regions generate cells with the opposingly signed heat transfer. In this figure the positions marked by 'a' and 'b' correspond to the appearance of new cells. Once more as A increases the cell-splitting positions get closer to the leading edge.

Figure 6.15 is a blow-up of frame (v) of Figure 6.14. Vertical lines are again drawn to count easily the number of cells. The left vertical line has 8 cells while it becomes 16 at the third line and 24 at the fourth line. Although the third line from the left has 16 intervals, they are unequal in size which corresponds to the unequal loops of frames (d) and (e) of Figure 6.12.

6.4.3 1 : 4 Superharmonic transition

This is the final section of the superharmonic transition. Here we present the nonlinear evolution of the flow on considering a value of the forcing frequency which is close to $\lambda = 0.1$. This is termed a 1 : 4 superharmonic transition as the nonlinear self-interaction of the wavetrain generates new waves which finally become four times the original local spatial wavenumber. These results are shown in Figures 6.16 to 6.20.

Figure 6.16 shows the waveform development where the disturbance amplitude is $A = 2 \times 10^{-1}$ (i.e. $d = 7.30$ in equation (6.15)), and $\lambda = 0.09$. This figure shows clearly that there are four different oscillating wavelengths present. The first region is in $\xi \in (70, 132)$, where the waves oscillate with the forcing frequency $\lambda = 0.09$. At the end of this region there is the first transition and two unequal waves appear within each forcing period. Thus the second region is in $\xi \in (132, 257)$. Here the waves constituting each pair are close to one another with a relatively undisturbed region in between pairs. It is in this region that a new wave develops (hence three waves per period in $\xi \in (257, 300)$) and subsequently a second wave (hence four waves for $\xi > 300$). At $\xi = 500$ each wave appears identical to each other wave and they are equivalent to those generated by a $\lambda = 0.36$ thermal forcing.

Figure 6.17 shows the limit cycles of the phase trajectories of the surface rate of heat transfer at various different positions along the surface. Like previous cases

frame (a) shows almost elliptic shape, again indicating that near the leading edge the waves are sinusoidal. The development of superharmonic flow is very clear downstream; for examples see frame (d) – double loops, frame (g) – triple loops, and finally frame (l) – quadruple loops.

In Figure 6.18 we have plotted a corresponding set of perturbation isotherms over 8 equally spaced time intervals of a complete period in time since $1491.3 - 1421.4 = 69.9 \approx 2\pi/0.09$. Successive contours in this figure again correspond to negative integer powers of 10 multiplied by the values of the maximum ($+10^{-1}$) and the minimum (-10^{-1}) amplitude of the perturbation isotherms. Black triangles shown in this figure again represent one spatial wavelength corresponding to the thermal forcing. As t progresses the leading cell elongates compared with the trailing cell and finally it splits into seven by generating successively six small cells.

Zero level contours in Figure 6.19 also represent the splitting of cells. The position of the appearance of new cells is marked by 'a', 'b', and 'c'. In this figure we see a complicated variation in the way the superharmonic transition takes place as A increases. In frame (i) a region of positive perturbation rate of heat transfer generates two negative regions (so one cell becomes five) while a negative region generates one positive region (so one cell becomes three). As the positions marked by a, b and c are at roughly the same value of x this means that we have a very sudden change from, say, one pair of cells to four pairs.

Similar comments may be made about frame (ii) which corresponds to a larger forcing amplitude. However the cell marked 'a' now appears before that marked 'b'. As A increases further cell-splitting occurs much closer to the leading edge and the manner in which the $1:4$ transition takes place alters markedly. When A is as large as 1.34×10^{-1} (frame (iv)) the first cell splitting creates a "positive" cell which subsequently splits to create a "negative" cell. At larger amplitudes three "positive" cells appear within a negative cell, as displayed in Figure 6.18.

A detailed indication of how the turning points displayed in Figure 6.19 vary with A is shown in Figure 6.20.

6.5 Subharmonic transitions ($\lambda > 0.4$)

In §6.4 we presented some superharmonic transition cases by considering the forcing frequency to be less than 0.4. In the present section we will present some cases for which the forcing frequency is greater than 0.4 with various values of the forcing amplitude. We find exactly the opposite transitional effects here. We find that for a wide range of the forcing frequency ($\lambda \in (0.55, 1.0)$) the developing nonlinearity causes cell merging which means that the wavetrain loses half of its cells, and the local wavenumber halves. Examples are given for the frequency $\lambda = 0.8$. This could be termed a subharmonic transition and these results are shown in Figures 6.21 to 6.23.

However, in Figure 6.21 we will first provide an overview of our results for different values of both the forcing amplitude and the forcing frequency. The results are presented in terms of the relative maximum local asymptotic response, $M(x)$ which is defined as

$$M(x) = M_1(x) - M_1(x_{min}) \tag{6.16}$$

where

$$M_1(x) = \log_{10} \left| \max_{t_{max}-200<t<t_{max}} \left(\frac{\partial \hat{\theta}}{\partial \eta} \right)_{\eta=0} \right|, \tag{6.17}$$

and the relative minimum local asymptotic response, $N(x)$ as

$$N(x) = N_1(x) - N_1(x_{min}) \tag{6.18}$$

where

$$N_1(x) = \log_{10} \left| \min_{t_{max}-200<t<t_{max}} \left(\frac{\partial \hat{\theta}}{\partial \eta} \right)_{\eta=0} \right|. \tag{6.19}$$

The value $M_1(x)$ is the logarithm of the maximum perturbation temperature gradient at the surface over time, and is a measure of how strong the waves are. The quantity $M(x)$ measures this strength relative to that at $x = x_{min}$. Thus the computed curves for $M(x)$ should be identical once A is sufficiently small and hence nonlinear effects are negligible.

In Figure 6.21 each solid curve corresponds to values of $M(x)$ while the dashed curve corresponds to values of $N(x)$. In each frame we have plotted four pairs of curves each for different values of A and which are marked by 'a', 'b', 'c', and

'd'. Frame (i) of this figure shows that there is no differece between the results $M(x)$ and $N(x)$, and even against A. Thus the development of the waves follows the linearised theory of Chapter 5 (see Figure 5.32 for $\lambda = 0.55$).

For $\lambda = 0.6$ and 0.65 the situation is almost exactly the same, although the curves for the largest amplitude, $A = 0.01$, are beginning to be distinct from those of smaller amplitudes. When λ is as large as 0.8 and 1.0 the curves for the different amplitudes are very distinct, and the shapes of the curves could be interpreted in a variety of ways, including the possibility of mean flow saturation effects. However, linear theory leads us to expect that all the curves for $\lambda = 0.8$ and 1.0 should decay, but three of them do not. Therefore we have investigated this more closely in Figures 6.22 and 6.23.

These figures display isotherms over two forcing periods for $\lambda = 0.8$ and for $A = 10^{-2}$ and 10^{-3}, respectively. It is essential to note that nonlinear effects are sufficiently strong that there is an appreciable change in the mean perturbation temperature field, and therefore we plot contours of $\hat{\theta} - \hat{\theta}_{mean}$ rather than $\hat{\theta}$ only. In these figures 50000 timesteps are taken to obtain time periodic solutions.

The immediate response in the region near to the leading edge consists of the travelling waves of the type which is consistent with linearised theory for $\lambda = 0.8$. However, much further downstream the cells are more consistent with the $\lambda = 0.4$ case.

Black triangles are used in Figures 6.22 and 6.23 to show clearly the transition

between these two states. At $t = 4984.3$ the two triangles on the left hand side contain 4 cells over 2 complete periods. As time increases to $t = 5000$ these transform into what is effectively 2 cells between the two right black triangles by a process of cell merging. This is what we call a subharmonic transition where the wavenumber becomes half of its original value.

Figure 6.23 shows a similar trend of the subharmonic transition where $A = 10^{-3}$. This corresponds to the results corresponding to curves (b) of frame (v) in Figure 6.21. Again 2 complete periods in between the two left black triangles become 1 in between the two right black triangles. On comparing with Figure 6.22, it is clear that the transition takes place further from the leading edge as A decreases since the nonlinearities are less effective at smaller amplitudes.

6.6 Conclusions

In this chapter we have studied the nonlinear boundary layer instabilities of the free convection flow from a vertical heated flat plate. A time periodic thermal disturbance is introduced near the leading edge to generate waves and to find its receptivity in the boundary layer. We have found that the nonlinearity has a great effect on the evolution of waves in the boundary layer and the waveforms are strongly dependent on the thermal forcing frequency and initial disturbance amplitude.

First, we have studied a case by considering the forcing frequency value 0.4 – this value is very close to the most dangerous value found in Chapter 5. However when $\lambda < 0.4$ we found that different types of superharmonic transition take place. In these cases the nonlinear interaction of the corresponding wavetrain with itself generates new waves with double, triple, or quadruple the local spatial wavenumber.

Finally, we studied some subharmonic transition cases which correspond to higher forcing frequencies ($\lambda > 0.4$). In these cases the wavenumber become half of the original local wavenumber.

Chapter 7

Conclusions

We have studied the stabilty of free convective flow from a uniform heated surface with the respect of wave (vertical surface) and vortex (inclined surface) disturbance mechanisms. We have dealt with four related problems with a variety of analytical and numerical techniques. First we considered a general investigation of the *linear stability* of the vertical boundary layer with small 2D wave disturbances. This uses the well-known method where the Navier-Stokes and energy equations are used to derive Orr-Sommerfeld type equations. Many authors have formulated such stability analyses for a variety of boundary layer flows, but they have considered only the leading term of the boundary layer approximation as the basic flow. The novelty of our approach was to find a more accurate solution of the basic flow using matched asymptotic theory, and then study its stability. Chapter 3 contains the details of this analysis where we consider the two fluids,

water ($Pr = 6.7$) and air ($Pr = 0.7$). In general we find that the shape of the external domain has a large influence on the stability criterion.

In Chapter 4 we used the same methods to study the vortex mode of instabilities from inclined surfaces. Experimental work indicates that this is the primary mode except when the heated surface is close to the vertical. An extra parameter now appears – the inclination angle. For a fixed value of the inclination angle we found that the critical distance is again strongly dependent on the wedge angle. The only exception to this general conclusion is when the surface is near to the vertical, but in this regime wave instabilities are more important.

We have performed a full numerical investigation of wave instabilities in Chapter 5. The numerical method uses second order accurate finite differences in both time and space. Here we have considered full elliptic linearised Navier-Stokes and energy equations rather than the boundary layer approximation. The growing shape of the boundary layer was accounted for using a Schwartz-Christoffel coordinate transformation. First we solved directly the nonlinear system to obtain the steady state solution. Secondly, we used these steady solutions to linearise the full equations. Finally full elliptic linearised perturbation equations have been solved to study the stability characteristics.

Our main objective in Chapter 5 was to see how the heated thermal boundary layer responds to both initial conditions and time-periodic disturbances. Both point and distributed disturbances placed in the boundary layer at $t = 0$ were

formed to travel downstream and elongate spatially. Eventually they leave the computational domain at outflow and therefore the instability is confirmed as convective. For unsteady perturbations the amplitude of the response depends very strangly on the disturbance frequency. Both global and local values of the most dangerous disturbance frequency were obtained, and comparisons made with PFA theory.

We extended the numerical computations to the full nonlinear system in Chapter 6. When the disturbance amplitude is small we can recover the results of Chapter 5. But when it is larger, we obtain a variety of nonlinear self-interactions. When $\lambda < 0.4$ there can exist what is called here a superharmonic transition since the relatively long travelling waves split into two or more cells, thereby increasing the local wavenumber. On the other hand, for $\lambda > 0.4$ there can be a corresponding subharmonic transition with cell merging.

7.1 Recommendation for future work

In view of the work accomplished to date, the following extensions are envisaged

- Three-dimensional numerical simulations using full nonlinear Navier-Stokes and energy equations. Many different aspects of stability could be covered with such a code. The weakly nonlinear study of vortex merging on inclined surfaces by Chen *et al* (1991) may be validated and extended into

the nonlinear regime. The possibility of oblique TS-waves embedded in a primary vortex structure may be evaluated. Szewczyk's (1962) observation of a secondary vortex instability in the presence of primary waves in a vertical boundary layer may also be investigated.

- Use the Parabolised Stability Equations (PSE) technique to study linear and nonlinear wave instability. PSE is an approximate technique, a fairly recent development by Bertolotti *et al* (1992). In this method, streamwise properties are assumed to vary very slowly, hence the boundary layer approximation is utilised.

- Finally most of the quoted experimental studies of external thermal boundary layer flows were performed approximately 30 years ago. The recent upsurge in DNS studies brought about by greatly increased computer speeds and storage has meant that such studies are now very advanced. It is essential to conduct suitable experiments to determine possible modes of secondary instability for both vertical and inclined surfaces.

References

Arakawa, A. 1966 Computational design of long-term numerical integration of the equations of fluid motion: I. Two dimensional incompressible flow. *J. Computational Physics* **1**. 119–143.

Bake, S., Meyer, D. G. W., & Rist, U. 2002 Turbulence mechanism in Klebanoff transition: a quantitative comparison of experiment and direct numerical simulation. *J. Fluid Mech.* **459**, 217–243.

Bertolotti, F. P., Herbert, T. & Spalart, P. R. 1992 Linear and nonlinear stability of the Blasius boundary layer. *J. Fluid Mech.* **242**, 441–474.

Briggs, W. L. 1987 A Multigrid Tutorial. *Lancaster Press.*

Brooker, A. M. H., Patterson, J. C. & Armfield, S. W. 1997 Non-parallel linear stability analysis of the vertical boundary layer in a differentially heated cavity. *J. Fluid Mech.* **352**. 265–281.

Brooker, A. M. H., Patterson, J. C., Graham, T. & Schöpf, W. 2000 Convective instability in a time-dependent buoyancy driven boundary layer. *Int. J. Heat and Mass Transfer.* **43**. 297–310.

Chen, C. C., Labhari, A., Chang, H. C. & Kelly, R. E. 1991 Spanwise pairing of finite-amplitude longitudinal vortex rolls in inclined free-convection boundary layers. *J. Fluid Mech.* **231**, 73–113.

Chen, T. S. & Tzuoo, K. L. 1982 Receptivity to surface roughness near a swept leading edge. *J. Heat Transfer* **104**, 637–543.

Chiu, W. K., Soria, J. & Norton, M. P. 1995 Laminar boundary layer receptivity to transverse structural vibration. *J. Sound and Vibration.* **186(3)**, 463–493.

Collis, S. S. & Lele, S. K. 1999 Receptivity to surface roughness near a swept leading edge. *J. Fluid Mech.* **380**, 141–168.

Crouch, J. D. 1997 Excitation of secondary instabilities in boundary layers. *J. Fluid Mech.* **336**, 245–266.

Daniels, P. G. & Patterson, J. C. 1997 On the long-wave instability of natural-convection boundary layers. *J. Fluid Mech.* **335**, 57–73.

Daniels, P. G. & Patterson, J. C. 2001 On the short-wave instability of natural convection boundary layers. *Proc. R. Soc. Lond. A.* **457**, 519–538.

Dietz, A. J. 1998 Boundary-layer receptivity to transient convected disturbances. *A.I.A.A. Journal.* **36(7)**, 1171–1177.

Dietz, A. J. 1999 Local boundary-layer receptivity to a convected free-stream disturbance. *J. Fluid Mech.* **378**, 291–317.

Fasel, H. & Konzelmann, U. 1990 Non-parallel stability of a flat-plate boundary layer using the complete Navier-Stokes equations. *J. Fluid Mech.* **221**, 331–347.

Fasel, H. F., Rist, U. & Konzelmann, U. 1990 Numerical investigation of the three-dimensional development in boundary-layer transition. *A.I.A.A. Journal.* **28(1)**, 29–37.

Fasel, H. F. 2002 Numerical investigation of the interaction of the Klebanoff-mode with a Tollmien-Schlichting wave. *J. Fluid Mech.* **450**, 1–33.

Gebhart, B. 1979 Buoyancy induced fluid motions characteristic of applications in technology. *Trans. A.S.M.E. J. Fluid Engineering* **101**, 5–28.

Godaux, F. & Gebhart, B. 1974 An experimental study of the transition of natural convection flow adjacent to a vertical surface. *Int. J. Heat Mass Transfer* **17**, 93–107.

Goldstein, M. E. 1983 The evolution of Tollmien-Schlichting waves near a leading edge. *J. Fluid Mech.* **127**, 59–81.

Goldstein, M. E. 1985 Scattering of acoustic waves into Tollmien-Schlichting waves by small streamwise variations in surface geometry. *J. Fluid Mech.* **154**, 509–529.

Haddad, O. M. & Corke, T. C. 1998 Boundary layer receptivity to free-stream sound on parabolic bodies. *J. Fluid Mech.* **368**, 1–26.

Haaland, S. E. & Sparrow, E. M. 1973a Vortex instability of natural convection flow on inclined surfaces. *Int. J. Heat Mass Transfer* **16**, 2355–2367.

Haaland, S. E. & Sparrow, E. M. 1973b Wave instability of natural convection on inclined surfaces accourding for nonparallelism of the basic flow. *J. Heat Transfer* **95**, 405–407.

Haaland, S. E. & Sparrow, E. M. 1973c Stability of buoyant boundary layers and plumes, taking account of nonparallelism of the basic flows. *J. Heat Transfer* **95**, 293–301.

Hall, P. 1982 Taylor-Görtler vortices in fully developed or boundary layer flows: linear theory. *J. Fluid Mech.* **125**, 475–494.

Hall, P. 1983 The linear development of Görtler vortices in growing boundary layers. *J. Fluid Mech.* **130**, 41–58.

Hall, P. & Smith, F. T. 1988 The nonlinear interaction of Tollmien-Schlichting waves and Taylor-Görtler vortices in curved channel flows. *Proc. Roy. Soc. Lond.* **A417**, 255–282.

Healey, J. J. 1995 On the neutral curve of the flat-plate boundary layer: comparison between experiment, Orr-Sommerfeld theory and asymptotic theory. *J. Fluid Mech.* **288**, 59–73.

Hieber, C. A. & Gebhart, B. 1971 Stability of vertical natural convection boundary layers: some numerical solutions. *J. Fluid Mech.* **48**, 625–646.

Hsu, C. T. & Cheng, P. 1979 Vortex instability in buoyancy-induced flow over inclined heated surfaces in porous media *Trans. A.S.M.E. J. Heat Transfer* **101**, 660–665.

Huser, A. & Biringen, S. 1993 Direct numerical simulation of turbulent flow in a square duct. *J. Fluid Mech.* **257**, 65–95.

Israeli, M. & Orszag, S. A. 1981 Approximation of radiation boundary conditions. *J. Comp. Physics.* **41**, 115–135.

Iyer, P. A. & Kelly, E. R. 1974 The stability of the laminar free convection flow included by a heated inclined plate. *Int. J. Heat Mass Transfer* **17**, 517–525.

Kahawita, A. & Meroney, R. N. 1974 The vortex mode of instability in natural convection flow along inclined plate. *Int. J. Heat Mass Transfer* **17**, 541–548.

King, R. A. & Breuer, K. S. 2001 Acoustic receptivity and evolution of two-dimensional and oblique disturbances in a Blasius boundary layer. *J. Fluid Mech.* **432**, 69–90.

Kloker, M., Konzelmann, U. & Fasel, H. 1993 Outflow boundary conditions for spatial Navier-Stokes simulations of transitional boundary layers. *A.I.A.A. Journal* **31**, 620–628.

Kral, L. D. & Fasel, H. F. 1994 Direct numerical simulation of passive control of three-dimensional phenomena in boundary-layer transition using wall heating. *J. Fluid Mech.* **264**, 213–254.

Lewis, S., Bassom, A. P. & Rees, D. A. S. 1995 The stability of vertical thermal boundary layer flow in a porous medium *Eur. J. Mech. B* **14**, 395–408.

Lingwood, R. J. 1997 Absolute instability of the Ekman layer and related rotating flows. *J. Fluid Mech.* **331**, 405–428.

Lloyd, J. R. & Sparrow, E. M. 1970 On the instability of natural convection flow on inclined plates. *J. Fluid Mech.* **42(3)**, 465.

Morkovin, M. V. 1969 Critical evaluation of transition from laminar to turbulent shear layers with emphasis on hypersonically travelling bodies. *AFFDL-TR 68-149.* US Air Force Flight Dynamics Laboratory, Wright Patterson Air Force Base, Ohio.

Nachtsheim, P. R. 1963 Stability of free convection boundary layer flows. *NASA report TN D-2089.*

Orr, W. 1907 The stability or instability of the steady motions of a perfect liquid and of a viscous fluid. *Proc. Roy. Irish Acad.* **A27**, 121–165.

Ostrach, S. 1953 An analysis of laminar free-convection flow and heat transfer about a flat plate parallel to the direction of the generating body force. *NACA Rep.* **1111**.

Patterson, J. C., Graham, T., Schöpf, W. & Armfield, S. W. 2002 Boundary layer development on a semi-infinite suddenly heated vertical plate. *J. Fluid Mech.* **453**, 39–55.

Pohlhausen, E. 1921 Der Wärmeaustausch zwischen festen Körpern und Flüssigkeiten mit kleiner Wärmeleitung. *Zeitschrift für angewandte Mathematik und Mechanik* **1**, 115–120.

Rees, D. A. S. 2001 Vortex instability from a near-vertical heated surface in a porous medium. I Linear theory. *Proc. Roy. Soc. Lond. A.* **457**, 1721–1734.

Rees, D. A. S. 2002 Vortex instability from a near-vertical heated surface in a porous medium. II Nonlinear evolution. *Proc. Roy. Soc. Lond. A.* **458**, 1575–1592.

Rees, D. A. S. & Bassom, A. P. 1993 The nonlinear nonparallel wave instability of boundary layer flow induced by a horizontal heated surface in porous media. *J. Fluid Mech.* **253**, 267–296.

Rist, U. & Fasel, H. 1995 Direct numerical simulation of controlled transition in a flat-plate boundary layer. *J. Fluid Mech.* **298**, 211–248.

Rogler, H. L. & Reshotko, E. 1975 Disturbances in a boundary layer introduced by a low intensity array of vortices. *SIAM J. Appl. Maths.* **28**, 431–462.

Sandham, N. D. & Kleiser, L. 1992 The late stages of transition to turbulence in channel flow. *J. Fluid Mech.* **245**, 319–348.

Schöpf, W. & Patterson, J. C. 1996 Visualization of natural convection in a side-heated cavity: transition to the final steady state. *Int. J. Heat Mass Transfer* **39(16)**, 3497–3509.

Shu, J. J. & Wilkes, G. 1995 Mixed convection laminar film condensation on a semi-infinite vertical plate. *J. Fluid Mech.* **300**, 207–229.

Schlichting, H. 1933 Zur entstehung der turbulenz bei der plattenströmung. *Nachr. Ges. Wiss. Gottingen, Math-Phys.* **KI**, 182–208.

Smith, F. T. 1979 On the non-parallel flow stability of the Blasius boundary layer. *Proc. Roy. Soc. Lond.* **A366**, 91–109.

Sommerfeld, A. 1908 Ein beitrag zur hydrodynamischen erkläerung der turbulenten flüessigkeitsbewegungen. *In Proc. 4th Int. Cong. of Maths.* **III**, 116–124.

Storesletten, L. & Rees, D. A. S. 1998 The influence of higher-order effects on the linear instability of thermal boundary layer flow in porous media. *Int. J. Heat Mass Transfer* **41**, 1833–1843.

Sparrow, E. M. & Husar, R. B. 1969 Longitudinal vortices in natural convection flow on inclined plates. *J. Fluid Mech.* **37(2)**, 261.

Szewczyk, A. A. 1962 Stability and transition of the free-convection layer along a vertical flat plate. *Int. J. Heat Mass Transfer.* **5**, 903–914.

Tam, C. K. W. 1981 The excitation of Tollmien-Schlichting waves in low subsonic boundary layers by free-stream sound waves. *J. Fluid Mech.* **109**, 483–501.

Tollmien, W. 1929 Uber die entstehung der turbulenz. *Nachr. Ges. Wiss. Gottingen, Math-Phys.* **KI**, 21–44.

Wanderley, J. B. V. & Corke, T. C. 2001 Boundary layer receptivity to free-stream sound on elliptic edges of flat plates. *J. Fluid Mech.* **429**, 1–21.

Wassermann, P. & Kloker, M. 2002 Mechanisms and passive control of crossflow-vortex-induced transition in a three-dimensional boundary layer. *J. Fluid Mech.* **456**, 49–84.

Westin, K. J. A., Bakchinov, A. A., Kozlov, V. V. & Alfredsson, P. H. 1998 Experiments on localized disturbances in a flat plate boundary layer. Part 1. The receptivity and evolution of a localized free stream disturbance. *Eur. J. Mech. B/Fluids.* **17(6)**, 823–846.

Yang, K. T. & Jerger, E. W. 1964 First-order perturbations of laminar free-convection boundary layers on a vertical plate. *J. Heat Transfer* **86**, 107–115.

Zuercher, E. J., Jacobs, J. W. & Chen, C. F. 1998 Experimental study of the stability of boundary-layer flow along a heated, inclined plate. *J. Fluid Mech.* **367**, 1–25.

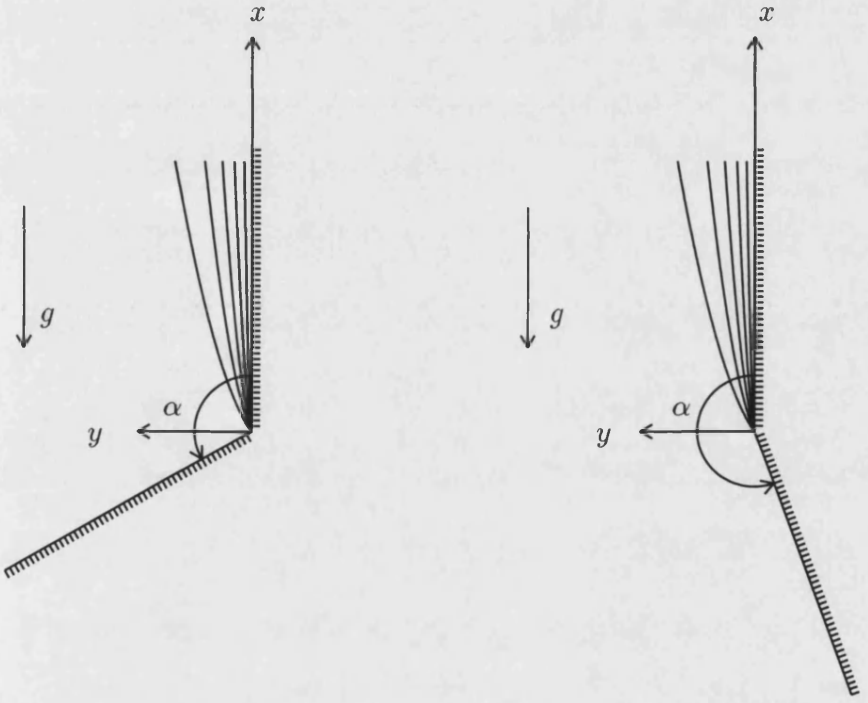

Figure 3.1: Schematic diagram of the flow configuration showing the coordinate directions, the orientation of surfaces, and displaying two different wedge-angles, α.

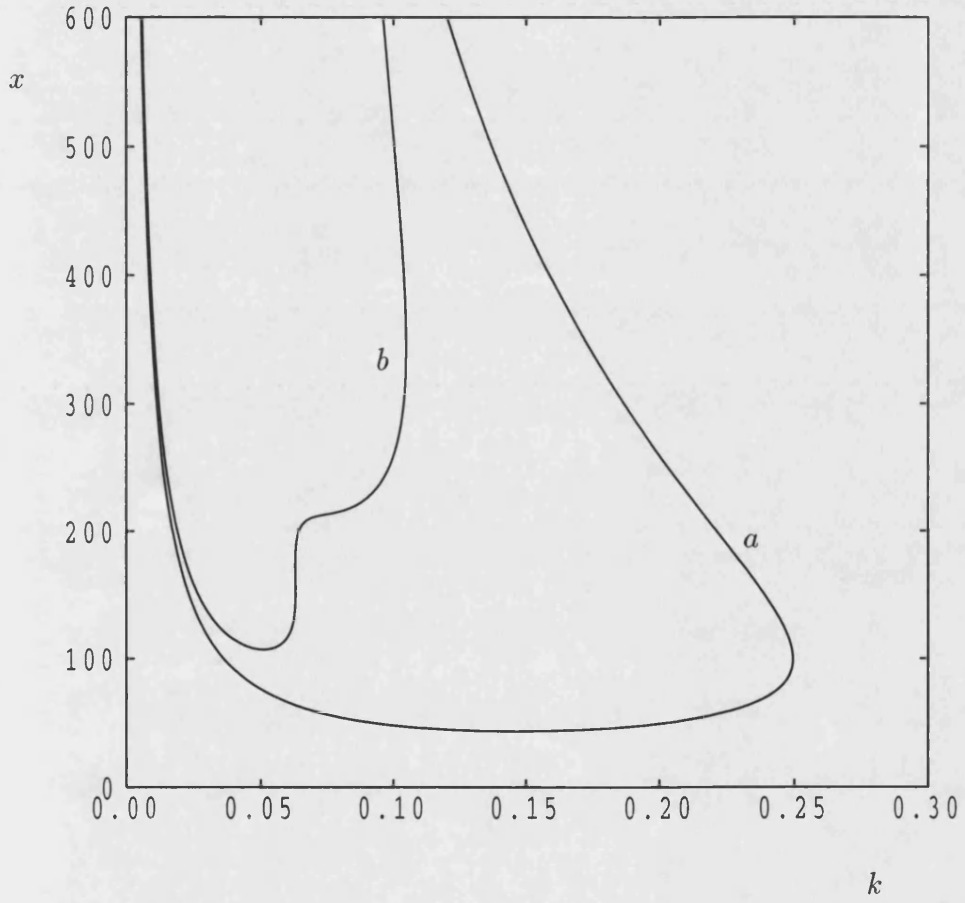

Figure 3.2: Neutral curves for (a) $Pr = 6.7$ and (b) $Pr = 0.7$ corresponding to the leading order basic boundary layer flow.

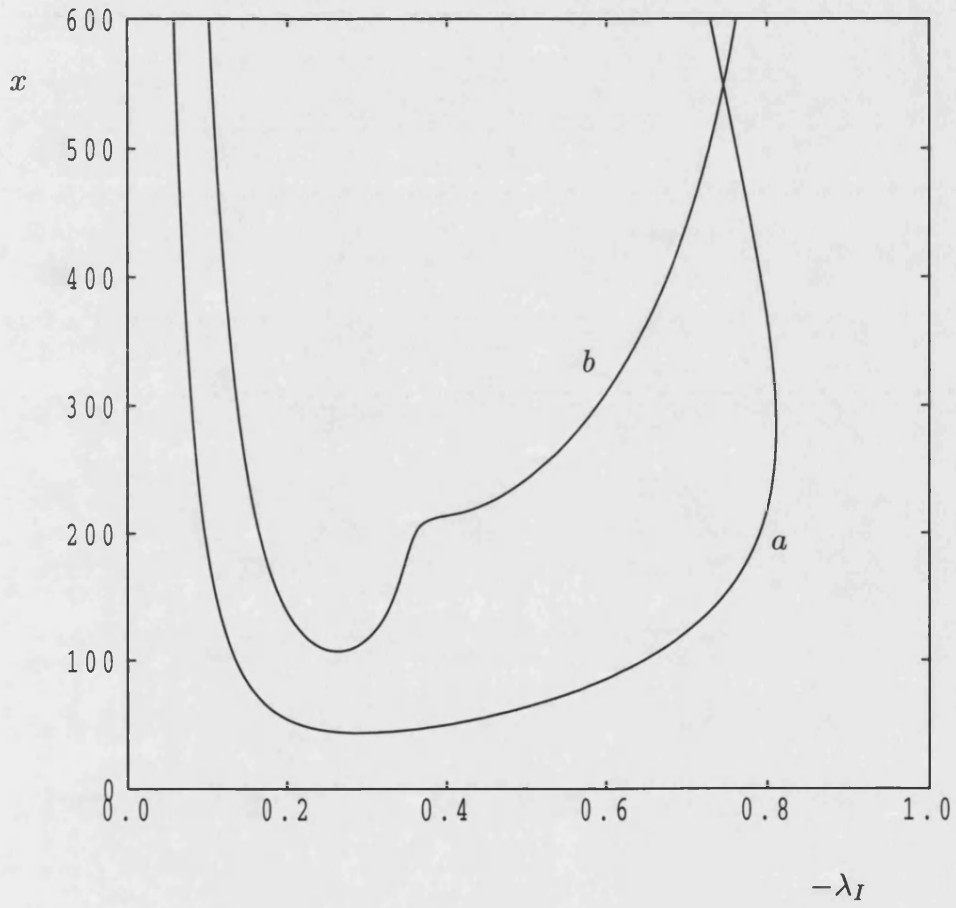

Figure 3.3: Variation of the disturbance frequency $(-\lambda_I)$ on the neutral curves plotted in Figure 3.2: (a) $Pr = 6.7$ and (b) $Pr = 0.7$.

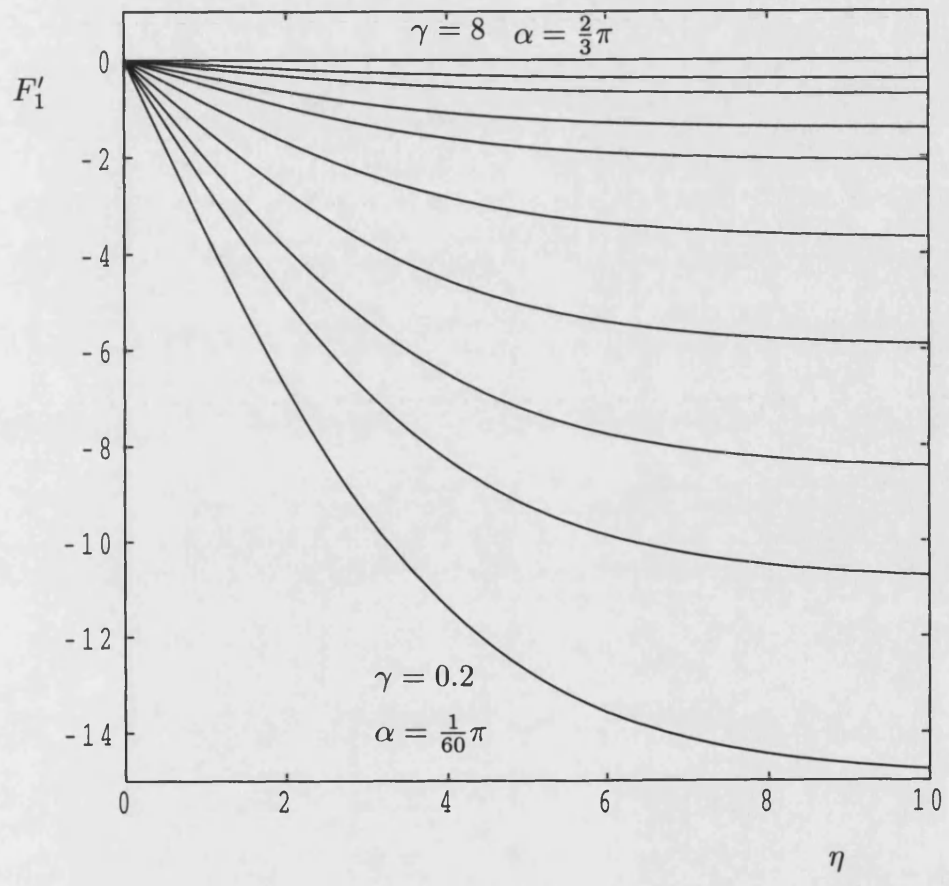

Figure 3.4: First order streamwise velocity profiles of the basic flow for water ($Pr = 6.7$), corresponding to $\gamma = 0.2$, 0.3, 0.4, 0.6, 0.8, 1, 2, 4, 6, 8 where $\gamma = 12\alpha/\pi$. This corresponds to α varying between just above 0 and $2\pi/3$.

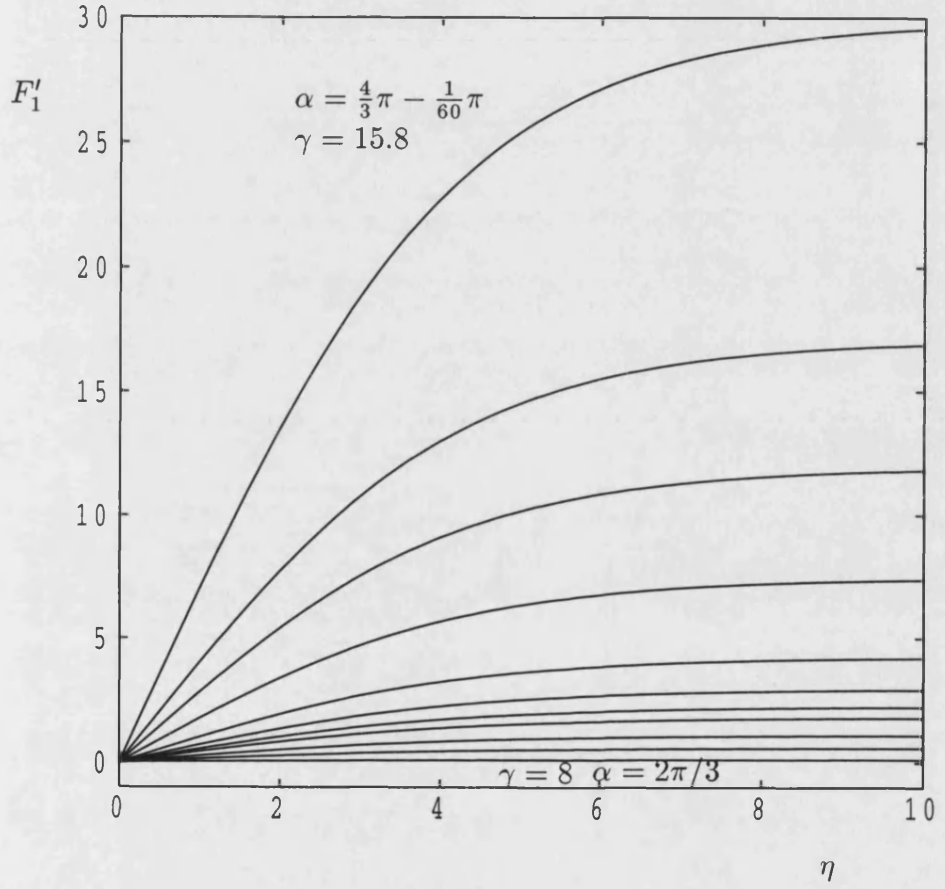

Figure 3.5: First order streamwise velocity profiles of the basic flow for water ($Pr = 6.7$), corresponding to $\gamma = 8$, 9, 12, 14, 14.4, 14.6, 14.8, 15, 15.2, 15.4, 15.6, 15.8, where $\gamma = 12\alpha/\pi$. This corresponds to α varying between $2\pi/3$ and almost $4\pi/3$.

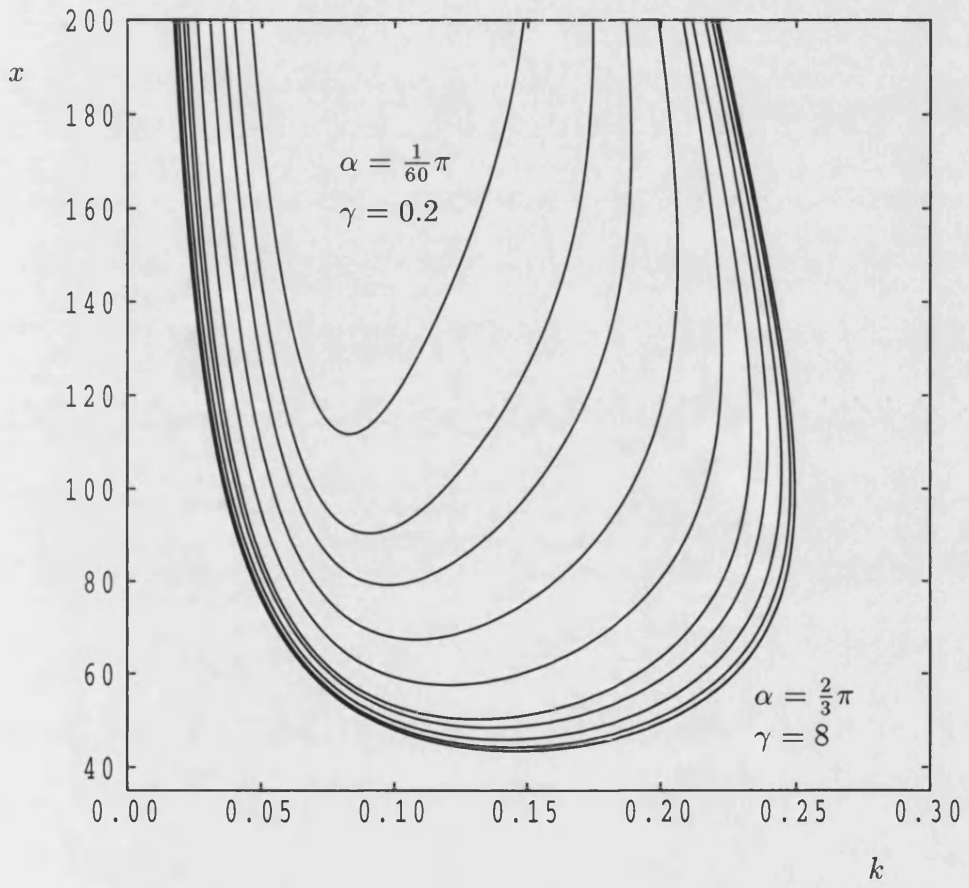

Figure 3.6: Neutral curves for water ($Pr = 6.7$), corresponding to $\gamma = 0.2$, 0.3, 0.4, 0.6, 0.8, 1, 2, 4, 6, 8 where $\gamma = 12\alpha/\pi$. This corresponds to α varying between just above 0 and $2\pi/3$.

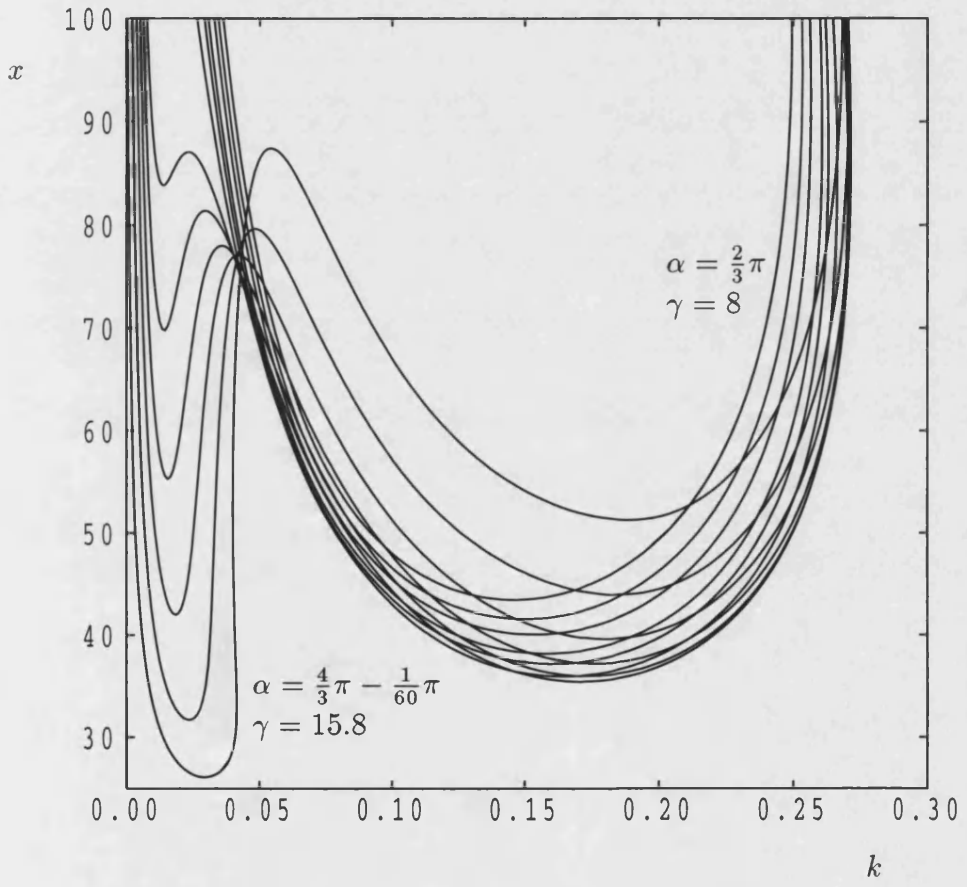

Figure 3.7: Neutral curves for water ($Pr = 6.7$), corresponding to $\gamma = 8$, 9, 12, 14, 14.4, 14.6, 14.8, 15, 15.2, 15.4, 15.6, 15.8, where $\gamma = 12\alpha/\pi$. This corresponds to α varying between $2\pi/3$ and almost $4\pi/3$.

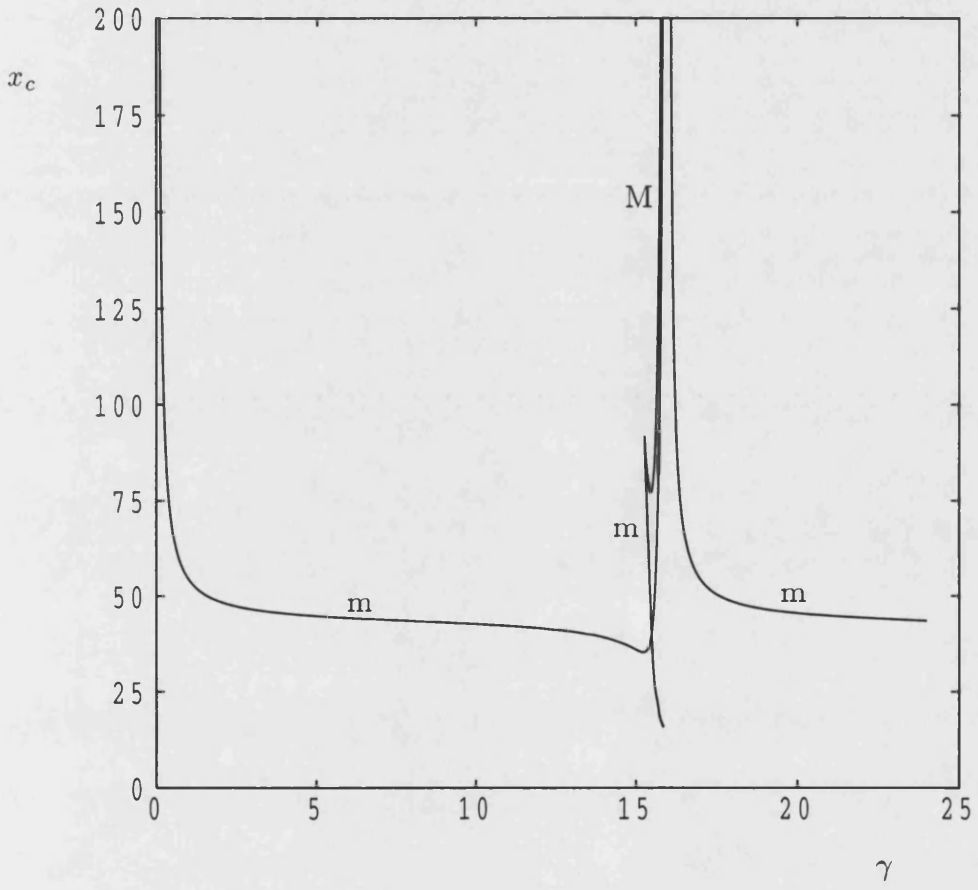

Figure 3.8: Variation of the critical distances on the neutral curves with $\gamma = 12\alpha/\pi$ for water ($Pr = 6.7$). M denotes a local maximum while m denotes a local minimum.

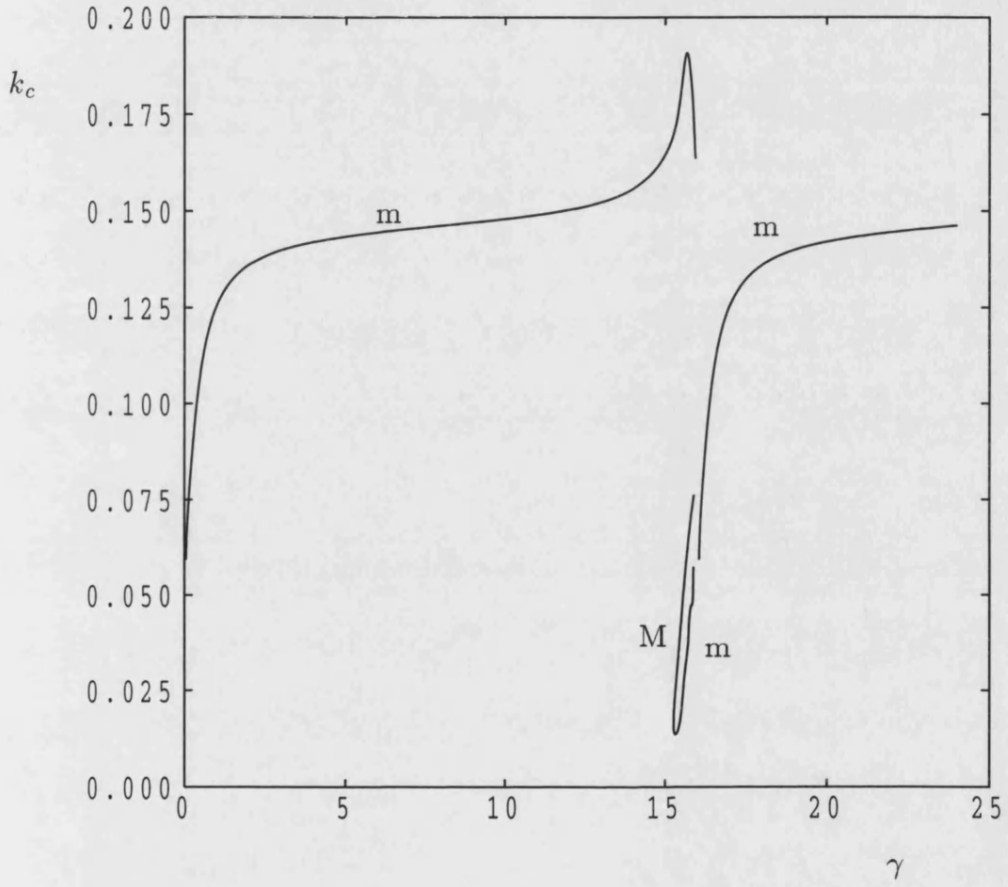

Figure 3.9: Variation of the critical wavenumbers on the neutral curves with $\gamma = 12\alpha/\pi$ for water ($Pr = 6.7$). M denotes a local maximum while m denotes a local minimum.

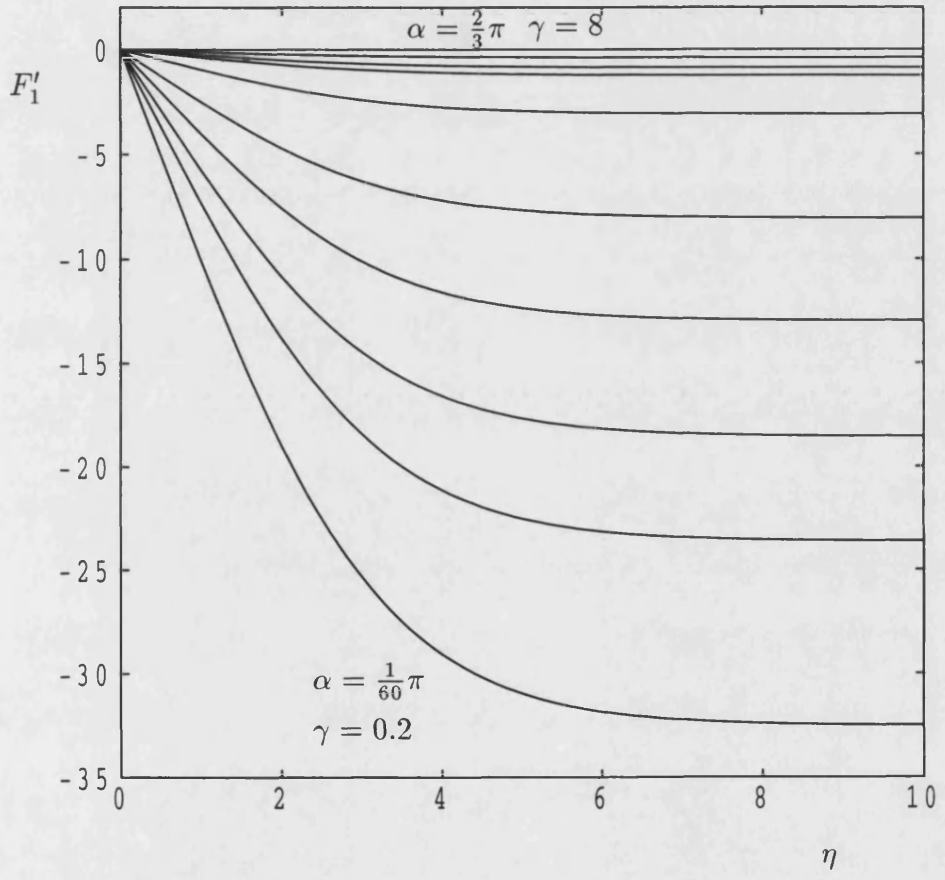

Figure 3.10: First order streamwise velocity profiles of the basic flow for air ($Pr = 0.7$), corresponding to $\gamma = 0.2$, 0.3, 0.4, 0.6, 0.8, 1, 2, 4, 6, 8 where $\gamma = 12\alpha/\pi$. This corresponds to α varying between just above 0 and $2\pi/3$.

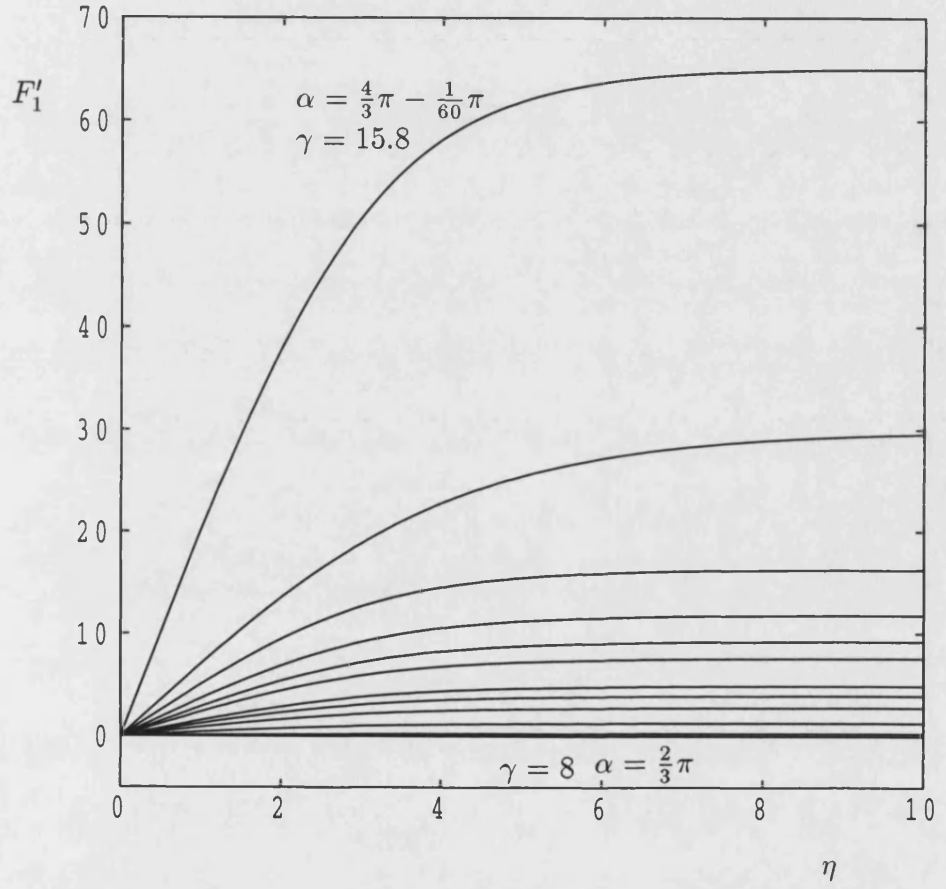

Figure 3.11: First order streamwise velocity profiles of the basic flow for air ($Pr = 0.7$), corresponding to $\gamma = 8$, 9, 12, 14, 14.4, 14.6, 14.8, 15, 15.2, 15.4, 15.6, 15.8, where $\gamma = 12\alpha/\pi$. This corresponds to α varying between $2\pi/3$ and almost $4\pi/3$.

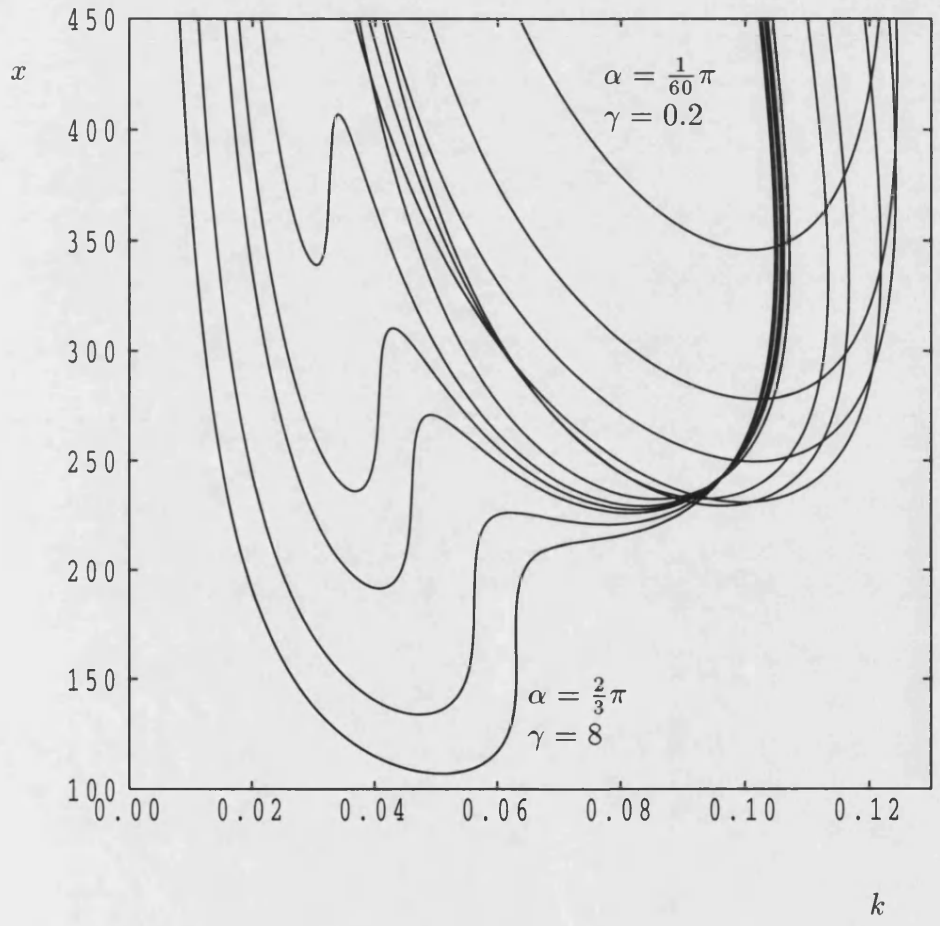

Figure 3.12: Neutral curves for air ($Pr = 0.7$), corresponding to $\gamma = 0.2$, 0.3, 0.4, 0.6, 0.8, 1, 2, 4, 6, 8 where $\gamma = 12\alpha/\pi$. This corresponds to α varying between just above 0 and $2\pi/3$.

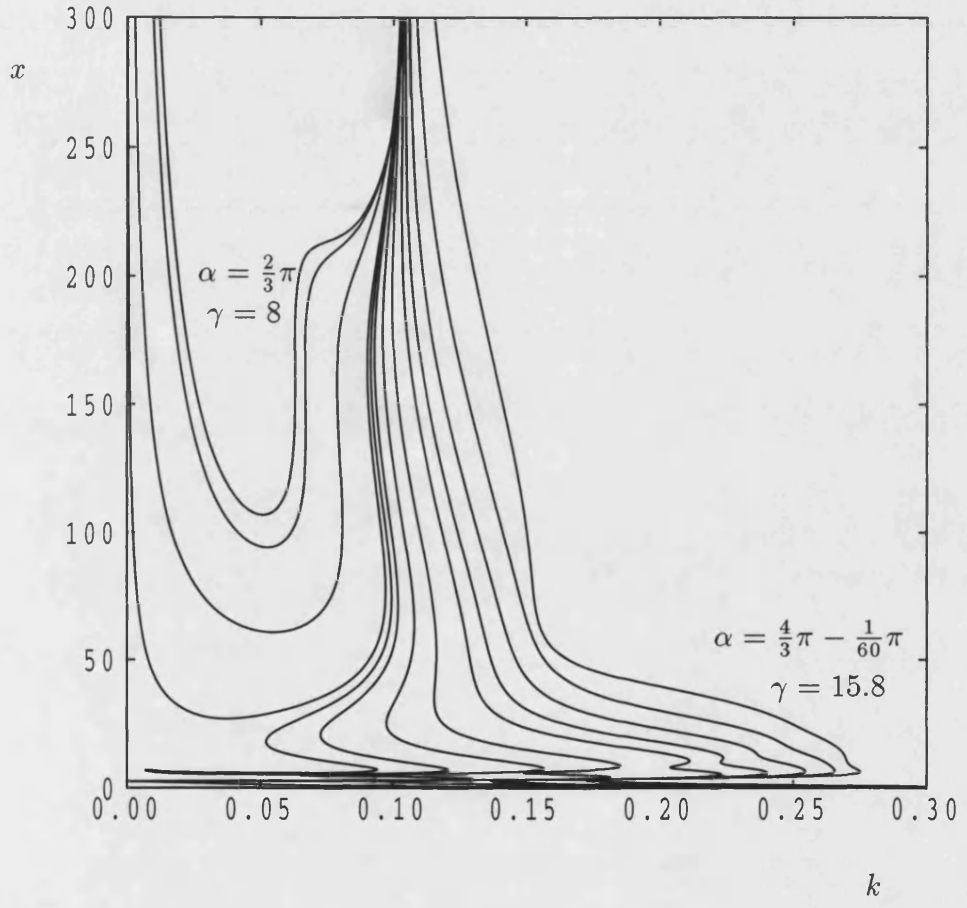

Figure 3.13: Neutral curves for air ($Pr = 0.7$), corresponding to $\gamma = 8$, 9, 12, 14, 14.4, 14.6, 14.8, 15, 15.2, 15.4, 15.6, 15.8, where $\gamma = 12\alpha/\pi$. This corresponds to α varying between $2\pi/3$ and almost $4\pi/3$.

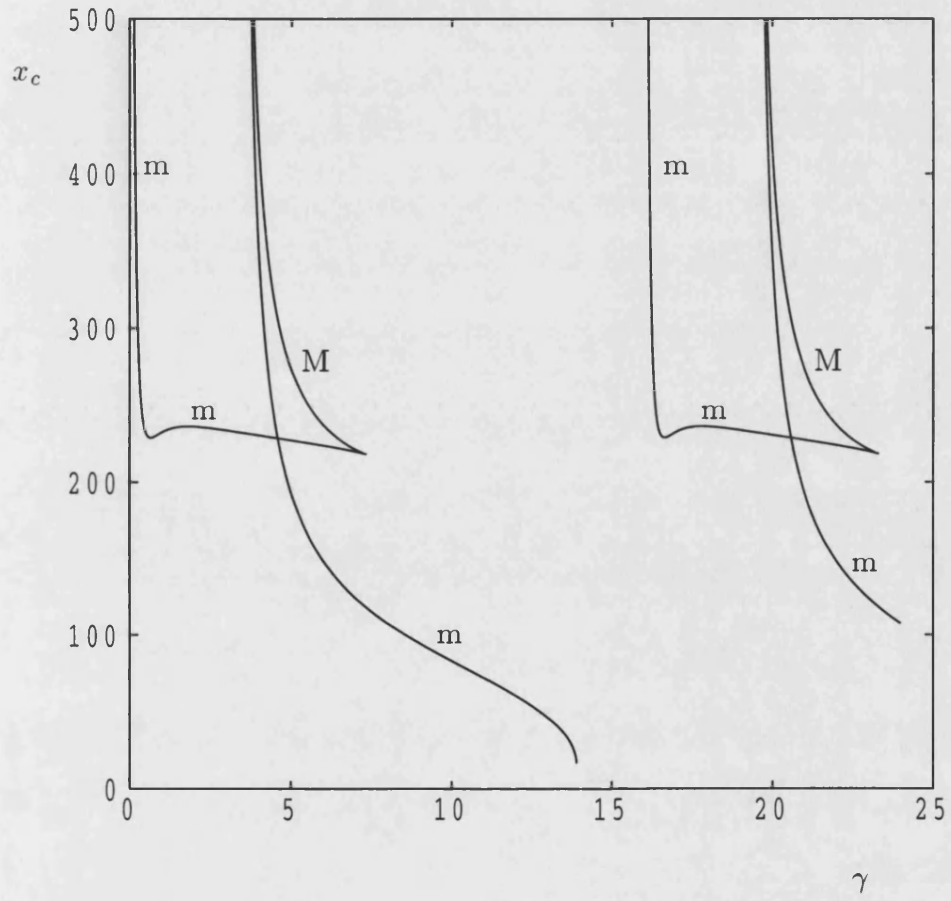

Figure 3.14: Evolution of the critical distances on the neutral curves against $\gamma = 12\alpha/\pi$ for air ($Pr = 0.7$). M denotes a local maximum while m denotes a local minimum.

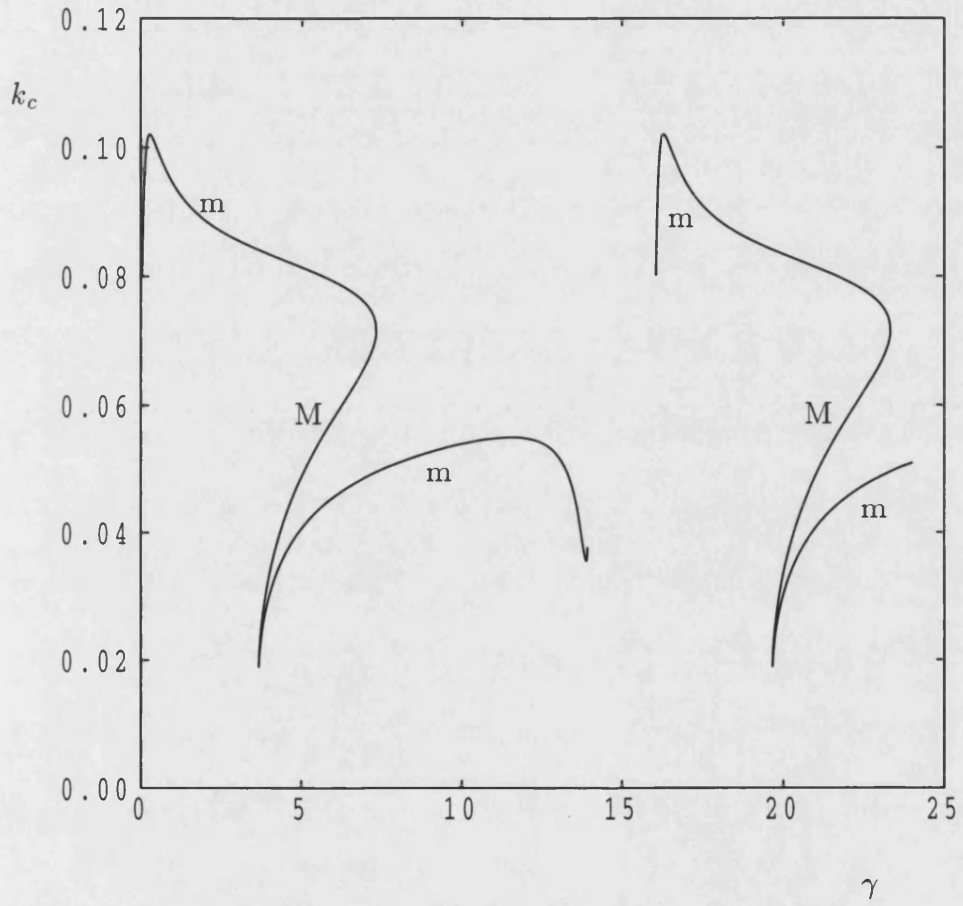

Figure 3.15: Variation of the critical wavenumbers on the neutral curves against $\gamma = 12\alpha/\pi$ for air ($Pr = 0.7$). M denotes a local maximum while m denotes a local minimum.

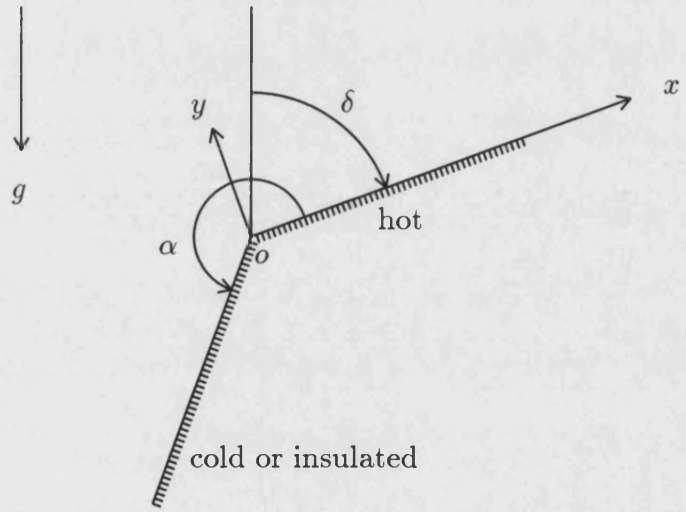

Figure 4.1: A sketch of the flow domain and coordinate system displaying the wedge angle (α) and the inclination angle (δ).

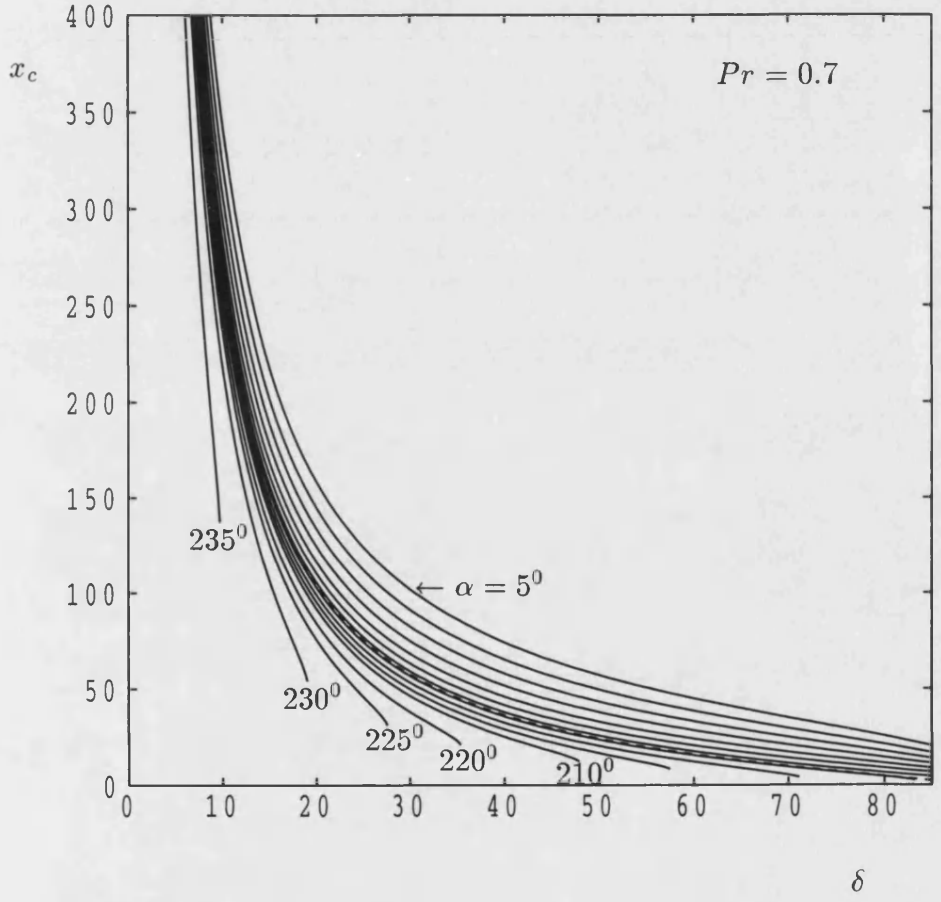

Figure 4.2: The variation of critical distance x_c with inclination angle δ for air ($Pr = 0.7$) and $\alpha = 5^0$ to 235^0; see Figure 4.4 for the choice of α values. The dashed line corresponds to the result for the one-term basic boundary layer solution.

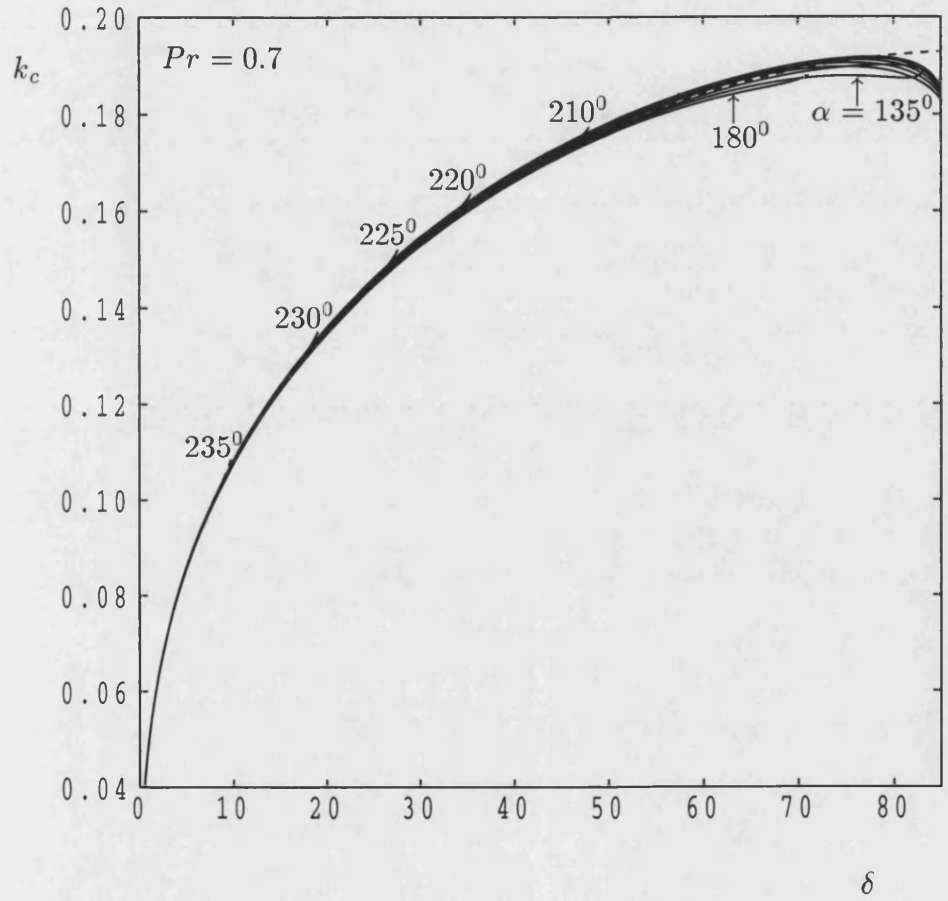

Figure 4.3: The variation of critical wavenumber k_c with inclination angle δ for air ($Pr = 0.7$) and $\alpha = 5^0$ to 235^0. The dashed line corresponds to the result for the one-term basic boundary layer solution.

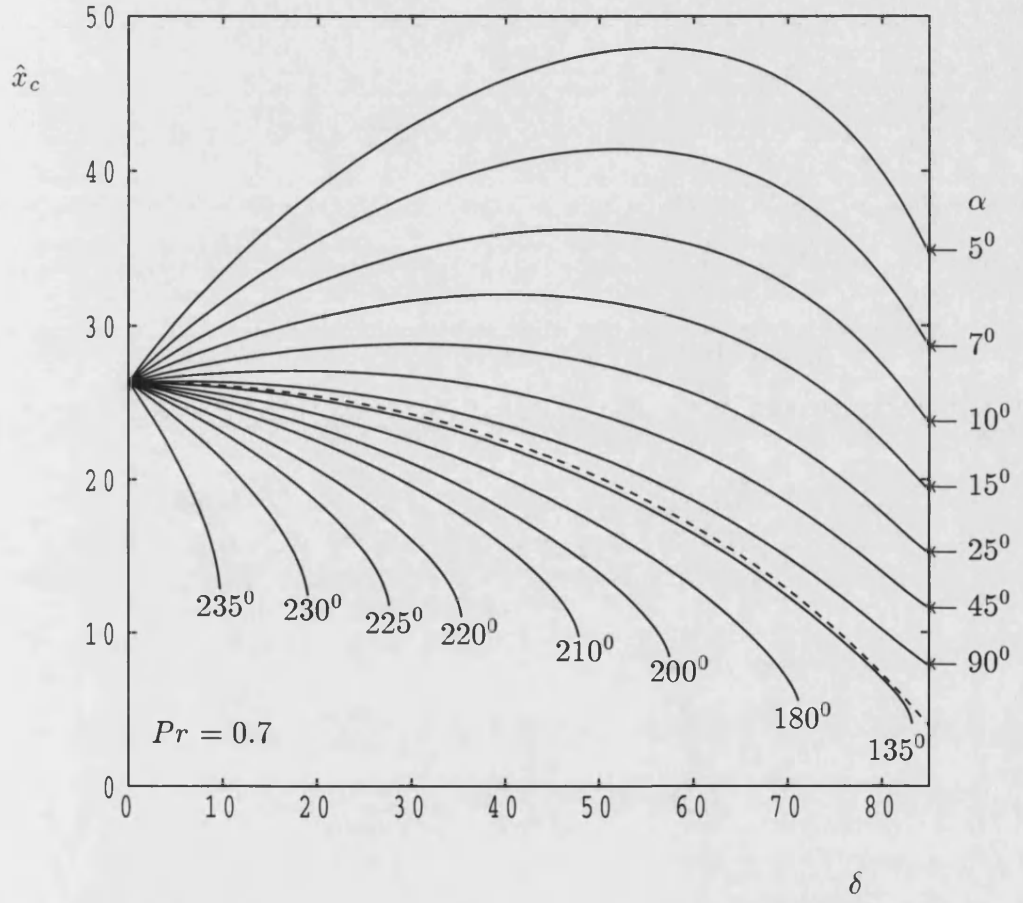

Figure 4.4: The variation of critical distance $\hat{x}_c$ with inclination angle δ for air ($Pr = 0.7$) and $\alpha = 5^0$ to 235^0. The dashed line corresponds to the result for the one-term basic boundary layer solution.

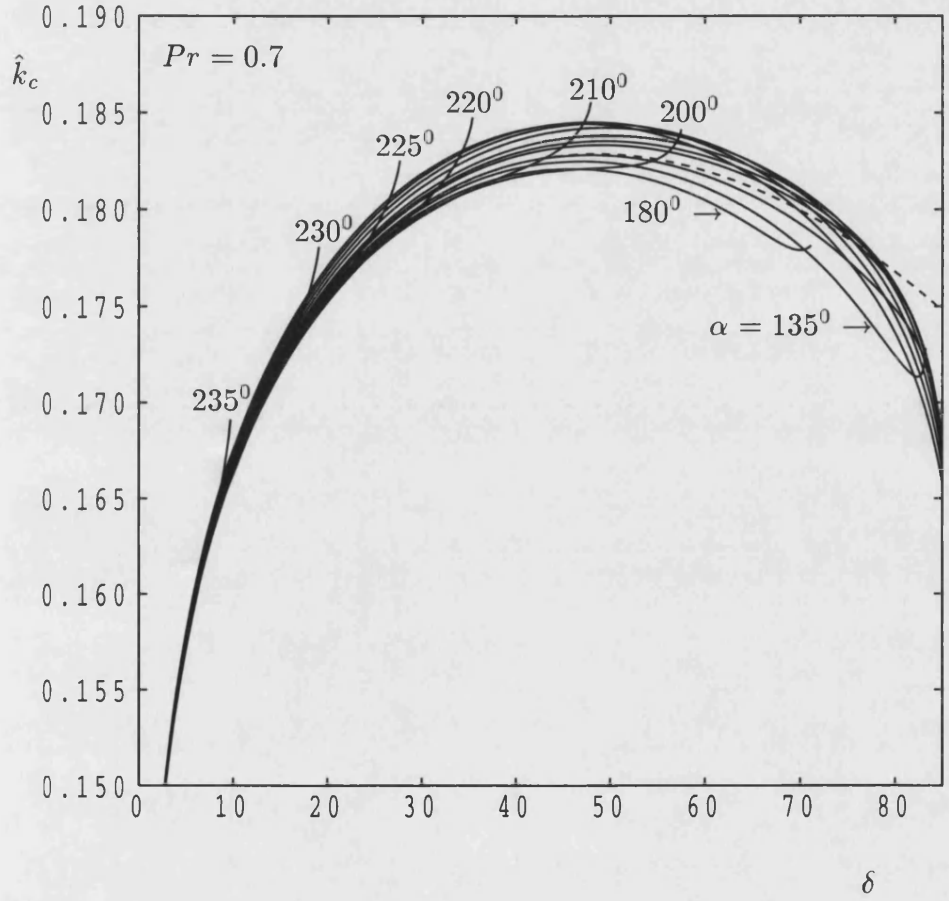

Figure 4.5: The variation of critical wavenumber $\hat{k}_c$ with inclination angle δ for air ($Pr = 0.7$) and $\alpha = 5^0$ to 235^0. The dashed line corresponds to the result for the one-term basic boundary layer solution.

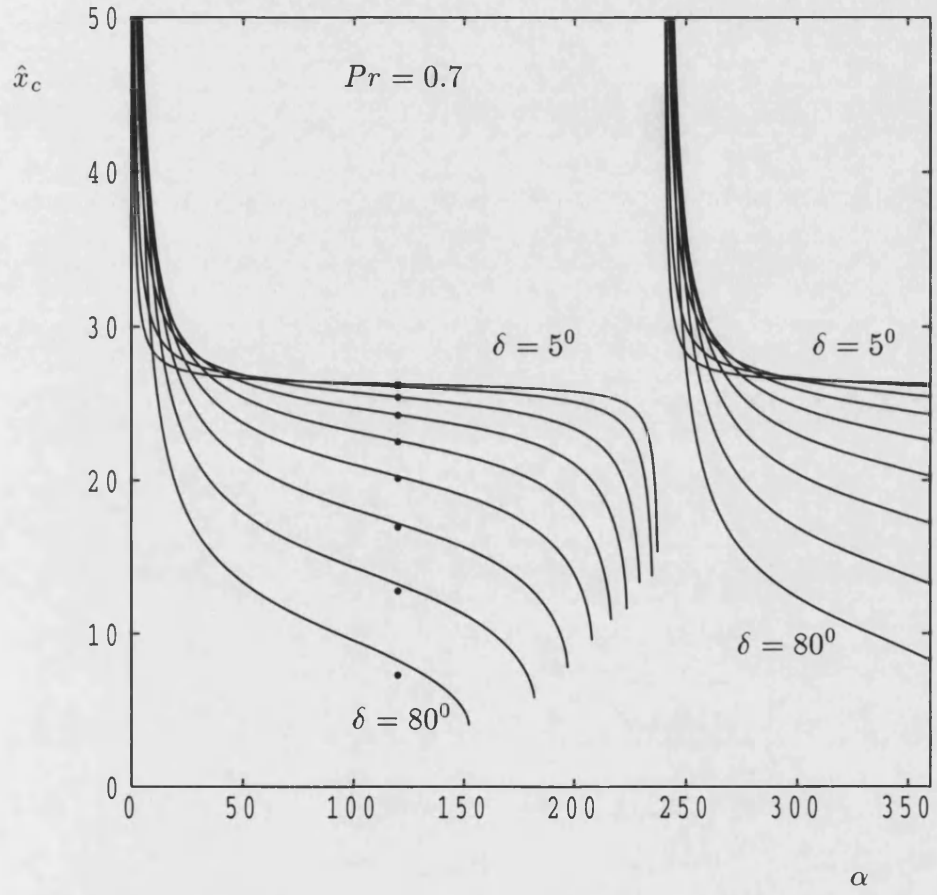

Figure 4.6: The variation of critical distance $\hat{x}_c$ with wedge angle α for air ($Pr = 0.7$) and $\delta = 5^0$, 10^0, 20^0, 30^0, 40^0, 50^0, 60^0, 70^0, 80^0. The symbol, $\bullet$ denotes corresponding results for the one-term basic boundary layer solution.

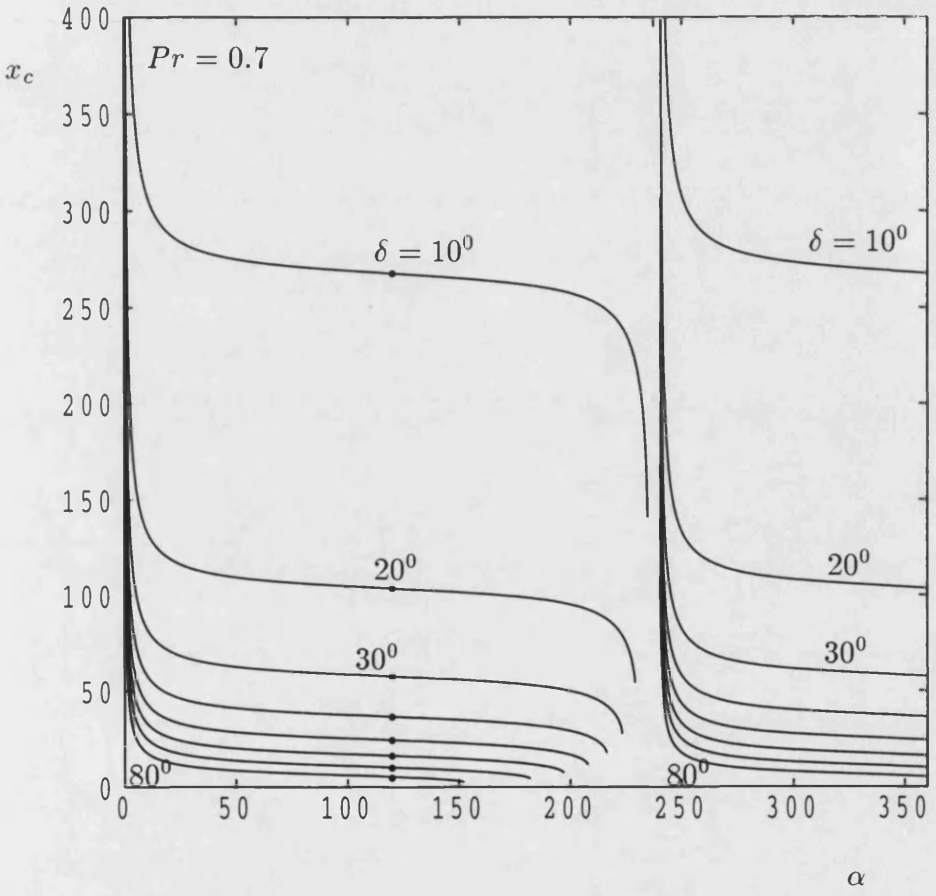

Figure 4.7: The variation of critical distance x_c with wedge angle α for air ($Pr = 0.7$) and $\delta = 10^0$, 20^0, 30^0, 40^0, 50^0, 60^0, 70^0, 80^0. The symbol, • denotes corresponding results for the one-term basic boundary layer solution.

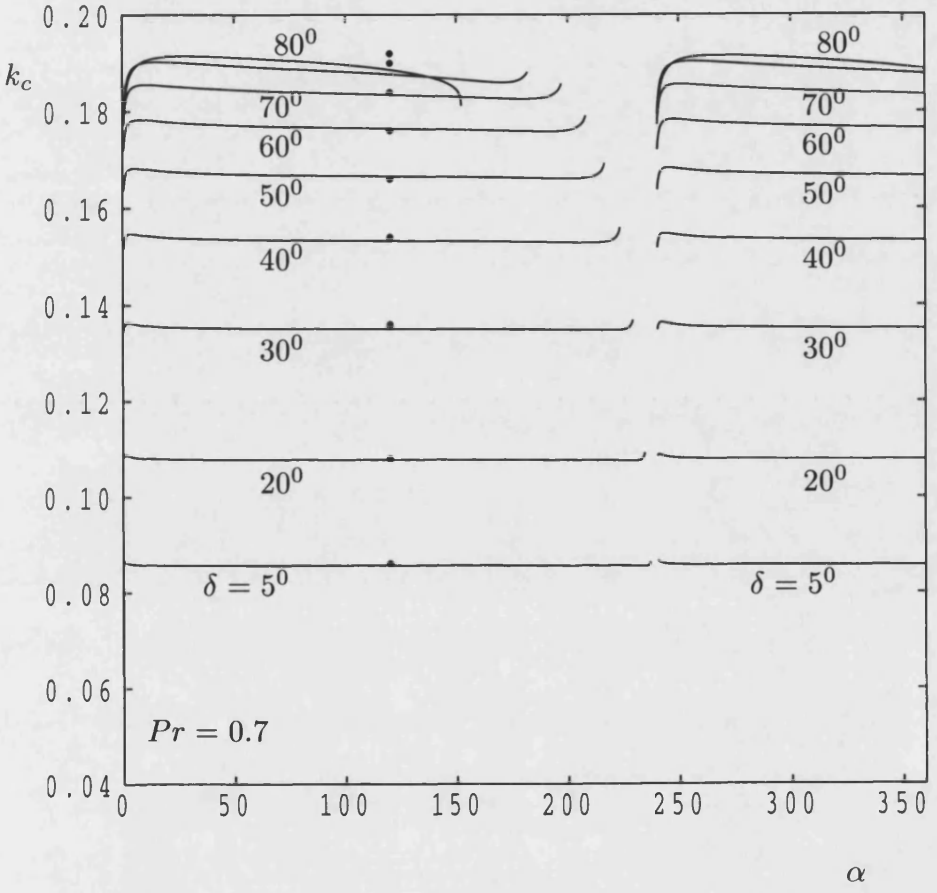

Figure 4.8: The variation of critical wavenumber k_c with wedge angle α for air ($Pr = 0.7$) and $\delta = 5^0$, 10^0, 20^0, 30^0, 40^0, 50^0, 60^0, 70^0, 80^0. The symbol, • denotes corresponding results for the one-term basic boundary layer solution.

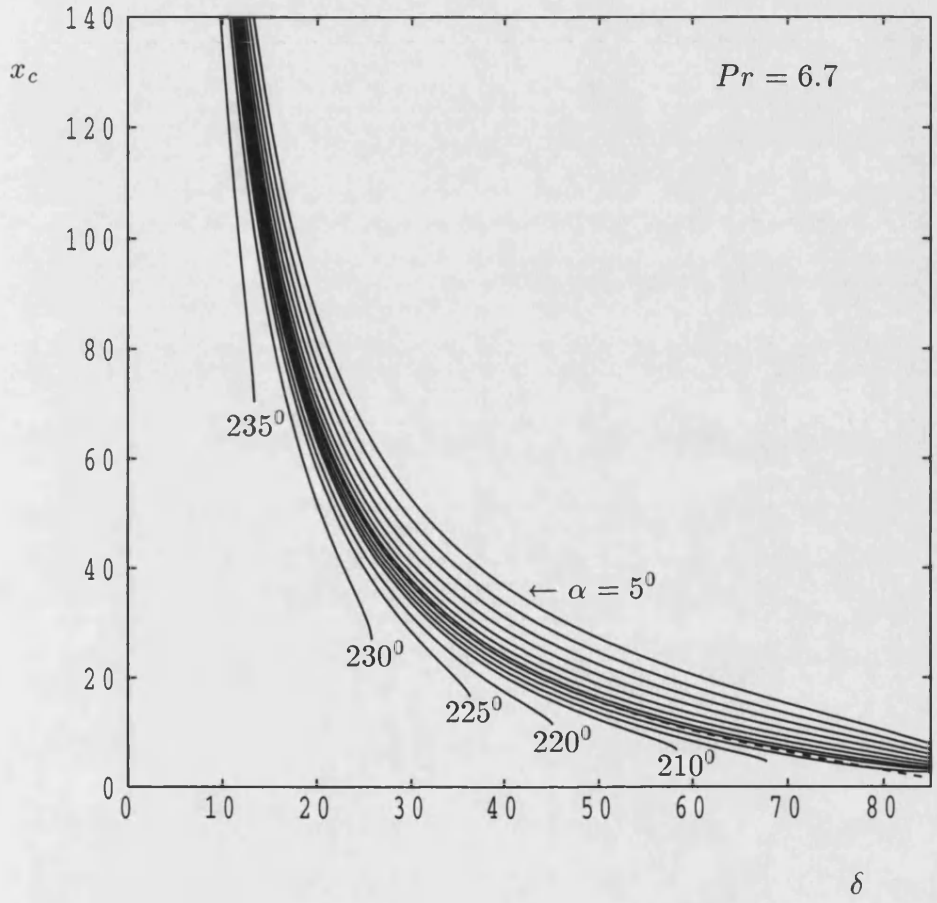

Figure 4.9: The variation of critical distance x_c with inclination angle δ for water ($Pr = 6.7$) and $\alpha = 5^0$ to 235^0; see Figure 4.11 for the choice of α values. The dashed line corresponds to the result for the one-term basic boundary layer solution.

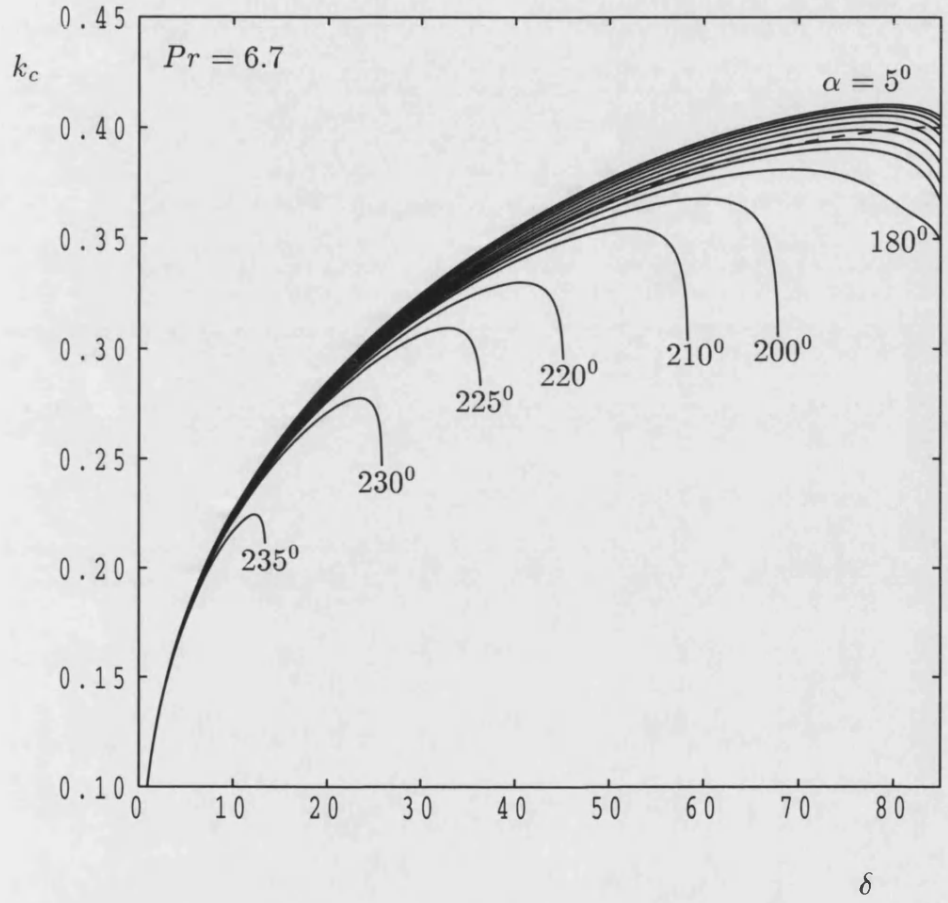

Figure 4.10: The variation of critical wavenumber k_c with inclination angle δ for water ($Pr = 6.7$) and $\alpha = 5^0$ to 235^0. The dashed line corresponds to the result for the one-term basic boundary layer solution.

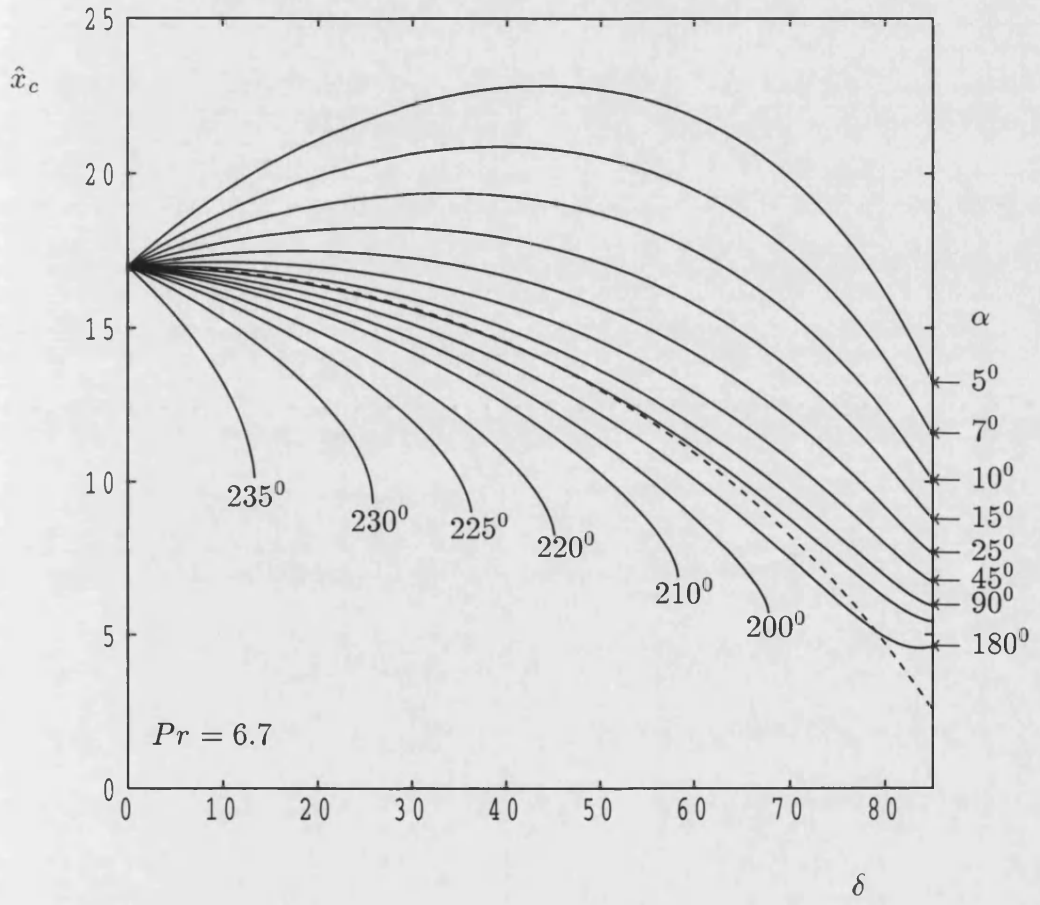

Figure 4.11: The variation of critical distance $\hat{x}_c$ with inclination angle δ for water ($Pr = 6.7$) and $\alpha = 5^0$ to 235^0. The dashed line corresponds to the result for the one-term basic boundary layer solution.

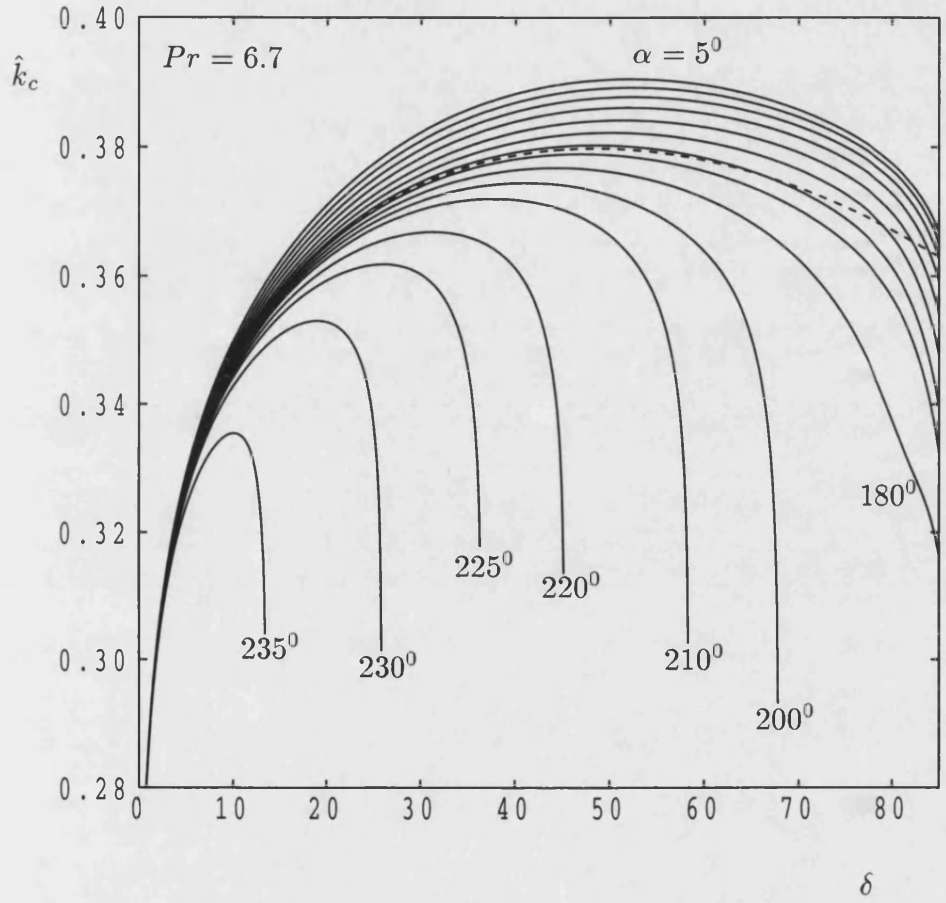

Figure 4.12: The variation of critical wavenumber $\hat{k}_c$ with inclination angle δ for water ($Pr = 6.7$) and $\alpha = 5^0$ to 235^0. The dashed line corresponds to the result for the one-term basic boundary layer solution.

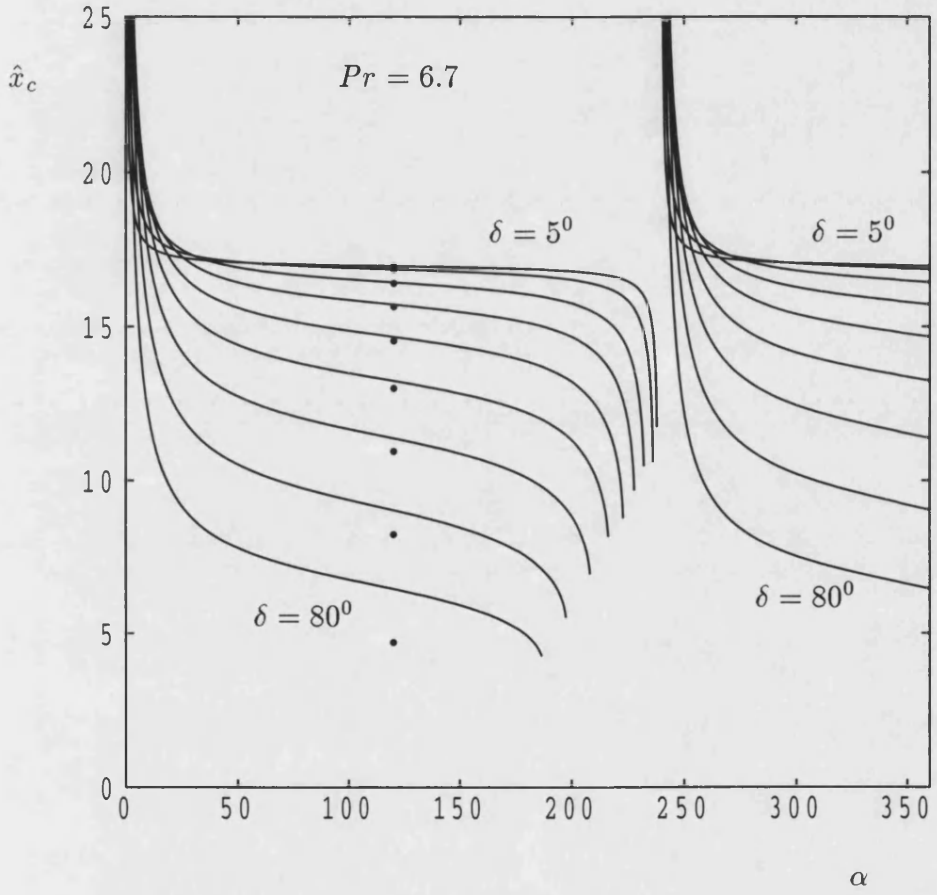

Figure 4.13: The variation of critical distance $\hat{x}_c$ with wedge angle α for water ($Pr = 6.7$) and $\delta = 5^0$, 10^0, 20^0, 30^0, 40^0, 50^0, 60^0, 70^0, 80^0. The symbol, $\bullet$ denotes corresponding results for the one-term basic boundary layer solution.

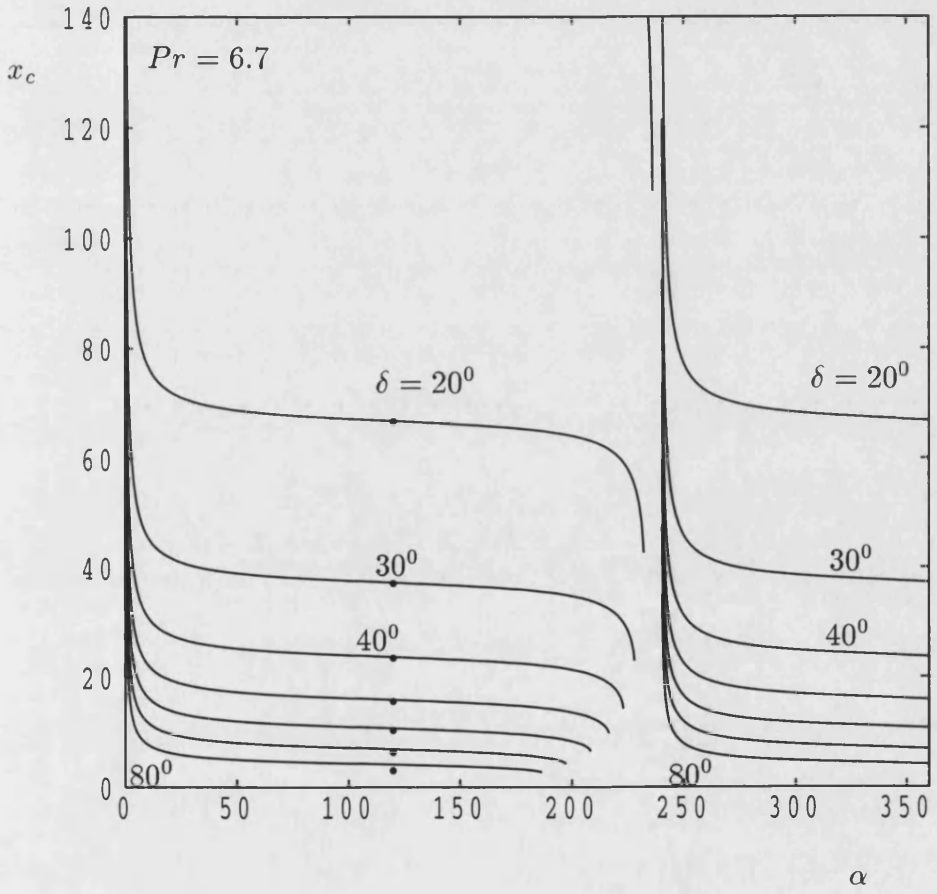

Figure 4.14: The variation of critical distance x_c with wedge angle α for water ($Pr = 6.7$) and $\delta = 20^0$, 30^0, 40^0, 50^0, 60^0, 70^0, 80^0. The symbol, • denotes corresponding results for the one-term basic boundary layer solution.

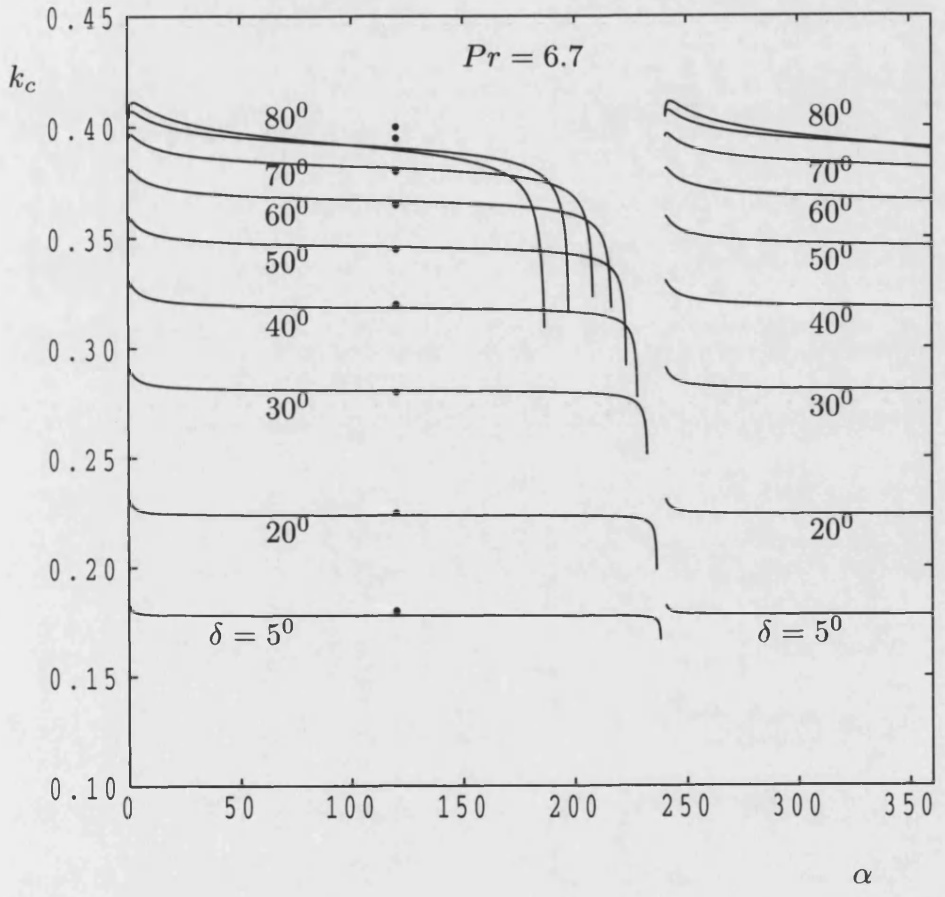

Figure 4.15: The variation of critical wavenumber k_c with wedge angle α for water ($Pr = 6.7$) and $\delta = 5^0$, 10^0, 20^0, 30^0, 40^0, 50^0, 60^0, 70^0, 80^0. The symbol, • denotes corresponding results for the one-term basic boundary layer solution.

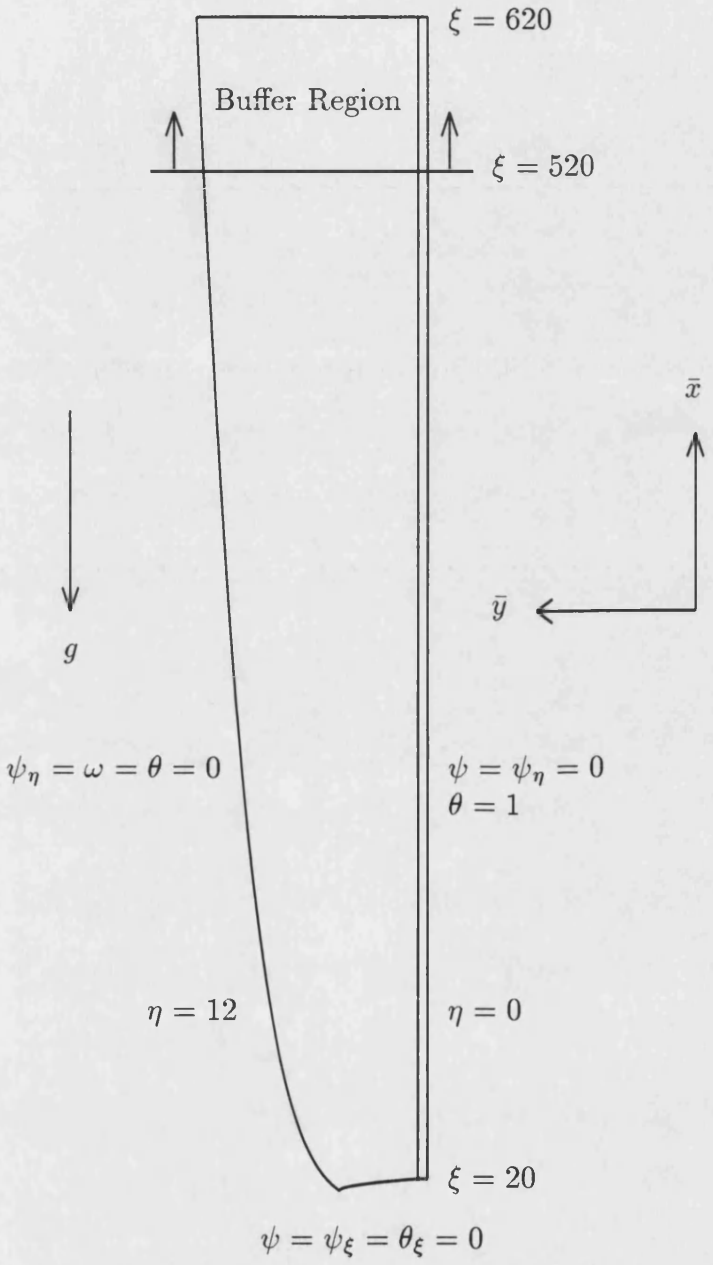

Figure 5.1: A schematic diagram of the flow configuration showing the coordinate directions and boundary conditions for direct numerical simulations.

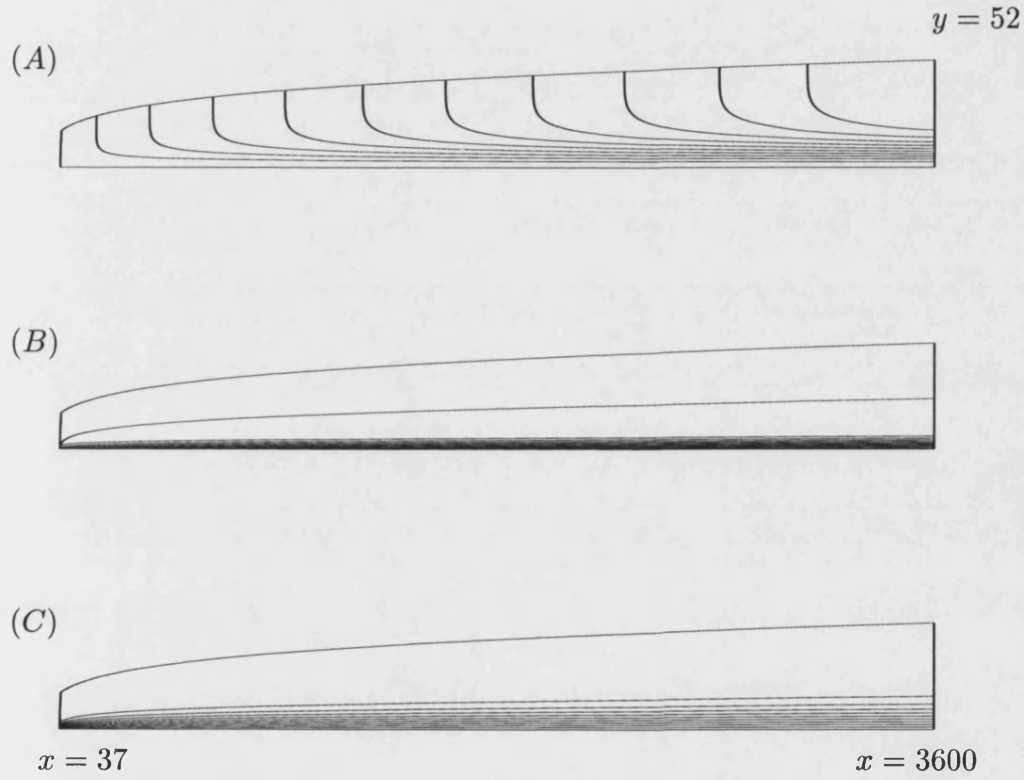

Figure 5.2: Steady state solutions obtained using direct numerical simulations: (A) contours of streamfunction ($\bar{\psi}$), (B) contours of vortices ($\bar{\omega}$), and (C) contours of isotherms ($\bar{\theta}$). In each frame 10 levels of contour are plotted between their maximum and minimum values.

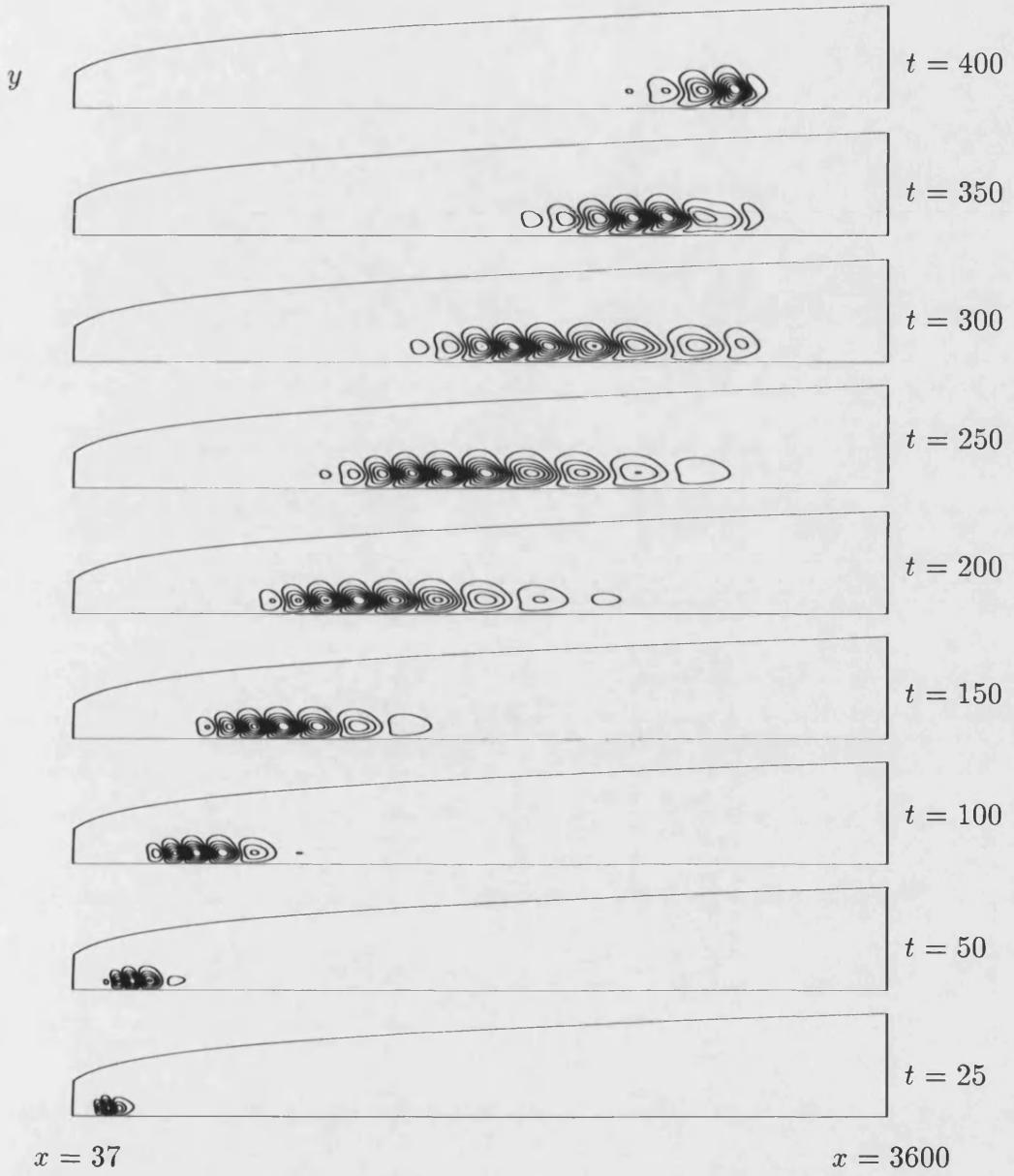

Figure 5.3: Contours of the perturbation isotherms depicting the response of the boundary layer to a point disturbance. Individual frames correspond to the times $t = 25$, 50, 100, 150, 200, 250, 300, 350 and 400. The contour levels in each frame are plotted for the values of $\hat{\theta} = \hat{\theta}_{min} + i\left(\frac{\hat{\theta}_{max} - \hat{\theta}_{min}}{N}\right)$, for $i = 0, 1, 2, \ldots N$ and where $N = 11$.

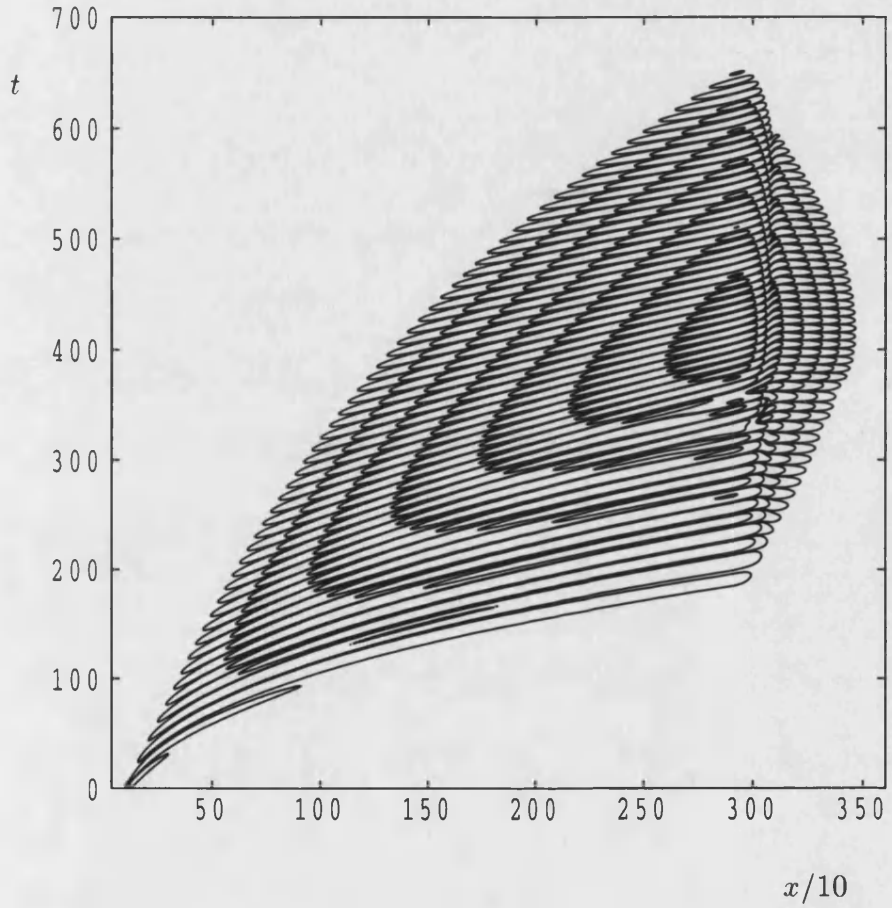

Figure 5.4: Variation of the surface rate of heat transfer with time after the introduction of a point disturbance at $(x, \eta) \simeq (110, 1.5)$. The contour levels at the bottom left hand corner are $\pm 10^{-8}$. Successive bands are at levels of $\pm 10^{-7}$, $\pm 10^{-6}$ to $\pm 10^{-2}$.

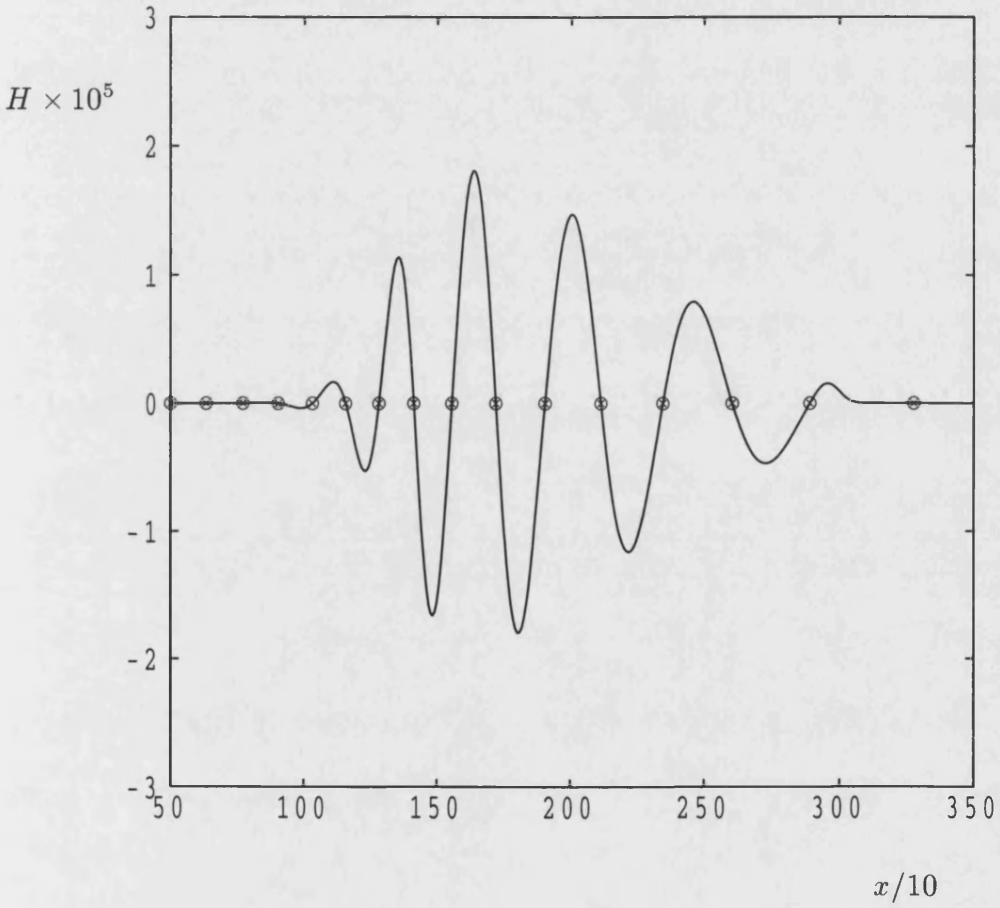

Figure 5.5: The variation with x of the surface rate of heat transfer at time $t = 250$, after introducing a point disturbance.

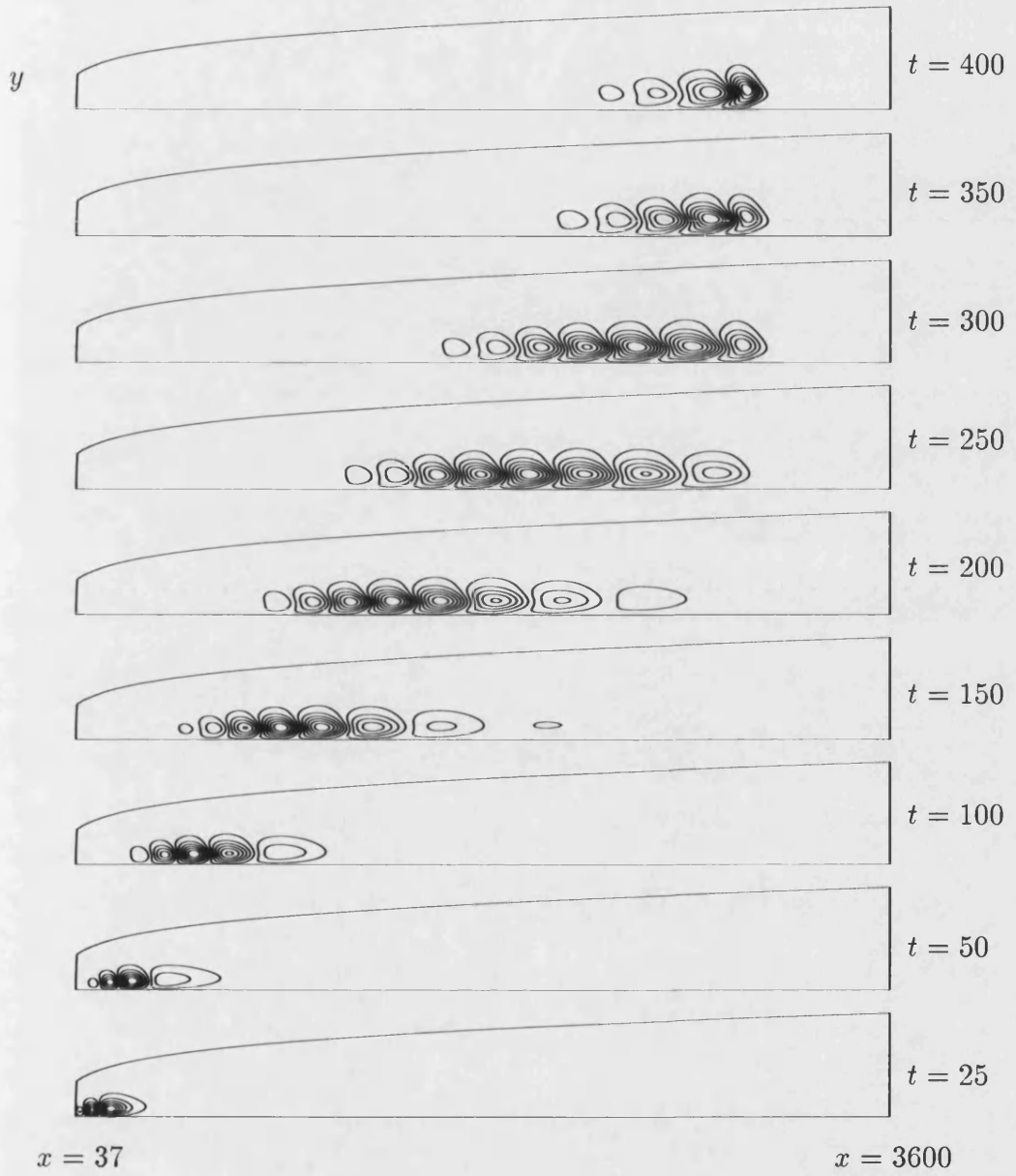

Figure 5.6: Contours of the perturbation isotherms depicting the response of the boundary layer to a distributed disturbance equal to $\eta e^{-\eta} e^{-a(\xi-\xi_0)^2}$ where $a = 0.1$. Individual frames correspond to the times, $t = 25$, 50, 100, 150, 200, 250, 300, 350 and 400. The contour levels in each frame are plotted for the values of $\hat{\theta} = \hat{\theta}_{min} + i\left(\frac{\hat{\theta}_{max} - \hat{\theta}_{min}}{N}\right)$, for $i = 0, 1, 2, \ldots N$ and where $N = 11$.

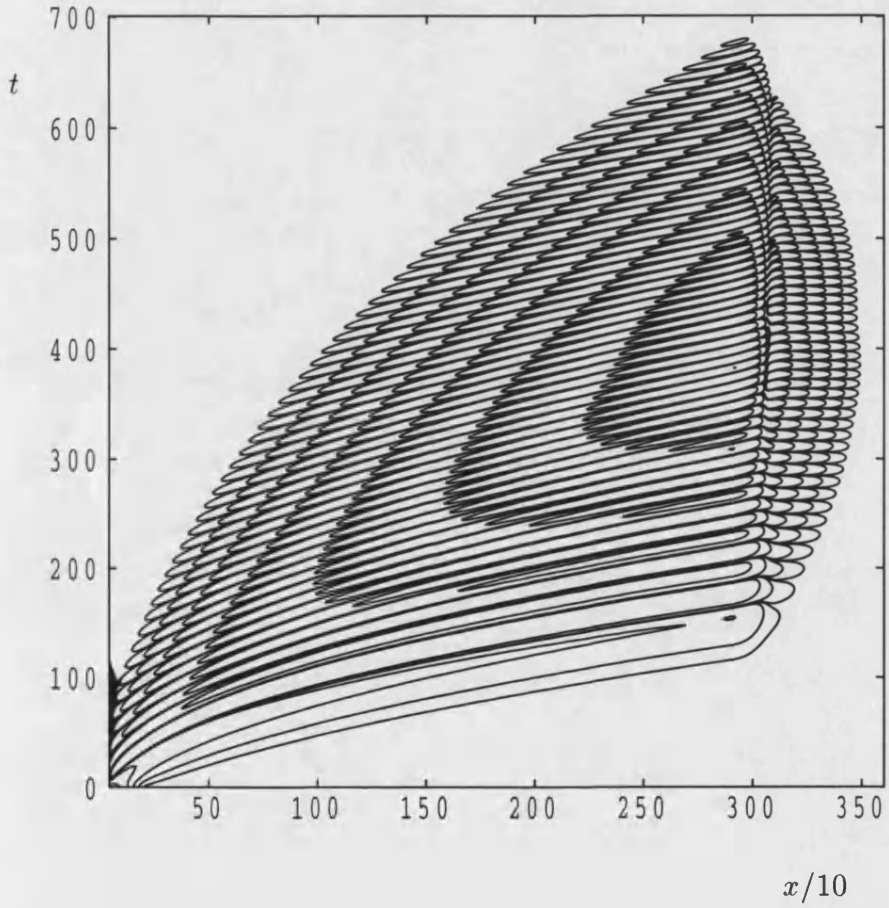

Figure 5.7: Variation of the surface rate of heat transfer with time after the introduction of a distributed disturbance equal to $\eta e^{-\eta} e^{-a(\xi-\xi_0)^2}$ at the leading edge, where $a = 0.1$. The contour levels at the bottom left hand corner are $\pm 10^{-9}$. Successive bands are at levels of $\pm 10^{-8}$, $\pm 10^{-7}$ to $\pm 10^{-3}$.

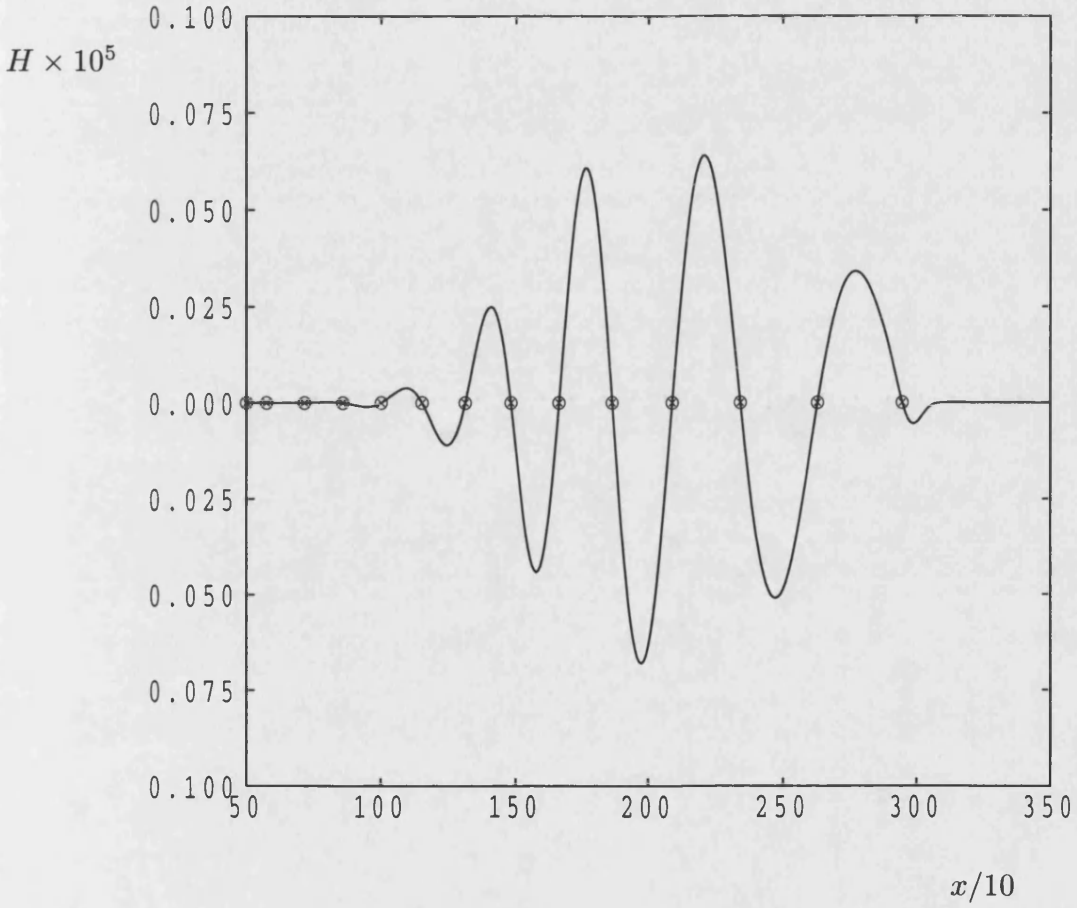

Figure 5.8: The variation with x of the surface rate of heat transfer at time $t = 250$, after introducing a distributed disturbance equal to $\eta e^{-\eta} e^{-a(\xi-\xi_0)^2}$.

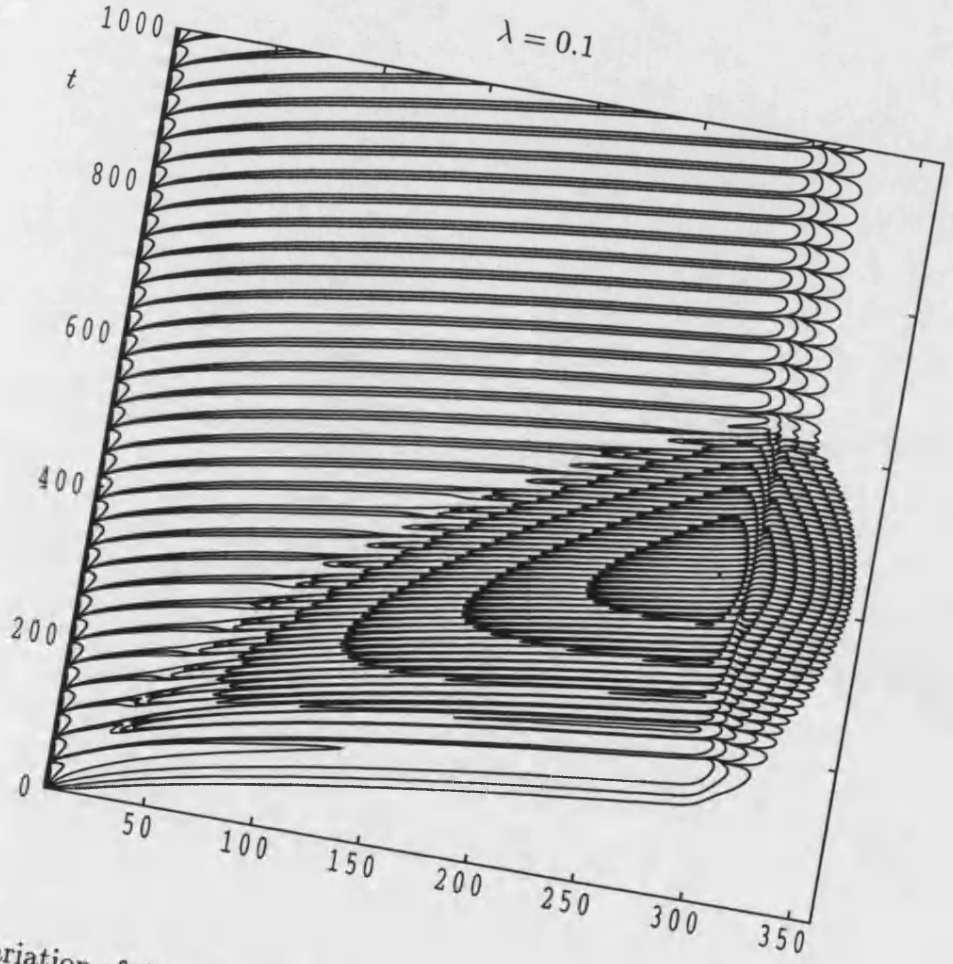

Figure 5.9: Variation of the surface rate of heat transfer with time due to a time-periodic disturbance equal to $e^{-a(\xi-\xi_0)^2}\sin(\lambda t)$, where the temporal frequency is $\lambda = 0.1$ and the scaling factor is $a = 0.1$.

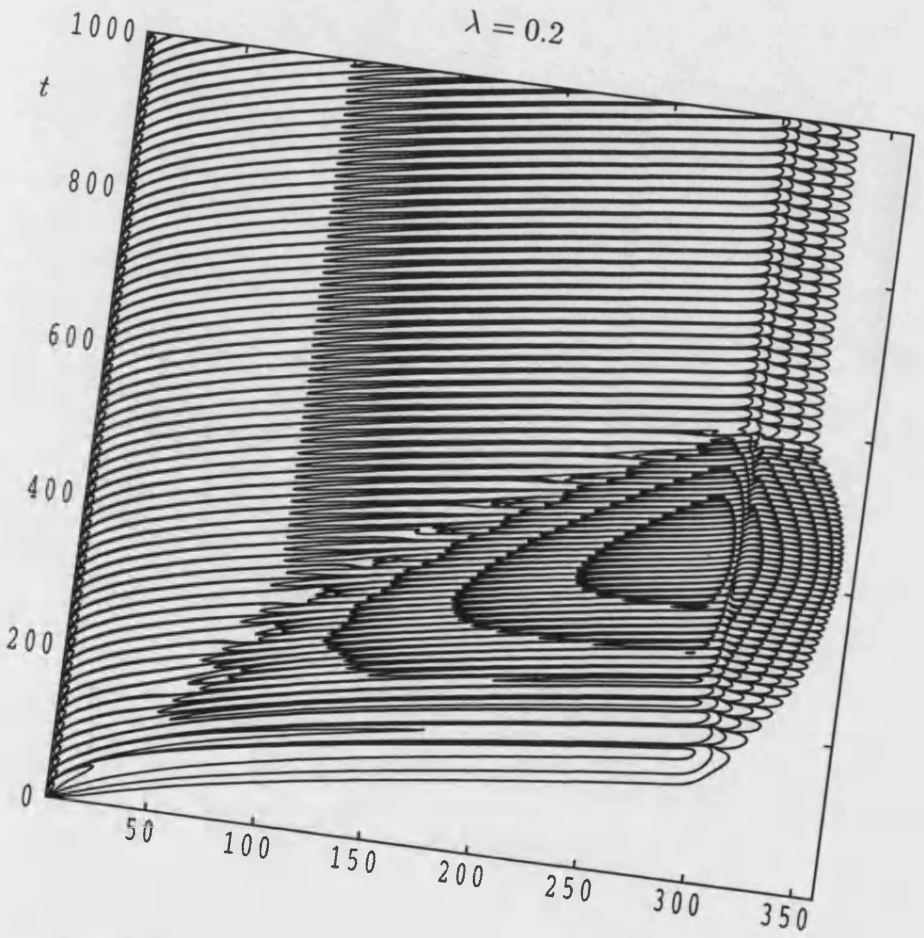

Figure 5.10: Variation of the surface rate of heat transfer with time due to a time-periodic disturbance equal to $e^{-a(\xi-\xi_0)^2}\sin(\lambda t)$, where the temporal frequency is $\lambda = 0.2$ and the scaling factor is $a = 0.1$.

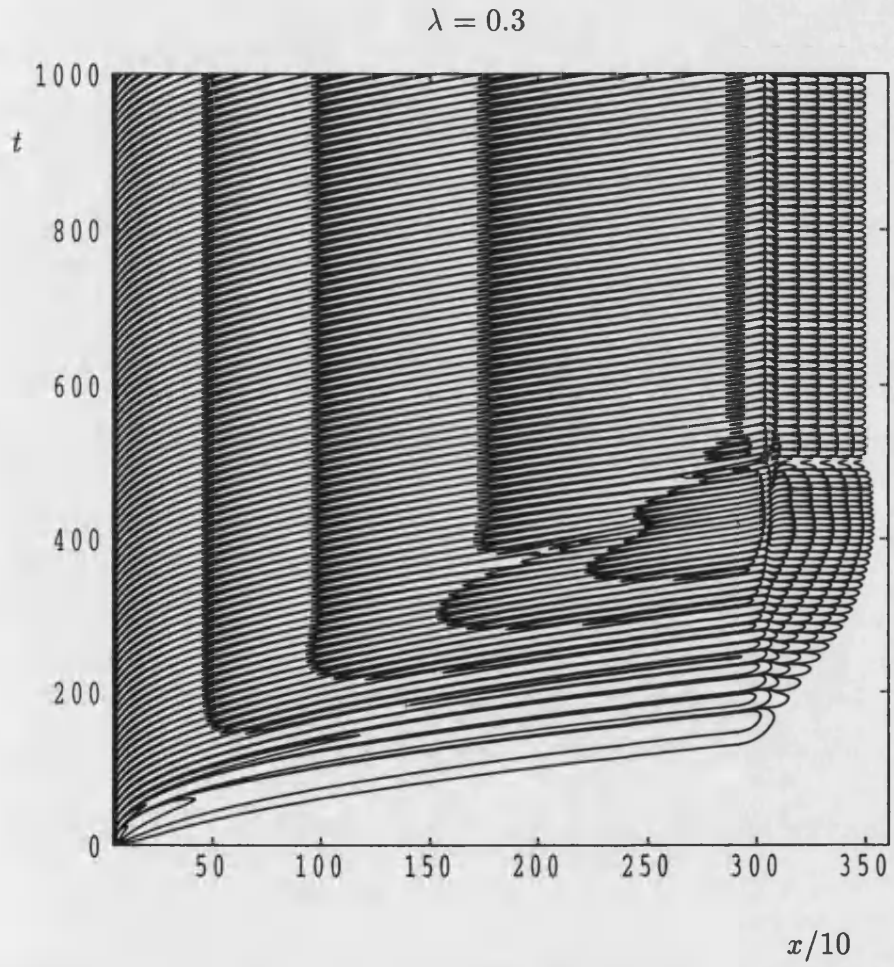

Figure 5.11: Variation of the surface rate of heat transfer with time due to a time-periodic disturbance equal to $e^{-a(\xi-\xi_0)^2}\sin(\lambda t)$, where the temporal frequency is $\lambda = 0.3$ and the scaling factor is $a = 0.1$.

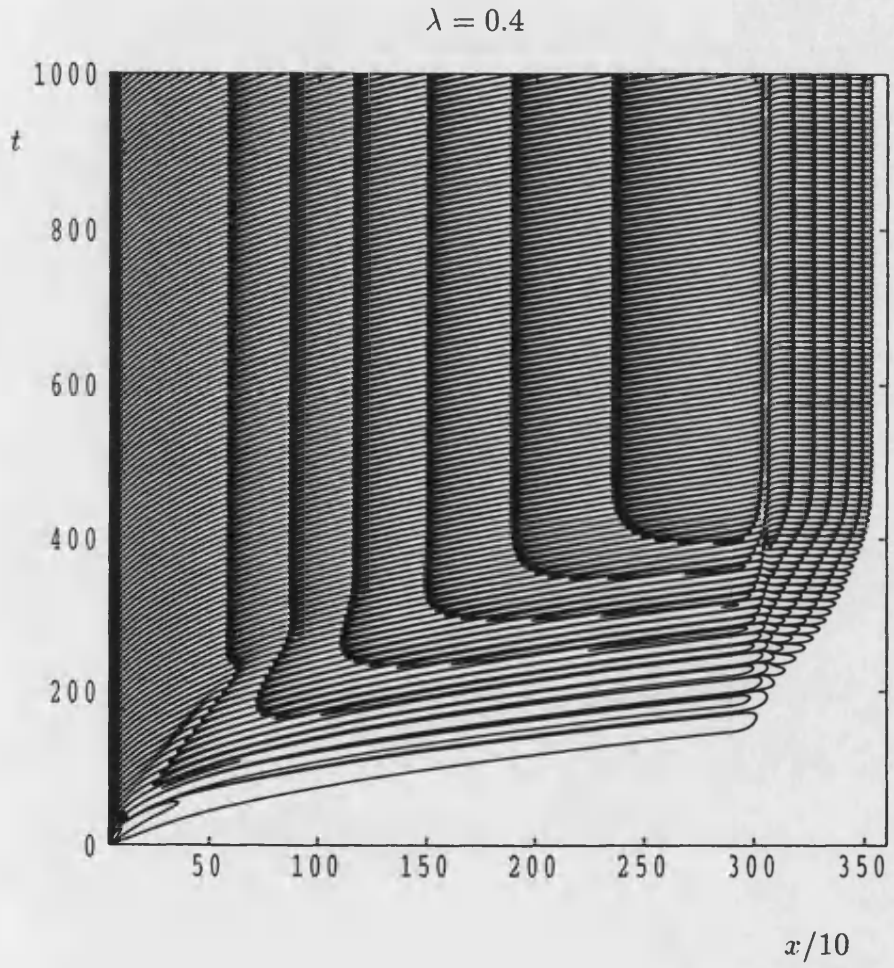

Figure 5.12: Variation of the surface rate of heat transfer with time due to a time-periodic disturbance equal to $e^{-a(\xi-\xi_0)^2}\sin(\lambda t)$, where the temporal frequency is $\lambda = 0.4$ and the scaling factor is $a = 0.1$.

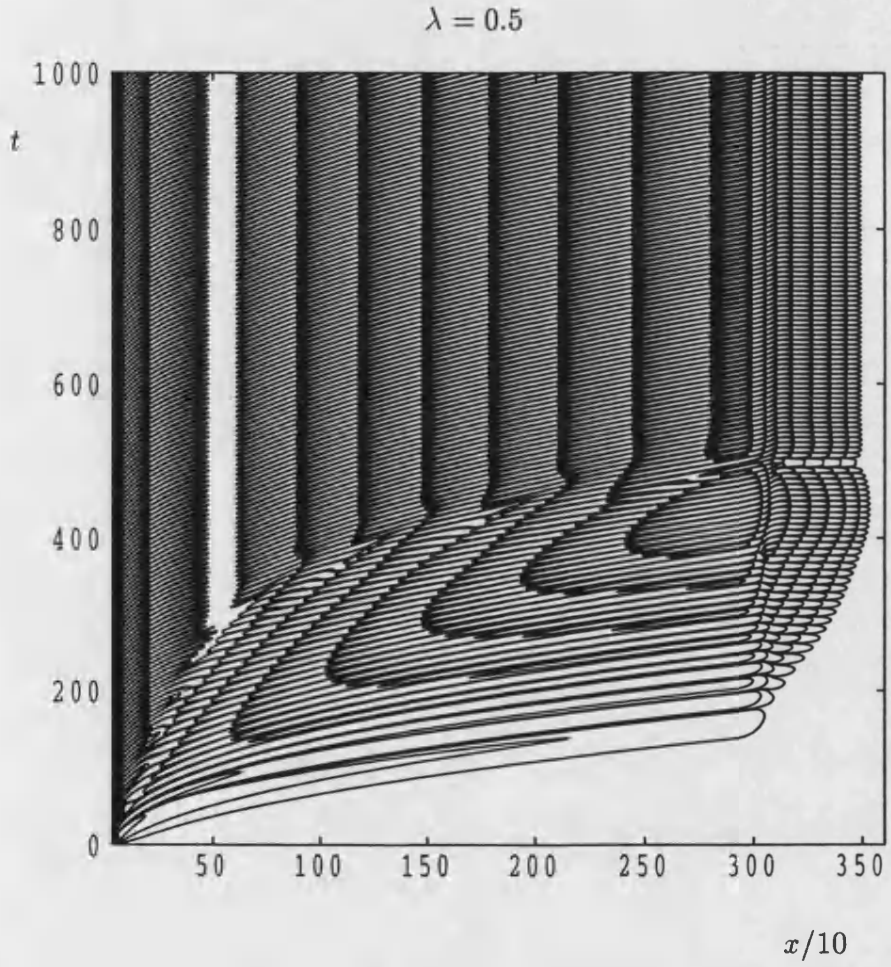

Figure 5.13: Variation of the surface rate of heat transfer with time due to a time-periodic disturbance equal to $e^{-a(\xi-\xi_0)^2}\sin(\lambda t)$, where the temporal frequency is $\lambda = 0.5$ and the scaling factor is $a = 0.1$.

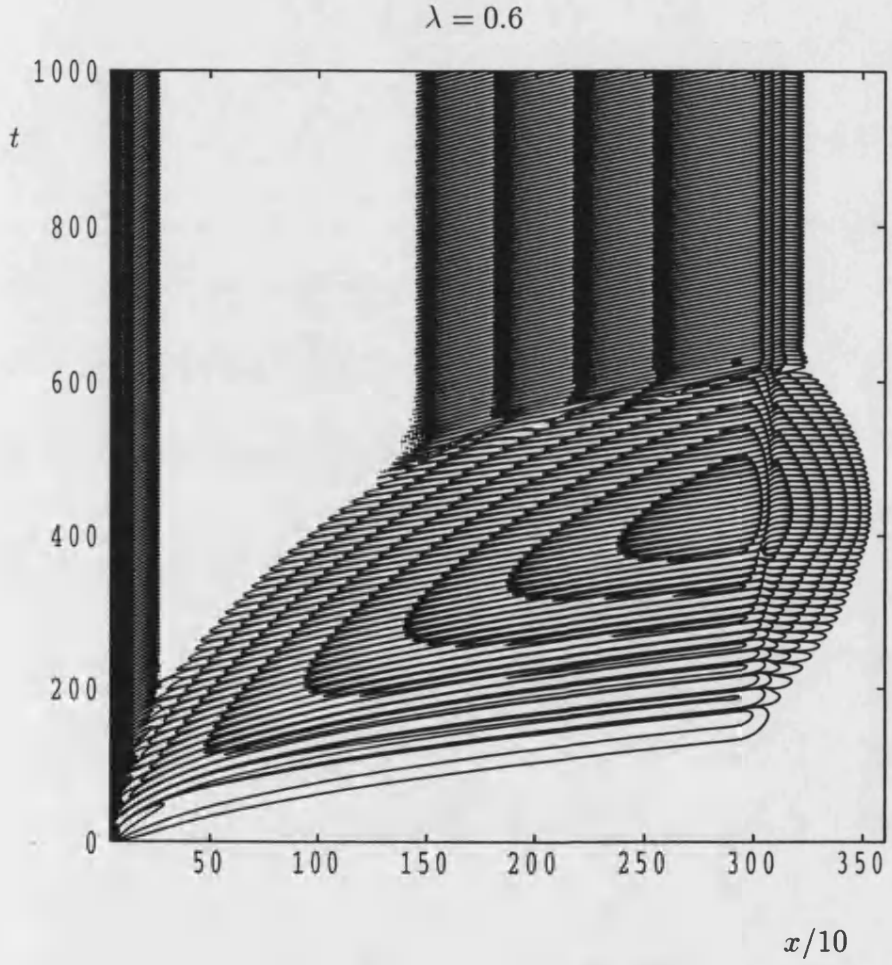

Figure 5.14: Variation of the surface rate of heat transfer with time due to a time-periodic disturbance equal to $e^{-a(\xi-\xi_0)^2}\sin(\lambda t)$, where the temporal frequency is $\lambda = 0.6$ and the scaling factor is $a = 0.1$.

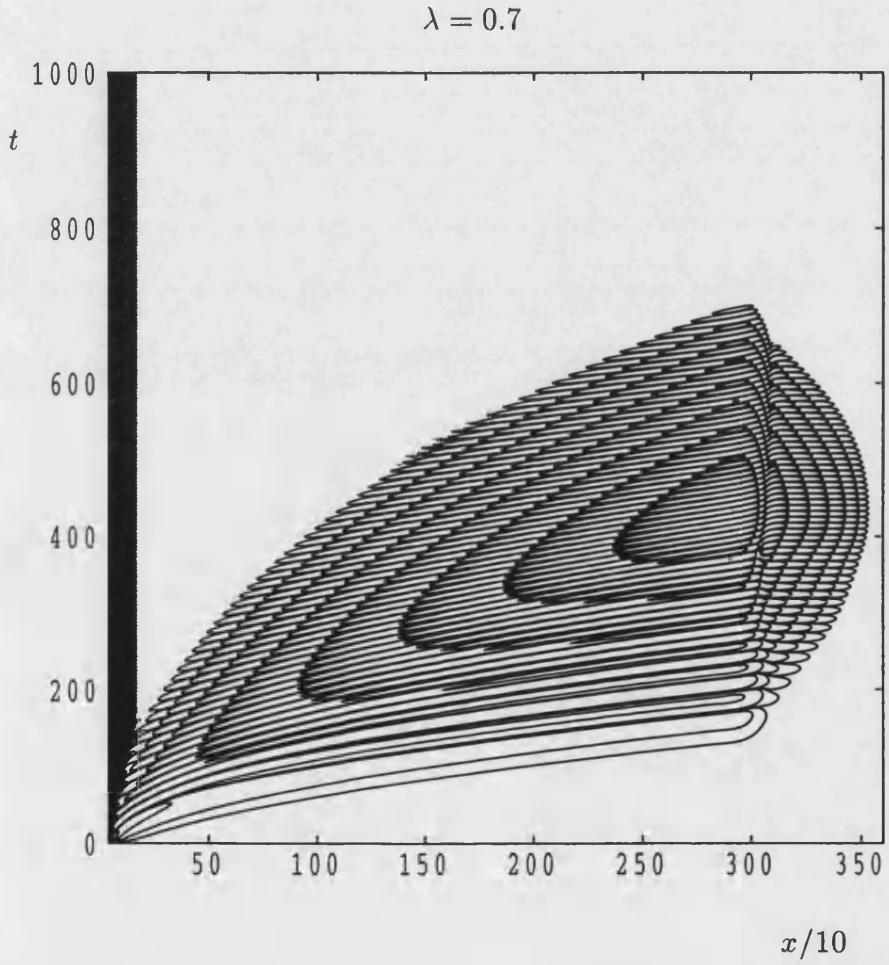

Figure 5.15: Variation of the surface rate of heat transfer with time due to a time-periodic disturbance equal to $e^{-a(\xi-\xi_0)^2}\sin(\lambda t)$, where the temporal frequency is $\lambda = 0.7$ and the scaling factor is $a = 0.1$.

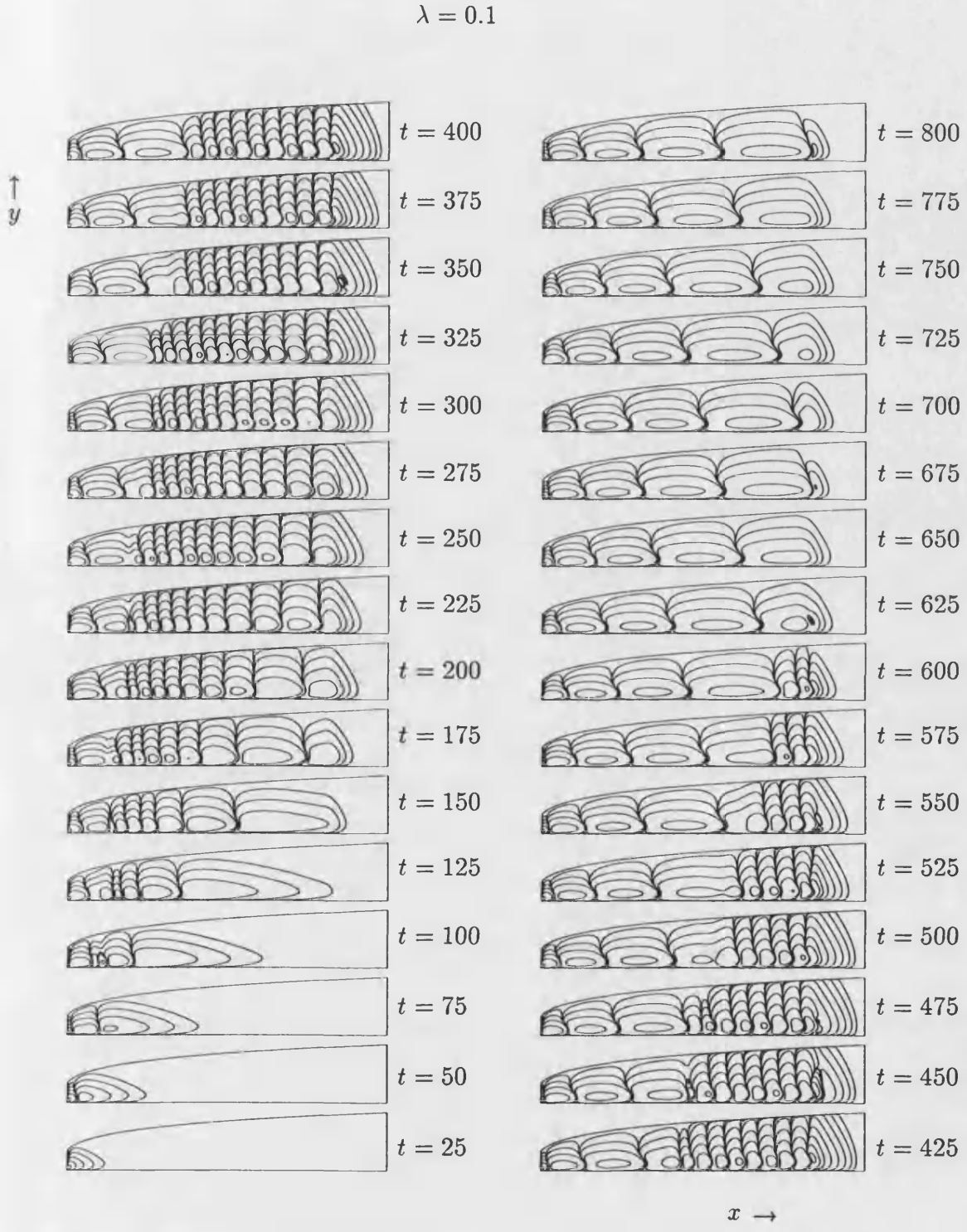

Figure 5.16: Contours of the perturbation isotherms depicting the response to a time periodic disturbance. Individual frames correspond to times, $t = 25$, 50, 75 ,... 800, where $\lambda = 0.1$.

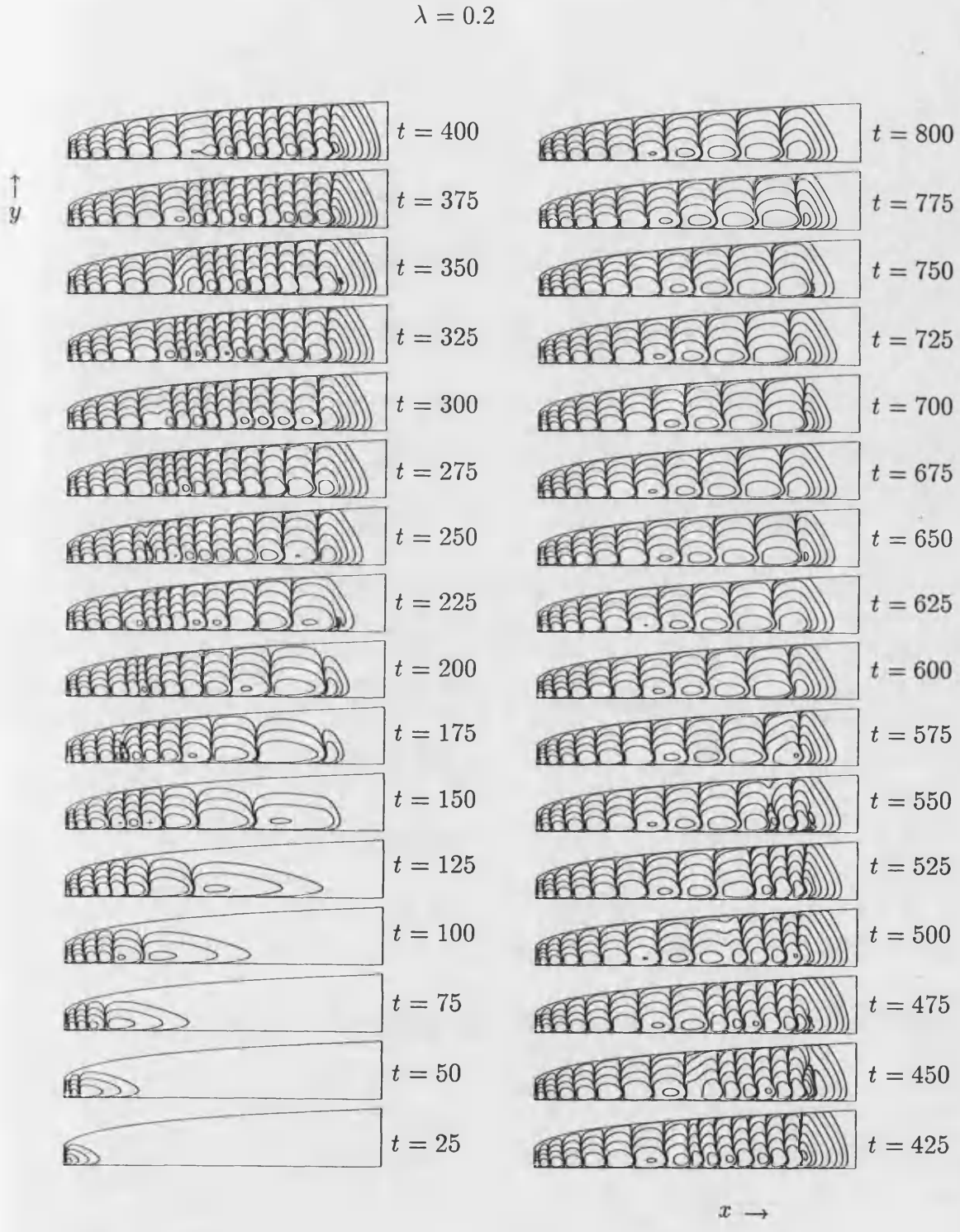

Figure 5.17: Contours of the perturbation isotherms depicting the response to a time periodic disturbance. Individual frames correspond to times, $t = 25$, 50, 75 ,... 800, where $\lambda = 0.2$.

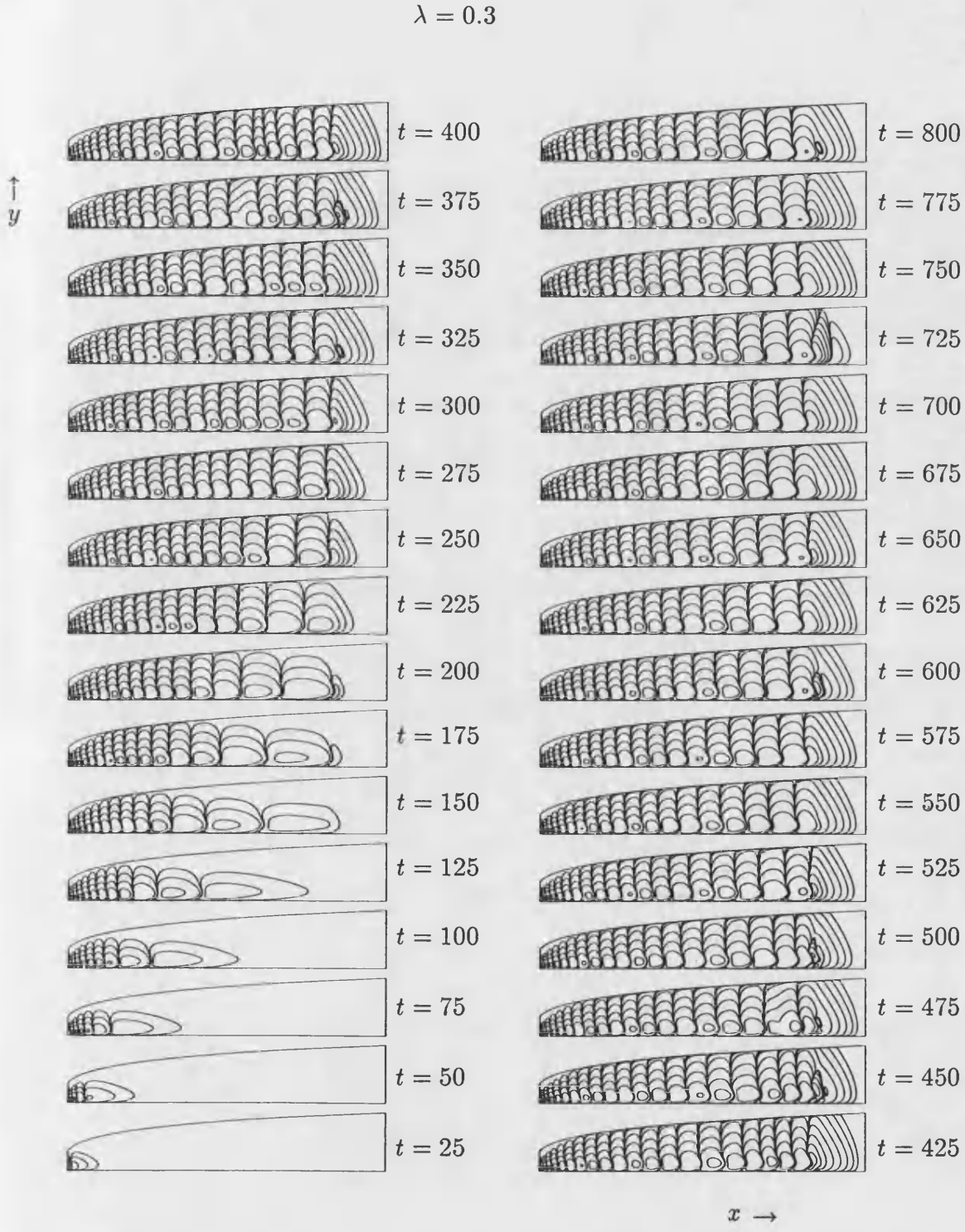

Figure 5.18: Contours of the perturbation isotherms depicting the response to a time periodic disturbance. Individual frames correspond to times, $t = 25$, 50, 75 ,... 800, where $\lambda = 0.3$.

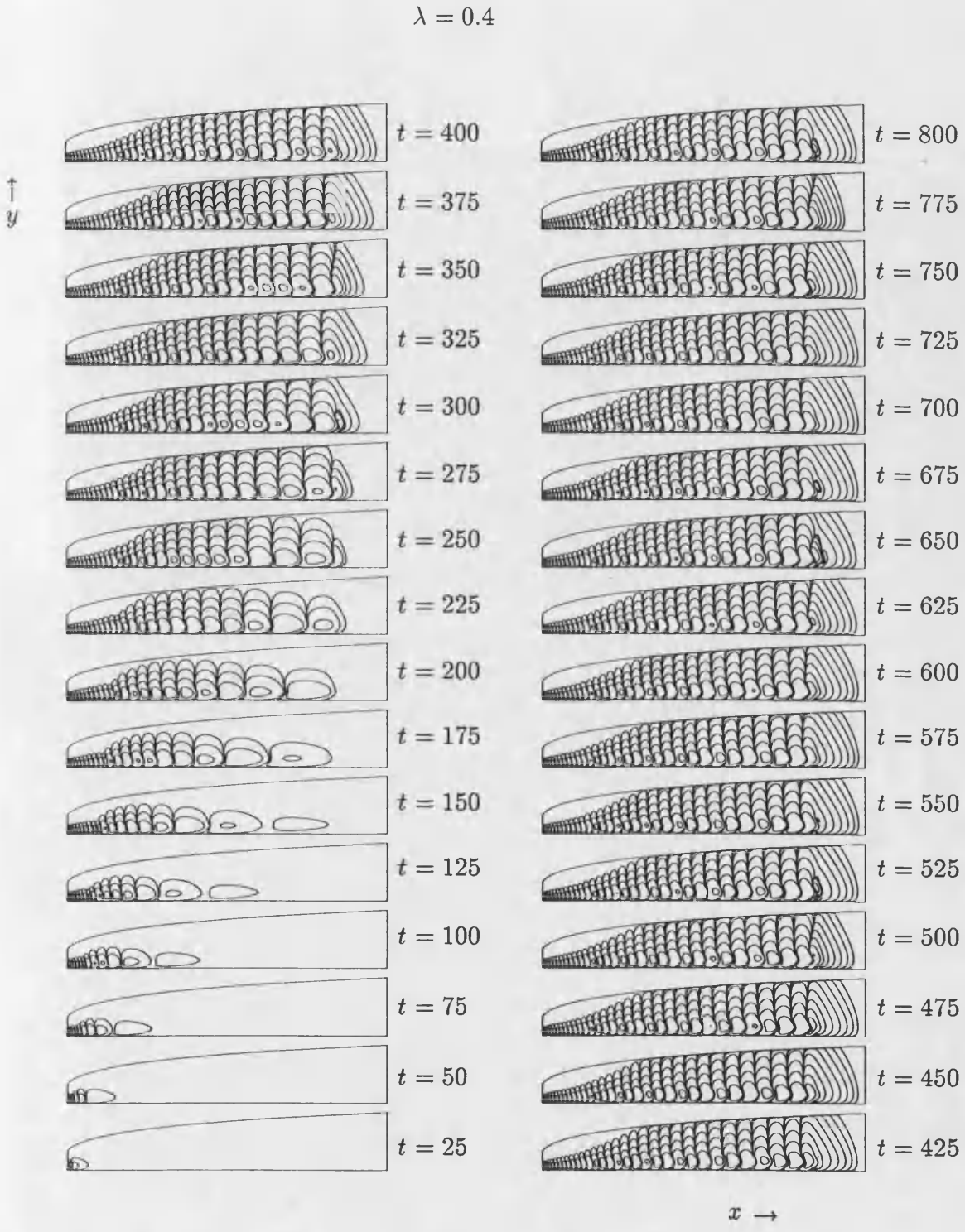

Figure 5.19: Contours of the perturbation isotherms depicting the response to a time periodic disturbance. Individual frames correspond to times, $t = 25$, 50, 75 ,... 800, where $\lambda = 0.4$.

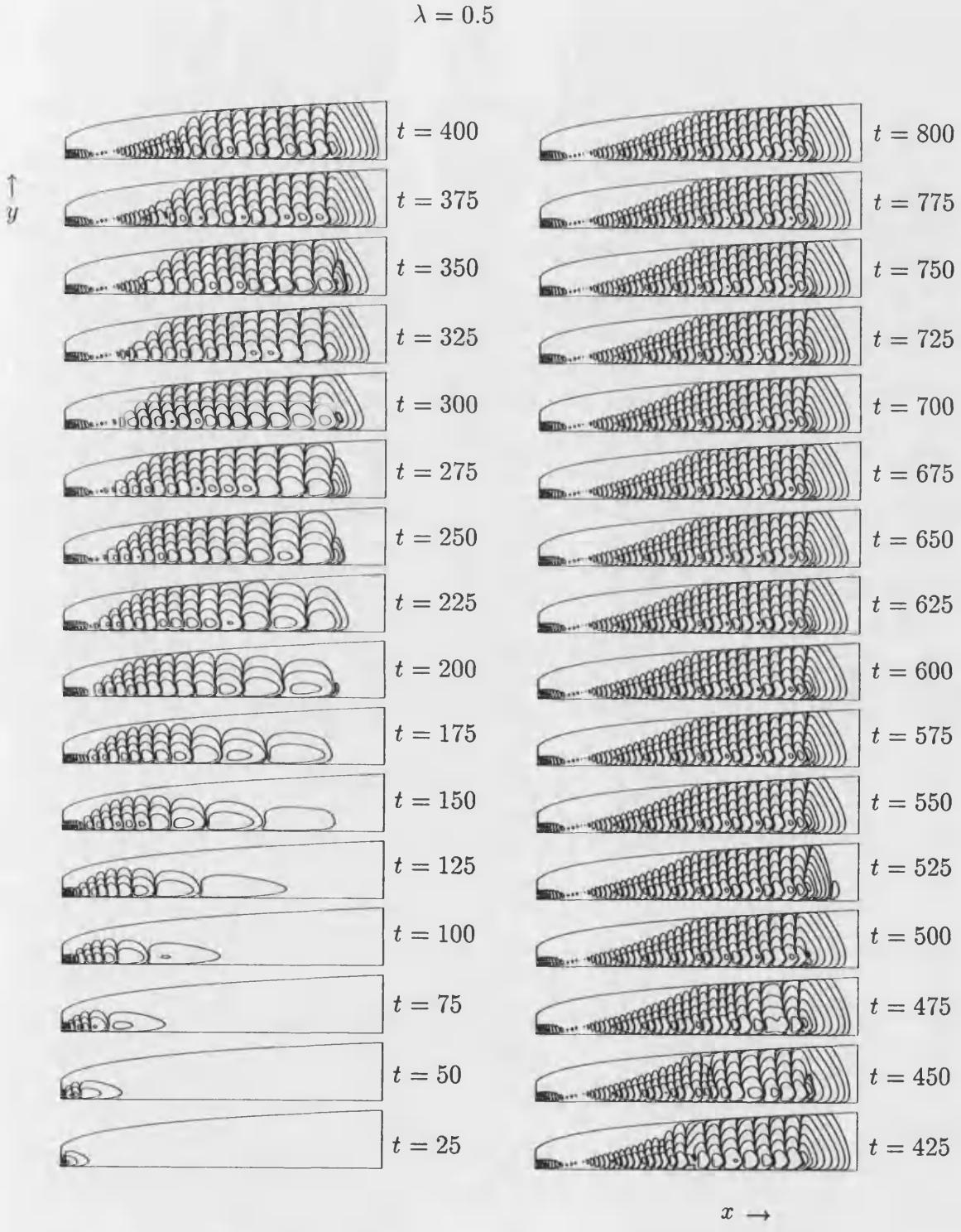

Figure 5.20: Contours of the perturbation isotherms depicting the response to a time periodic disturbance. Individual frames correspond to times, $t = 25$, 50, 75 ,... 800, where $\lambda = 0.5$.

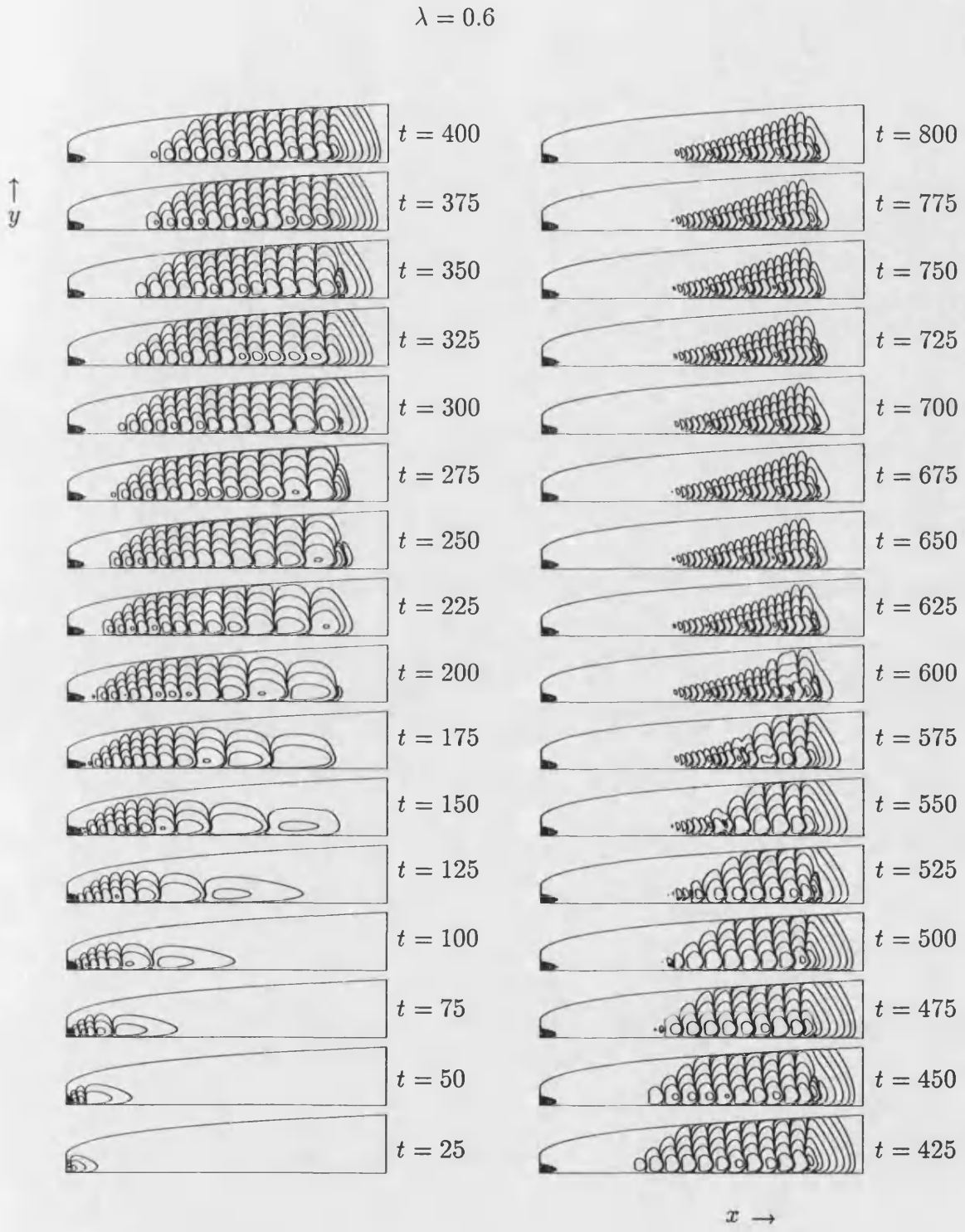

Figure 5.21: Contours of the perturbation isotherms depicting the response to a time periodic disturbance. Individual frames correspond to times, $t = 25$, 50, 75 ,... 800, where $\lambda = 0.6$.

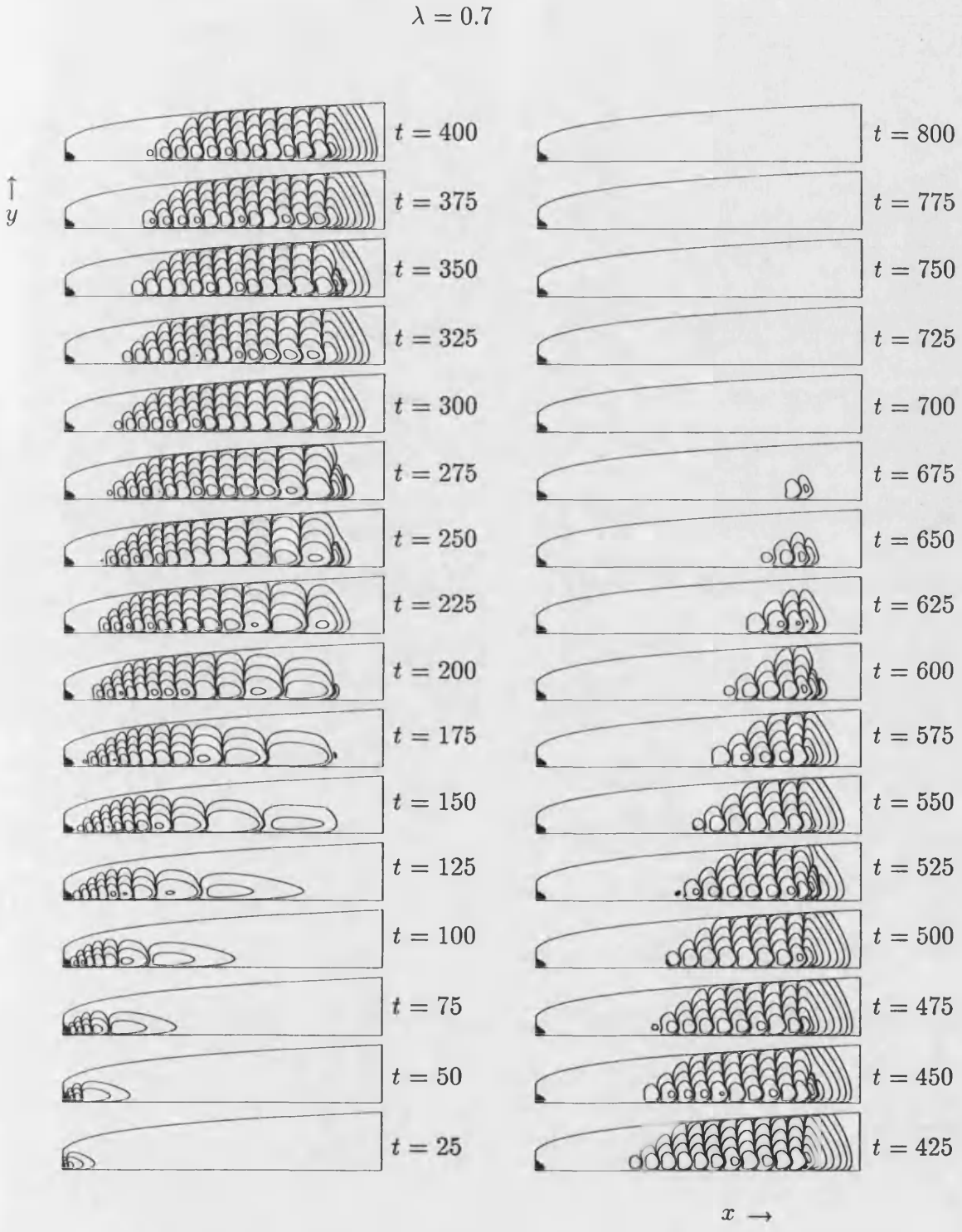

Figure 5.22: Contours of the perturbation isotherms depicting the response to a time periodic disturbance. Individual frames correspond to times, $t = 25$, 50, 75 ,... 800, where $\lambda = 0.7$.

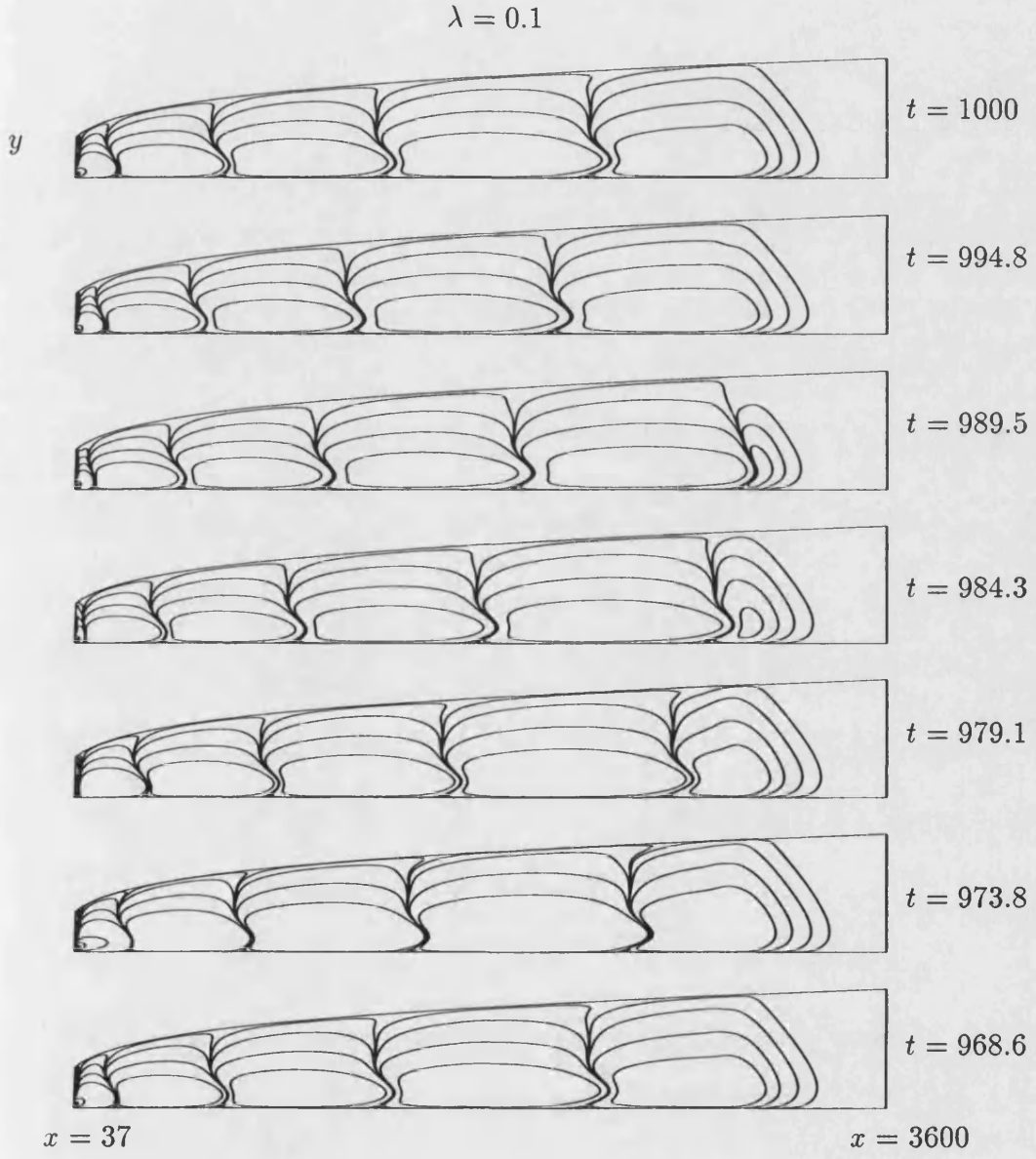

Figure 5.23: Contours represent the perturbation isotherms at 7 equally spaced points in time in a half period for the temporal frequency λ=0.1.

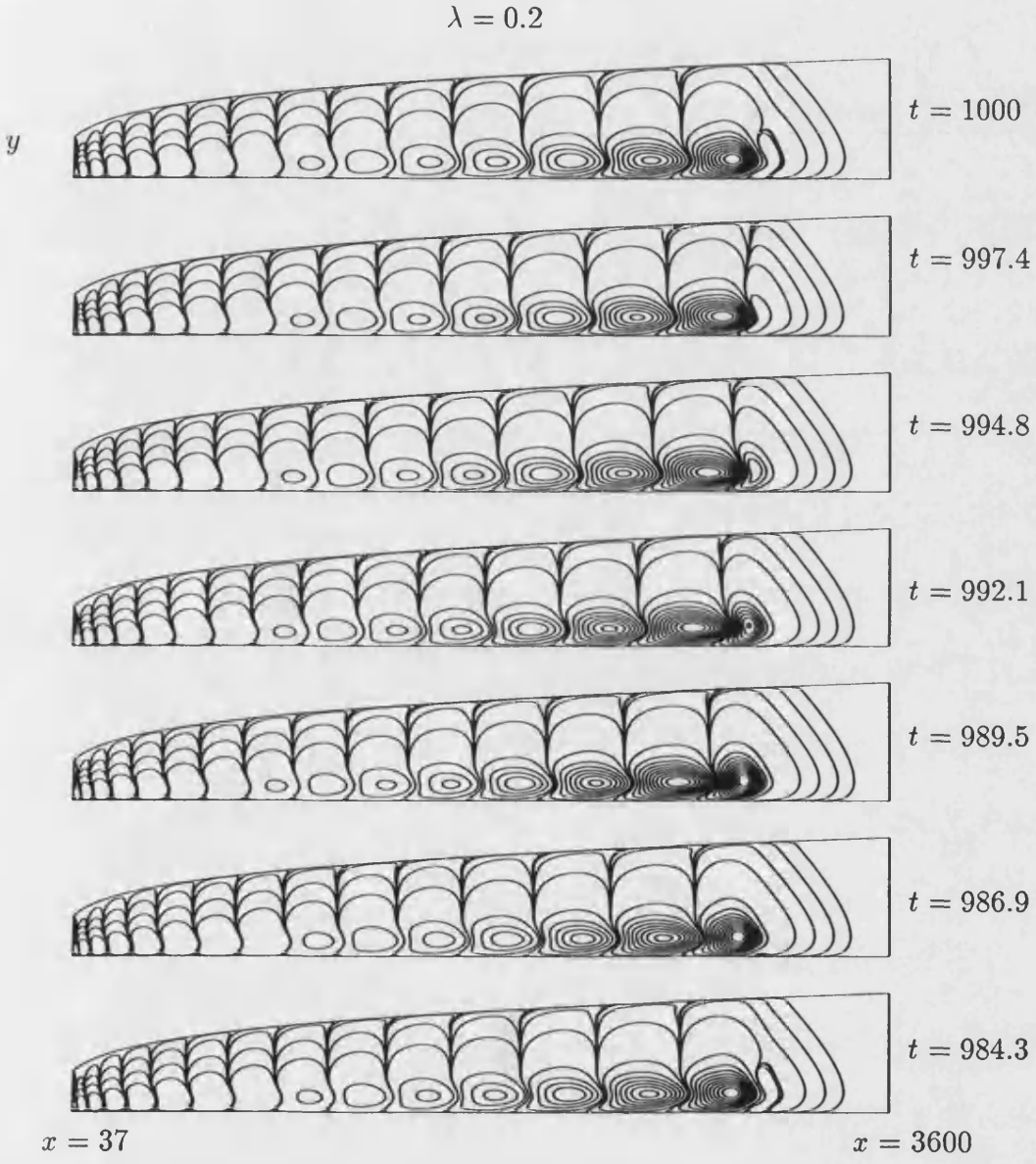

Figure 5.24: Contours represent the perturbation isotherms at 7 equally spaced points in time in a half period for the temporal frequency λ=0.2.

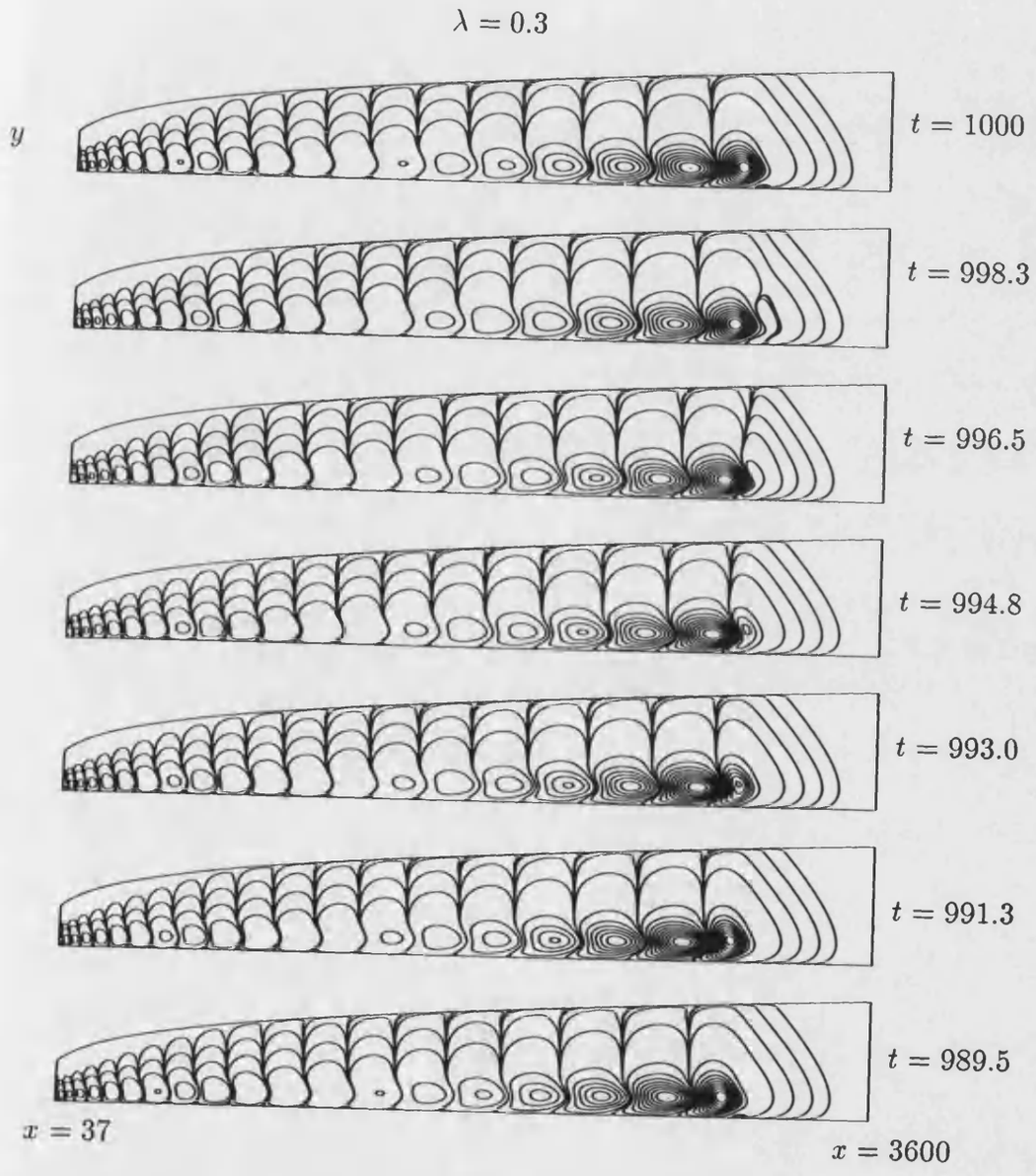

Figure 5.25: Contours represent the perturbation isotherms at 7 equally spaced points in time in a half period for the temporal frequency λ=0.3.

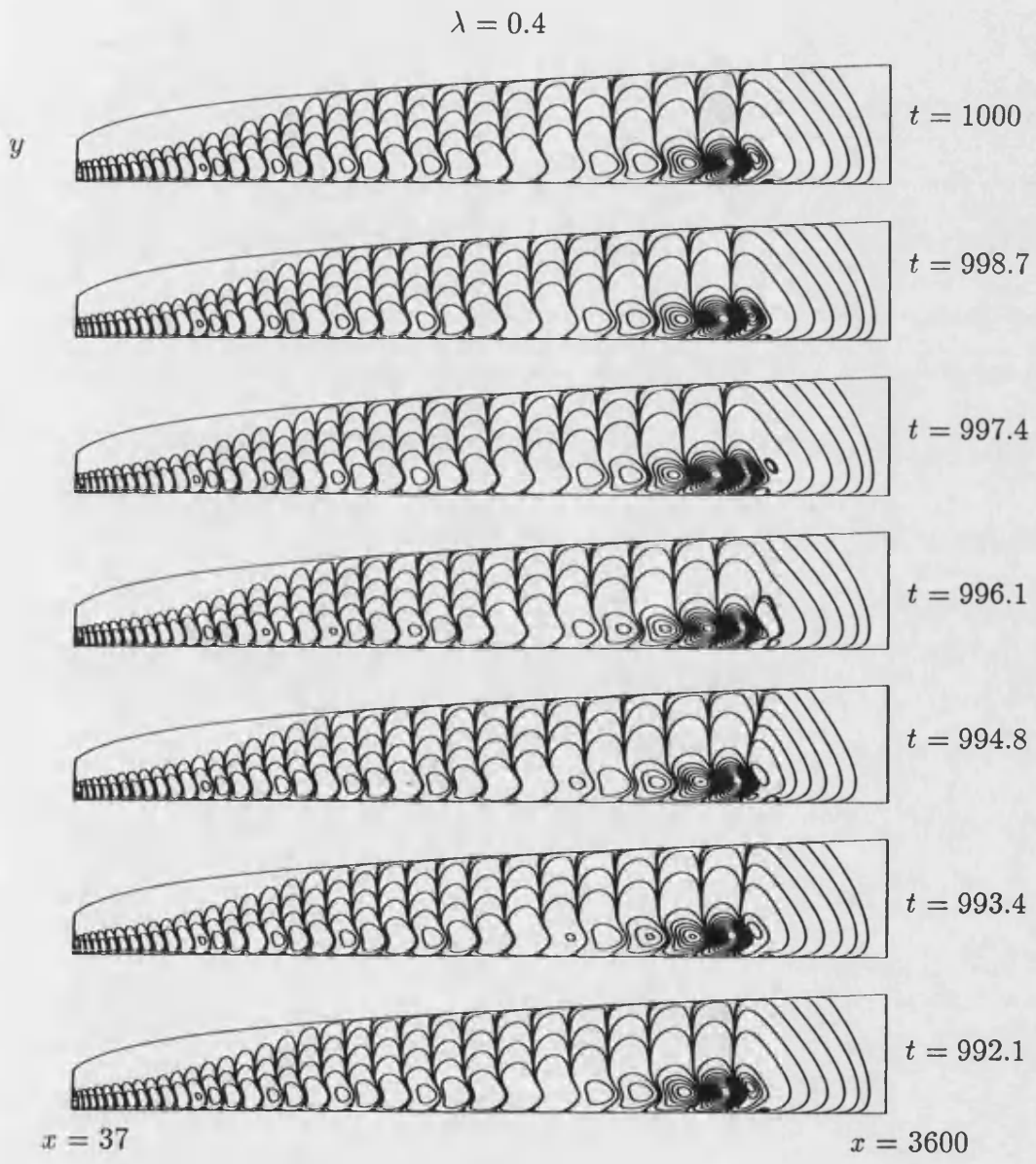

Figure 5.26: Contours represent the perturbation isotherms at 7 equally spaced points in time in a half period for the temporal frequency λ=0.4.

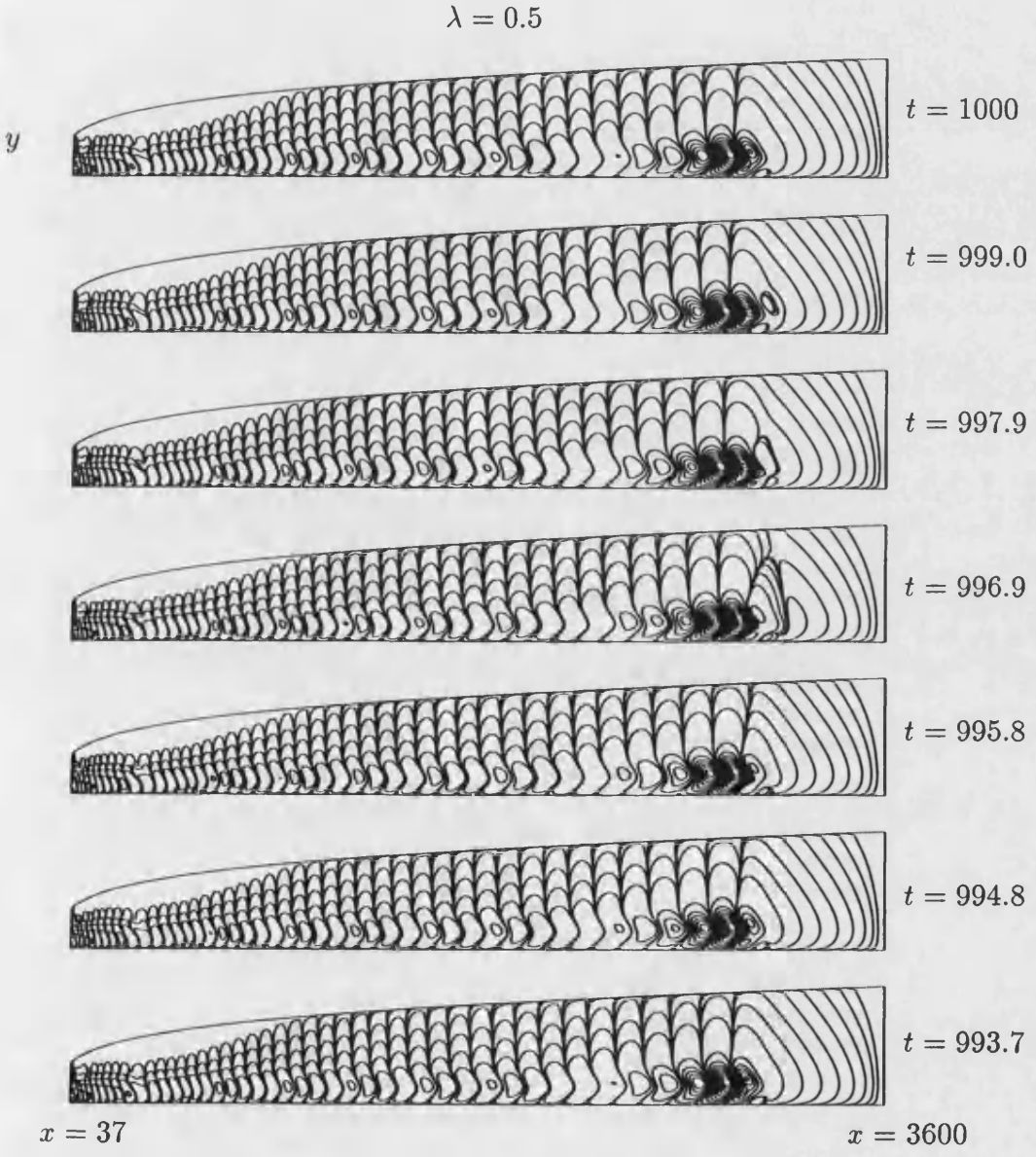

Figure 5.27: Contours represent the perturbation isotherms at 7 equally spaced points in time in a half period for the temporal frequency λ=0.5.

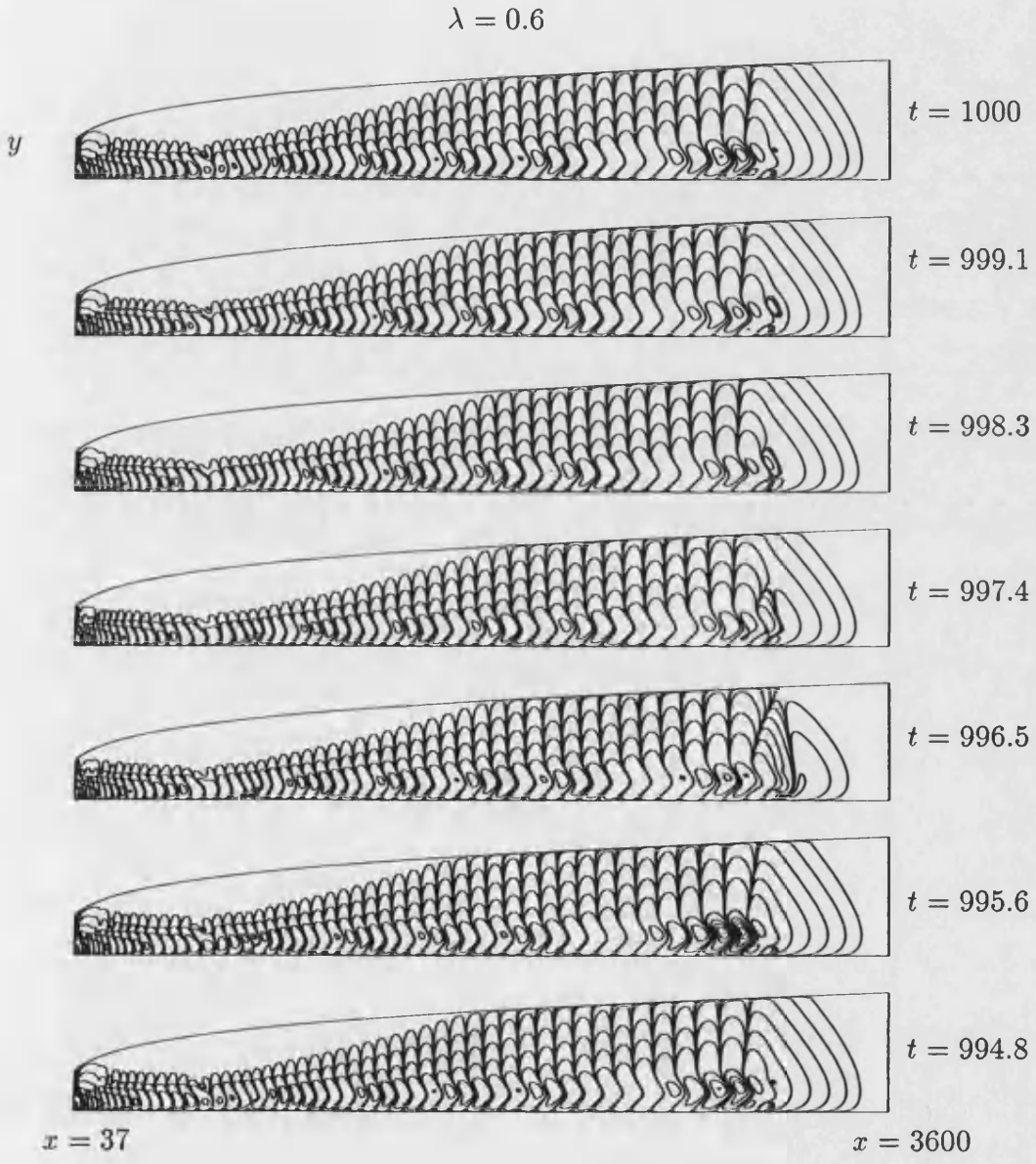

Figure 5.28: Contours represent the perturbation isotherms at 7 equally spaced points in time in a half period for the temporal frequency λ=0.6.

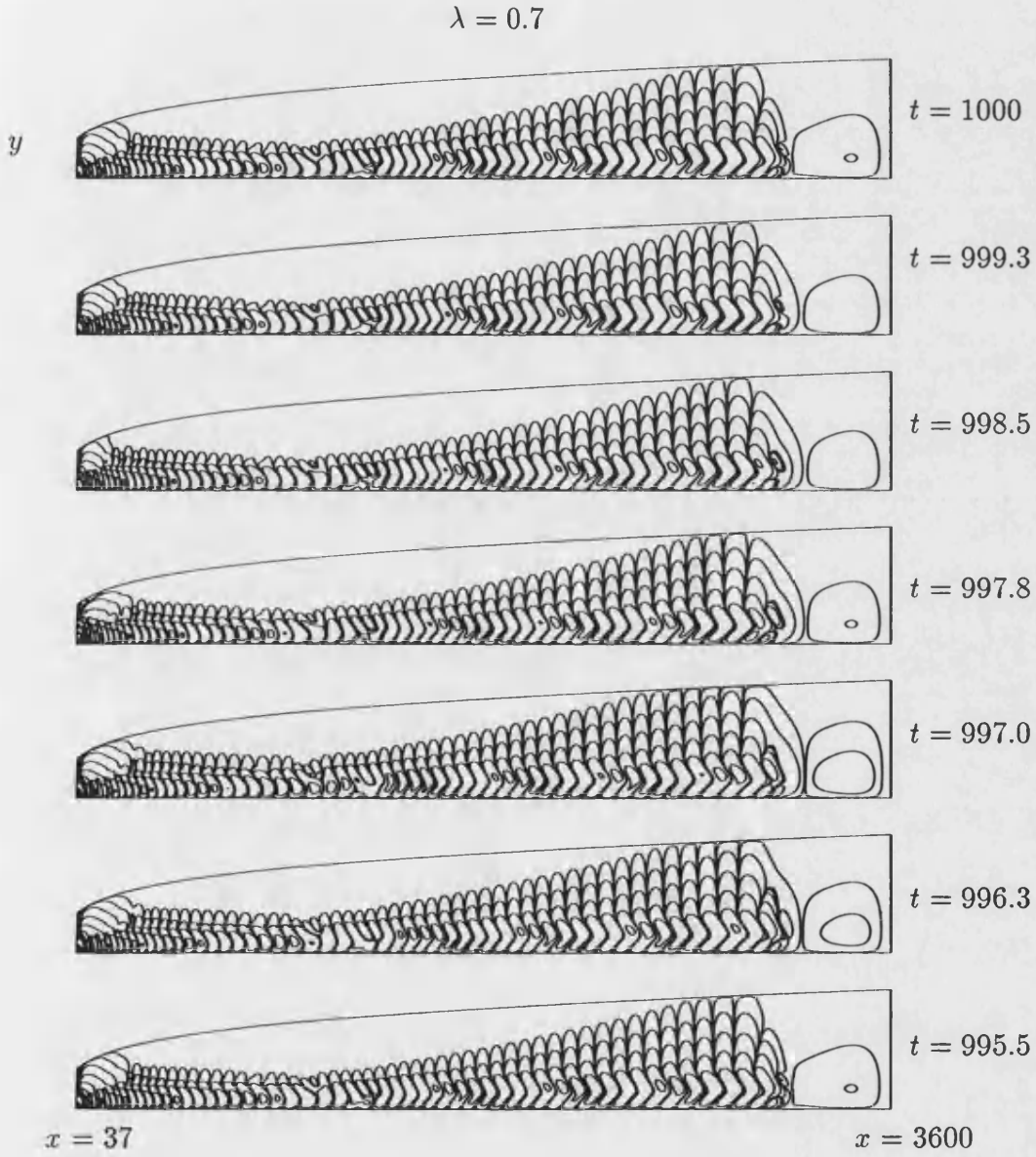

Figure 5.29: Contours represent the perturbation isotherms at 7 equally spaced points in time in a half period for the temporal frequency λ=0.7.

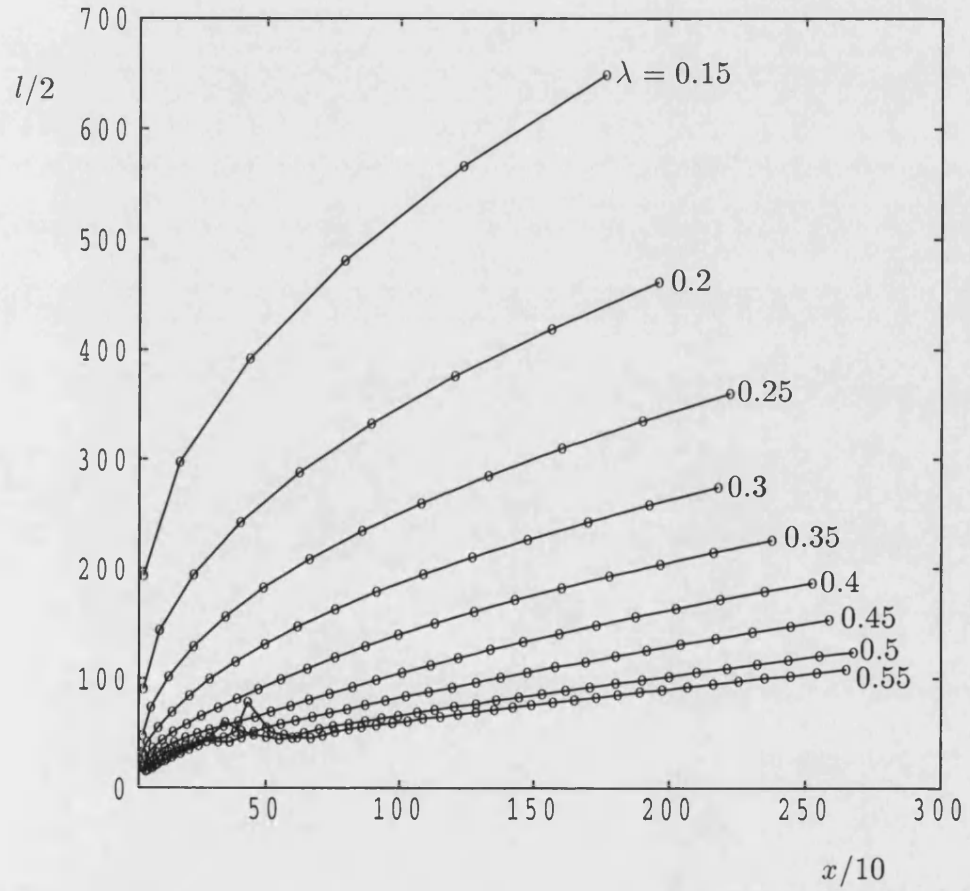

Figure 5.30: The variation in the spatial wavelength, l, with distance downstream.

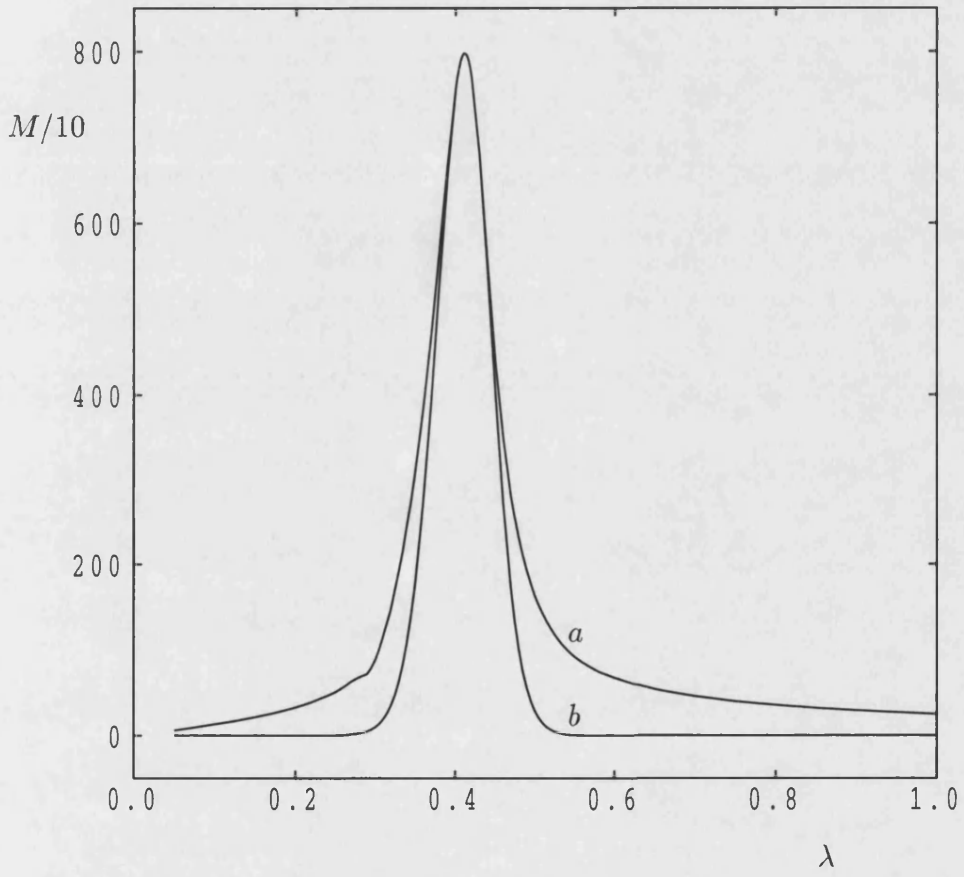

Figure 5.31: The maximum absolute surface rate of heat transfer as a function of λ for (a) the transient response and (b) the asymptotic response.

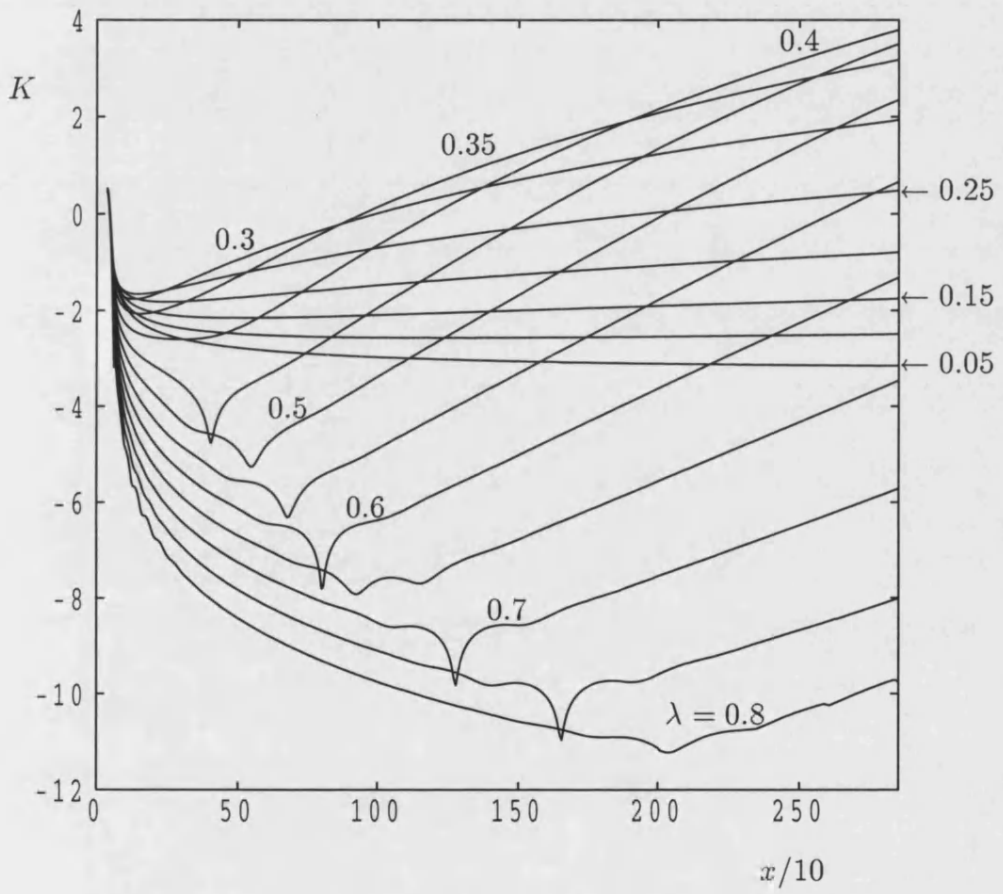

Figure 5.32: The variation with x of K, the maximum local asymptotic response of the boundary layer to time-periodic disturbances, for various values of λ.

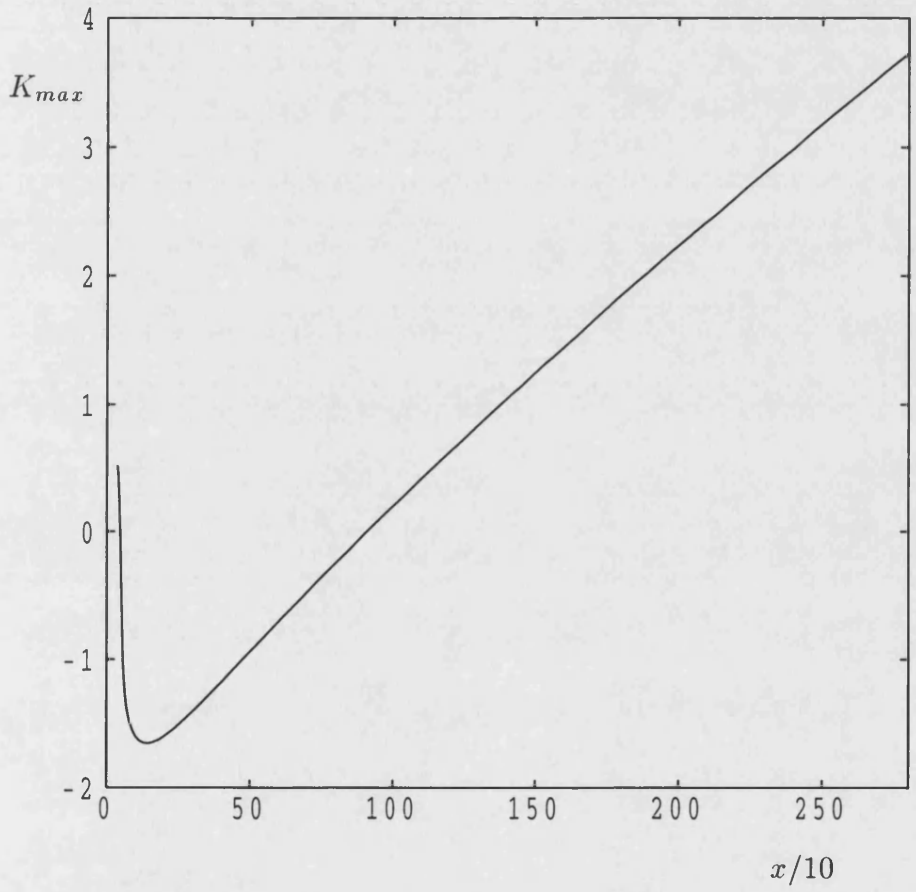

Figure 5.33: The maximum local asymptotic response to the time-periodic forcing as a function of x.

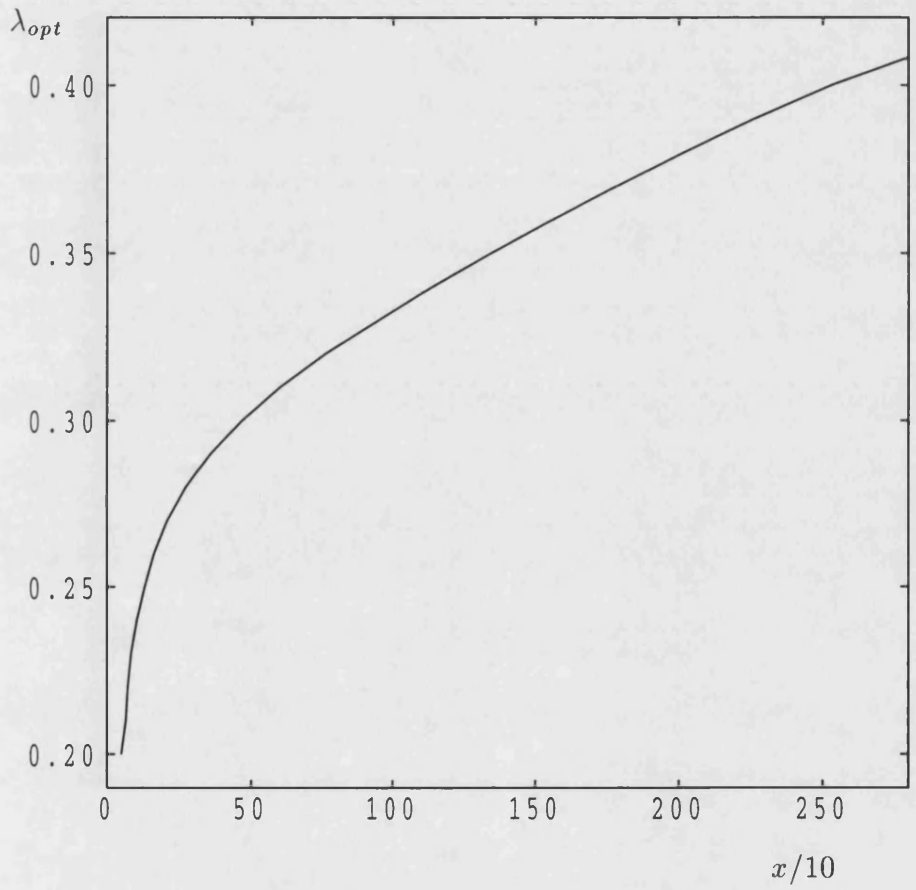

Figure 5.34: Variation with x of the optimum frequency which maximises the local maximum asymptotic response.

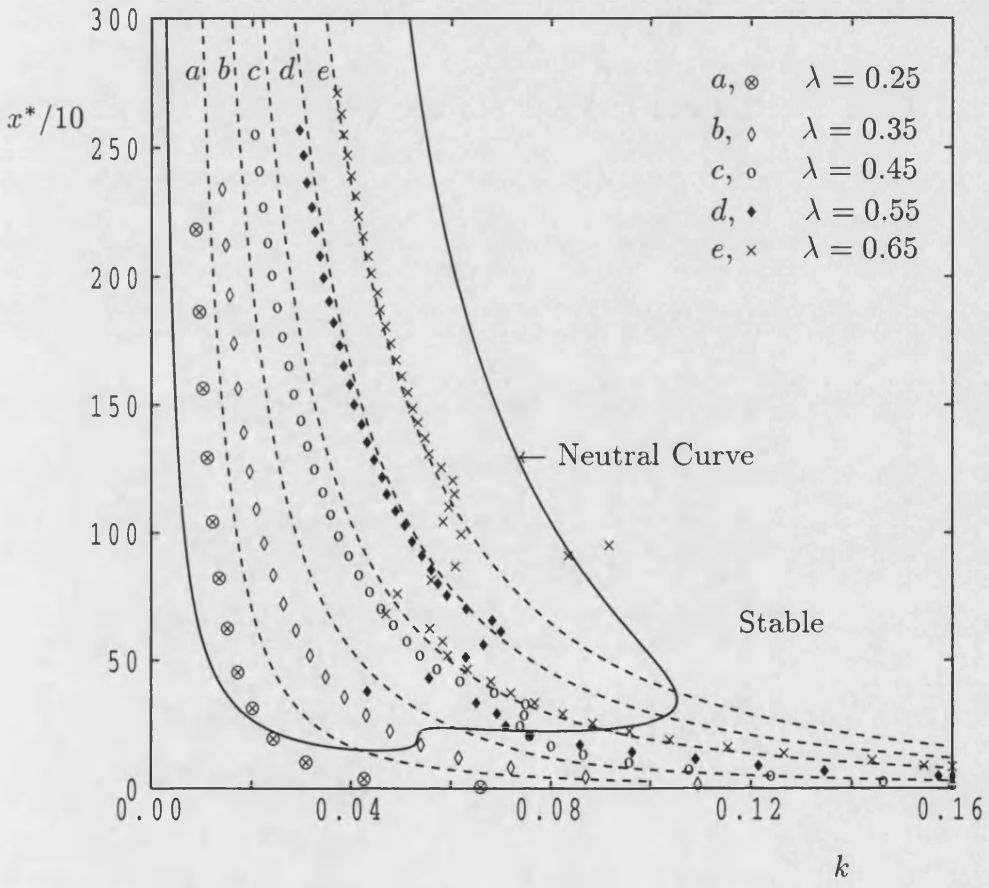

Figure 5.35: Comparison between the present elliptic linear stability results and those obtained by assuming the parallel flow approximation.

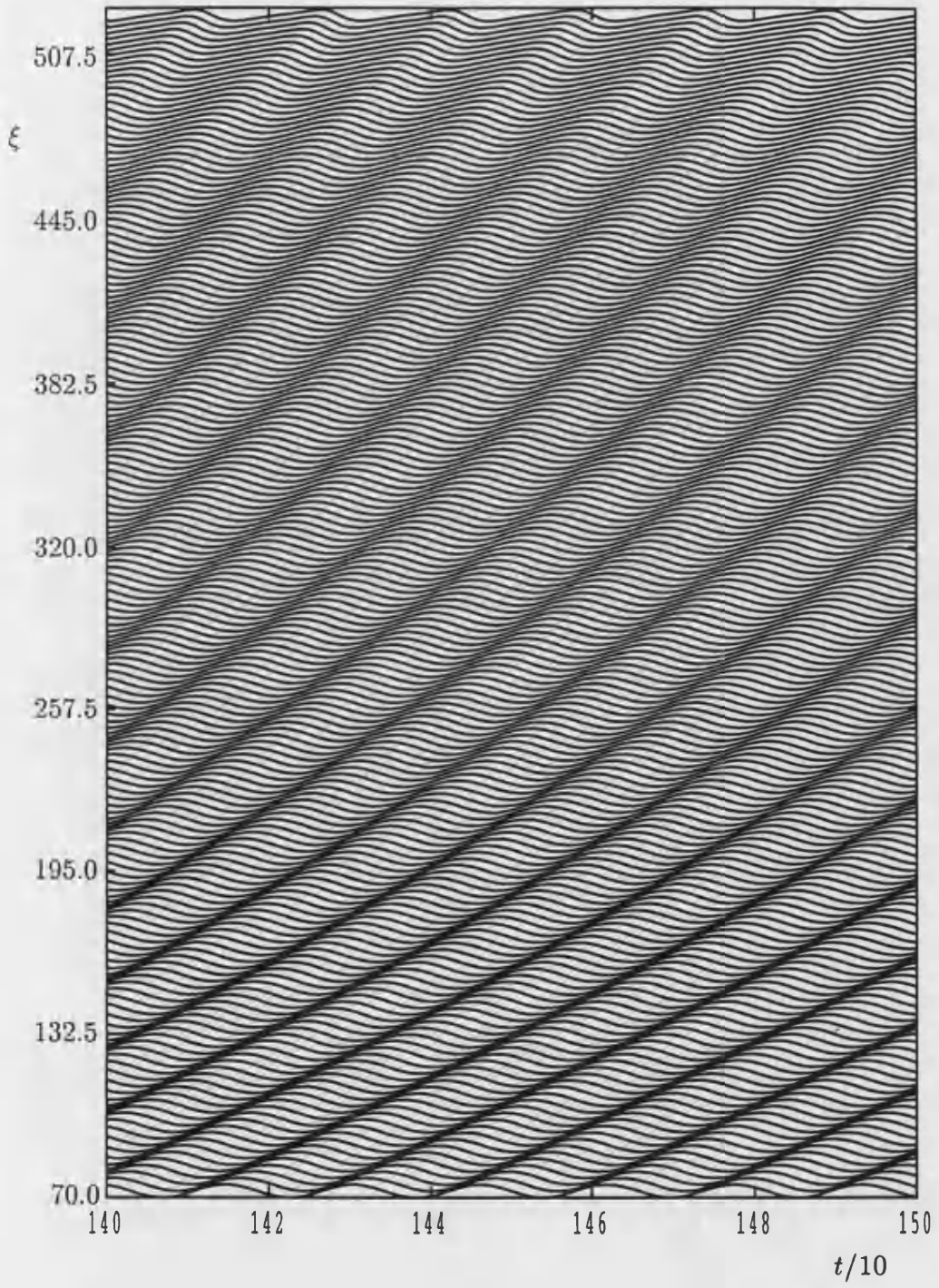

Figure 6.1: Variation of the normalised perturbation heat transfer with t for many values of ξ. Here the forcing frequency is $\lambda = 0.4$ and $A = 2 \times 10^{-5}$.

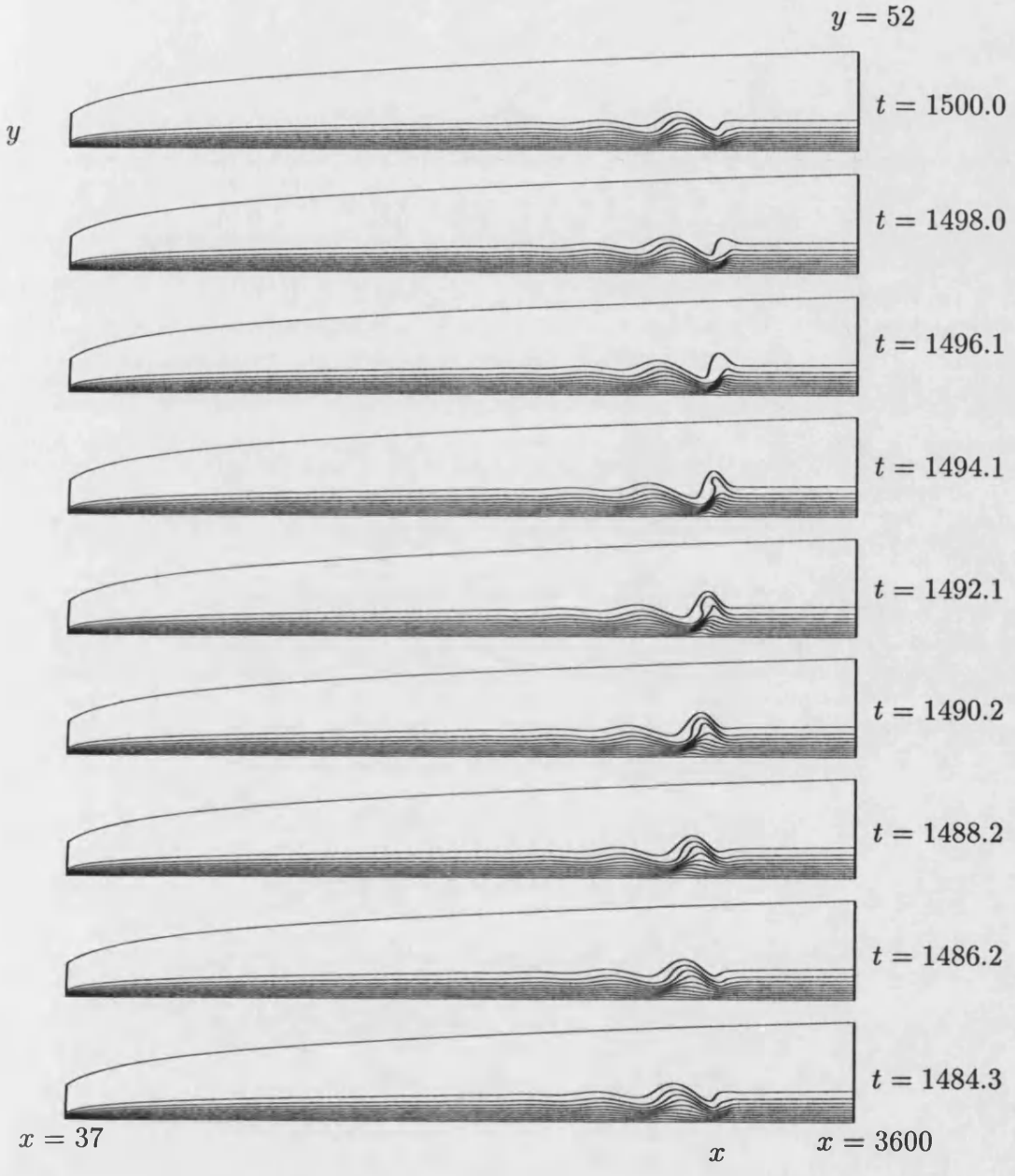

Figure 6.2: Full isotherm (θ) contours at 8 equally spaced time intervals in the last period for $\lambda = 0.4$ and $A = 2 \times 10^{-5}$. Contours are at intervals of 0.1.

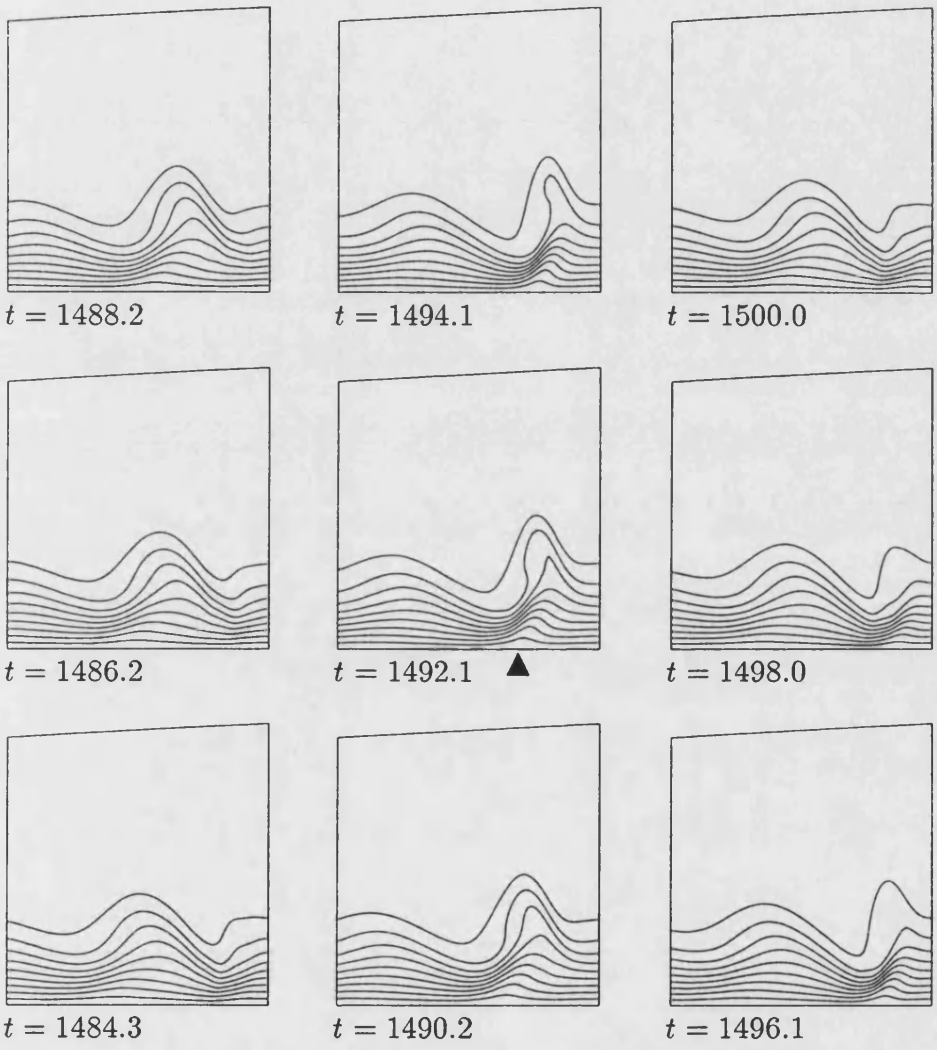

Figure 6.3: Close view of the isotherms (θ) of Figure 6.2. Each frame is plotted in the x range 2500 to 3080. The black triangle indicates where the surface rate of heat transfer is at its minimum.

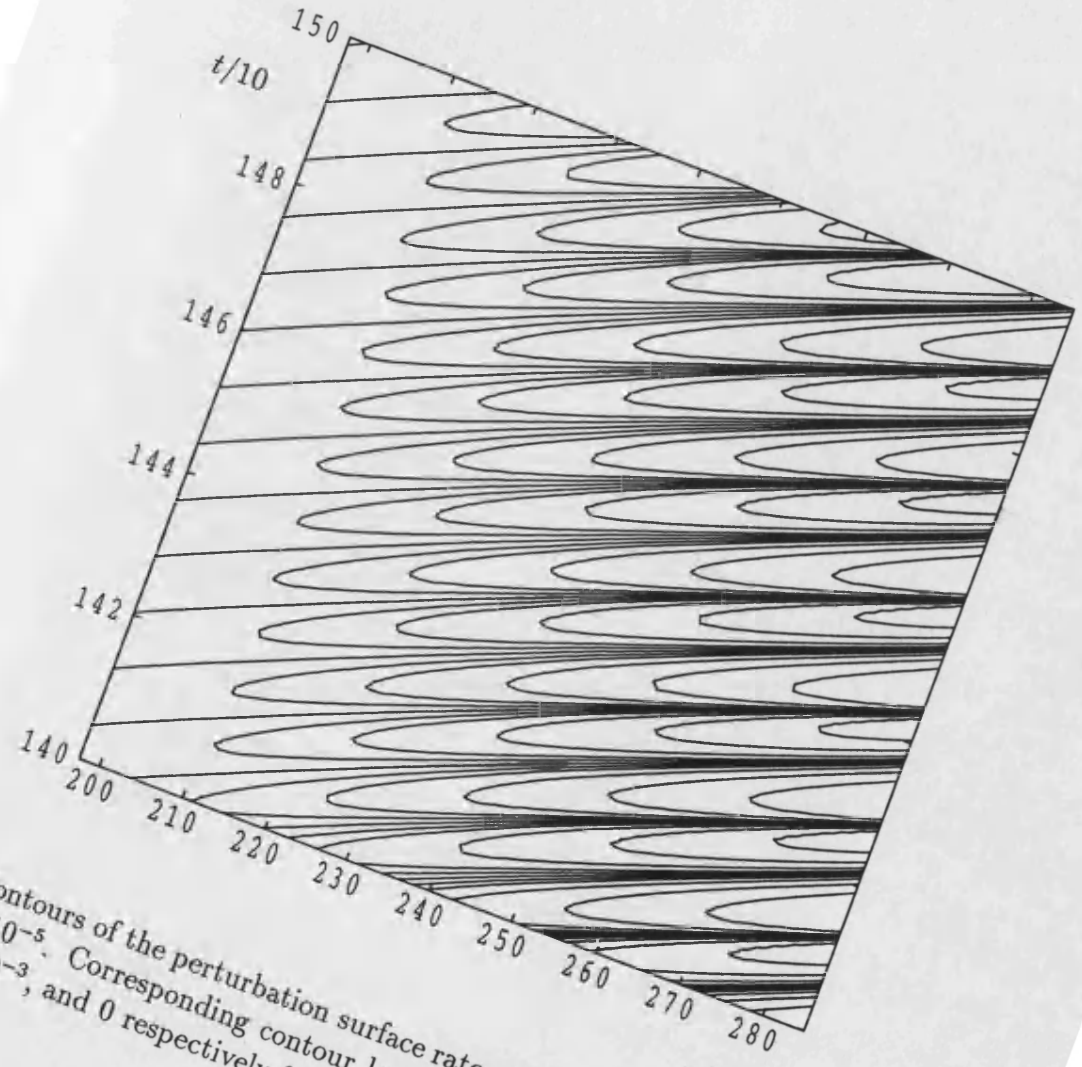

Figure 6.4: Contours of the perturbation surface rate of heat transfer for $\lambda = 0.4$, and $A = 2 \times 10^{-5}$. Corresponding contour levels are at $\pm 8 \times 10^{-2}$, $\pm 4 \times 10^{-2}$, $\pm 10^{-2}$, $\pm 5 \times 10^{-3}$, and 0 respectively from right to left.

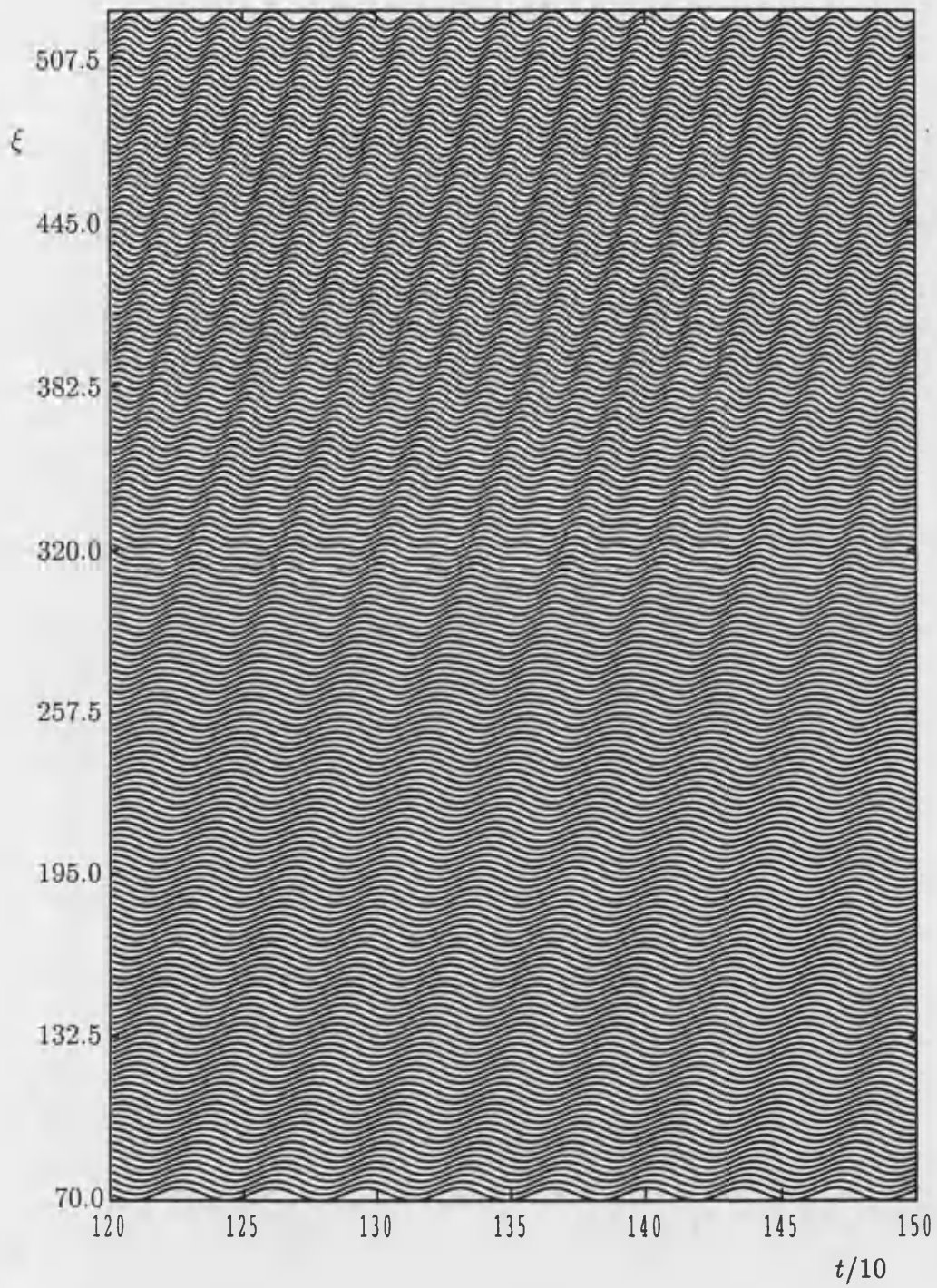

Figure 6.5: Waveforms showing the 1:2 superharmonic transition in the case when $\lambda = 0.18$ and $A = 2 \times 10^{-3}$. The wave amplitude is normalised for each value of ξ.

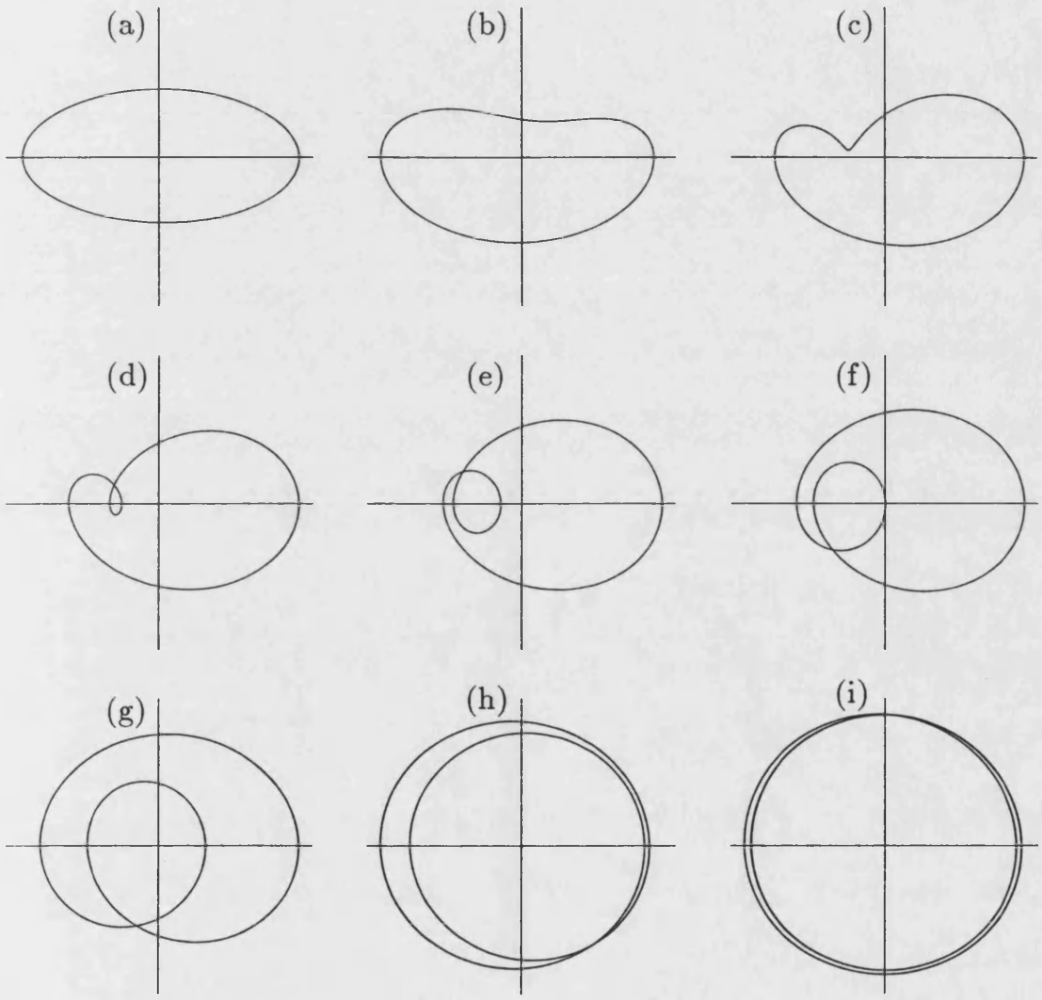

Figure 6.6: Limit cycles of the phase trajectories of the surface rate of heat transfer at various positions along the surface for $\lambda = 0.18$, $A = 2 \times 10^{-3}$, and (a) $\xi = 175$, (b) $\xi = 270$, (c) $\xi = 288$, (d) $\xi = 300$, (e) $\xi = 313$, (f) $\xi = 325$, (g) $\xi = 350$, (h) $\xi = 425$, (i) $\xi = 500$. The horizontal axis is the local value of $\frac{\partial \hat{\theta}}{\partial \eta}\Big|_{\eta=0}$ while the vertical axis is its time rate of change.

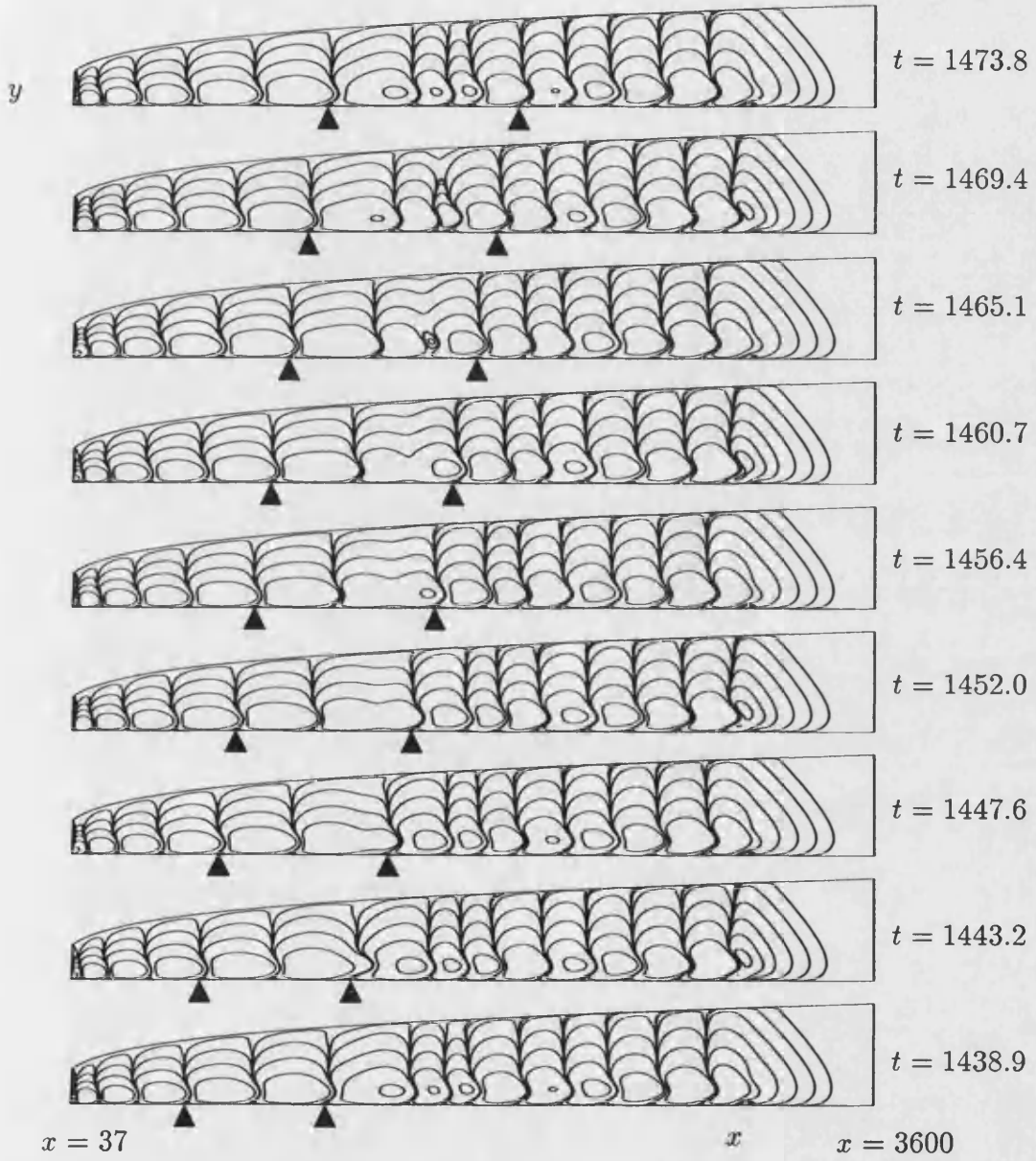

Figure 6.7: Contours of perturbation isotherms ($\hat{\theta}$) at 8 equally spaced time intervals in a period (period considered at late stage when the oscillation is steady state periodic) for $\lambda = 0.18$ and $A = 2 \times 10^{-3}$. Corresponding contour levels are plotted for $\hat{\theta} = \pm\ (10^{-2}, 10^{-3}, 10^{-4}, 10^{-5}, 10^{-6}, 10^{-7})$. The black triangles mark the start and end of a complete cell pair at $t = 1438.9$ which becomes four at time $t = 1473.8$.

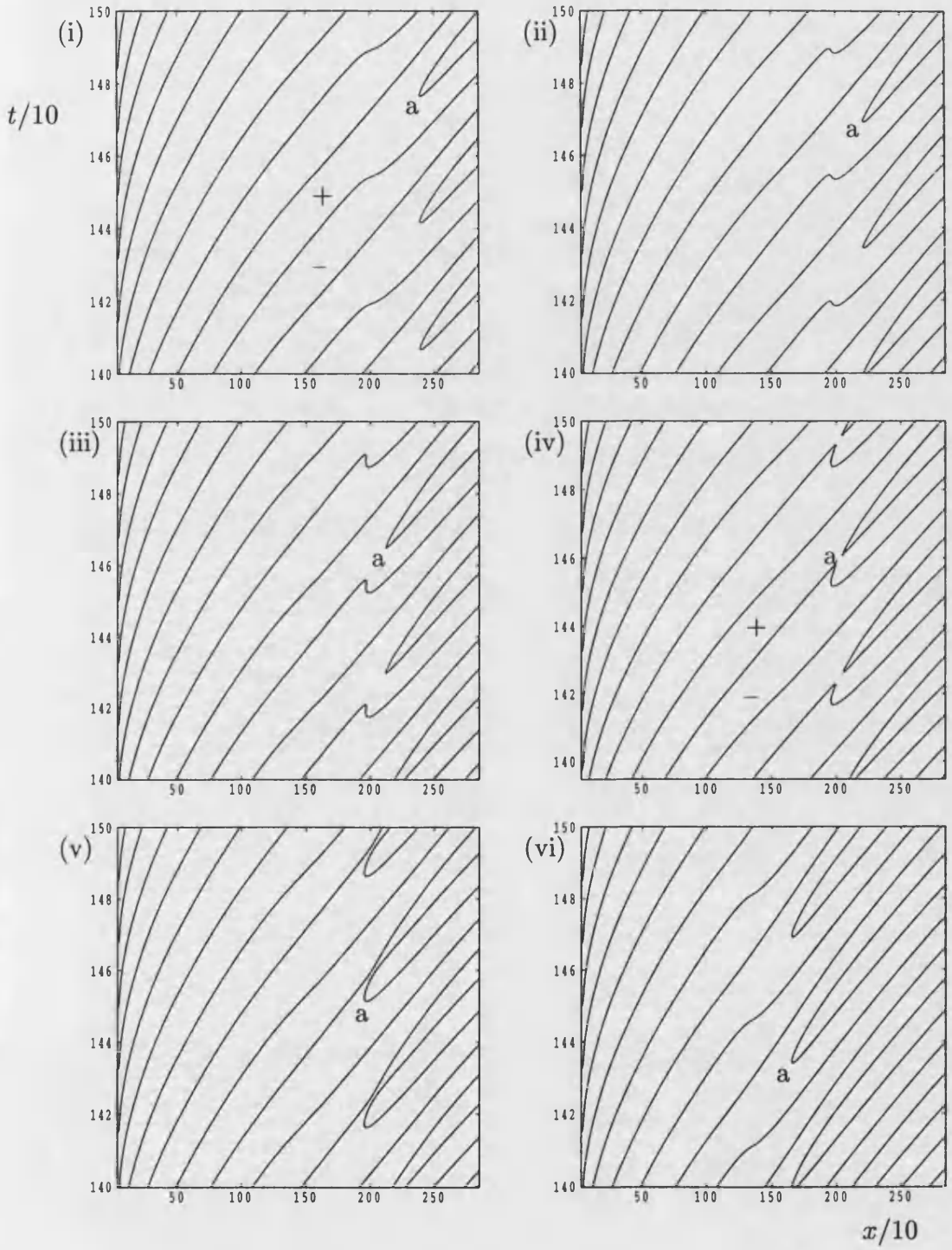

Figure 6.8: Contours of the zero level surface rate of heat transfer over the last few periods in time for $\lambda = 0.18$, and where (i) $A = 2 \times 10^{-4}$, (ii) $A = 3 \times 10^{-4}$, (iii) $A = 3.5 \times 10^{-4}$, (iv) $A = 3.8 \times 10^{-4}$, (v) $A = 4 \times 10^{-4}$, (vi) $A = 20 \times 10^{-4}$.

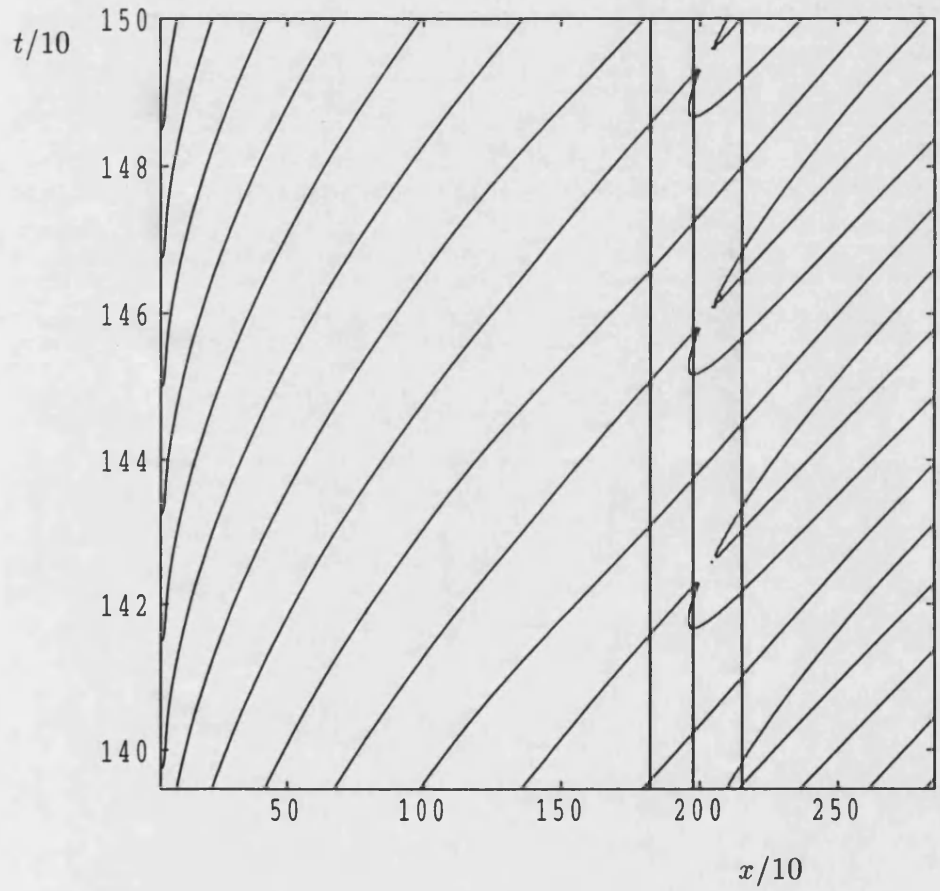

Figure 6.9: Close-up view of Figure 6.8(iv) where $A = 3.8 \times 10^{-4}$ and $\lambda = 0.18$. Each vertical line is drawn in order to count the number of cells per forcing period.

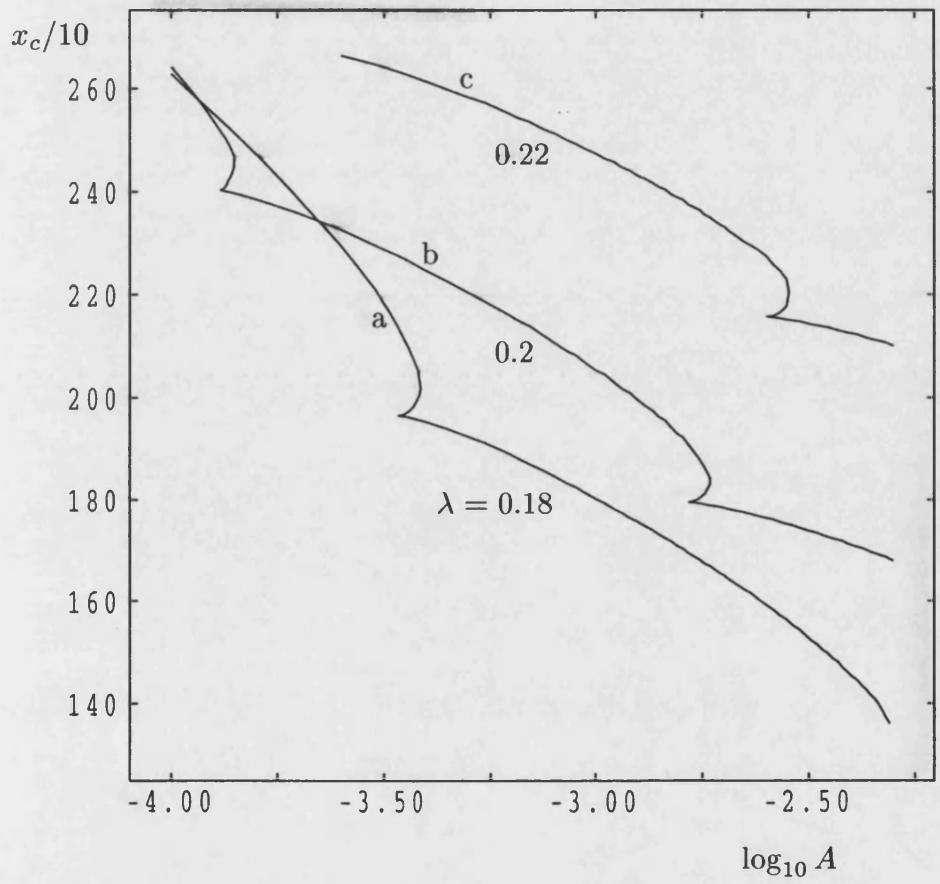

Figure 6.10: Variation with A of the position of the 1:2 superharmonic transition for (a) $\lambda = 0.18$, (b) $\lambda = 0.2$, and (c) $\lambda = 0.22$.

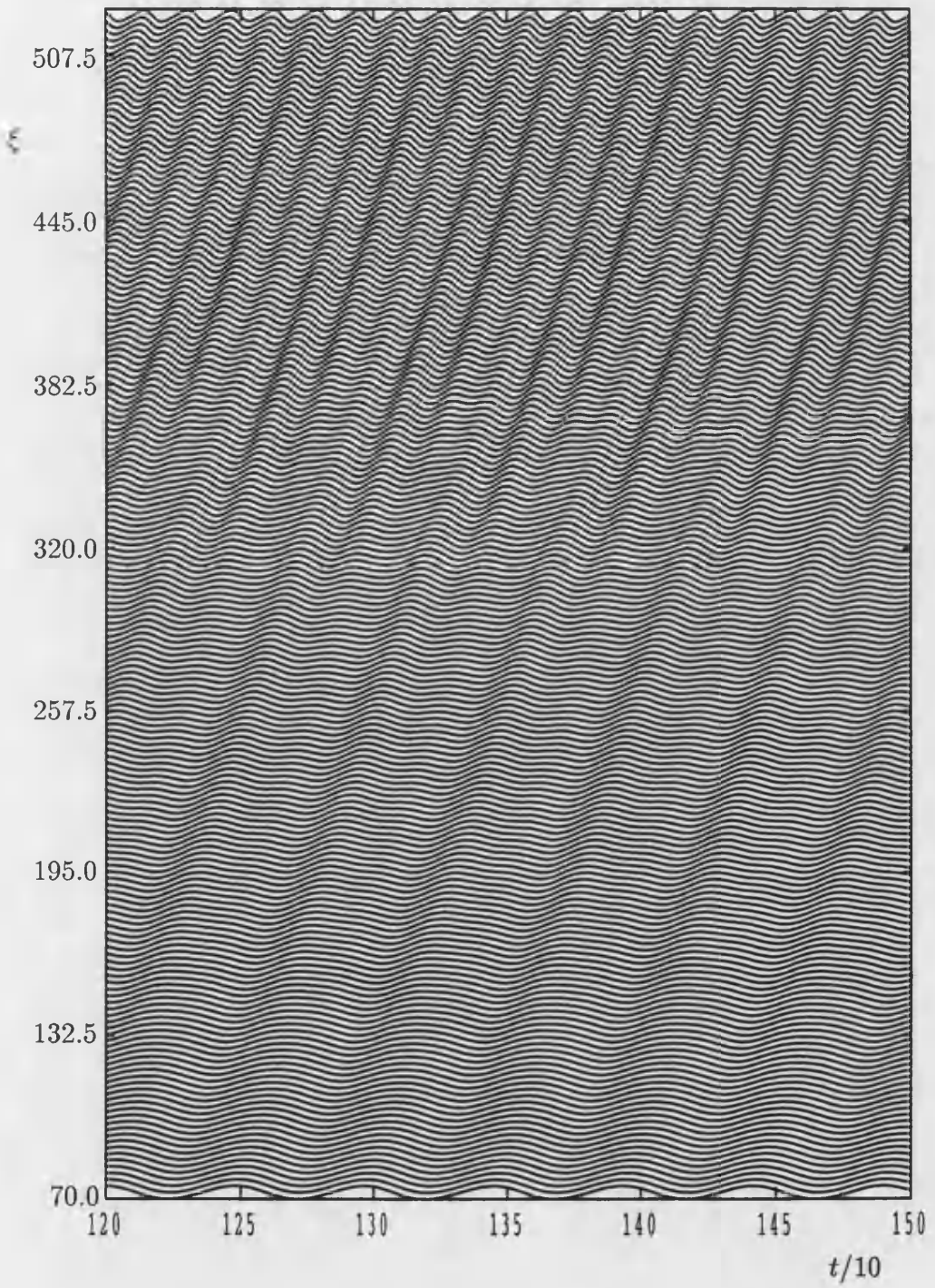

Figure 6.11: Waveforms showing the 1:3 superharmonic transition in the case when $\lambda = 0.13$ and $A = 4 \times 10^{-2}$. The wave amplitude is normalised for each value of ξ.

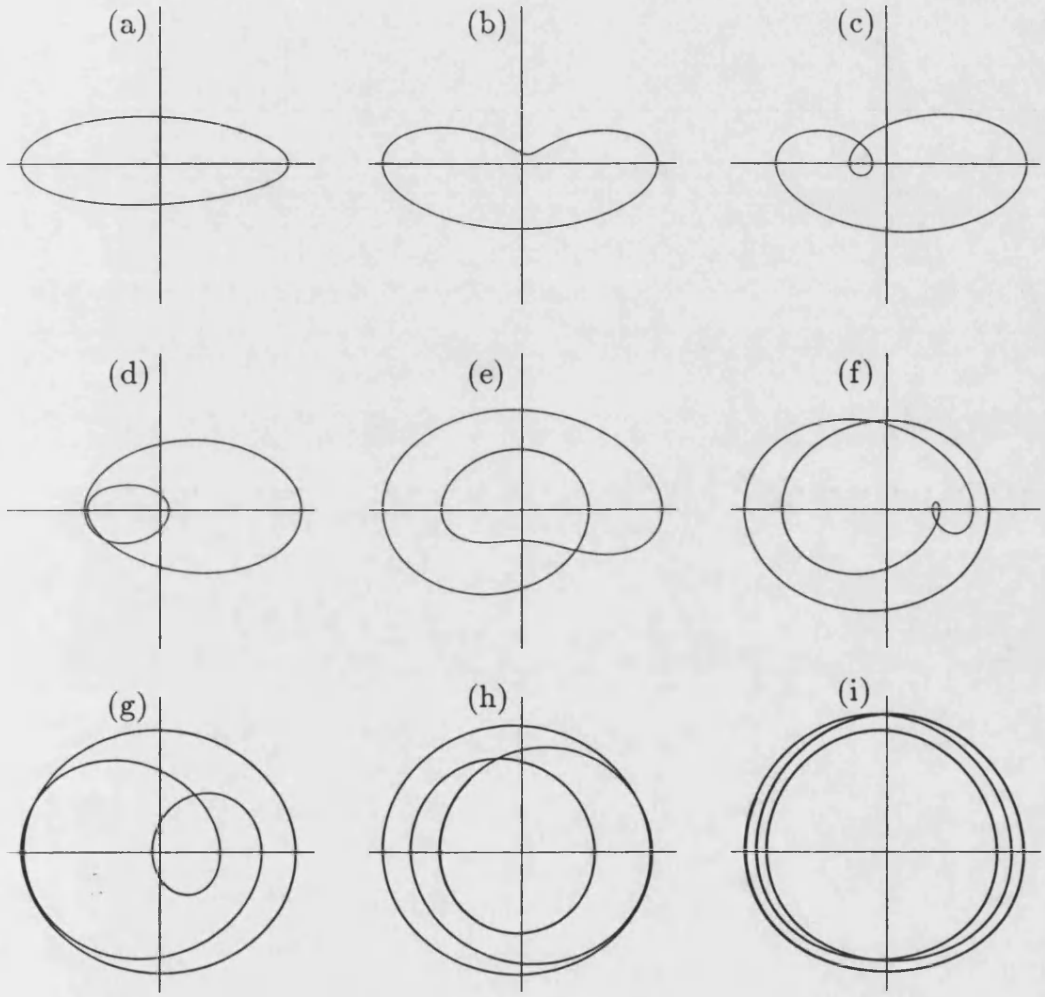

Figure 6.12: Limit cycles of the phase trajectories of the surface rate of heat transfer at various positions along the surface for $\lambda = 0.13$, $A = 4 \times 10^{-2}$, and (a) $\xi = 75$, (b) $\xi = 175$, (c) $\xi = 225$, (d) $\xi = 275$, (e) $\xi = 313$, (f) $\xi = 338$, (g) $\xi = 363$, (h) $\xi = 400$, (i) $\xi = 450$. The horizontal axis is the local value of $\frac{\partial \hat{\theta}}{\partial \eta}\Big|_{\eta=0}$ while the vertical axis is its time rate of change.

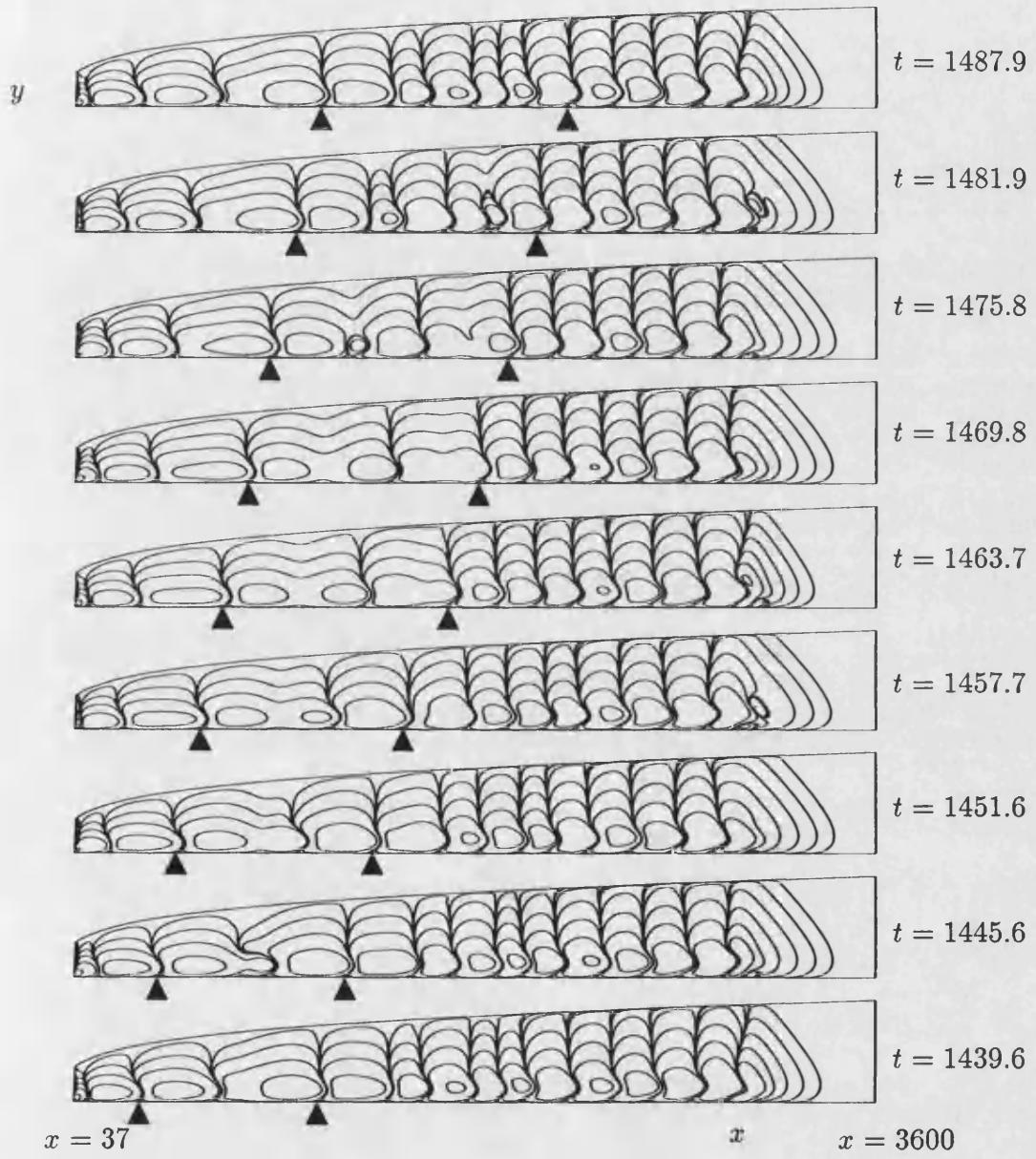

Figure 6.13: Contours of perturbation isotherms ($\hat{\theta}$) at 8 equally spaced time intervals in a period (period considered at late stage when the oscillation is steady state periodic) for $\lambda = 0.13$ and $A = 4 \times 10^{-2}$. Corresponding contour levels are plotted for $\hat{\theta} = \pm\ (10^{-1}, 10^{-2}, 10^{-3}, 10^{-4}, 10^{-5}, 10^{-6})$. The black triangles mark the start and end of a complete cell pair at $t = 1439.6$ which becomes six at time $t = 1487.9$.

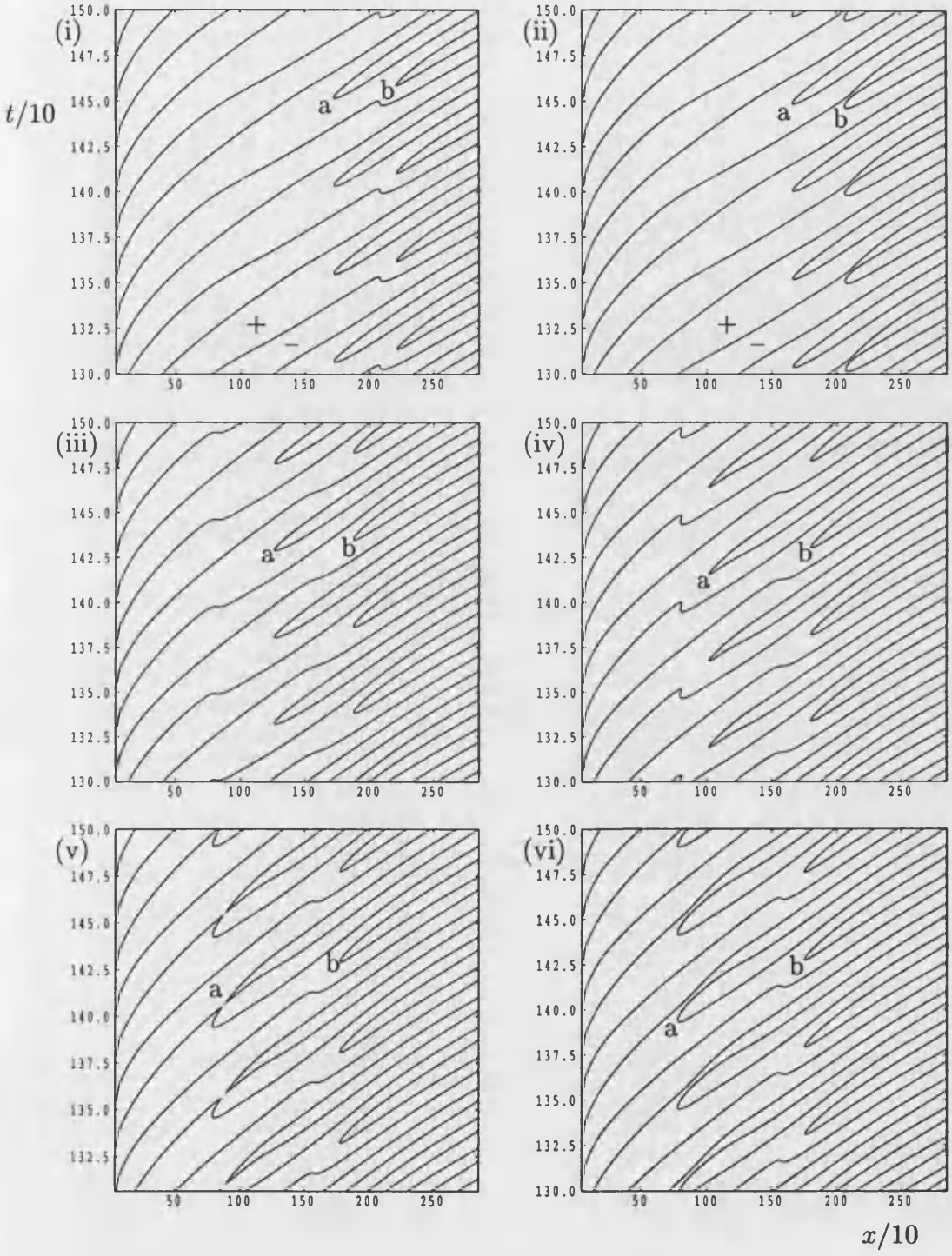

Figure 6.14: Contours of the zero level surface rate of heat transfer over the last few periods in time for $\lambda = 0.13$, and where (i) $A = 1.4 \times 10^{-2}$, (ii) $A = 1.6 \times 10^{-2}$, (iii) $A = 4 \times 10^{-2}$, (iv) $A = 5.2 \times 10^{-2}$, (v) $A = 5.6 \times 10^{-2}$, (vi) $A = 6 \times 10^{-2}$.

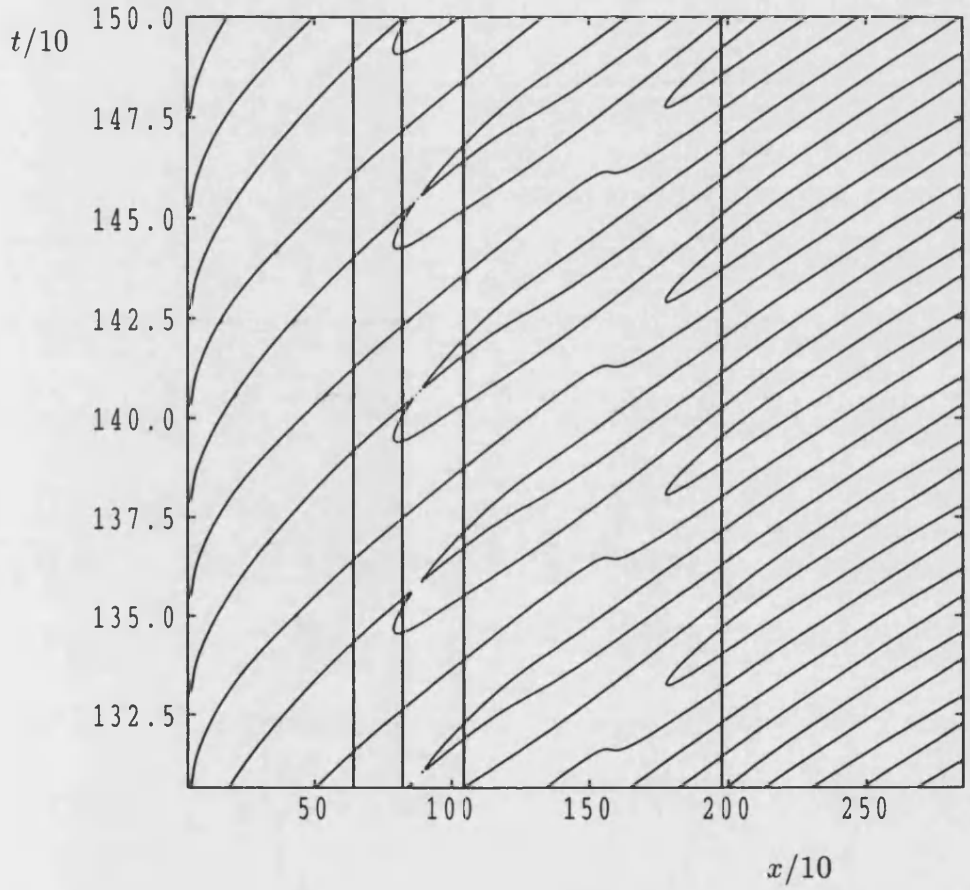

Figure 6.15: Close-up view of Figure 6.14(v) where $A = 5.6 \times 10^{-2}$ and $\lambda = 0.13$. Each vertical line is drawn in order to count the number of cells per forcing period.

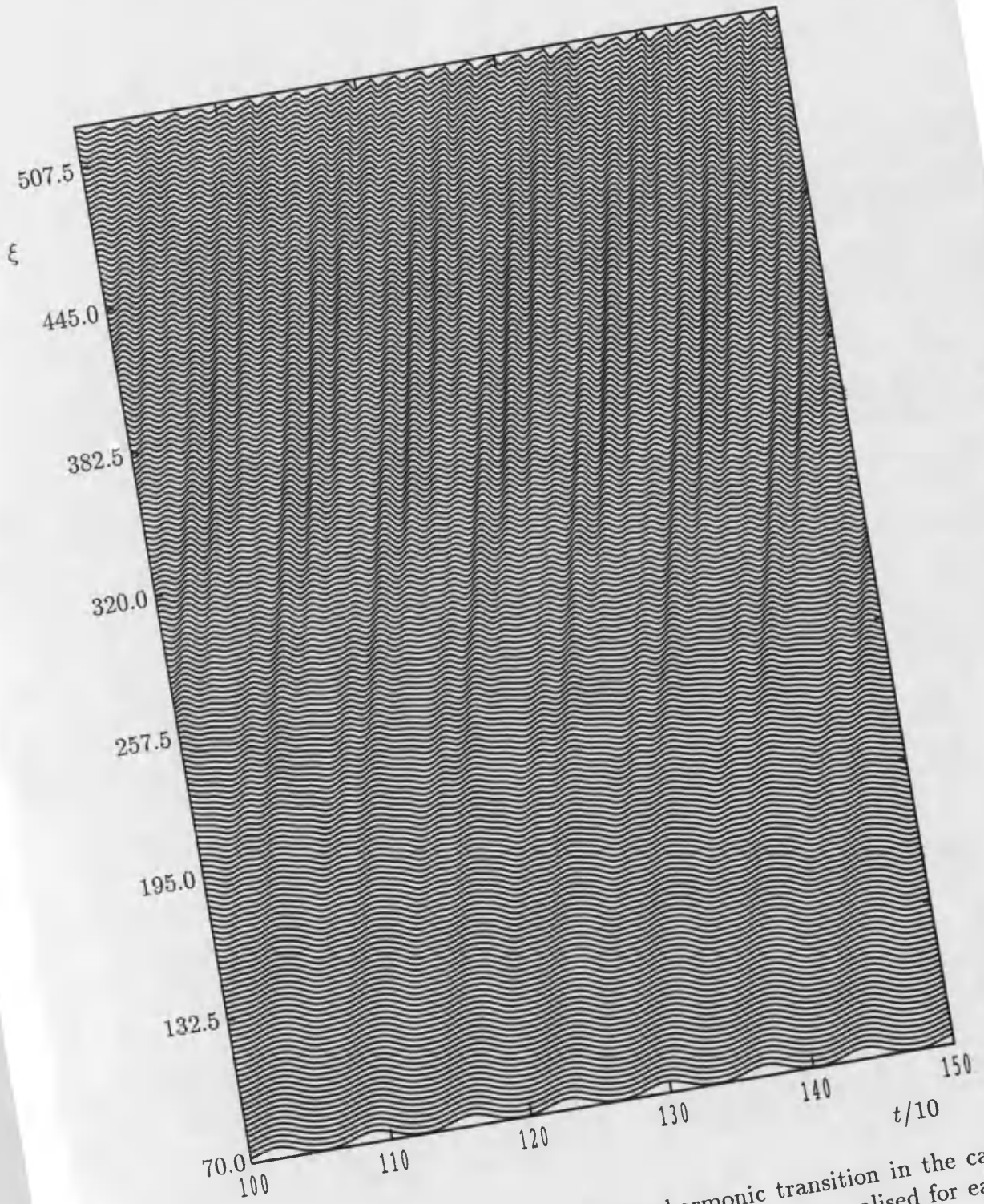

Figure 6.16: Waveforms showing the 1:4 superharmonic transition in the case when $\lambda = 0.09$ and $A = 2 \times 10^{-1}$. The wave amplitude is normalised for each value of ξ.

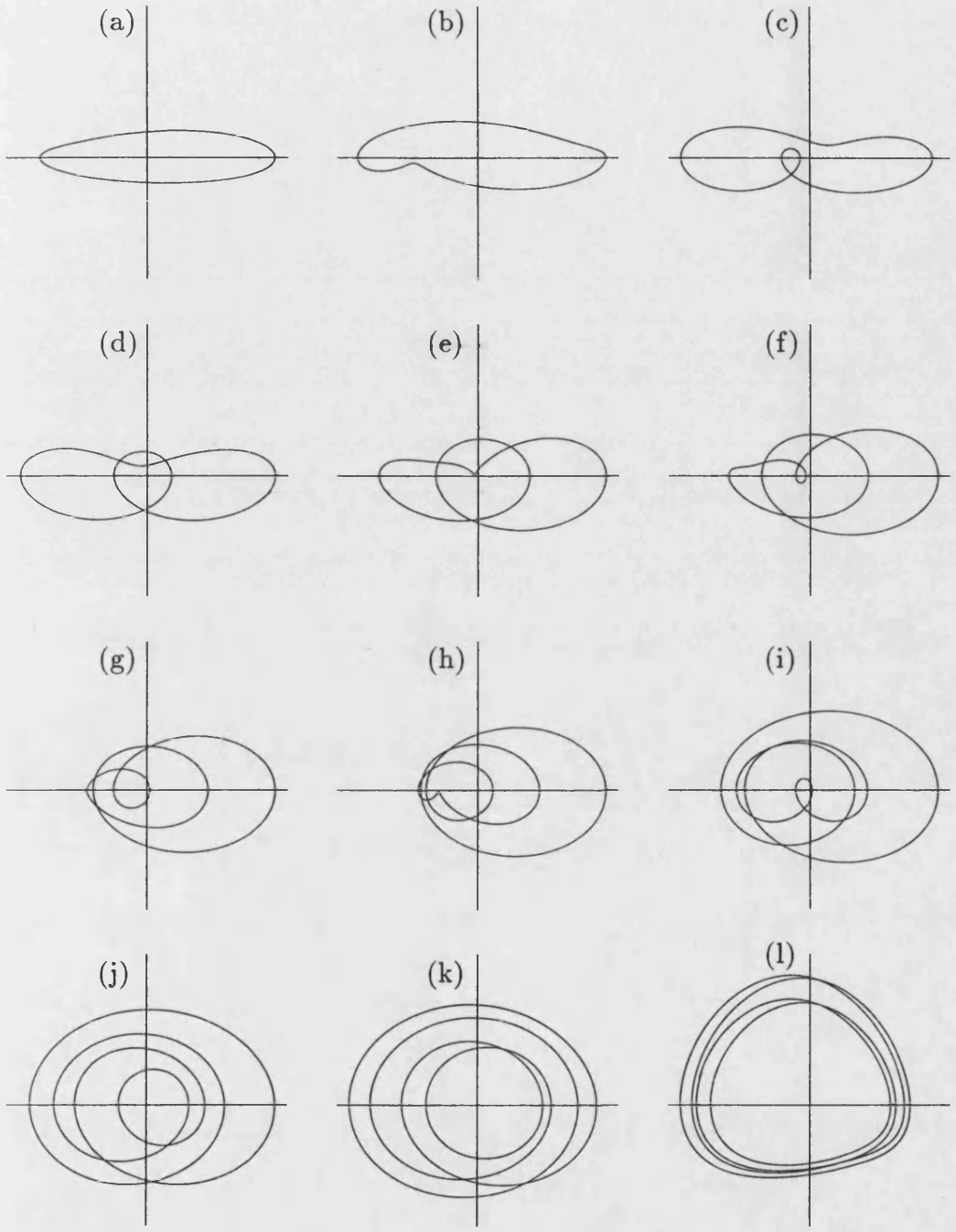

Figure 6.17: Limit cycles of the phase trajectories of the surface rate of heat transfer at various positions along the surface for $\lambda = 0.09$, $A = 2 \times 10^{-1}$, and (a) $\xi = 50$, (b) $\xi = 125$, (c) $\xi = 175$, (d) $\xi = 200$, (e) $\xi = 225$, (f) $\xi = 238$, (g) $\xi = 250$, (h) $\xi = 263$, (i) $\xi = 288$, (j) $\xi = 313$, (k) $\xi = 338$, (l) $\xi = 450$. The horizontal axis is the local value of $\frac{\partial \hat{\theta}}{\partial \eta}\Big|_{\eta=0}$ while the vertical axis is its time rate of change.

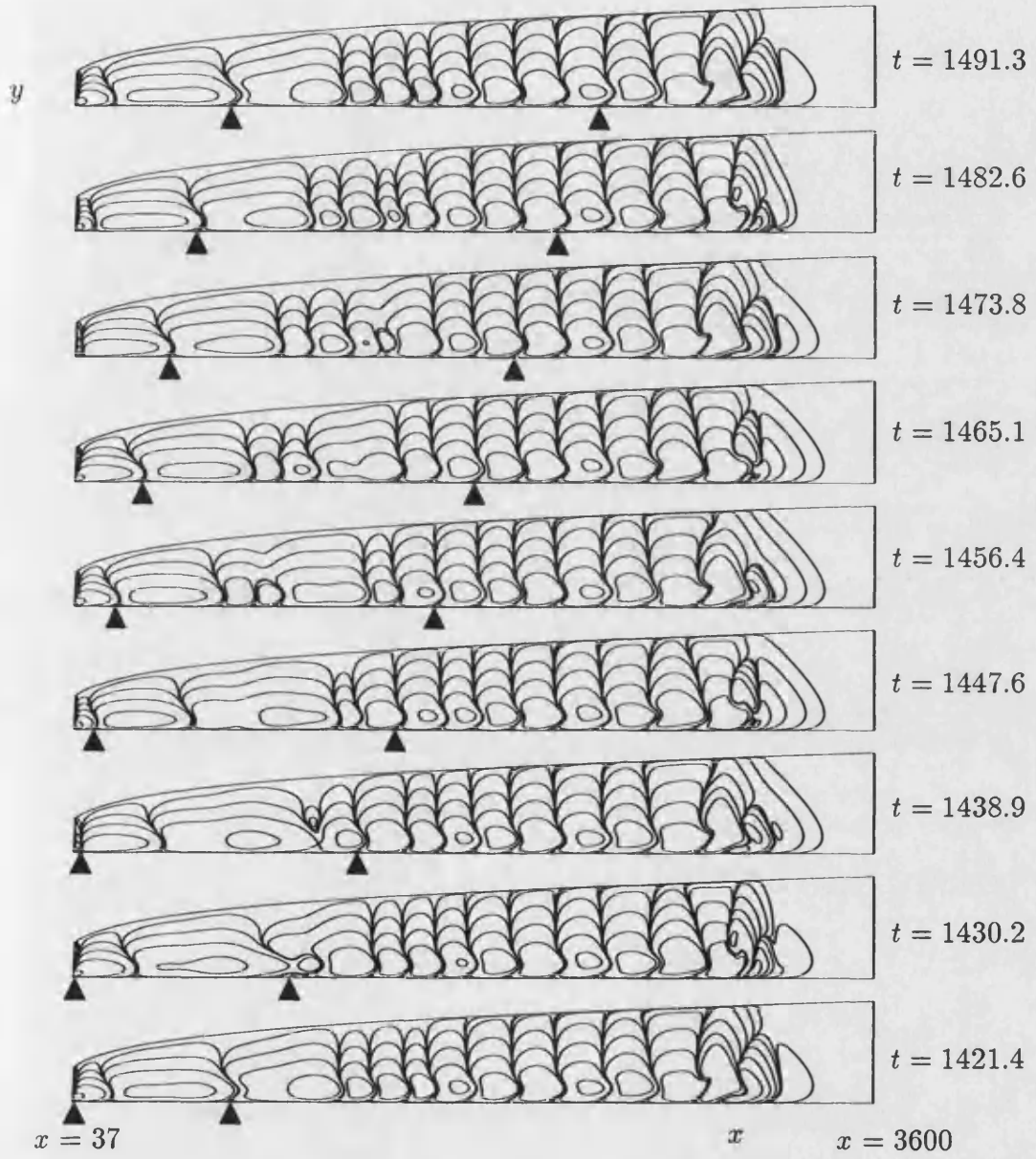

Figure 6.18: Contours of perturbation isotherms ($\hat{\theta}$) at 8 equally spaced time intervals in a period (period considered at late stage when the oscillation is steady state periodic) for $\lambda = 0.09$ and $A = 2 \times 10^{-1}$. Corresponding contour levels are plotted for $\bar{\theta} = \pm 5(10^{-1}, 10^{-2}, 10^{-3}, 10^{-4}, 10^{-5}, 10^{-6})$. The black triangles mark the start and end of a complete cell pair at $t = 1421.4$ which becomes eight at time $t = 1491.3$.

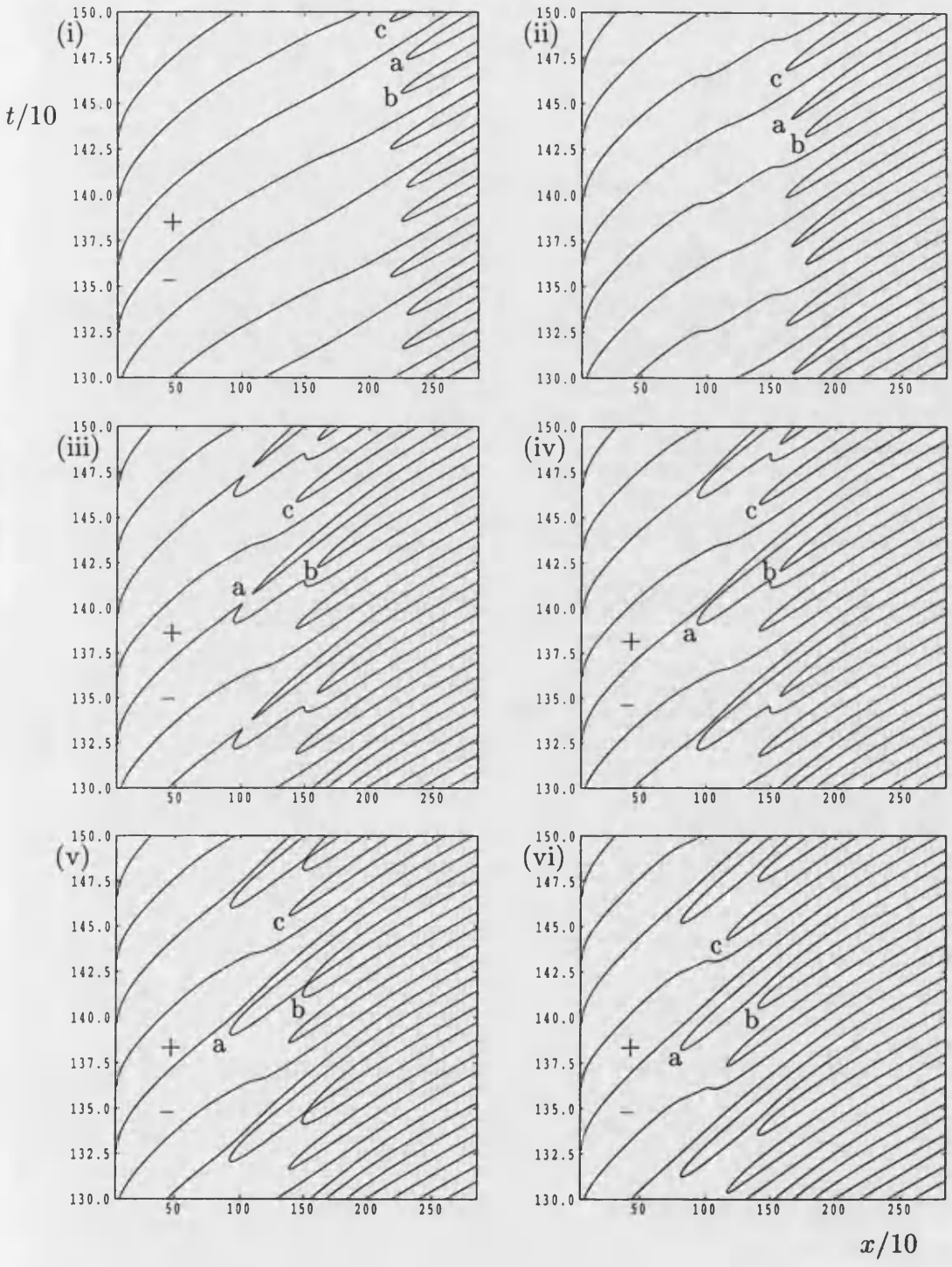

Figure 6.19: Contours of the zero level surface rate of heat transfer over the last few periods in time for $\lambda = 0.09$, and where (i) $A = 0.5 \times 10^{-1}$, (ii) $A = 1 \times 10^{-1}$, (iii) $A = 1.3 \times 10^{-1}$, (iv) $A = 1.34 \times 10^{-1}$, (v) $A = 1.4 \times 10^{-1}$, (vi) $A = 2 \times 10^{-1}$.

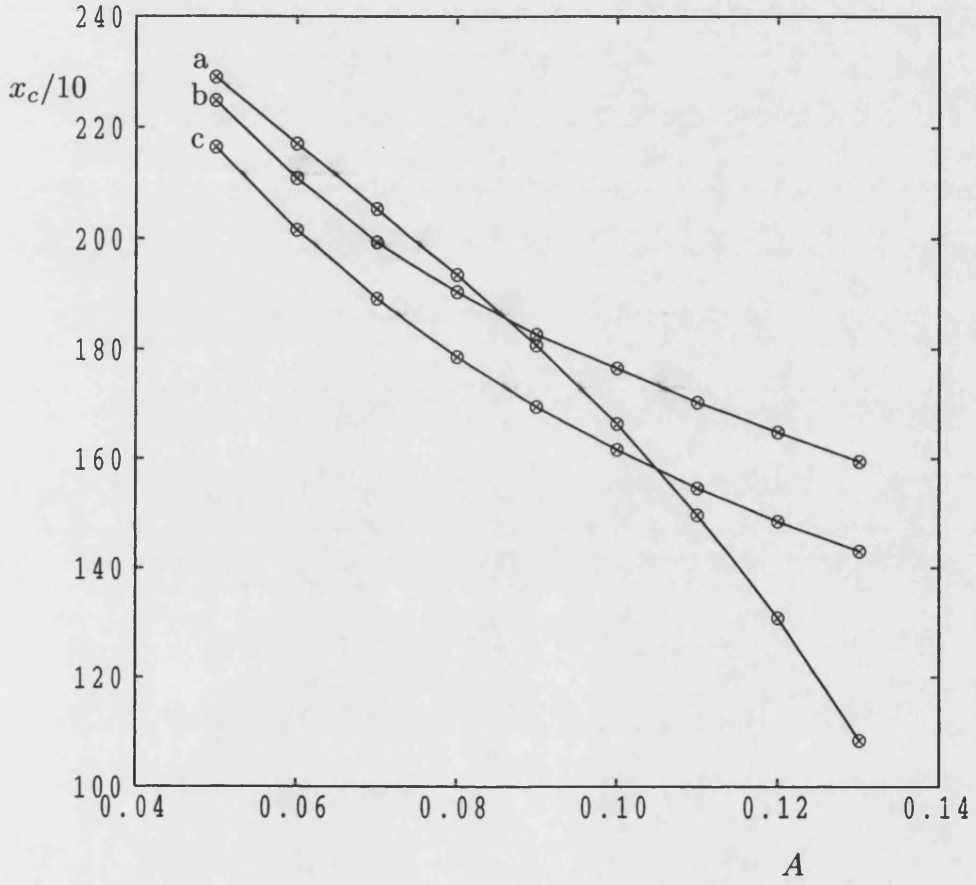

Figure 6.20: Variation of the turning points of the heat transfer with amplitude A for $\lambda = 0.09$. Curves marked 'a', 'b', and 'c' are the positions of three different turning points in Figure 6.19.

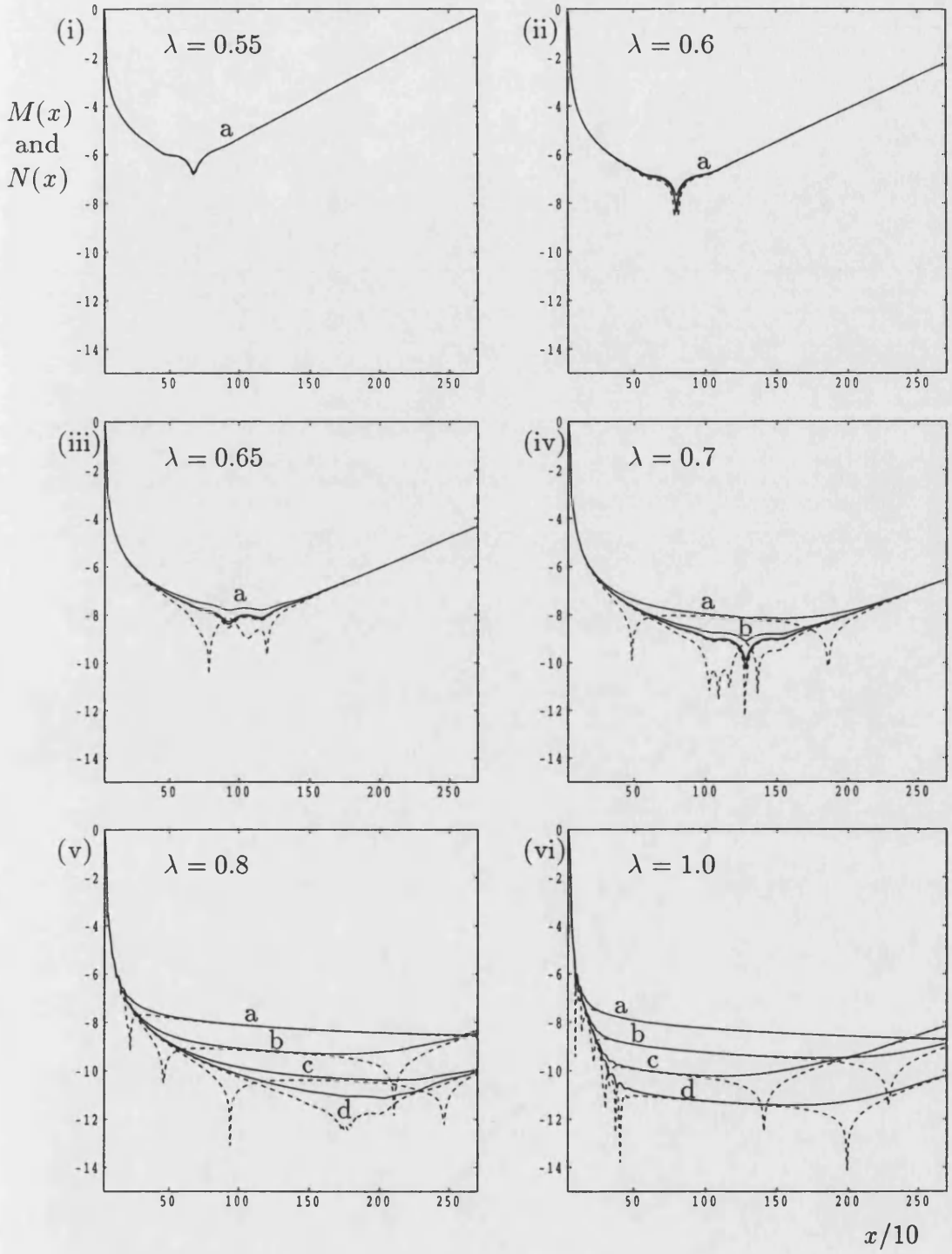

Figure 6.21: Curves representing the growth of instabilities for frequencies greater than 0.4: $M(x)$ for solid curves and $N(x)$ for dashed curves which are defined in equations (6.16) and (6.18). Here (a) $A = 10^{-2}$, (b) $A = 10^{-3}$, (c) $A = 10^{-4}$, and (d) $A = 10^{-5}$.

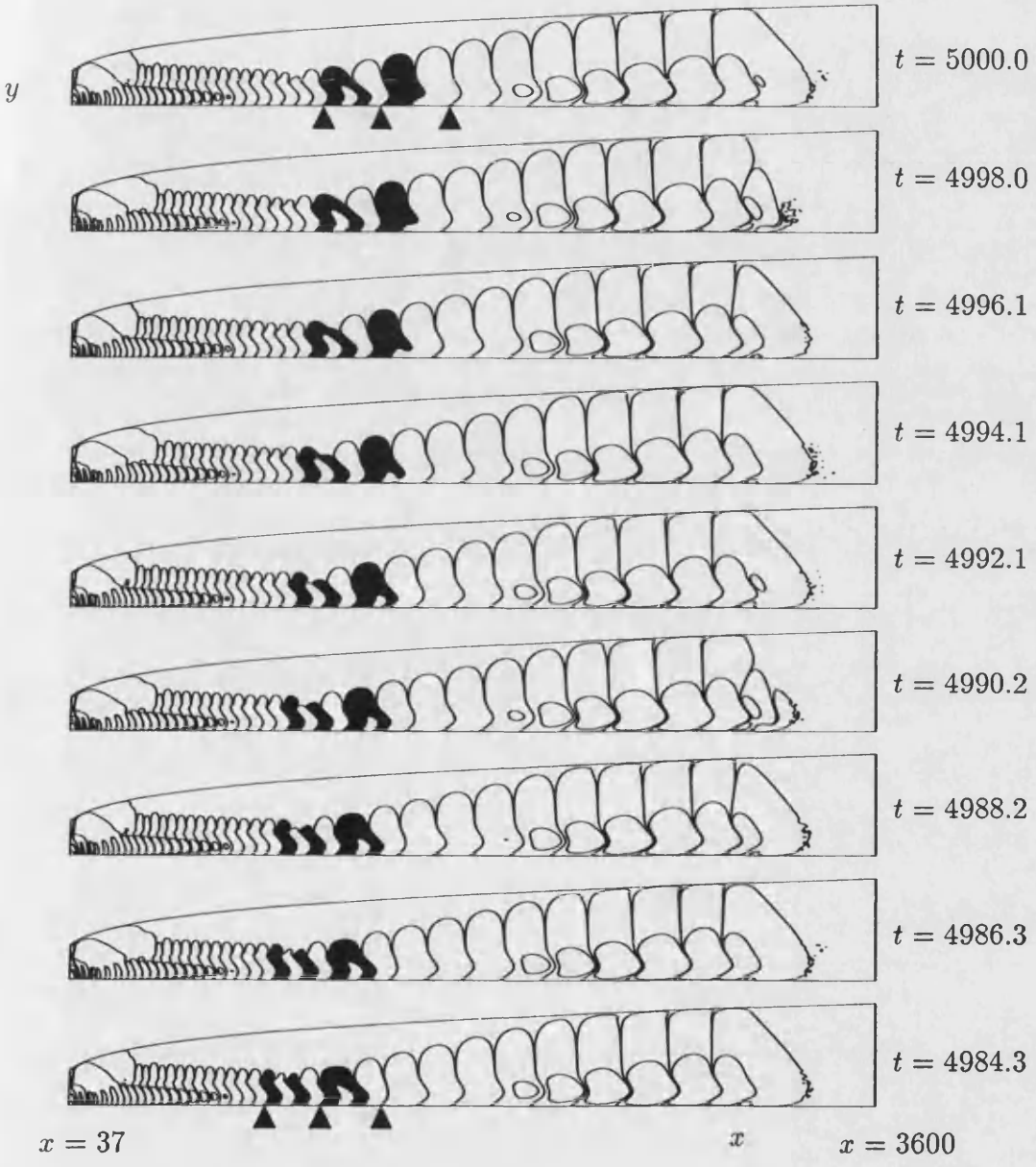

Figure 6.22: Contours of $\hat{\theta} - \hat{\theta}_{mean}$ at 8 equally spaced time intervals in the last two periods of time. Here $\lambda = 0.8$ and the maximum amplitude is at $A = 10^{-2}$. The corresponding contour levels are at $\pm 6.5(10^{-3}, 10^{-4}, 10^{-5}, 10^{-6}, 10^{-7})$.

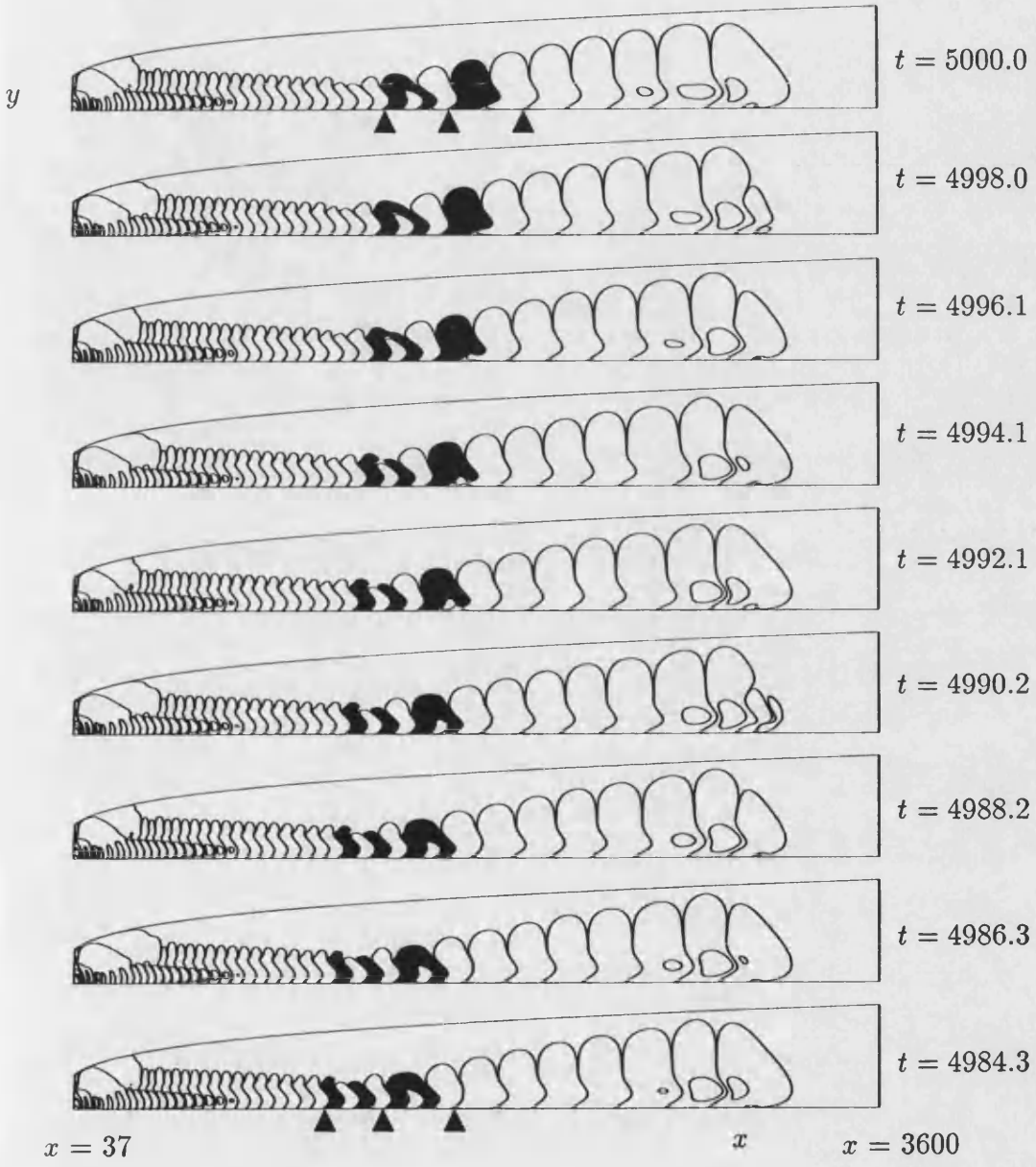

Figure 6.23: Contours of $\hat{\theta} - \hat{\theta}_{mean}$ at 8 equally spaced time intervals in the last two periods of time. Here $\lambda = 0.8$ and the maximum amplitude is at $A = 10^{-3}$. The corresponding contour levels are at $\pm 6.5(10^{-4}, 10^{-5}, 10^{-6}, 10^{-7}, 10^{-8})$.